

Distribution Agreement

In presenting this thesis or dissertation as a partial fulfillment of the requirements for an advanced degree from Emory University, I hereby grant to Emory University and its agents the non-exclusive license to archive, make accessible, and display my thesis or dissertation in whole or in part in all forms of media, now or hereafter known, including display on the world wide web. I understand that I may select some access restrictions as part of the online submission of this thesis or dissertation. I retain all ownership rights to the copyright of the thesis or dissertation. I also retain the right to use in future works (such as articles or books) all or part of this thesis or dissertation.

Signature:

Eric J. Miller

Date

Part 1. Discovery of a Fluorinated Enigmol Analog with Enhanced Pharmacokinetic and Anti-Tumor Properties. Part 2. Preferential Activation of Metabotropic Glutamate Receptor 3 over Metabotropic Glutamate Receptor 2

By

Eric J. Miller

Doctor of Philosophy

Chemistry

Dennis Liotta, Ph.D.
Advisor

David Lynn, Ph.D.
Committee Member

Simon Blakey, Ph.D.
Committee Member

Accepted:

Lisa A. Tedesco, Ph.D.

Dean of the James T. Laney School of Graduate Studies

Date

Part 1. Discovery of a Fluorinated Enigmol Analog with Enhanced Pharmacokinetic and Anti-Tumor Properties. Part 2. Preferential Activation of Metabotropic Glutamate Receptor 3 over Metabotropic Glutamate Receptor 2

By

Eric J. Miller

B.S., University of Rochester, 2009

Advisor: Dennis Liotta, Ph.D.

An abstract of

a dissertation submitted to the Faculty of the

James T. Laney School of Graduate Studies of Emory University

in partial fulfillment of the requirements for the degree of

Doctor of Philosophy

in Chemistry

2015

Abstract

Part 1. Discovery of a Fluorinated Enigmol Analog with Enhanced Pharmacokinetic and Anti-Tumor Properties. Part 2. Preferential Activation of Metabotropic Glutamate Receptor 3 over Metabotropic Glutamate Receptor 2

By Eric J. Miller

Part 1: Sphingolipids are a structurally diverse class of biomolecules that perform various functions within the cell. Of particular interest are sphingosine, which signals for programmed cell death and cell growth arrest, and sphingosine-1-phosphate, which signals for cell growth and proliferation. Via acute regulation of the intracellular concentrations of sphingosine and sphingosine-1-phosphate, the sphingolipid metabolic pathway balances cell growth and cell death signaling, rendering modulation of this pathway a reasonable strategy for the treatment of cancer. In the late 80s, our lab hypothesized that a sphingosine mimic incapable of phosphorylation by sphingosine kinase would slow cancer cell proliferation. Such a compound, Enigmol, which does not contain the primary hydroxyl group phosphorylated by sphingosine kinase, was developed in our lab. This compound is efficacious against the proliferation of a variety of human cancer cell lines *in vitro* and *in vivo*, most notably against those from prostate cancer. Enigmol also demonstrates attractive pharmacokinetic, metabolic, and toxicity profiles. The primary objective was to discover novel Enigmol analogs with maintained or enhanced tumor growth inhibition in animal models of prostate cancer. It was hypothesized that fluorinated Enigmol analogs with higher lipophilicity would demonstrate enhanced efficacy against prostate cancer cell proliferation due to increased tissue uptake as compared to Enigmol. Accordingly, a series of fluorinated Enigmol analogs were designed, synthesized, evaluated for cytotoxicity which indicated an equipotent relationship between Enigmol and fluorinated analogs. Pharmacokinetic studies demonstrated that while drug concentrations in plasma correlated with fluorine content, drug concentrations in various tissues did not. While the most lipophilic analog CF₃-Enigmol achieved significantly higher tissue concentrations than Enigmol, CF₂-Enigmol, which is more lipophilic than Enigmol but less than CF₃-Enigmol, absorbed into tissue at even higher concentrations. Furthermore, while CF₃-Enigmol was not as efficacious as Enigmol in mouse xenograft models of prostate cancer, CF₂-Enigmol is the first analog to demonstrate improved tumor growth inhibition *in vivo* as compared to Enigmol. Intellectual property was subsequently claimed, and CF₂-Enigmol has been licensed to Que Oncology.

Part 2: Glutamate is one of the main neurotransmitters in the CNS, and it activates two classes of glutamate receptors: metabotropic (mGluRs) and ionotropic (iGluRs). The mGluRs, of which there are 8 subtypes, are class C GPCRs that are further classified into groups I – III based on sequence homology, signal transduction, and pharmacology. While few subtype-selective agonists have been reported, group-selective agonists are widely used as pharmacological tools and have been implicated as potential therapeutic agents for a wide array of neurological disorders. In particular, several group II mGluR agonists have demonstrated neuroprotective activity in a variety of *in vivo* settings, highlighting the potential of group II mGluRs (mGluR2 and mGluR3) as drug targets for treating neurodegenerative diseases. Contrary to early viewpoints however, a large volume of recent literature

stresses that each individual mGluR has unique functions distinct from those of the other mGluRs, even others amongst the same group. In particular, several studies using mGluR2^{-/-} and mGluR3^{-/-} knockout mice revealed that the neuroprotective actions of selective group II mGluR agonists are entirely mediated through mGluR3, whereas selective activation of mGluR2 may be toxic. Thus, the project goal was to achieve selective mGluR3 activation, and investigation began with design and synthesis of a series of analogs of *N*-acetyl-*L*-aspartyl glutamate (NAAG) for evaluation of mGluR3 activity *in vitro* using the GloSensor cAMP Biosensor. During assay implementation, it was discovered that chloride affects activation of mGluR3 but not mGluR2. Although NAAG and analogs proved to be inactive at mGluR3 in the GloSensor assay, a combination of computational molecular modeling, pharmacology, and site-directed mutagenesis enabled elucidation of chloride as an endogenous agonist of mGluR3 that preferentially activates mGluR3 over mGluR2. Furthermore, these studies support a proposed molecular mechanism of chloride discrimination between mGluR3 and mGluR2, which can likely be exploited for the discovery of an mGluR3-selective agonist with neuroprotective properties.

Part 1. Discovery of a Fluorinated Enigmol Analog with Enhanced Pharmacokinetic and Anti-Tumor Properties. Part 2. Preferential Activation of Metabotropic Glutamate Receptor 3 over Metabotropic Glutamate Receptor 2

By

Eric J. Miller

B.S., University of Rochester, 2009

Advisor: Dennis Liotta, Ph.D.

A dissertation submitted to the Faculty of the
James T. Laney School of Graduate Studies of Emory University
in partial fulfillment of the requirements for the degree of
Doctor of Philosophy
in Chemistry

2015

Acknowledgements

I am extremely grateful to my advisor Dr. Dennis Liotta, not only for providing support and guidance during my thesis work, but also for granting me the opportunity to freely follow my intellectual curiosity. I would also like to thank my committee members Dr. Simon Blakey and Dr. David Lynn (and Dr. Lanny Liebeskind) for continued interest and encouragement. Dr. Huw Davies, Dr. Albert Padwa, Dr. Frank McDonald, Dr. Justin Gallivan, and Dr. James Snyder also deserve acknowledgement as much of my success in graduate school stemmed from early coursework with them. Additionally, I must express my sincerest appreciation for sphingolipid collaborators Dr. John Petros, Suzanne Mays, Dr. Manohar Saindane, the Emory Institute for Drug Development, and the Biomarkers Core Lab, as well as mGluR collaborators and Dr. Jarda Wroblewski, Dr. Barbara Wroblewska, Dr. John DiRaddo, Dr. Jim Snyder, Dr. Bryan Cox, and Dr. Haipeng Hu. Furthermore, the dedication and positive attitudes of Liotta Group staff members Cynthia Gaillard, Tegest Edo, Carolyn Wright, Meredith Swartz, Erica Bitten, and Marcus Rodriguez made even the most frustrating of times surmountable. Gratitude must also be extended to Emory University Chemistry Department staff members Ann Dasher, Todd Polley, Steve Krebs, Patti Barnet, Patrick Morris, Tim Stephens, Stephanie Thioubou, Ethyl Ellington, and Atasha Sutton. Finally I would like to thank my family (Mom, Bryan, Steve, Grandmom Berman, Aunt Val, Aunt Ruth, and Grandmom Miller) and friends (Dr. Pieter Burger, Dr. Mark Baillie, Dr. Jason Holt, Dr. Terry Moore, Dr. Tim Acker, Dr. Val Truax, Katie Strong, Dr. Kevin Yehl, Matthew Smentek, and Le Doan) for unwavering support during this endeavor.

Table of Contents

Part 1. Discovery of a Fluorinated Enigmol Analog with Enhanced Pharmacokinetic and Anti-Tumor Properties

1.1. Introduction

1.1.a. Roles of Sphingolipid Biochemistry and Cancer.....	1
1.1.b. Enigmol, a 1-Deoxy-Sphingoid Base with Anti-Cancer Activity.....	4
1.1.c. Design, Synthesis, and <i>in vitro</i> Cytotoxicity of Enigmol Analogs.....	7

1.2. Results and Discussion

1.2.a. Design and Synthesis of CF ₂ -Enigmol.....	11
1.2.b. Cytotoxicity against Human Prostate Cancer Cells <i>in vitro</i>	22
1.2.c. 1 st Scale Up Preparation of CF ₂ -Enigmol.....	26
1.2.d. Pharmacokinetics of Fluorinated Enigmol Analogs.....	31
1.2.e. 2 nd Scale Up Preparation of CF ₂ -Enigmol.....	36
1.2.f. Synthesis and <i>in vitro</i> Cytotoxicity of CF ₂ -Enigmol Metabolites.....	52
1.2.g. Anti-Tumor Activity of Fluorinated Enigmol Analogs <i>in vivo</i>	54

1.3. Conclusions.....

1.4. Experimental Methods

1.4.a. Synthetic Procedures.....	59
1.4.b. cLogP Calculations.....	87
1.4.c. Human Prostate Cancer Viability Assays.....	88
1.4.d. Rat Plasma Pharmacokinetic Assays (i.v.).....	88
1.4.e. Rat Plasma Pharmacokinetic Assays (p.o.).....	89
1.4.f. Rat Tissue Distribution Assays (p.o.).....	90
1.4.g. Mouse Xenograft Studies.....	91
1.4.h. Bioanalytical LC-MS/MS Assays.....	92

*Part 2. Preferential Activation of Metabotropic Glutamate Receptor 3 over Metabotropic
Glutamate Receptor 2*

2.1. Introduction

2.1.a. Seven-Transmembrane Receptors and G Protein Coupling.....	94
2.1.b. Metabotropic Glutamate Receptors.....	98
2.1.c. Subtype-Selective mGluR3 Activation and Neuroprotection.....	104

2.2. Results and Discussion

2.2.a. Design of NAAG Analogs.....	109
2.2.b. Synthesis of NAAG Analogs.....	115
2.2.c. GloSensor Assay Measures Group II and III mGluR Activity.....	119
2.2.d. mGluR3 Activity of NAAG and Analogs.....	129
2.2.e. Group II mGluR Antagonist-Mediated Inverse Agonism.....	130
2.2.f. Pharmacological Characterization of Chloride.....	134
2.2.g. Implications for Selective mGluR3 Drug Design.....	146

2.3. Conclusions..... 148

2.4. Experimental Methods

2.4.a. Synthetic Procedures.....	149
2.4.b. Molecular Modeling.....	159
2.4.c. GloSensor Assays.....	162
2.4.d. LANCE cAMP Assays.....	165

Part 3. Overall Conclusions

3.1. Crossover between Sphingolipids and mGluRs..... 166

3.2. References..... 171

List of Tables and Figures

Part 1. Discovery of a Fluorinated Enigmol Analog with Enhanced Pharmacokinetic and Anti-Tumor Properties

Figure 1: Sphingolipid Biosynthetic and Metabolic Pathway.....	2
Figure 2: Equilibrium between Cell Death and Cell Survival Signaling.....	4
Figure 3: Design Principles Leading to the Discovery of Enigmol.....	5
Scheme 1: Synthetic Routes Established in the Liotta Group to Access Enigmol and Analogs.....	8
Table 1: Cytotoxicity of Enigmol Analogs against Human Prostate Cancer Cells <i>in vitro</i>	10
Figure 4: New Strategy to Enhance Anti-Tumor Activity by Increasing Lipophilicity.....	11
Scheme 2: Retrosynthetic Analysis for CF ₂ -Enigmol.....	12
Scheme 3: Synthesis of α,α -Difluoro Aldehyde 17	13
Scheme 4: New Retrosynthetic Analysis for CF ₂ -Enigmol.....	14
Scheme 5: Synthesis of α -Keto Ester 28	15
Scheme 6: Synthesis of α,α -Difluoro Methyl Ketone 26	16
Scheme 7: Synthesis of <i>N,N</i> -Dibenzyl- α -Amino Aldehyde 25 and Subsequent Aldol Reaction.....	18
Scheme 8: Assignment of Relative Stereochemistry for β -Hydroxy Ketone 35	19
Scheme 9: β -Hydroxy Ketone Reduction and Determination of Relative Diol Stereochemistry.....	21
Scheme 10: Final Deprotection of All Four Diastereomers of 2 <i>S</i> -CF ₂ -Enigmol.....	22
Table 2: Cytotoxicity of 2 <i>S</i> -CF ₂ -Enigmol Diastereomers against Human Prostate Cancer Cells <i>in vitro</i>	23
Table 3: Cytotoxicity of Fluorinated Enigmol Analogs against Human Prostate Cancer Cells <i>in vitro</i>	24
Figure 5: Concentration-Response Curves of Enigmol, CF ₃ -Enigmol, and CF ₂ -Enigmol.....	25
Scheme 11: 1 st Scale Up of α,α -Difluoro Methyl Ketone 26	27

Table 4: Optimization of BH ₃ -Me ₂ S Reduction of Carboxylic Acid 6	30
Scheme 12: 1 st Scale Up of CF ₂ -Enigmol.....	31
Figure 6: Plasma Pharmacokinetics after 2 mg/kg i.v. Administration.....	32
Figure 7: Plasma Pharmacokinetics and Tissue Distribution after 10 mg/kg p.o. Administration.....	33
Figure 8: Plasma Pharmacokinetics in the Same Vehicle.....	35
Scheme 13: Retrosynthetic Analysis and 2 nd Scale Up Preparation of α,α -Difluoro Ester 27	38
Table 5: Optimization of Hydrogenation of Olefin 48 to α,α -Difluoro Ester 27	40
Scheme 14: 2 nd Scale Up of α,α -Difluoro Methyl Ketone 26	41
Scheme 15: Retrosynthetic Analyses for <i>N,N</i> -Dibenzyl- α -Amino Aldehyde 25	42
Scheme 16: 2 nd Scale Up Preparation of <i>N,N</i> -Dibenzyl- α -Amino Aldehyde 25	43
Figure 9: Diastereoselectivity of Aldol Reaction between Methyl Ketone 26 and Aldehyde 25	45
Table 6: 2 nd Scale Up of β -Hydroxy Ketone 35	46
Figure 10: Diastereoselectivity of Reduction of β -Hydroxy Ketone 35	49
Scheme 17: 2 nd Scale Up Preparation of CF ₂ -Enigmol.....	51
Scheme 18: Synthesis of CF ₂ -Enigmol Metabolites.....	53
Table 7: Cytotoxicity of CF ₂ -Enigmol Metabolites against Human Prostate Cancer Cells <i>in vitro</i>	54
Figure 11: Enigmol vs. CF ₃ -Enigmol in Mouse Xenograft Model of Prostate Cancer.....	56
Figure 12: Enigmol vs. CF ₂ -Enigmol in Mouse Xenograft Model of Prostate Cancer.....	57

***Part 2. Preferential Activation of Metabotropic Glutamate Receptor 3 over Metabotropic
Glutamate Receptor 2***

Figure 13: Current Model of 7TMR Activation.....	95
Figure 14: G Protein Activation Cycle.....	96
Figure 15: Structural Comparison of Class A (β_2 AR) and Class C (mGluR3) 7TMRs.....	98
Figure 16: mGluR-Mediated G Protein Signaling.....	99

Figure 17: Homodimeric Arrangement of mGluRs.....	100
Table 8: Group-Selectivity of Competitive mGluR Agonists.....	101
Table 9: Group-Selectivity of Competitive mGluR Antagonists.....	102
Figure 18: mGluR-Mediated Glutamatergic Synaptic Transmission.....	103
Table 10: Potency and Subtype-Selectivity of Competitive Group II mGluR Agonists.....	107
Figure 19: mGluR3 Orthosteric Binding Pocket Interactions with Glutamate and DCG-IV.....	110
Figure 20: Control Docking Experiments at mGluR3 <i>in silico</i> Models.....	111
Figure 21: Predicted NAAG Docking Poses at mGluR3.....	113
Scheme 19: Design of NAAG Analogs to Probe Putative Binding Poses at mGluR3.....	114
Scheme 20: Retrosynthetic Analyses of NAAG Analogs.....	115
Scheme 21: Preparation of Amino Acid Synthons for Synthesis of NAAG Analogs.....	116
Scheme 22: Synthesis of NAAG Analogs.....	118
Figure 22: Forskolin-Stimulated cAMP Production in CHO-Glo Cells.....	119
Figure 23: Ion Sensitivity of Glutamate-Mediated Group II and III mGluR Activation.....	121
Table 11: Composition of Buffers Used to Examine Group II and III mGluR Ion Sensitivity.....	122
Figure 24: Group II and III mGluR-Mediated Inhibition of cAMP Production.....	123
Figure 25: Concentration-Dependent, PTX-Sensitive, Agonist-Mediated mGluR Activation.....	124
Table 12: Comparison of Previously Reported Agonist Potencies with those from GloSensor.....	125
Figure 26: Real-Time Reversibility of Agonist and Antagonist Effects on cAMP Production.....	126
Figure 27: Quantitation of mGluR Antagonist Potency Using GloSensor.....	127
Figure 28: Schematic Representation of the GloSensor Assay.....	128
Figure 29: Activity of NAAG and Analogs and mGluR3.....	129
Figure 30: Group II and III mGluR Antagonist-Mediated, PTX-Sensitive Inverse Agonism.....	131
Figure 31: Antagonist-Mediated, Glutamate-Independent Inverse Agonism at mGluR3.....	132
Figure 32: Chloride-Specific Activity at Group II and III mGluRs.....	134
Figure 33: Chloride Activation of mGluR3, mGluR4, mGluR6, and mGluR8, but not mGluR2....	135

Table 13: Quantitation of Chloride-Mediated Group II and III mGluR Activity.....	136
Figure 34: Disruption of the mGluR3 Chloride Binding Pocket at mGluR2.....	137
Figure 35: Definition of Chloride as Both an Agonist and a PAM at Group II and III mGluRs.....	139
Figure 36: “Arginine Flip”-Mediated Chloride Discrimination between mGluR3 and mGluR2.....	140
Figure 37: Molecular Switch-Controlled Chloride Sensitivity at mGluR3 and mGluR2.....	142
Figure 38: Chloride Sensitivity Unaffected by Mutation of D279 or E273.....	144
Figure 39: Preferential Activation of mGluR3 over mGluR2 by Quisqualate.....	146
Scheme 23: New Design Principles for mGluR3 Selectivity.....	148

Part 1. Discovery of a Fluorinated Enigmol Analog with Enhanced Pharmacokinetic and Anti-Tumor Properties

1.1. Introduction

1.1.a. Roles of Sphingolipid Biochemistry in Cancer

Sphingolipids are a structurally diverse class of endogenous lipids that contain a common sphingoid base core, which is 18 carbons in length and decorated with a 2*S*-amino-1,3-diol head group. Exhibiting this core structure, sphingosine is a versatile biosynthetic intermediate that is enzymatically modified to generate a wide array of sphingolipid species, many of which act as second messengers¹. The mammalian sphingolipid biosynthetic pathway (**Figure 1**) begins with serine palmitoyl transferase (SPT)-catalyzed coupling of *L*-serine and palmitoyl-CoA to generate 3-ketosphinganine, which can then be reduced to sphinganine by 3-ketosphinganine reductase (KSR). Sphinganine is a substrate for dihydroceramide synthase (DS), which facilitates acylation of the sphingoid basic amine to produce dihydroceramide, which can subsequently be converted to fatty amide-containing ceramide via enzymatic activity of dihydroceramide desaturase (DD), a type of ceramide synthase (CS). Ceramide, which is a key component of lipid rafts², can then be subjected to glycosyltransferase (GT)-mediated glycosylation of the primary hydroxyl group to generate a class of glycosphingolipids, including cerebrosides and gangliosides, which are integrally involved in cell-cell communication and can be converted back to ceramide via action of glycosylceramidase³ (GCD). Alternatively, sphingomyelin synthase (SMS) can catalyze the coupling of ceramide and phosphatidylcholine to yield sphingomyelin, a structural component of the myelin sheath that is subject to sphingomyelinase (SM)-mediated retrograde biosynthesis of ceramide. Sphingosine can instead be generated from fatty amide-containing ceramide via ceramidase (CD)-facilitated deacylation, a reaction that can be reversed by the activity of sphingosine *N*-acyltransferase (SNT), another type of CS. The primary hydroxyl group of sphingosine is susceptible to phosphorylation by sphingosine kinase (SK), leading to sphingosine-1-phosphate

(S1P), which is the endogenous agonist of a class of seven-transmembrane S1P receptors⁴; this reaction can be reversed via sphingosine-1-phosphate phosphatase (S1PP)-mediated dephosphorylation. Notably, sphingosine is also a substrate for *N*-methyltransferase (NMT), which converts sphingosine to *N*-methyl sphingosine and *N,N*-dimethyl sphingosine⁵. Finally, S1P can be degraded by sphingosine-1-phosphate lyase (S1PL) to yield phosphoethanolamine and hexadec-2-enal, marking the sole exit of the sphingolipid metabolic pathway. **Figure 1** highlights only a small subset of the sphingolipid biosynthetic route, which can be generally characterized as a complex, highly fluid, and rapid equilibrium between a large number of pleiotropic signaling molecules^{1,2}.

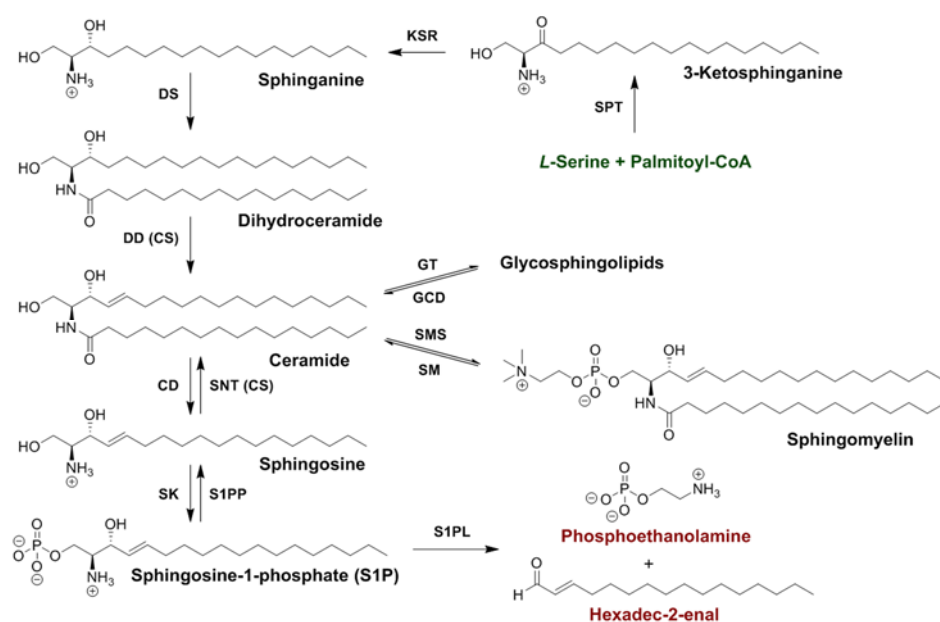


Figure 1: Sphingolipid Biosynthetic and Metabolic Pathway. This simplified depiction of the sphingolipid biochemical pathway begins with serine palmitoyl transferase (SPT)-mediated coupling of *L*-serine and palmitoyl-CoA, involves enzymatic activity of dihydroceramide synthase (DS), dihydroceramide desaturase (DD), ceramidase (CD), sphingosine *N*-acyltransferase (SNT), sphingosine kinase (SK), and sphingosine-1-phosphate phosphatase (S1PP), and ends with sphingosine-1-phosphate lyase (S1PL)-catalyzed degradation of sphingosine-1-phosphate to phosphoethanolamine and hexadec-2-enal.

Such rapid interconversion has made the cellular processes elicited by specific sphingolipids difficult to elucidate, typically requiring addition of enzyme inhibitors to control metabolic conversion⁶, upregulation⁷ or downregulation⁸ of metabolic enzymes to shift the sphingolipid equilibrium, or

lipidomics to relate changes in numerous sphingolipid concentrations to variations in cellular function⁵. Further complicating this scenario are the opposing roles of sphingosine and S1P in processes relating to cell death and cell survival, respectively (**Figure 2**). For example, while exogenous sphingosine inhibited Chinese hamster ovary (CHO) cell viability *in vitro*⁹, cultured 3T3 fibroblasts overexpressing recombinant SK demonstrated substantially increased SK activity and concomitant intracellular levels of S1P, resulting in elevated DNA synthesis, increased cell proliferation, and decreased serum deprivation-induced apoptosis, as compared to mock transfects¹⁰. Thus, the relative intracellular concentrations of sphingosine and S1P, which are acutely regulated by the activity of SK and other metabolic enzymes, crucially influence cell fate decisions. Such functionally contrasting, cell fate-related activities have implicated a critical role in cancer progression for S1P, as well as for SK, which has been deemed an oncogene¹¹. Supporting this claim are reports of (1) reduced doxorubicin-induced and sphingosine-induced human breast cancer cell death in cultured MCF-7 cells transfected with SK1, as compared to mock-transfected cells⁷, (2) pronounced tumor formation in BALB/c nu/nu mice with mammary fat pads injected with SK1-transfected MCF-7 cells, versus those injected with mock-transfected cells, (3) induction of tumorigenicity in NOD/SCID mice subcutaneously injected with recombinant SK-expressing 3T3 fibroblasts, as compared to those injected with mock-transfected fibroblasts¹¹, (4) decreased intestinal adenoma diameter in *Apc*^{Min/+} SK1^{-/-} knockout mice⁸ versus *Apc*^{Min/+} SK1^{+/+} mice, and (5) elevated expression of SK1 mRNA in solid tumors localized in the human breast, uterus, ovary, lung, colon, small intestine, and rectum as compared to healthy human tissue of the same type¹². Alternatively, the intrinsic cell death signaling profile of sphingosine is highlighted by (1) sphingosine-induced cytotoxicity against CHO cell viability *in vitro*⁹, (2) increased apoptosis in 3T3 fibroblasts transfected with recombinant S1PP, as compared to mock-transfected fibroblasts¹³, (3) sphingosine-mediated apoptosis in human leukemia (HL60, CMK7, and U937) cells and human colon cancer (HT29, HRT18, MKN74, and COLO205) cells *in vitro*¹⁴, and (4) dose-dependent, sphingosine-induced cytotoxicity against cultured human melanoma (C8161 and A2058) cells¹⁵. Despite pro-apoptotic signaling however, the potential for exogenous sphingosine as a

chemotherapeutic agent is substantially limited by rapid conversion to S1P and other metabolites. Accordingly, inhibition of SK is an anti-cancer strategy that many laboratories have explored^{16,17}.

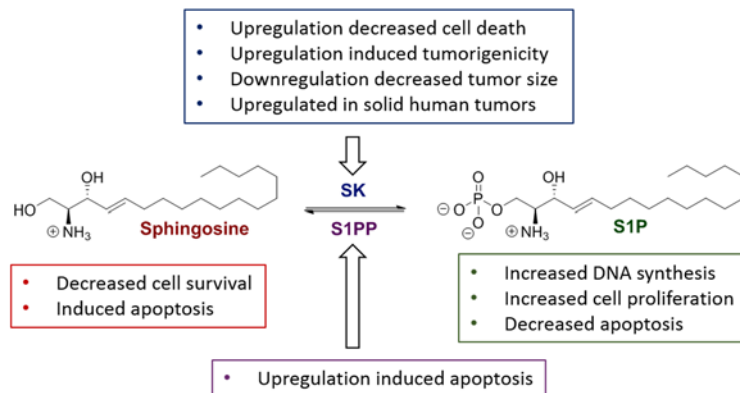


Figure 2. Equilibrium between Cell Death and Cell Survival Signaling. Sphingosine kinase (SK) and sphingosine-1-phosphate phosphatase (S1PP) regulate relative intracellular concentrations of cytotoxic sphingosine and growth-stimulatory sphingosine-1-phosphate.

1.1.b. *Enigmol*, a 1-Deoxy-Sphingoid Base with Anti-Cancer Activity

In contrast, our research group envisioned that a sphingosine mimic insusceptible to phosphorylation by SK could reestablish a proper balance of sphingosine and S1P activity, which could result in the inhibition of cancer progression. Specifically, it was hypothesized that sphingoid base analogs lacking the C-1 hydroxyl group would adopt the cytotoxic signaling profile of sphingosine, while avoiding conversion to potentially pro-mitotic, S1P-like metabolites; accordingly, 1-deoxy-sphingosine analogs were pursued (**Figure 3**). As sphingosine ($IC_{50} = 2.8 \mu M$) was more potent against CHO cell viability than both ceramide ($IC_{50} > 100 \mu M$) and sphingosines of different lengths⁹ ($3.2 \mu M \leq IC_{50} \leq 95 \mu M$), analogs were designed to retain the sphingoid basic amino group and to be 18 carbons in length. Notably, 1-deoxysphingosine analogs would demonstrate lower aqueous solubility and higher lipophilicity than sphingosine, due to the decrease in hydrophilicity. Therefore, an additional secondary hydroxyl group was proposed to facilitate close replication of sphingosine hydrophilicity. C-5 was chosen as an appropriate position because a class of 5-hydroxy sphingolipids called fumonisins are fungal toxins that act via inhibition of CS to elevate intracellular concentrations of sphingoid bases^{6,18}.

Of course, adding a hydroxyl group to the C-5 position of sphingosine would result in a tautomerizable enol with poor stability. Even if the equilibrium between tautomers heavily favored the enol form due to intramolecular hydrogen bonding interactions, any keto tautomer that formed would be prone to intramolecular cyclocondensation and subsequent enamine formation. Because sphingosine ($IC_{50} = 2.8 \mu\text{M}$) and sphinganine ($IC_{50} = 2.9 \mu\text{M}$) demonstrated equipotent cytotoxicity against CHO cell viability *in vitro*⁹, as well as very similar efficacy against cultured human melanoma (C8161 and A2058) cell survival¹⁵, the 4,5-olefin of sphingosine was deemed unnecessary for activity, and thus, unnecessary for 1-deoxy-sphingosine analogs. The application of these design principles led to the pursuit of fully saturated, 1-deoxy-5-hydroxy-sphingoid base enigmol.

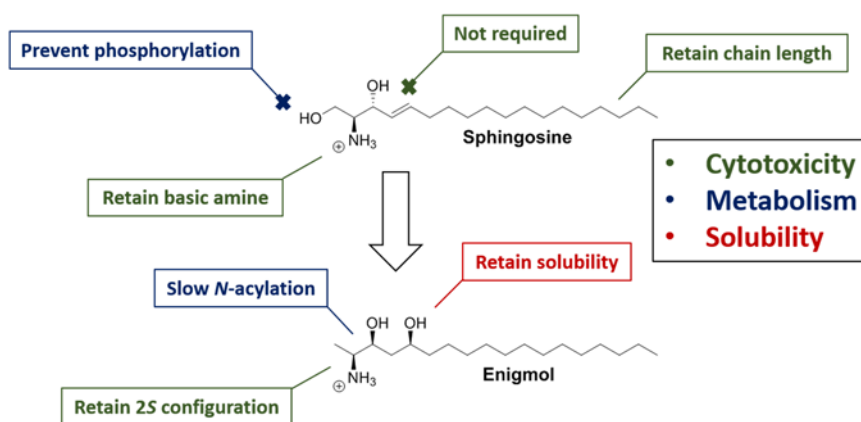


Figure 3. Design Principles Leading to the Discovery of Enigmol. Structural motifs highlighted in green, blue, and red were retained or modified to optimize drug properties relating to cytotoxicity, metabolism, and solubility, respectively.

While the three unnatural stereoisomers of sphingosine demonstrated equipotent cytotoxicity to naturally occurring *D-erythro*-sphingosine against CHO cell viability⁹ ($2.0 \mu\text{M} \leq IC_{50} \leq 2.8 \mu\text{M}$), *2S,3S,5S*-enigmol was > 3-fold more potent than *2R,3S,5S*-enigmol against human ovarian cancer (A2780, $IC_{50} = 3.5 \mu\text{M}$ and $13 \mu\text{M}$, respectively) and human lung cancer (SW1573, $IC_{50} = 3.0 \mu\text{M}$ and $9.7 \mu\text{M}$, respectively) cell proliferation¹⁹, suggesting preference for the natural *2S* configuration. Additionally, *2S,3R,5R*-enigmol was ≥ 5 -fold less active against PC3 and LNCaP cell viability ($IC_{50} = 49.3 \mu\text{M}$ and $50.0 \mu\text{M}$, respectively) than the other three *2S*-enigmol diastereomers²⁰ ($5.0 \mu\text{M} \leq IC_{50} \leq$

9.7 μM and $9.7 \mu\text{M} \leq \text{IC}_{50} \leq 10.3 \mu\text{M}$, respectively). Furthermore, a substantially slower rate of CS-mediated *N*-acylation was observed for the *threo* isomers, 2*S*,3*S*,5*S*-enigmol ($V_{\text{max}}/K_{\text{m}} = 5 \text{ pmol}\cdot\text{mg}^{-1}\cdot\text{min}^{-1}\cdot\mu\text{m}^{-1}$) and 2*S*,3*S*,5*R*-enigmol ($V_{\text{max}}/K_{\text{m}} = 4 \text{ pmol}\cdot\text{mg}^{-1}\cdot\text{min}^{-1}\cdot\mu\text{m}^{-1}$), than for the corresponding *erythro* stereoisomers, 2*S*,3*R*,5*R*-enigmol ($V_{\text{max}}/K_{\text{m}} = 125 \text{ pmol}\cdot\text{mg}^{-1}\cdot\text{min}^{-1}\cdot\mu\text{m}^{-1}$) and 2*S*,3*R*,5*S*-enigmol²¹ ($V_{\text{max}}/K_{\text{m}} = 42 \text{ pmol}\cdot\text{mg}^{-1}\cdot\text{min}^{-1}\cdot\mu\text{m}^{-1}$). Since *N*-acylation would result in ceramide-like compounds that would likely demonstrate significantly weaker cytotoxicity than the corresponding sphingoid bases⁹, a slow rate of CS-mediated metabolism, and accordingly, a *syn*-relationship between the 2*S* amine and the C-3 hydroxyl group, was desired. These considerations, coupled with a highly diastereoselective aldol approach developed in our laboratory to furnish 2*S*,3*S*,5*S*-enigmol²² (hereafter referred to as Enigmol), indicated Enigmol as the lead compound for further experimentation. Importantly, Enigmol is not phosphorylated by SK or other kinases²³, and notably, its mechanism of action involves inhibition of SK²³, CS²¹, and protein kinase C²⁴ (PKC).

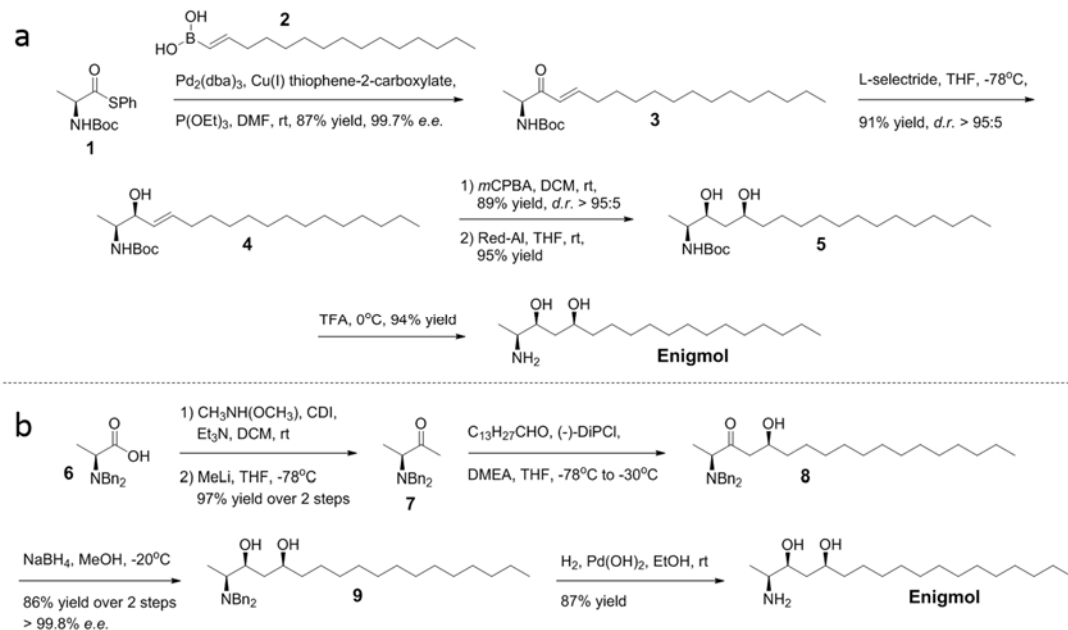
Enigmol demonstrated cytotoxic activity *in vitro* ($0.4 \mu\text{M} \leq \text{IC}_{50} \leq 14\mu\text{M}$) against the proliferation of all 57 human cancer cell lines screened by the National Cancer Institute, and it additionally outperformed both the cytotoxic and caspase-stimulatory properties of sphingosine in human colon carcinoma (HT29) cells and human prostate cancer (DU145) cells²³. Enigmol is also active *in vitro* against the viability of both androgen-sensitive (LNCaP, $\text{IC}_{50} = 9.7 \mu\text{M}$) and androgen-insensitive (PC3, $\text{IC}_{50} = 10.3 \mu\text{M}$) human prostate cancer cell lines²⁰. While the majority of compounds with micromolar anti-cancer activity *in vitro* cannot achieve therapeutically effective tumor concentrations *in vivo*, Enigmol efficiently partitions into tissue²⁵, allowing the buildup of drug reservoirs after multiple oral doses. This is consistent with the significant anti-tumor efficacy of Enigmol in multiple mouse models of cancer, including Min mouse models of intestinal cancer (6 weeks, once daily oral dosing, 0.025% food by mass, $n \geq 8$ per treatment group), as well as DU145 cell nu/nu Balb/c mouse (32 days, once daily oral dosing, 8 mg/kg via intraperitoneal injection for the first 5 days, $n = 10$ per treatment group) and PC3 cell nu/nu athymic mouse (40 days, once daily oral dosing, 10 mg/kg via gavage, $n = 15$ per treatment group) xenograft models of prostate cancer²³. Notably,

inhibition of tumor growth was not accompanied by systemic toxicity as evaluated using histopathology, clinical pathology, body mass monitoring, and liver and kidney function biomarkers. In a subsequent study, Enigmol (once daily oral dosing, 10 mg/kg) was compared head-to-head with surgical androgen-derivation therapy (castration, n = 10-12) and with hormone-refractory prostate cancer standard of care docetaxel (once weekly dosing, 15 mg/kg via intraperitoneal injection, n = 15) in LNCaP cell (45 days, once daily oral dosing, 10 mg/kg via gavage, n = 10-12) and PC3 cell (32 days, once daily oral dosing, 10 mg/kg via gavage, n = 15) mouse xenograft models of prostate cancer, respectively²⁰. Throughout the time courses of these experiments, Enigmol demonstrated comparable efficacy to both castration and docetaxel treatment, emphasizing the clinical chemotherapeutic potential of Enigmol.

1.1.c. Design, Synthesis, and *in vitro* Cytotoxicity of Enigmol Analogs

These results encouraged the synthesis and subsequent cytotoxic evaluation of various Enigmol analogs^{20,26,27}, the drug discovery process for which was enabled by two highly diastereoselective syntheses of Enigmol, including a Liebeskind-Srogl cross-coupling approach²⁰, as well as the aforementioned aldol-based methodology²². The former synthetic route (**Scheme 1a**) began with Liebeskind-Srogl cross-coupling between thioester **1** and boronic acid **2** to yield enone **3**, which was then subjected to substrate-directed, diastereoselective reduction with L-selectride to generate 2,3-*syn*-aminoalcohol **4**. Subsequent substrate-directed diastereoselective epoxidation with *m*CPBA, followed by regioselective epoxide opening with Red-Al, produced aminodiol **5**, which was finally deprotected under acidic conditions to yield Enigmol. Alternatively, the aldol approach to access Enigmol (**Scheme 1b**) began with a two-step Weinreb ketone synthesis to convert carboxylic acid **6** to methyl ketone **7**, which subsequently underwent (-)-DiPCl-mediated diastereoselective aldol reaction with tetradecanal to yield β -hydroxy ketone **8**. This crude intermediate, which was carried forward without chromatographic purification to prevent epimerization of the susceptible C-2 chiral center, was then subjected to substrate-directed, diastereoselective ketone reduction with sodium borohydride,

producing aminodiol **9** as a single diastereomer. Finally, deprotection under palladium-catalyzed hydrogenolysis conditions afforded **Enigmol**.



Scheme 1: Synthetic Routes Established in the Liotta Group to Access Enigmol and Analogs. Synthetic preparation of Enigmol and analogs was enabled by two diastereoselective syntheses of Enigmol involving either (a) Liebeskind-Srogl coupling²⁰ or (b) aldol reaction²².

These two synthetic approaches to Enigmol were employed for the preparation of various Enigmol analogs, which were subsequently assayed for cytotoxicity against human prostate cancer cells *in vitro* (**Table 1**). While LNCaP cells represent a cell-based model for hormone-dependent prostate cancer with low metastatic potential, PC3 cells exemplify an *in vitro* model of hormone-independent prostate cancer with high metastatic potential²⁸. As described previously, Enigmol potency is relatively insensitive to change in C-3 or C-5 hydroxyl stereocenter, but changing both to the *R* configuration (2*S*,3*R*,5*R*-enigmol) decreased cytotoxicity 5-fold²⁰. Furthermore, SK-mediated conversion of Enigmol to S1P-like derivatives of opposing function was not observed²³, CS-mediated transformation to less active ceramide-like metabolites was relatively slow²¹, and NMT-mediated metabolism results in the production of *N*-methyl Enigmol and *N,N*-dimethyl Enigmol²⁵, both of which retain Enigmol-like activity. Although *N*-methyl Enigmol is 2.5-fold less potent than Enigmol against PC3 cell viability,

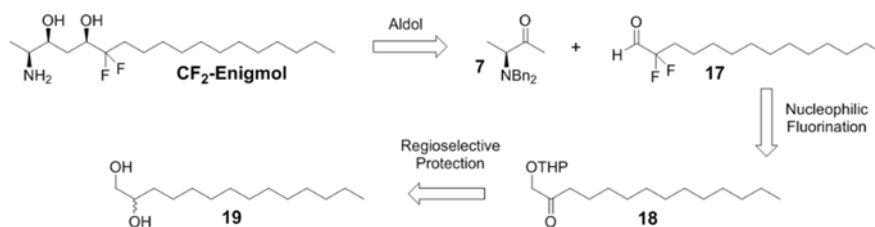
N-methyl Enigmol would likely exhibit a slower rate of CS-mediated *N*-acylation due to the increase in steric bulk at the reaction center, which could result in a longer biological lifetime than Enigmol. Coupled with the increase in lipophilicity, which could lead to enhanced oral bioavailability, these considerations highlight the potential for *N*-methyl Enigmol to overcome *in vivo* the drop in PC3 cell cytotoxicity *in vitro*. This is consistent with the enhanced systemic exposure and terminal plasma half-life ($t_{1/2}$) of *N*-methyl Enigmol versus Enigmol in mice after oral administration (10 mg/kg or 30 mg/kg via gavage, $n = 3$ per treatment group), as well as the similar efficacy of Enigmol and *N*-methyl Enigmol in a PC3 cell mouse xenograft model of prostate cancer²⁰ (20 days, once daily oral dosing, 10 mg/kg via gavage, $n = 10$ per treatment group). Additionally, three unsaturated analogs were synthesized to evaluate the effects of lipid chain rigidification on potency²⁷. While *cis*-olefin **10** and *trans*-olefin **11** retained the cytotoxic profile of Enigmol, these compounds were less active against human prostate cancer cells *in vitro*. In contrast, alkyne **12** was inactive up to 100 μ M against both LNCaP and PC3 cell lines. These results suggest that not all of the proteins that Enigmol targets can accommodate tail rigidification, and they demonstrate that the flexibility of the fully saturated lipid tail is optimal for anti-cancer activity. Furthermore, *gem*-dimethyl analogs **13**, **14**, and **15** were prepared in order to evaluate the activity of analogs with decreased stereochemical complexity and increased steric bulk proximal to the amino group²⁶. It was hypothesized that these changes would further decrease CS-mediated *N*-acylation, which was expected to result in improved cytotoxicity *in vitro* due to increased biological lifetime. While oxime **15** demonstrated 2.5-fold diminished activity against both LNCaP and PC3 cells as compared to Enigmol, analogs **13** and **14** were equipotent to Enigmol against PC3 cell viability, but 2.5-fold less active against LNCaP cells. These results indicate not only the lack of preference between 5*S* analog **13** and 5*R* analog **14**, as was observed for Enigmol and 2*S*,3*S*,5*R*-enigmol, but also that anti-cancer activity was not enhanced. Overall, an Enigmol analog with significantly improved activity had not been achieved at this point, which is likely due to the pleiotropic activity of these compounds, whereby a single structural modification may simultaneously tune in and out multiple target proteins. However, as evidenced by the translation of Enigmol's relatively weak,

micromolar cytotoxicity *in vitro* to its striking, docetaxel-like anti-tumor efficacy *in vivo*, mediocre potency can be overcome by appropriately tuning pharmacokinetic properties.

Compound	Structure	LNCaP IC ₅₀ (μM)	PC3 IC ₅₀ (μM)
Enigmol		10	10
2S,3S,5R-enigmol		10	10
2S,3R,5S-enigmol		10	5
2S,3R,5R-enigmol		49	50
N-methyl Enigmol		11	25
10		19	25
11		19	33
12		> 100	> 100
13		23	10
14		25	10
15		24	24

Table 1: Cytotoxicity of Enigmol Analogs against Human Prostate Cancer Cells *in vitro*. LNCaP or PC3 human prostate cancer cells were incubated with enigmol²⁰ or Enigmol analog²⁷, and cell viability was quantified by measuring mitochondrial activity with the WST-1 reagent. Experiments were performed in triplicate, and IC₅₀ values were calculated using GraphPad Prism software from concentration-response curves that were generated via nonlinear regression using a four parameter logistic equation.

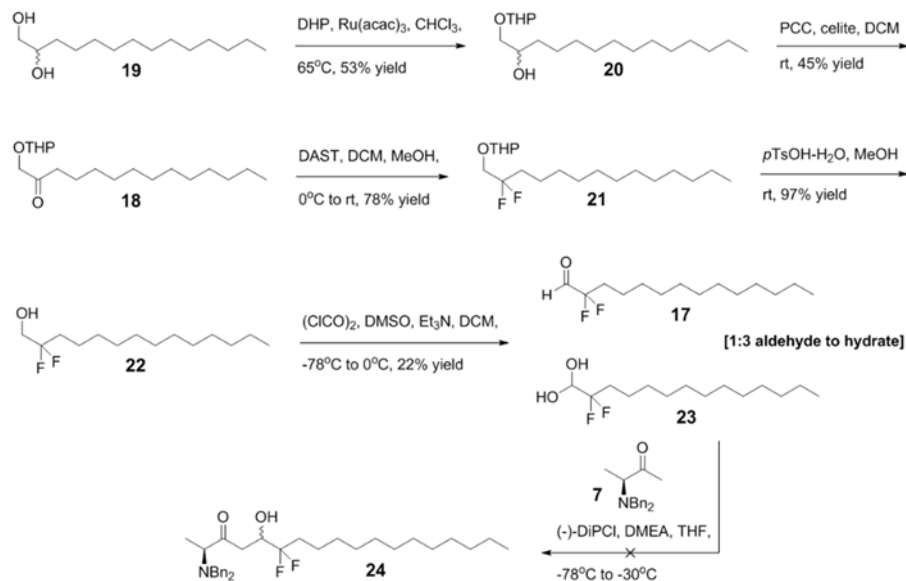
1.2. Results and Discussion



Scheme 2: Retrosynthetic Analysis for CF₂-Enigmol. Initial retrosynthetic analysis of CF₂-Enigmol involved aldol reaction between methyl ketone **7** and aldehyde **17** as the key step.

Upon joining the Liotta Group, my preliminary goal was to synthesize CF₂-Enigmol, and accordingly, boron-mediated aldol methodology, similar to that utilized for the synthesis of Enigmol²², was envisioned to deliver the desired product. Retrosynthetic analysis (**Scheme 2**) illustrates that CF₂-Enigmol was anticipated to come from aldol reaction between *N,N*-dibenzyl- α -amino methyl ketone **7** and α,α -difluoro aldehyde **17**, followed by reduction of the resulting ketone, and final amino group deprotection. While electron-withdrawing amine protecting groups, such as *tert*-butyloxycarbonyl (Boc) or carboxybenzyl (Cbz), elevate the α -proton acidity of α -amino carbonyl compounds, the *N,N*-dibenzyl protecting group contrastingly shields chiral α -amino carbonyls from potential racemization via both steric bulk and bond rotation hindrance, disallowing proper orbital alignment for enol formation³³. Aldehyde **17** was expected to form via nucleophilic fluorination of ketone **18**, followed by primary alcohol deprotection, and subsequent oxidation. Synthesis of ketone **18** was envisioned to proceed via oxidation of the intermediate resulting from regioselective protection of the primary alcohol of diol **19**. While both Brønsted and Lewis acids are well known to catalyze the tetrahydropyranyl ether (THP) protection of alcohols, efficient regioselective THP protection of primary alcohols in the presence of secondary alcohols has been demonstrated with bulky Lewis acid catalysts, such as ruthenium(III) acetylacetonate³⁴. Accordingly, this methodology was employed to selectively protect the primary hydroxyl group of diol **19**, yielding mono-THP ether **20**, the secondary alcohol of which was subsequently oxidized with pyridinium chlorochromate (PCC) to generate ketone

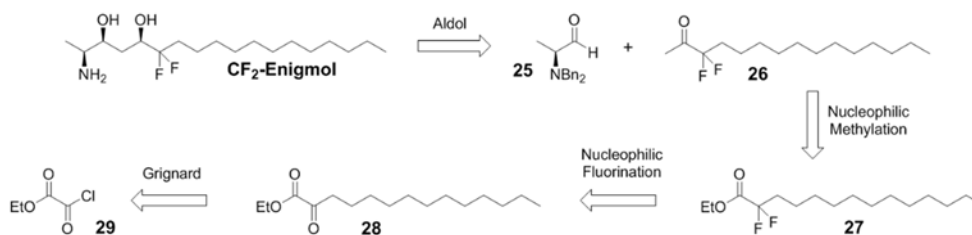
18 (Scheme 3). Nucleophilic difluorination was then carried out with diethylaminosulfur trifluoride (DAST) to produce intermediate **21**, which was then subjected to *para*-toluenesulfonic acid-mediated



Scheme 3: Synthesis of α,α -Difluoro Aldehyde 17. Preparation of aldehyde **17** resulted in a 1:3 ratio of aldehyde to the corresponding hydrate, the mixture of which did not undergo aldol reaction with methyl ketone **7** to produce β -hydroxy ketone **24**.

deprotection to yield alcohol **22**. Subsequent oxidation of the resulting primary alcohol to desired aldehyde **17**, however, proved to be less straightforward. While attempted Dess-Martin and Ley oxidations mediated by Dess-Martin periodinane (in the absence³⁵ or presence³⁶ of water) or by tetrapropylammonium perruthenate³⁷ (TPAP), respectively, failed to facilitate any conversion of the starting material, reactions with PCC led to the generation of multiple undesired products. Similar results were previously reported for the oxidation of α,α -difluoro alcohols to the corresponding aldehydes, where Dess-Martin periodinane led to low yields and messy product mixtures and pyridinium dichromate (PDC) led to several overoxidation products³⁸. Alternatively, Parikh-Doering and Swern oxidations each facilitated formation of desired aldehyde **17**, which demonstrated poor stability to silica gel chromatography. Instead, the crude material was subjected to purification by vacuum distillation at 190°C, which furnished the desired product in relatively low yield as a 1:3 mixture

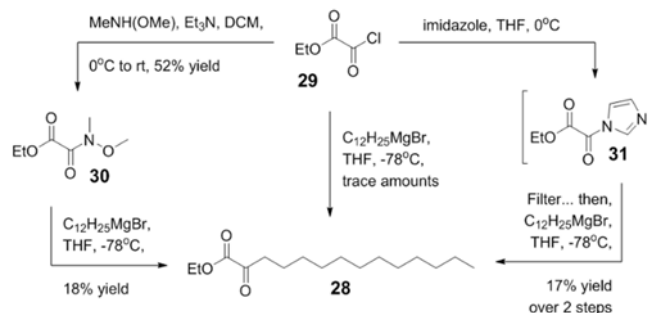
of aldehyde to the corresponding hydrate. Notably a 1:4 ratio of aldehyde to hydrate was reported previously for structurally similar species³⁸. Despite low quantities of aldehyde, the hydrate is, in principle, capable of reverting back to the aldehyde under the basic conditions used for subsequent aldol reaction²². Accordingly, the synthesis of β -hydroxy ketone **24** was attempted via preformation of the boron enolate of methyl ketone **7** (prepared by Dr. Manohar Saindane in the Liotta Group using previously reported methods²²) with (-)-DiPCl and dimethylethylamine (DMEA), followed by addition of the 1:3 mixture of aldehyde **17** to hydrate **23**. Unfortunately, aldol reaction under these conditions failed to produce the desired intermediate *en route* to CF₂-Enigmol, which could have involved complications with *in situ* generation of water upon conversion of hydrate to aldehyde. Alternatively, aldol reactions were also attempted using crude aldehyde **17** produced via Swern oxidation or Parikh-Doering oxidation, neither of which resulted in the detection of desired β -hydroxy ketone **24**.



Scheme 4 New Retrosynthetic Analysis for CF₂-Enigmol. Revised retrosynthetic analysis of CF₂-Enigmol involved aldol reaction between aldehyde **25** and methyl ketone **26** as the key step.

Since synthesis and reactivity of α,α -difluoro aldehyde **17** appeared to be problematic, a modified aldol strategy was designed, for which aldehyde and methyl ketone functionalities were swapped between coupling partners so as to involve α,α -difluoro methyl ketone **26** and previously reported *N,N*-dibenzyl- α -amino aldehyde **25**³³ (**Scheme 4**). Synthesis of methyl ketone **26** was envisioned to involve nucleophilic methylation of α,α -difluoro ester **27**, which was expected to be produced via nucleophilic fluorination of α -keto ester **28**. Additionally, installation of the lipid tail of intermediate **28** was anticipated to involve alkyl Grignard addition into chlorooxalate **29**. Accordingly, a solution of dodecylmagnesium bromide was freshly prepared from magnesium turnings and commercially available 1-bromododecane, and the resulting Grignard solution was added in dropwise

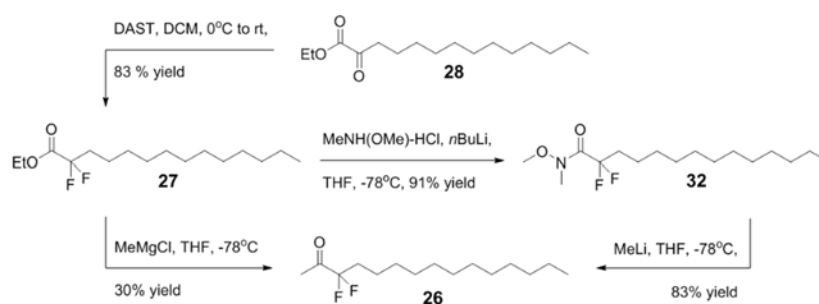
fashion to a solution of commercially available **29** at -78°C (*Scheme 5*). As soon as the addition was complete, TLC indicated no remaining starting material and four products. After immediate workup,



Scheme 5: Synthesis of α -Keto Ester 28. Ketone **28**, not produced in sufficient quantity via Grignard reaction with acid chloride **29**, was alternatively afforded by Grignard reaction with Weinreb amide intermediate **30** or with imidazolide intermediate **31**.

^1H NMR of the crude material indicated an 11:1 ratio of the symmetrical 1,2-diketone to the desired α -keto ester **28**, as well as the presence of the corresponding tertiary alcohol byproduct. While this result indicated that Grignard addition directly into chloroacetate **29** would not be a viable approach for the preparation of α -keto ester **28**, it represented a baseline for subsequent changes to the reaction conditions. In particular, synthesis of α -keto esters via Grignard addition has been reported to proceed through α -amido ester intermediates that are prepared by addition of the Weinreb amine or imidazole to chloroacetate **29**. For example, while Weinreb amide intermediate **30**³⁹ facilitated the production of alkynyl α -keto esters in significantly better yield than α -imidazolide **31**, synthesis of α -keto esters via aryl Grignard addition to α -imidazolide intermediate **31**⁴⁰ proceeded in moderate to good yield. Although reported yields from both studies suffered with the use of alkyl nucleophiles, addition of freshly prepared dodecylmagnesium bromide to each of these intermediates was attempted towards the synthesis of α -keto ester intermediate **28**. Firstly, reaction of starting material **29** with the Weinreb amine³⁹ at 0°C in the presence of triethylamine delivered desired intermediate **30** (52% yield after column chromatography), which subsequently underwent Grignard addition at -78°C to produce α -keto ester **28** (18% yield after column chromatography) in 9% yield over two steps. Alternatively,

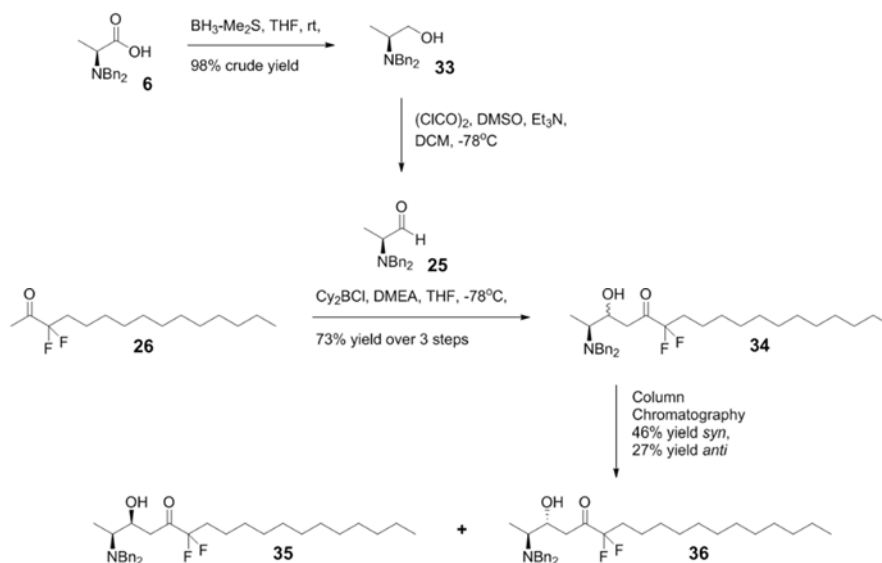
imidazole⁴¹ was treated with chlorooxalate **29** at 0 °C to generate intermediate **31**, which proved to be unstable to both silica gel and heat (100 °C) during attempted column chromatography and distillation, respectively. To bypass these purification issues, imidazolid **31** was prepared *in situ*, and the resulting solid imidazole hydrochloride was filtered off. The mother liquor was then cooled to -78 °C, and the Grignard solution was added in dropwise fashion to yield α -keto ester **28** in 17% yield over two steps after column chromatography. While 17% yield over the first two steps is certainly not ideal, it was better than the 9% yield obtained with Weinreb amide intermediate **30**, it was on par with yields of similar reactions reported in the literature⁴⁰, and it provided enough material to proceed with the synthesis of CF₂-Enigmol.



Scheme 6: Synthesis of α, α -Difluoro Methyl Ketone 26. Grignard reaction with ester **27** produced methyl ketone **26**, but this reaction was not scalable, unlike preparation of **26** via Weinreb ketone synthesis.

With ample quantities of intermediate **28** in hand, the next goal was to prepare α, α -difluoro methyl ketone **26** for subsequent aldol reaction. Difluorination of alkyl-substituted α -keto esters with DAST has been demonstrated to deliver the corresponding α, α -difluoro esters in good yield, without fluoride addition to the adjacent ester carbonyl⁴². Accordingly, a solution of α -keto ester **28** in DCM at 0 °C was treated with DAST (**Scheme 6**), which was subsequently allowed to warm to room temperature, producing desired α, α -difluoro ester **27** in 83% yield on both analytical scale (200 mg) and preparatory scale (5.46 g). Although conversion of esters to the corresponding ketones via Grignard addition generally does not proceed in high yield due to the increased electrophilicity of the ketone product as compared to the ester starting material, reaction of an α -fluoro ester with

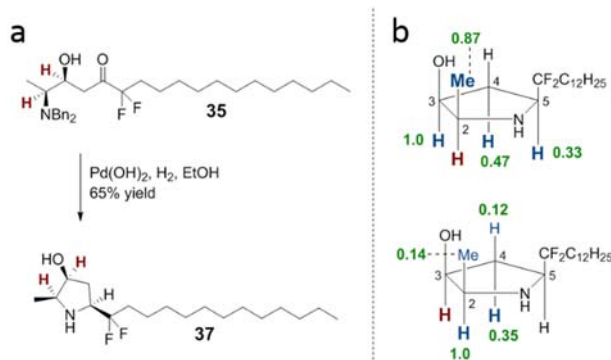
methylmagnesium chloride was reported to yield the corresponding α -fluoro methyl ketone in 88% yield⁴³. In similar fashion, α,α -difluoro ester **27** was treated with a solution of methylmagnesium chloride at -78°C . While this reaction led to isolation of the desired α,α -difluoro methyl ketone **26** in 30% yield on a small scale (150 mg), the corresponding *gem*-dimethyl tertiary alcohol was the only detectable product on a moderate scale (3.73 g). Alternatively, addition of magnesium- and lithium-based organometallic nucleophiles, including methyllithium, to Weinreb amide intermediates derived from α,α -difluoro esters was reported to deliver the corresponding α,α -difluoro ketones in excellent yield⁴⁴. Attractively, these Weinreb amides were prepared from the appropriate α,α -difluoro esters in one step that involved deprotonation of both the acidic HCl proton and the remaining amino proton of Weinreb's salt with *n*-butyllithium, followed by addition of the resulting lithium amide into the starting ester. Accordingly, *n*-butyllithium was slowly added to a solution of Weinreb's salt at -78°C , and a solution of α,α -difluoro ester **27** was subsequently added at -78°C in dropwise fashion. The reaction produced desired Weinreb amide **32** in 91% yield after column chromatography. Furthermore, addition of methyllithium to intermediate **32** facilitated the preparation of α,α -difluoro ketone **26** in 83% after column chromatography. Highlighting the efficiency of this two-step sequence, crude ^1H NMR of Weinreb amide **32** indicated pure product, which could be carried forward to the next reaction to cleanly generate methyl ketone **26** in 93% crude yield over two steps without the need for purification.



Scheme 7: Synthesis of *N,N*-Dibenzyl- α -Amino Aldehyde **25 and Subsequent Aldol Reaction.** Aldol reaction between aldehyde **25** and methyl ketone **26** successfully furnished the CF₂-Enigmol scaffold exhibited by β -hydroxy ketone **34**.

The next goal was to prepare previously reported *N,N*-dibenzyl- α -amino aldehyde **25**³³ for aldol reaction with α,α -difluoro methyl ketone **26**. As Enigmol and analogs have been synthesized by the original aldol route beginning with *N,N*-dibenzyl- α -amino acid **6** (**Scheme 1b**), large quantities of starting material **6** have been produced by Dr. Manohar Saindane in the Liotta Group using previously reported methods²². With ample material available, carboxylic acid **6** was reduced to corresponding *N,N*-dibenzyl- α -amino alcohol **33** with borane-dimethyl sulfide complex (**Scheme 7**); ¹H NMR of the crude material indicated a very clean reaction, and that further purification was unnecessary. Alcohol **33** was then subjected to several oxidative conditions to screen for optimal yield and enantiopurity of desired *N,N*-dibenzyl- α -amino aldehyde **25**. While attempted Dess-Martin³⁵ and Ley³⁷ oxidations led to relatively messy reaction mixtures with minimal aldehyde detected by crude ¹H NMR, Swern oxidation⁴⁵ proceeded smoothly to deliver relatively pure aldehyde before purification. Attempted purification by column chromatography, however, resulted in decomposition of aldehyde **25**. Alternatively, the crude material was taken directly forward to subsequent aldol reaction, after which desired β -hydroxy ketone **34** was not detected. Instead, quick exposure of crude *N,N*-dibenzyl- α -amino

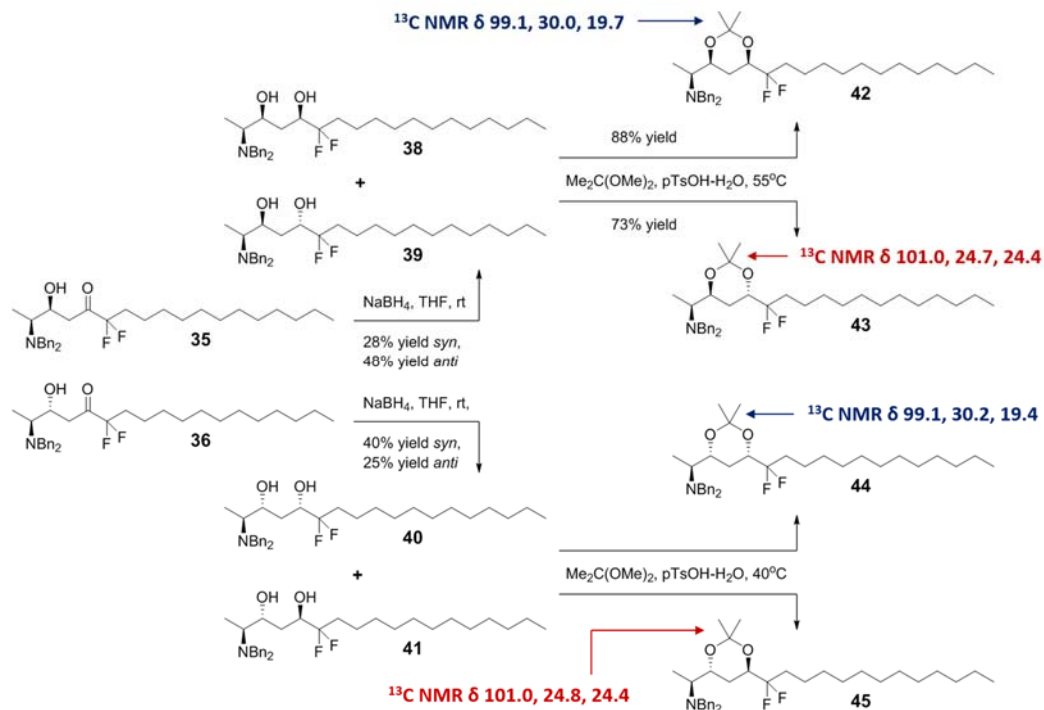
aldehyde **25** to a short silica plug with a relatively polar mobile phase facilitated rapid isolation of pure desired product, the optical rotation of which was consistent with values reported in the literature⁴⁶.



Scheme 8: Assignment of Relative Stereochemistry for β -Hydroxy Ketone **35.** (a) Subjecting β -hydroxy ketone **35** to hydrogenolysis conditions resulted in *N,N*-dibenzyl group removal, followed by intramolecular reductive amination, yielding pyrrolidinol **37**. (b) Irradiated protons are bolded and colored red, protons corresponding to detected NOE signals are colored blue, and the green numbers represent integration values for each detected NOE signal. All integration values were normalized to that of the strongest NOE signal for a given 1D-NOE experiment. Since the C-2 amine stereocenter was known, the relative configuration of the hydroxyl group was assignable based on the relative proximities of the known C-2 chiral proton, the unknown C-3 chiral proton, and both diastereotopic protons on C-4.

Although the initial aldol-based synthesis of Enigmol employed a chiral borane for diastereoselective aldol reaction, diastereoselectivity appeared to be driven by the chiral center substituted with the bulky *N,N*-dibenzylamino group, as opposed to the chiral borane²². In addition to this apparent substrate-directed diastereoiduction, the need to define baseline reactivity and stereoselectivity, as well as the desire to synthesize all four diastereomers of 2*S*- CF_2 -Enigmol, led to the utilization of achiral chlorodicyclohexylborane. Notably, chlorodicyclohexylborane-mediated aldol reaction between alkyl-substituted methyl ketones and *N*-Boc- α -amino aldehydes proceeded with moderate to high substrate-directed diastereoiduction⁴⁷. Accordingly, chlorodicyclohexylborane and DMEA were employed for the preformation of the boron enolate of α,α -difluoro methyl ketone **26** *in situ* at -78°C , and a solution of *N,N*-dibenzyl- α -amino aldehyde **25** was added in slow dropwise fashion (**Scheme 7**). Gratifyingly, liquid chromatography-mass spectrometry (LC-MS) analysis of a small aliquot that was subjected to mini-workup indicated a 61:39 ratio of diastereomers, suggesting that

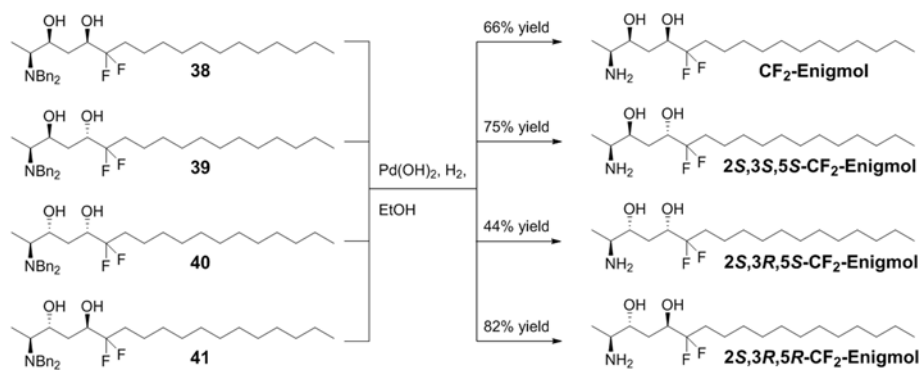
each diastereomer could be isolated in sufficient quantity to facilitate synthesis of each diastereomer of 2*S*-CF₂-Enigmol. The reaction sequence involving reduction of carboxylic acid **6** with borane-dimethyl sulfide complex, Swern oxidation of resulting alcohol **33**, and subsequent aldol reaction with aldehyde **25** to generate the mixture of β -hydroxy ketone diastereomers **34** proceeded in 73% over 3 steps; column chromatography facilitated isolation of *syn*- and *anti*-stereoisomers **35** and **36** in 46% and 27% yields, respectively. Importantly, preparation of a racemic standard of the higher yielding diastereomer and comparative chiral HPLC analysis indicated 96% *e.e.*, and thus, that little to no racemization occurred during this 3 step sequence. In order to assign relative stereochemistry of the resulting 2,3-aminoalcohols **35** and **36**, the higher yielding diastereomer **35** was subjected to palladium-catalyzed hydrogenolysis conditions, which resulted in cleavage of the *N,N*-dibenzyl protecting group, followed by tandem intramolecular reductive amination⁴⁸, generating pyrrolidinol **37** in 65% yield (**Scheme 8a**). Subsequent ¹H NMR Nuclear Overhauser Effect (NOE) spectroscopy facilitated assignment of C-3 stereochemistry relative to the 2*S*-amino group (**Scheme 8b**). Upon irradiation of the chiral proton on C-2, which was known to be in the *S* configuration, strong NOE signals were detected for the methyl group and the chiral proton on C-3, as well as for one of the diastereotopic protons on C-4 and the chiral proton on C-5 that arose from intramolecular reductive amination. Consistently, irradiation of the chiral proton on C-3, for which the stereochemical configuration was unknown, resulted in strong NOE signals for the chiral proton on C-2 and for the same diastereotopic proton on C-4 that produced an intense NOE signal in the first experiment. As much weaker NOE signals were observed for the C-2 methyl group and the other diastereotopic proton on C-4, these results provide convincing evidence to support the assignment of a *syn*-relationship between C-2 and C-3 chiral protons of β -hydroxy ketone **35**.



Scheme 9. β -Hydroxy Ketone Reduction and Determination of Relative Diol Stereochemistry. Reduction of ketones **35** and **36** yielded four diastereomeric 1,3-diols, the stereochemical arrangement of which was determined using Rychnovsky's acetonide method involving ^{13}C NMR analysis.

Although a variety of methods for diastereoselective reduction of β -hydroxy ketones to the corresponding 1,3-diols are known, synthesis of all four diastereomers of 2*S*-CF₂-Enigmol was desired for comparison of *in vitro* cytotoxicity against human prostate cancer cell proliferation. Accordingly, sodium borohydride was chosen as an appropriate reagent to reduce chirally pure *syn*- and *anti*- β -hydroxy ketones **35** and **36**, respectively, for the expected absence of diastereoselectivity. Therefore, intermediates **35** and **36** were each treated with sodium borohydride at room temperature, which resulted in the production and isolation of all four diastereomers of 2*S*-*N,N*-dibenzylamino-CF₂-Enigmol **38-41** after chromatographic separation (**Scheme 9**). Notably, the difference in yield between each pair of *syn*- and *anti*-diols was a result of column chromatography and not due to inherent diastereoselectivity of the reaction. Since the C-3 chiral centers of β -hydroxy ketones **35** and **36** were assigned relative to the known C-2 stereocenter, determination of the relative configurations of each 1,3-diol **38-41** would facilitate assignment of absolute stereochemistry. Accordingly, Rychnovsky's

acetonide method, by which 1,3-diols undergo acid-catalyzed cyclization with 2,2-dimethoxypropane to generate the corresponding acetonides⁴⁹, was employed. Based on this analytical method, the quaternary carbon of *syn*- and *anti*-acetonides resonate at ¹³C NMR shifts < 100 ppm and > 100 ppm, respectively. Additionally, *syn*-acetonide *gem*-dimethyl carbons correspond to ¹³C NMR shifts around 30 ppm and 20 ppm, while *gem*-dimethyl carbons of *anti*-acetonides both resonate around 24 ppm. Hence, diols **38-41** were converted to the corresponding acetonides **42-45**, which were then subjected to Rychnovsky's ¹³C NMR analysis. These experiments indicated a *syn*-relationship between the hydroxyl groups of diols **38** and **40**, as well as an *anti*-relationship between the hydroxyl groups of diols **39** and **41**. With the stereochemical configuration of each chiral center proposed, diols **38-40** were finally subjected to palladium-mediated hydrogenolysis conditions to facilitate reductive cleavage of *N,N*-dibenzyl protecting groups, resulting in the production of all four diastereomers of 2*S*-CF₂-Enigmol in 44-82% yield (**Scheme 10**).



Scheme 10. Final Deprotection of All Four Diastereomers of 2*S*-CF₂-Enigmol.

1.2.b. Cytotoxicity against Human Prostate Cancer Cells *in vitro*

Each of the four diastereomers was submitted to our collaborators in the laboratory of Dr. John Petros (Department of Urology, Emory University School of Medicine) for evaluation of cytotoxic activity against both LNCaP and PC3 human prostate cancer cells *in vitro*. In similar fashion to assays conducted for the previously described Enigmol analogs, cultured LNCaP and PC3 cells were

incubated overnight at 37°C to allow the cells to adhere to 96-well plates. The next day, cells were treated with increasing concentrations of 1:1 complexes of drug and fatty-acid free bovine serum albumin (BSA), which were freshly prepared 1 hr prior to use. Drugs were formulated as 1:1 BSA complexes not only to enhance drug solubility, but also to mimic the physiological transfer to and penetration of cancer tissue by sphingolipid analogs bound to BSA in the bloodstream⁹. BSA was used as a negative control, and each treatment was performed in triplicate for each cell type. After addition of the formulated drugs, cells were incubated at 37°C for 24 hrs, and then WST-1 reagent, a substrate for mitochondrial reductase that results in a luminescent byproduct, was added to each well. Mitochondrial reductase activity is commonly used as a measure of cellular metabolism, and therefore, of cell viability. Cells were then incubated at 37°C for 1 hr, and luminescence was measured at 450 nm with a reference wavelength of 690 nm. Baseline luminescence was measured before assay and subtracted from these data, which were subsequently normalized to

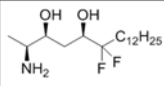
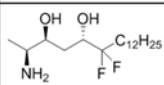
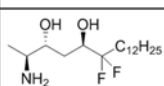
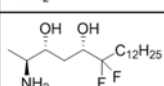
Compound	Structure	LNCaP IC ₅₀ (μM)	PC3 IC ₅₀ (μM)
CF ₂ -Enigmol		13.4 ± 1.1	11.7 ± 1.1
2S,3S,5S-CF ₂ -Enigmol		17.2 ± 1.1	≈ 10.5
2S,3R,5R-CF ₂ -Enigmol		16.8 ± 1.1	≈ 10.1
2S,3R,5S-CF ₂ -Enigmol		19.6 ± 1.1	≈ 11.6

Table 2. Cytotoxicity of 2S-CF₂-Enigmol Diastereomers against Human Prostate Cancer Cells *in vitro*. LNCaP or PC3 human prostate cancer cells were incubated with drug, and cell viability was quantified by measuring mitochondrial activity with the WST-1 reagent. Experiments were performed in triplicate, and IC₅₀ values were calculated using GraphPad Prism software from concentration-response curves that were generated via nonlinear regression using a four parameter logistic equation.

BSA treatment. Concentration response curves were generated via nonlinear regression using Graphpad Prism software, and IC₅₀ values (± S.E.M.) were calculated from curves using a four parameter logistic equation (**Table 2**). While each diastereomer of 2S-CF₂-Enigmol demonstrated

virtually equipotent cytotoxicity against both LNCaP ($13 \mu\text{M} \leq \text{IC}_{50} \leq 20 \mu\text{M}$) and PC3 ($10 \mu\text{M} \leq \text{IC}_{50} \leq 12 \mu\text{M}$) human prostate cancer cell lines, it is notable that the diastereomer least potent against LNCaP cell viability (2*S*,3*R*,5*S*-CF₂-Enigmol) has the same aminodiol configuration as the least potent Enigmol diastereomer²⁰. As CF₂-Enigmol exhibits the same stereochemical arrangement as CF₃-Enigmol²⁷ and difluoro-Enigmol analog **16**²⁶, both of which were synthesized by Dr. Mark Baillie in the Liotta Group similarly to Enigmol via the original aldol route²², comparison of the *in vitro* anti-cancer activities of these compounds was also important. Concentration response curves were generated via nonlinear regression using Graphpad Prism software, and IC₅₀ values (\pm S.E.M.) were calculated from curves fit with a four parameter logistic equation (**Table 3**). Similar to the flat structure-activity relationship observed for previously described Enigmol analogs, as well as for the 2*S*-CF₂-Enigmol diastereomers, Enigmol (LNCaP, *n* = 4; PC3, *n* = 3), CF₃-Enigmol (LNCaP, *n* = 4; PC3, *n* = 3), **16** (LNCaP, *n* = 3; PC3, *n* = 3), and CF₂-Enigmol (LNCaP, *n* = 3; PC3, *n* = 3) demonstrated virtually equipotent cytotoxicity against both LNCaP ($11 \mu\text{M} \leq \text{IC}_{50} \leq 18 \mu\text{M}$) and PC3 ($12 \mu\text{M} \leq \text{IC}_{50} \leq 21 \mu\text{M}$) cells. These results indicate that replacement of Enigmol C-H bonds with C-F bonds did not alter cytotoxic activity, which is consistent with the hypothesis that fluorinated Enigmol analogs will exhibit enhanced anti-tumor efficacy *in vivo* by virtue of increased tissue absorption. Thus, the next

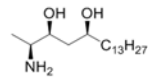
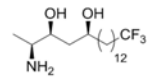
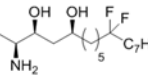
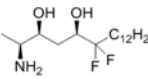
Compound	Structure	LNCaP IC ₅₀ (μM)	PC3 IC ₅₀ (μM)
Enigmol		11.7 ± 1.1	12.1 ± 1.0
CF ₃ -Enigmol		11.3 ± 1.1	21.4 ± 1.2
16		18	13
CF ₂ -Enigmol		13.4 ± 1.1	11.7 ± 1.1

Table 3. Cytotoxicity of Fluorinated Enigmol Analogs against Human Prostate Cancer Cells *in vitro*. LNCaP or PC3 human prostate cancer cells were incubated with drug, and cell viability was quantified by measuring mitochondrial activity with the WST-1 reagent. Experiments were performed

in triplicate, and IC_{50} values were calculated using GraphPad Prism software from concentration-response curves that were generated via nonlinear regression using a four parameter logistic equation.

series of experiments with which to discriminate between Enigmol analogs necessarily involved pharmacokinetic studies *in vivo* to compare plasma and tissue exposure after intravenous (i.v.) and oral (p.o.) administration. Since experiments involving whole animals are resource-intensive, it was not feasible to evaluate the pharmacokinetic properties of each fluorinated Enigmol analog. Due to both consistent stereochemical configuration and synthetic accessibility, CF_3 -Enigmol and CF_2 -Enigmol were chosen as the two fluorinated Enigmol analogs to scale up and submit for pharmacokinetic analysis *in vivo*. Small molecule therapeutics with attractive pharmacokinetic properties generally achieve IC_{90} levels (concentrations required to elicit 90% of the maximal effects) in the appropriate physiological compartment(s), and accordingly, IC_{90} values were also calculated from concentration-response curves (**Figure 5**) to indicate therapeutically effective concentrations desired to be reached *in vivo*.

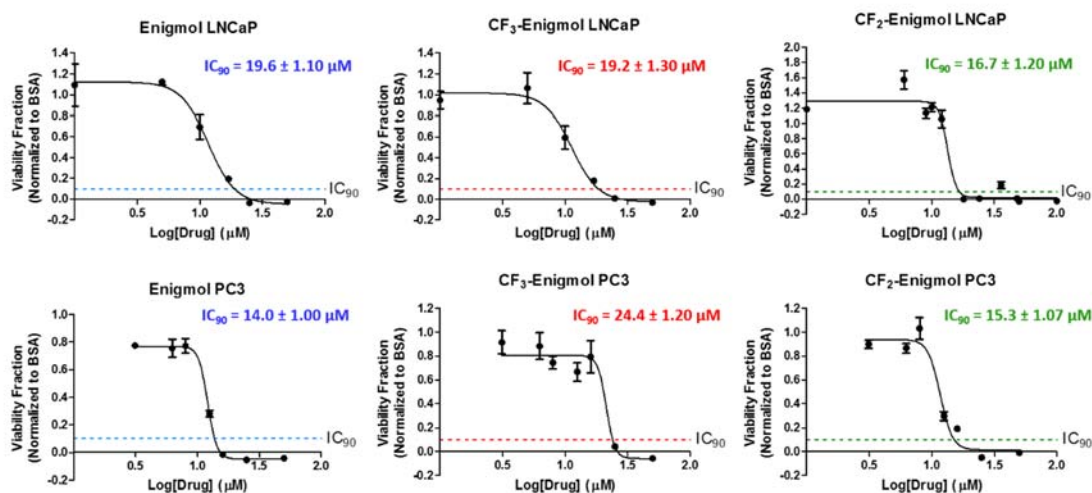
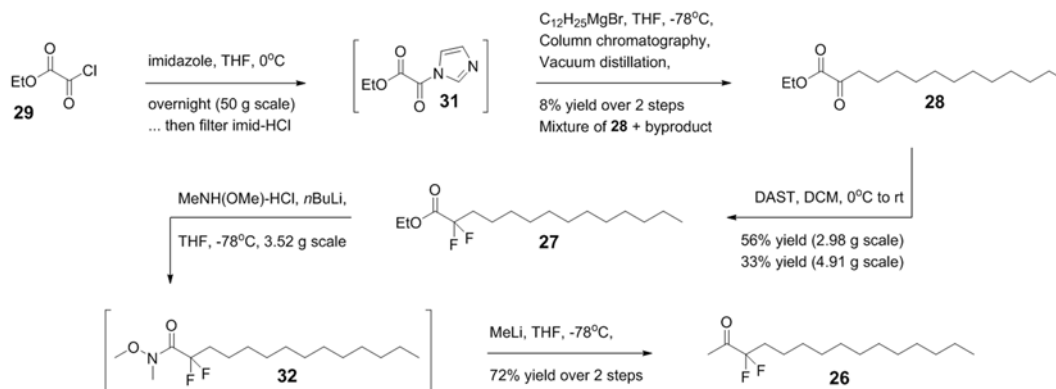


Figure 5: Concentration-Response Curves of Enigmol, CF_3 -Enigmol, and CF_2 -Enigmol. Concentration-response curves were generated with GraphPad Prism software via nonlinear regression using a four parameter logistic equation, from which IC_{90} values were calculated. Data are represented as the mean \pm S.E.M.

1.2.c. 1st Scale Up Preparation of CF₂-Enigmol

While CF₂-Enigmol had been prepared successfully on a small scale, it quickly became apparent that a larger scale synthesis would present more challenges. Starting with 50 g of chlorooxalate **29**, preformation of imidazolide intermediate **31**, filtration of the resulting imidazole hydrochloride, and subsequent reaction with dodecylmagnesium bromide at -78°C resulted in a much messier mixture of products than on a smaller scale (**Scheme 11**). After several attempts at purification via column chromatography, careful TLC analysis indicated that desired α -keto ester **28** was significantly contaminated with 2 undesired byproducts that virtually coeluted on silica gel. Secondly, separation of this mixture was attempted via vacuum distillation, during which intermediate **28** and one of the byproducts coevaporated and condensed into the collection flask, leaving the other undesired product in the distillation flask. At this point, α -keto ester **28** was still contaminated with a compound exhibiting very similar polarity and boiling point. Accordingly, a small fraction of this mixture was subjected to the nucleophilic difluorination conditions required for synthesis of α,α -difluoro ester **27**. Delightfully, DAST converted α -keto ester **28** to intermediate **27**, which was easily separated from the undesired byproduct via column chromatography. Therefore, the entire impure batch of α -keto ester **28** (8% yield over 2 steps assuming 100% purity) was split into two portions, each of which was subjected to DAST-mediated difluorination. These reactions resulted in the production of α,α -difluoro ester **27** in 56% and 33% yield on 2.98 g and 4.91 g scales, respectively, assuming that the starting α -keto ester **28** was 100% pure. While this 3-step sequence for the synthesis of intermediate **27** would clearly need to be improved if production of more material were necessary, an ample supply was obtained to continue the scale up of CF₂-Enigmol for pharmacokinetic evaluation. Accordingly, 3.52 g of α,α -difluoro ester **27** was slowly added to the *in situ*-generated, Weinreb amine-derived lithium amide, resulting in the delivery of Weinreb amide **32**. Intermediate **32** was then subjected to aqueous workup, and was directly submitted for methyl ketone synthesis without further purification. Addition of methyllithium at -78°C afforded desired α,α -difluoro methyl ketone **26** in 72% yield over 2 steps. Although a sufficient quantity of

methyl ketone **26** was obtained, the synthetic approach suffered substantially on this larger scale, proceeding in < 3% overall yield, as compared to 11% yield on the previous scale.

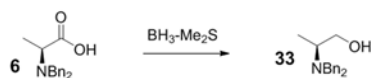


Scheme 11: 1st Scale Up of α,α -Difluoro Methyl Ketone **26.** Preparation of ketone **28** via Grignard reaction with imidazolide intermediate **31** suffered substantially on a large scale, but nonetheless enabled synthesis of a sufficient quantity of methyl ketone **26**.

Unexpected challenges were also encountered during larger scale synthesis of *N,N*-dibenzyl- α -amino aldehyde **25**, which began with the previously described borane-dimethyl sulfide (BH_3-Me_2S)-mediated reduction of carboxylic acid **6** to corresponding alcohol **33** on a 5.00 g scale (**Table 4**, Batch 1). Carboxylic acid **6** was dissolved in THF (0.6 M), and BH_3-Me_2S (1.5 eq) was added at room temperature in slow dropwise fashion via syringe pump. Partway through the addition, precipitation of a white solid was observed, and the resulting mixture was stirred overnight. The next morning, white precipitate remained, and LC-MS analysis indicated only 33% conversion of **6** to desired alcohol **33**. During the original synthesis of CF_2 -Enigmol, neither white precipitate, nor sluggish reactivity, was observed for this transformation. To examine the possibility that 1.5 eq BH_3-Me_2S from the current reagent bottle was not enough to push the reaction to completion, the reaction was attempted again on a 1.00 g scale with 3.5 eq BH_3-Me_2S (**Table 4**, Batch 2). This experiment similarly resulted in white precipitate formation during BH_3-Me_2S addition, as well as the exact same 33:67 ratio of starting material **6** to desired product **33** after stirring overnight at room temperature. The next hypothesis was that the dropwise addition of BH_3-Me_2S was too slow, allowing the formation and precipitation of

insoluble complexes involving BH_3 , Me_2S , THF, **6**, and/or **33**, which sequestered reagent and/or starting material, resulting in a stalled reaction. Accordingly, the experiment was attempted one more time on a 1.00 g scale (0.6 M), during which $\text{BH}_3\text{-Me}_2\text{S}$ (3.0 eq) was added by hand in dropwise fashion as fast as possible while maintaining control over the ensuing exothermic, gas-evolving reaction (**Table 4**, Batch 3). Precipitation of white solid was quickly observed, after which apparent reaction with additional $\text{BH}_3\text{-Me}_2\text{S}$ was nonexistent. Dilution with THF (0.2 M) did not facilitate dissolution of the white precipitate, nor did it reendow quickly added $\text{BH}_3\text{-Me}_2\text{S}$ (3.00 eq) with visually-detectable reactivity. Based on the hypothesis that dissolution of the white precipitate would liberate starting material **6** and/or BH_3 that was sequestered from the reaction medium via precipitation, 4 small aliquots were removed from the main reaction mixture and transferred to 4 mL screwcap vials equipped with stir bars. The first aliquot was taken as a control reaction, and therefore, the reaction mixture remained unaltered. The other aliquots were diluted with an equal volume (0.1 M) of either EtOAc, DCM, or Et_2O as $\text{BH}_3\text{-Me}_2\text{S}$ was reported to be soluble in each of these solvents⁵⁰, and all reaction vessels were stirred overnight at room temperature. While the reaction mixtures containing 1:1 THF/EtOAc (18% **33**, 82% **6**) and 1:1 THF/DCM (12% **33**, 88% **6**) resulted in a lower degree of conversion of **6** to **33** than the control aliquot containing THF only (32% **33**, 68% **6**), the reaction mixture containing 1:1 THF/ Et_2O outperformed all other aliquots with an 83:17 ratio of alcohol **33** to carboxylic acid **6**. This result is likely due to the decreased coordination ability of Et_2O as compared to THF, making the insoluble complexes less likely to form, ultimately freeing up more reagent and starting material to facilitate reaction progression. Accordingly, the main reaction vessel from which aliquots were removed was diluted with an equal volume of Et_2O , no additional $\text{BH}_3\text{-Me}_2\text{S}$ was added, and the reaction mixture was allowed to stir overnight at room temperature. The next morning, LC-MS analysis indicated a 96:4 ratio of alcohol **33** to carboxylic acid **6**, demonstrating that a reaction solvent of 1:1 THF/ Et_2O at a concentration of 0.1 M provided for a viable preparation of desired alcohol **33**. Therefore, these reaction conditions were reproduced on a 13.4 g scale, for which $\text{BH}_3\text{-Me}_2\text{S}$ (3.5 eq) was added in dropwise fashion via syringe pump, and the resulting reaction mixture was

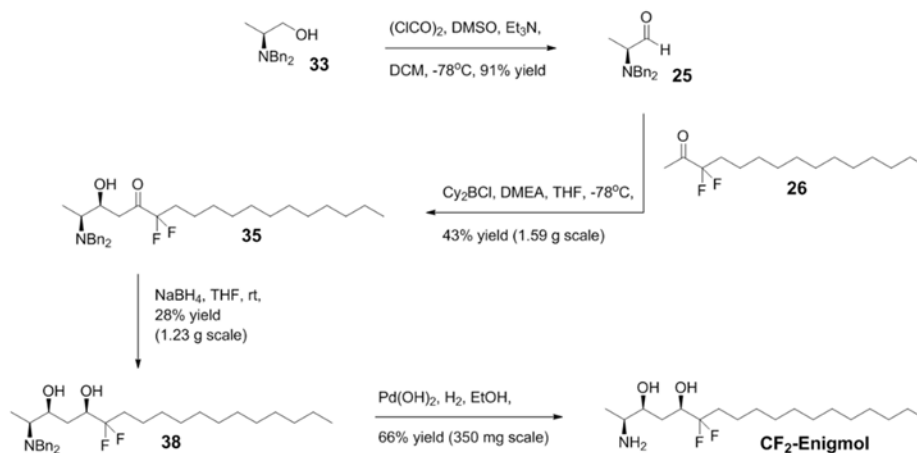
stirred overnight at room temperature (**Table 4**, Batch 4). The next morning, LC-MS analysis indicated a 14:86 ratio of alcohol **33** to carboxylic acid **6**, indicating that the reaction stalled even when diluted to 0.1 M with weaker coordinating Et₂O. At this point, it was hypothesized that gentle heating would help to disaggregate and solubilize the white precipitate, which was still present but much less prevalent than before. After heating the same reaction mixture to 40°C for 8 hrs, LC-MS analysis indicated a 98:2 ratio of alcohol **33** to carboxylic acid **6**. Verifying the success of these reaction conditions, a final 4.15 g scale batch was pushed through, for which BH₃-Me₂S (3.5 eq) was added in dropwise fashion via syringe pump, and the resulting reaction mixture was stirred overnight at 40°C (**Table 4**, Batch 5). The next morning, LC-MS analysis indicated 100% conversion of carboxylic acid **6** to desired alcohol **33**. Ultimately, by changing (1) the solvent from 100% THF to 1:1 THF/Et₂O, (2) the reaction concentration from 0.6 M to 0.1 M, (3) the temperature from ≈ 22°C to 40°C, and (4) the quantity of BH₃-Me₂S from 1.5 eq to 3.5 eq, the progression of carboxylic acid reduction was greatly improved from 33% to 100%, facilitating isolation of desired *N,N*-dibenzyl- α -aminoalcohol **33** in 91% yield on a 4.15 g scale.



Batch	Scale (g)	Solvent	Temperature (°C)	Concentration (M)	BH ₃ -Me ₂ S (eq)	Time	% 33	% 6
1	5.00	THF	rt	0.6	1.5	overnight	33	67
2	1.00	THF	rt	0.4	1.5	overnight	33	67
3	1.00	THF	rt	0.6	3.0 (quickly)	10 min	Reaction Stalled	
	1.00	THF	rt	0.2	3.0 (quickly)	10 min	Reaction Stalled	
	Aliquot 1	THF	rt	0.2	N/A	overnight	32	68
	Aliquot 2	1:1 THF/EtOAc	rt	0.1	N/A	overnight	18	82
	Aliquot 3	1:1 THF/DCM	rt	0.1	N/A	overnight	12	88
	Aliquot 4	1:1 THF/Et ₂ O	rt	0.1	N/A	overnight	83	17
	1.00	1:1 THF/Et ₂ O	rt	0.1	N/A	overnight	96	4
4	13.4	1:1 THF/Et ₂ O	rt	0.1	3.5	overnight	14	86
	13.4	1:1 THF/Et ₂ O	40°C	0.1	3.5	8 hrs	98	2
5	4.15	1:1 THF/Et ₂ O	40°C	0.1	3.5	overnight	100	0

Table 4. Optimization of BH₃-Me₂S Reduction of Carboxylic Acid 6. LC-MS analysis utilizing ion extraction was employed to measure relative quantities of carboxylic acid **6** and alcohol **33**.

With sufficient quantities of α,α -difluoro methyl ketone **26** and *N,N*-dibenzyl- α -aminoalcohol **33**, the subsequent aldol sequence began with Swern oxidation of alcohol **33** to generate the corresponding aldehyde **25**, which was purified via rapid silica plug (**Scheme 12**). This reaction proceeded in 91% yield, and measurement of optical rotation indicated that no racemization occurred during the reaction or during silica gel purification. Aldehyde **25** and methyl ketone **26** were then subjected to chlorodicyclohexylborane-mediated aldol reaction, resulting in the production of β -hydroxy ketone **35** in 43% yield after chromatographic separation of the ensuing mixture of diastereomers. While the previously described aldol sequence (740 mg scale in methyl ketone **26**) yielded in 46% desired *syn*-stereoisomer **35** over 3 steps (reduction, oxidation, and aldol reaction), scale up of this sequence (1.59 g scale in methyl ketone **26**) facilitated isolation of intermediate **35** in 36% yield over 3 steps. This reduced yield was due, in part, to purification via column chromatography of alcohol **33**, which was carried forward in crude form during the smaller scale synthesis. As before, β -hydroxy ketone **35** was then subjected to reduction with sodium borohydride on a 1.23 g scale, generating a 1:1 mixture of *syn*- and *anti*-diols *in situ*; column chromatography allowed isolation of the desired *N,N*-dibenzylamino CF₂-Enigmol precursor **38** in 28% isolated yield. This relatively low yield, which equals that obtained previously on a 300 mg scale, stemmed from difficult separation of diastereomers via column chromatography. While a sufficient quantity of *syn*-diol **38** was obtained, the low yield marks an opportunity for significant improvement of the synthetic route for future scale up endeavors, which would necessarily involve induction of diastereoselectivity during the reduction of β -hydroxy ketone **35**. Lastly, *syn*-diol **38** was subjected to palladium-mediated hydrogenolysis (350 mg scale) to remove the *N,N*-dibenzyl protecting group, producing CF₂-Enigmol in 66% yield, which was the same result obtained previously (93 mg scale).



Scheme 12: 1st Scale Up of CF₂-Enigmol. Aldol reaction between aldehyde **25** and methyl ketone **26**, as well as subsequent reduction of resulting β -hydroxy ketone **35**, suffered on a moderate scale due to little to no diastereoselectivity and difficult chromatographic separation of undesired diastereomers.

1.2.d. Pharmacokinetics of Fluorinated Enigmol Analogs

With sufficient quantities of CF₂-Enigmol submitted for pharmacokinetic analysis to the Emory Institute for Drug Development, a series of *in vivo* experiments involving Enigmol, CF₃-Enigmol, and CF₂-Enigmol were designed to evaluate the effect of compound lipophilicity on (1) plasma elimination, (2) oral absorption, and (3) tissue distribution. As rapid i.v. injection effectively normalizes the plasma absorption properties of different drugs, pharmacokinetic studies involving i.v. administration were conducted to enable reliable assessment of plasma elimination profiles and accurate estimation of $t_{1/2}$ and rate of clearance (Cl), in the absence of variable oral absorption kinetics. Accordingly, pre-cannulated SD rats (250-300 g) were injected i.v. with a single 2 mg/kg dose of either Enigmol ($n = 3$), CF₃-Enigmol ($n = 4$), or CF₂-Enigmol ($n = 4$) in a PEG400/EtOH/Tween80/H₂O (40:10:3:47) vehicle. Blood samples were taken at 8 or 9 time points up to 8 hrs after administration, and drug concentrations in isolated plasma were quantified using LC-MS/tandem mass spectrometry (LC-MS/MS) analysis (**Figure 6**). Although plasma elimination was anticipated to trend inversely with lipophilicity due to increased plasma protein binding, $t_{1/2}$ and Cl values, as well as the maximum observed plasma concentration (C_{max}) and area under the curve (AUC), indicated that CF₃-Enigmol was removed from plasma remarkably faster than both Enigmol and CF₂-Enigmol. Although this result

could have stemmed from increased metabolism or excretion, the high $c\text{LogP}$ value of $\text{CF}_3\text{-Enigmol}$ was consistent with rapid distribution out of circulation into tissue, which was a desirable property for maximal anti-tumor activity.

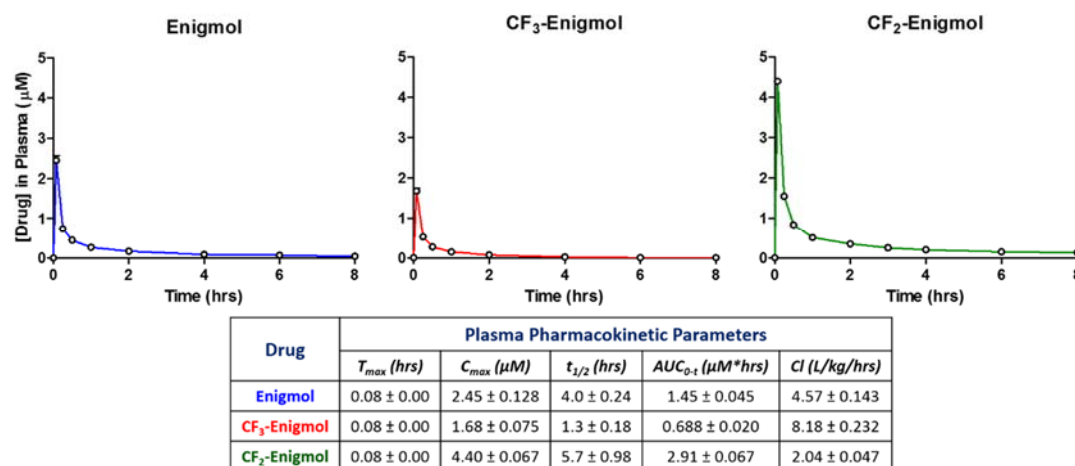


Figure 6. Plasma Pharmacokinetics after 2 mg/kg i.v. Administration. SD rats ($n = 3\text{-}4$ per group) were treated with 2 mg/kg of either Enigmol, $\text{CF}_3\text{-Enigmol}$, or $\text{CF}_2\text{-Enigmol}$ via i.v. injection (vehicle = 40:10:3:47 PEG400/EtOH/Tween80/ H_2O), and plasma concentrations were measured periodically using LC-MS/MS analysis. Graphs were generated using GraphPad Prism software, and data are represented as the mean \pm S.E.M.

With plasma elimination profiles characterized, further pharmacokinetic experiments were designed to compare both plasma absorption and tissue distribution properties after oral administration. Although plasma elimination after i.v. administration, as indicated by $t_{1/2}$ and Cl values, did not trend inversely with lipophilicity as expected, increased lipophilicity could improve penetration across the enterocyte lining of the intestinal wall, which was anticipated to translate to a positive correlation between lipophilicity and systemic exposure after p.o. administration. Accordingly, pre-cannulated SD rats (250-300 g) were dosed via oral gavage with 10 mg/kg of either Enigmol ($n = 4$), $\text{CF}_3\text{-Enigmol}$ ($n = 4$), or $\text{CF}_2\text{-Enigmol}$ ($n = 4$) in vehicles composed of 90:10 olive oil/EtOH (Enigmol and $\text{CF}_3\text{-Enigmol}$) or 95:5 PEG400/Tween80 ($\text{CF}_2\text{-Enigmol}$). Blood samples were taken at 10 time points up to 24 hrs after administration when rats were sacrificed for tissue harvest. Drug concentrations in isolated plasma and various vital tissue compartments were subsequently quantified

using LC-MS/MS. In contrast to results from i.v. experiments, systemic exposure, as indicated by C_{max} and AUC, trended with lipophilicity after p.o. administration (**Figure 7a**). Consistently, CF₃-Enigmol required the longest amount of time (T_{max}) to reach C_{max} , and it also demonstrated substantially improved oral bioavailability (68%) as compared to Enigmol (11%) and CF₂-Enigmol (10%). Although Enigmol and CF₃-Enigmol were dosed with a different vehicle than CF₂-Enigmol, results were very similar to those observed during previous pharmacokinetic experiments with Enigmol and CF₃-Enigmol in the same vehicle as CF₂-Enigmol (**Figure 8**). Therefore, these results suggest a positive correlation between compound lipophilicity and the rate of absorption into the portal blood supply via diffusion through enterocytes.

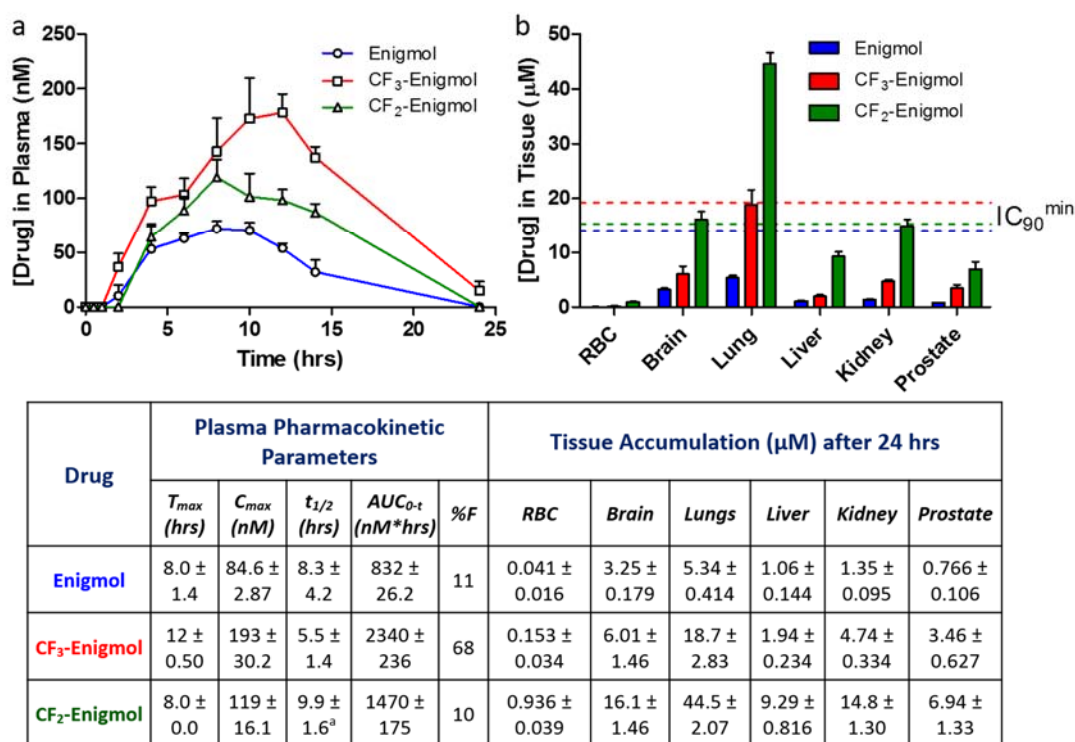
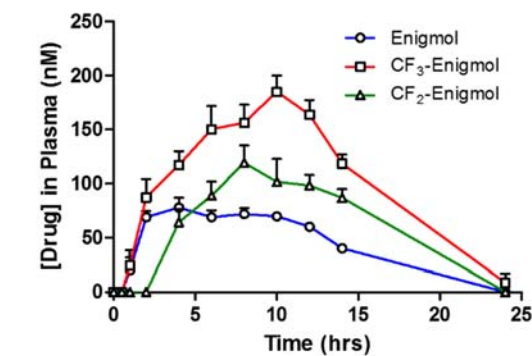


Figure 7: Plasma Pharmacokinetics and Tissue Distribution after 10 mg/kg p.o. Administration. SD rats ($n = 4$ per group) were treated via oral gavage with 10 mg/kg of either Enigmol (vehicle = 90:10 olive oil/EtOH), CF₃-Enigmol (vehicle = 90:10 olive oil/EtOH), or CF₂-Enigmol (vehicle = 95:5 PEG400/Tween80), and (a) plasma concentrations were measured periodically using LC-MS/MS. (b) After 24 hrs, animal subjects were sacrificed, the indicated tissues were harvested, and drug levels in tissue were measured by LC-MS/MS. Graphs were generated using GraphPad Prism software, and data are represented as the mean \pm S.E.M. ^aThe CF₂-Enigmol $t_{1/2}$ value

is reported with the exclusion of one rat from the group due to inappropriate semilog plots of the terminal 2, 3, or 4 non-zero data points (positive linear slopes or $R^2 = 0.038$).

Notably, the high oral bioavailability of CF₃-Enigmol (68-71%) is not only related to the high AUC after p.o. dose, but also to the low AUC after i.v. dose. Consistent with the i.v. experiments, CF₃-Enigmol exhibited an unexpectedly shorter $t_{1/2}$ than CF₂-Enigmol after p.o. dose, which could have been due to elevated tissue distribution, metabolic degradation, and/or drug excretion from the body. The $t_{1/2}$ values calculated for CF₃-Enigmol and CF₂-Enigmol after p.o. administration are likely less accurate than those calculated after i.v. administration because the p.o. curve shapes illustrate elimination phases that are convoluted by long, complex absorption phases. While exponential decay of CF₃-Enigmol plasma concentration after C_{max} was detectable due to a relatively short $t_{1/2}$, exponential decay in the p.o. curve for CF₂-Enigmol was not observed. This phenomenon is likely due to the combination of a relatively high $t_{1/2}$ and a long, complex absorption phase that overlaps with the elimination phase, all of which would be consistent with drug precipitation in the gut and/or with competing uptake via the lymphatic system. While CF₃-Enigmol demonstrated the highest oral bioavailability as hypothesized, CF₂-Enigmol unexpectedly showed no improvement over Enigmol in this respect, perhaps suggesting the role of differential absorption mechanisms for uptake of CF₃-Enigmol and CF₂-Enigmol.



Drug	Plasma Pharmacokinetic Parameters (Vehicle = 95:5 PEG400/Tween80)				
	T_{max} (hrs)	C_{max} (nM)	$t_{1/2}$ (hrs)	AUC_{0-t} (nM*hrs)	%F
Enigmol	4.5 ± 1.3	82.9 ± 7.62	5.1 ± 0.38	1050 ± 30.6	15
CF ₃ -Enigmol	9.0 ± 1.0	188 ± 15.6	6.5 ± 0.65	2450 ± 178	71
CF ₂ -Enigmol	8.0 ± 0.0	119 ± 16.1	9.9 ± 1.6	1470 ± 175	10

Figure 8: Plasma Pharmacokinetics in the Same Vehicle. SD rats ($n = 4$ per group) were treated via oral gavage with 10 mg/kg of either Enigmol, CF₃-Enigmol, or CF₂-Enigmol in a vehicle composed of 95:5 PEG400/Tween80, and plasma concentrations were measured periodically using LC-MS/MS. Graphs were generated using GraphPad Prism software, and data are represented as the mean ± S.E.M. The CF₂-Enigmol curve is reproduced from **Figure 7a** for comparison.

With plasma elimination virtually complete by the 24 hr time point for each orally administered compound, accumulation of Enigmol, CF₃-Enigmol, and CF₂-Enigmol in red blood cells, brain, lung, liver, kidney, and prostate was quantified using LC-MS/MS (**Figure 7b**). Although tissue distribution was anticipated to correlate with compound lipophilicity, CF₂-Enigmol ($n = 4$) unexpectedly achieved substantially higher concentrations than both Enigmol ($n = 4$) and CF₃-Enigmol ($n = 4$) in all tissue types analyzed. Thus, in unanticipated contrast to plasma exposure after oral administration, tissue accumulation did not trend with lipophilicity. As described previously, IC₉₀ concentrations represent the drug levels desired to be achieved at the site of action *in vivo*, and measurement of tissue accumulation facilitates prediction of relative absorption into tumor. While Enigmol did not achieve IC₉₀ levels ($\geq 14 \mu\text{M}$) in any tissue type, CF₃-Enigmol achieved the desired concentration ($\geq 19 \mu\text{M}$) in lung. Remarkably, CF₂-Enigmol achieved IC₉₀ levels ($\geq 15 \mu\text{M}$) in lung (45 μM), brain (16 μM), and kidney (15 μM), into which Enigmol and CF₃-Enigmol preferentially distributed as well. Also notable are the relative drug levels in prostate, where CF₂-Enigmol achieved 2-fold higher concentrations than

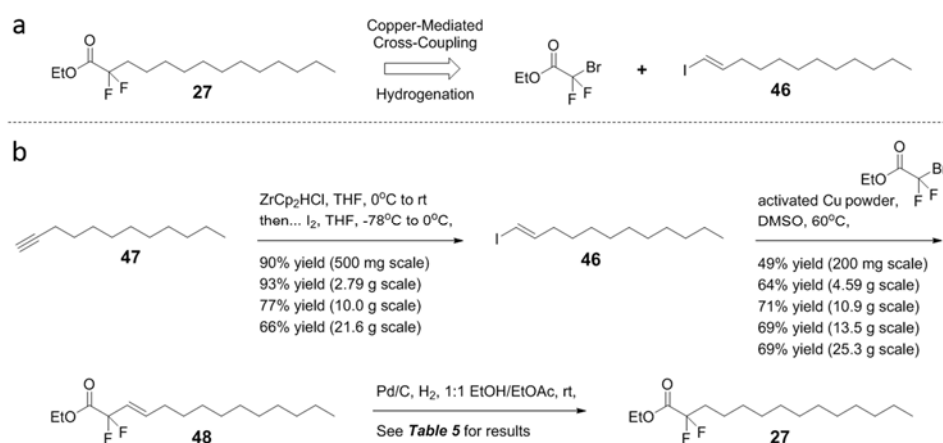
CF₃-Enigmol and 9-fold higher concentrations than Enigmol. The extremely high concentration of CF₂-Enigmol in lung is another piece of evidence to suggest an alternative mechanism of drug absorption. Partial uptake by the lymphatic system, for instance, would bypass the liver to deposit the drug into the thoracic duct, which empties into the superior vena cava, thereby transporting CF₂-Enigmol into the right atrium of the heart, passing it through the heart's right ventricle, and finally pumping it out through the pulmonary artery to the lungs. While CF₃-Enigmol was expected to achieve the highest tissue concentrations due to both lipophilicity and rapid elimination from plasma, it must be noted that tissue accumulation was only examined at a single time point. If efficient removal of CF₃-Enigmol from plasma was related to increased metabolism and/or excretion as opposed to tissue uptake, it is possible that CF₃-Enigmol was also eliminated from tissue faster than Enigmol and CF₂-Enigmol. If this were the case, CF₃-Enigmol could have achieved the highest maximum tissue concentrations at earlier time points, which were not examined during this study. While it is additionally tempting to speculate that highly lipophilic CF₃-Enigmol could have preferentially partitioned into fatty tissue as opposed to the organs examined during this study, a systematic series of pharmacokinetic studies involving quantitation of orally-administered compounds and corresponding metabolites in various tissue types at multiple time points would be required to appropriately address these considerations. Regardless of the reason for differences between tissue accumulation of CF₃-Enigmol and CF₂-Enigmol, both of these drugs achieved higher tissue concentrations than Enigmol, as originally anticipated, which is consistent with the hypothesis that increased lipophilicity will translate to enhanced *in vivo* anti-tumor efficacy.

1.2.e. 2nd Scale Up Preparation of CF₂-Enigmol

In order to compare the anti-cancer activities of Enigmol, CF₃-Enigmol, and CF₂-Enigmol *in vivo*, a 2nd scale up of CF₂-Enigmol was required. Accordingly, several of the synthetic challenges encountered during the 1st scale up endeavor, including detrimentally low yield of α,α -difluoro ester **27** and poor diastereoselectivity of both the aldol reaction and reduction of the resulting β -hydroxy ketone

35, needed to be addressed. First, the synthetic route previously employed for preparation of α,α -difluoro ester **27** was not amenable to large scale synthesis, as indicated by the low yields obtained during the 1st scale up synthesis (< 4% yield over 3 steps), as well as during the original small scale synthesis (14% yield over 3 steps). These low yields resulted largely from poor-yielding production of α -keto ester **28** via Grignard addition to chlorooxalate **29**-derived imidazolide **31** on both small (17% yield over 2 steps) and moderate scales (< 8% yield over 2 steps). Accordingly, a more efficient synthesis of α,α -difluoro ester **27** was sought. Although nucleophilic difluorination of α -keto ester **28** to generate α,α -difluoro ester **27** proceeded in good yield when the starting material was not contaminated, an alternative approach involving a commercially available synthon with the proper fluorination pattern already installed was envisioned. In particular, ethyl bromodifluoroacetate is such a reagent with a reactivity profile that was predicted to enable a transition metal-mediated cross-coupling approach. This versatile synthon has been demonstrated to undergo zinc-mediated Reformatsky reactions⁵¹ with aldehydes, ketones, and imines, as well as copper-mediated cross-couplings⁵² with aryl and vinyl iodides. While attempted copper-mediated cross-couplings between ethyl bromodifluoroacetate and alkyl iodides or alkynyl iodides resulted in no reaction or homocoupling, respectively, cross-couplings with both *cis* and *trans* vinyl iodides delivered the corresponding β,γ -unsaturated- α,α -difluoro esters in good yield⁵³. Accordingly, an alternative synthetic route to α,α -difluoro ester **27** was planned to proceed via copper-mediated cross-coupling of alkyl-substituted terminal vinyl iodide **46** and ethyl bromodifluoroacetate (**Scheme 13a**). Synthesis of terminal vinyl iodides has been reported to occur via tandem hydrozirconation/iodination of the corresponding terminal alkynes⁵⁴. Therefore, a solution of commercially available terminal alkyne **47** was treated with Schwartz reagent at 0°C (**Scheme 13b**), and the resulting reaction mixture was allowed to warm to room temperature to generate the corresponding terminal vinyl zirconium species. This solution was immediately cooled to -78°C, and a solution of electrophilic iodine was added slowly, resulting in the formation of desired terminal vinyl iodide **46**. This tandem hydrozirconation/iodination of terminal alkyne **47** occurred in good to excellent yield, which trended inversely with scale. While the reaction

sequence itself resulted in complete conversion of alkyne **47** to terminal vinyl iodide **46** on all scales, yields suffered as scale increased largely because of purification via column chromatography. Next, cross-coupling⁵³ between vinyl iodide **46** and ethyl bromodifluoroacetate was mediated by copper powder that was activated to remove copper oxides and salts⁵⁵. Activated copper powder was diluted with DMSO, terminal vinyl iodide **46** and ethyl bromodifluoroacetate were added in succession at room temperature, and the resulting mixture was warmed to 60°C and allowed to stir vigorously overnight. Although this copper-mediated cross-coupling produced β,γ -unsaturated- α,α -difluoro ester **48** in only 49% yield on a 200 mg scale, production of **48** on moderate to large scales was relatively consistent between 64 and 71% yield.

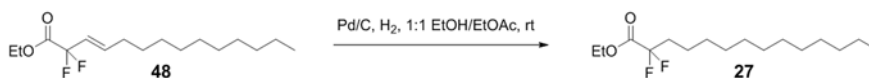


Scheme 13: Retrosynthetic Analysis and 2nd Scale Up Preparation of α,α -Difluoro Ester **27.** (a) Alternative retrosynthesis of ester **27** involved copper-mediated coupling of ethyl bromodifluoroacetate and vinyl iodide **46**, followed by hydrogenation of the resulting olefin. (b) Implementation of this new strategy facilitated robust, scalable production of ester **27**.

Generation of α,α -difluoro ester **27** via palladium-catalyzed hydrogenation⁵⁶ of allylic *gem*-difluoride **48**, however, was more variable (**Table 5**). While α,α -difluoro ester **27** was produced in 84% yield on a 97 mg scale (**Table 5**, Batch 1), the same conditions applied to a 2.07 g scale (**Table 5**, Batch 2) failed to facilitate complete conversion of olefin **48**, delivering a mixture of **48** and **27** that was not separable via silica gel chromatography. These results indicated not only that the reaction should be monitored by LC-MS instead of TLC, but also that the reaction would need to be pushed to completion

to allow isolation of pure α,α -difluoro ester **27**. Therefore, hydrogenation of olefin **48** was applied to a 4.1 g scale (*Table 5*, Batch 3), for which reaction progress was monitored by LC-MS via positive ion extraction, and an extra 0.05 eq of catalyst was added each additional day prior to complete conversion. Although pure α,α -difluoro ester **27** was produced in 64% yield after column chromatography, the reaction was quite inefficient, requiring 6 days and five times the initial catalyst loading, making further optimization desirable. Since each of the hydrogenation reactions of olefin **48** described thus far (*Table 5*, Batch 1-3) utilized a balloon of hydrogen at 14.7 psi, it was hypothesized that increased reaction efficiency would result from elevating the pressure of hydrogen. Accordingly, the reaction was carried out on a 2 g scale using a Parr shaker (*Table 5*, Batch 4), and the starting pressure at was set to 30 psi. After 1 hr, LC-MS analysis indicated 27% conversion of olefin **48** to saturated ester **27**, but unfortunately, an additional 1.5 hrs at 30 psi resulted in only 30% conversion total. Similarly, increasing the pressure to 40 psi for 2 hrs led to only 39% total reaction progress. While raising the pressure to 50 psi for an additional 1 hr pushed the reaction to 43% α,α -difluoro ester **27**, 5% of a **27**-derived byproduct whose mass corresponded to the replacement of one fluorine atom with a hydrogen atom was observed. Decreasing the pressure to 45 psi and shaking overnight resulted in little further conversion of olefin **48** to α,α -difluoro ester **27**, but 10% total conversion of **27** to the mono-defluorinated byproduct. While these results suggested that hydrogenation under elevated pressure would not be an optimal method for the preparation of α,α -difluoro ester **27** due byproduct formation, all hydrogenations attempted by that point emphasize the challenges and inconsistencies associated with scaling up a reaction that involves heterogeneous reaction medium and a gaseous reagent. Issues with scaling palladium-catalyzed hydrogenations are well documented, and poor reaction efficiency is commonly associated with insufficient reaction vessel head space, less than optimal stirring efficiency, and/or solid catalyst aggregation. In order to push hydrogenation reactions to completion efficiently, ample volume in the reaction flask should be available for gaseous hydrogen occupation, and mixing should be vigorous to maximize the surface area of the solid palladium catalyst, as well as to minimize catalyst aggregation. With these strategies in mind, the ratio of solvent volume to vessel volume was

dropped below 0.3, reaction mixtures were stirred with large stir bars as vigorously as possible, and fresh catalyst was added each day (if necessary) after removal of the old catalyst via filtration (**Table 5**, Batch 5-7). While application of these parameters to the hydrogenation of olefin **48** on a 3.06 g scale (**Table 5**, Batch 5) delivered α,α -difluoro ester **27** in 94% yield after 1 day without the need for catalyst replacement, scaling up to 5.88 g (**Table 5**, Batch 6) and 7.58 g (**Table 5**, Batch 7) both required 3 days of reaction time with fresh catalyst each day to produce α,α -difluoro ester **27** in 83% yield after column chromatography. Thus, the preparation of **27** was improved from 4% maximum yield over 3 steps during the 1st scale up (imidazolid formation, Grignard addition, and nucleophilic difluorination) to 62% maximum yield over 3 steps (hydrozirconation/iodination, cross-coupling, and hydrogenation) during the 2nd scale up.

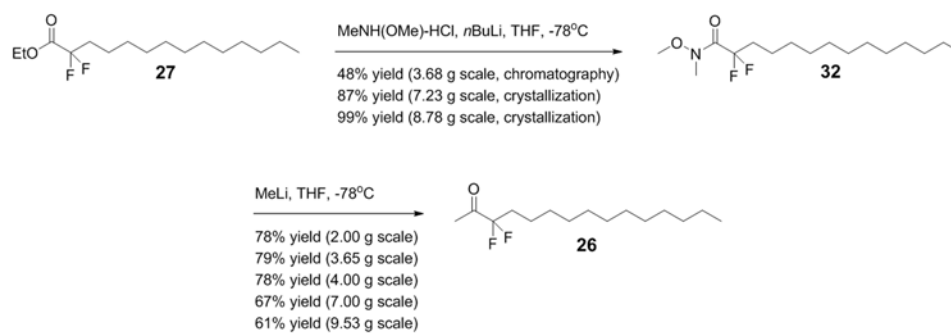


Batch	Scale (g)	Concentration (M)	Solvent Volume : Vessel Volume	Time	Catalyst Loading	H ₂ Pressure	H ₂ Vessel	Results
1	0.097	0.01	0.132	1 day	5 mol % (x 1)	14.7 psi	Balloon	84% yield
2	2.07	0.01	0.356	1 day	5 mol % (x 1)	14.7 psi	Balloon	Inseparable mixture of 48 and 27
3	4.10	0.02	0.415	6 days	5 mol % (x 5)	14.7 psi	Balloon	64% yield
4	2.00	0.10	0.138	1 hr	5 mol % (x 1)	30 psi	Parr	73% 48 , 27% 27
	2.00	0.10	0.138	1.5 hrs	N/A	30 psi	Parr	70% 48 , 30% 27
	2.00	0.10	0.138	2 hrs	N/A	40 psi	Parr	61% 48 , 39% 27
	2.00	0.10	0.138	1 hr	N/A	50 psi	Parr	52% 48 , 43% 27 , 5% 27 – 1F
	2.00	0.10	0.138	1 day	N/A	45 psi	Parr	47% 48 , 43% 27 , 10% 27 – 1F
5	3.06	0.04	0.264	1 day	10 mol % (x 1)	14.7 psi	Balloon	94% yield
6	5.88	0.06	0.169	3 days	10 mol % (x 3)	14.7 psi	Balloon	83% yield
7	7.58	0.05	0.174	3 days	10 mol % (x 3)	14.7 psi	Balloon	83% yield

Table 5: Optimization of Hydrogenation of Olefin 48 to α,α -Difluoro Ester 27. LC-MS analysis utilizing ion extraction was employed to measure relative quantities of starting material **48**, desired product **27**, and undesired byproduct **27** – **1F**.

Although this reaction sequence could have been optimized further, an ample quantity of α,α -difluoro ester **27** was available to continue with the 2nd scale up of CF₂-Enigmol. Accordingly, α,α -difluoro ester **27** was subjected to the subsequent 2-step Weinreb ketone synthesis for preparation of α,α -difluoro methyl ketone **26**, which proceeded in 72% yield over 2 steps during the 1st scale up.

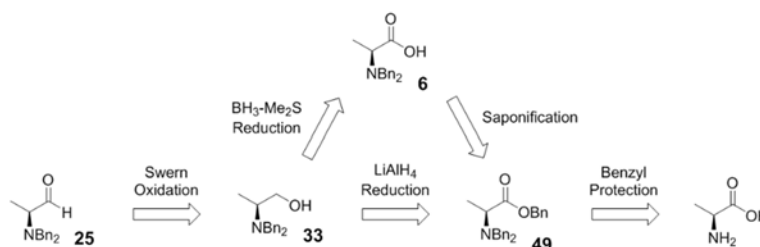
Although this moderate yield was obtained without purification of Weinreb amide intermediate **32**, it was desirable to examine the effect of increasing scale on yield during the 2nd scale up (**Scheme 14**). While Weinreb amidation of α,α -difluoro ester **27** applied to a 3.68 g scale produced Weinreb amide **32** in only 48% yield after column chromatography, purification via recrystallization on 7.23 g and 8.78 g scales delivered **32** in 87% yield and 99% yield, respectively. Thus, yield was improved drastically by using recrystallization instead of column chromatography as the method of purification, and increasing the scale maximized the yield of Weinreb amide **32** by ease of bulk solid precipitation and isolation. In contrast, preparation of α,α -difluoro methyl ketone **26**, which included purification via column chromatography, resulted in an inverse trend between scale and yield. While the yield was robustly stable at 78-79% on 2 g, 3.65 g, and 4 g scales, increasing the scale to 7 g and 9.53 g resulted in a reduction to 67% yield and 61% yield, respectively. Consequently, the preparation of α,α -difluoro methyl ketone **26** on scale was elevated slightly from 72% yield over 2 steps during the 1st scale up to 78% maximum yield over 2 steps during the 2nd scale up.



Scheme 14. 2nd Scale Up of α,α -Difluoro Methyl Ketone **26**. Preparation of methyl ketone **26** via Weinreb ketone synthesis of ester **27** proved to be robust on relatively large scale.

With a sufficient quantity of α,α -difluoro methyl ketone **26** for subsequent aldol reaction, the next task was moderate scale preparation of aldol coupling partner *N,N*-dibenzyl- α -amino aldehyde **25**. Although precursor *N,N*-dibenzyl- α -aminoalcohol **33** was previously synthesized via $\text{BH}_3\text{-Me}_2\text{S}$ -mediated reduction of carboxylic acid **6**, preparation of **6** required saponification of *N,N*-dibenzyl- α -amino ester **49**, which was derived from *L*-alanine²² (**Scheme 15**). In contrast, preparation of *N,N*-

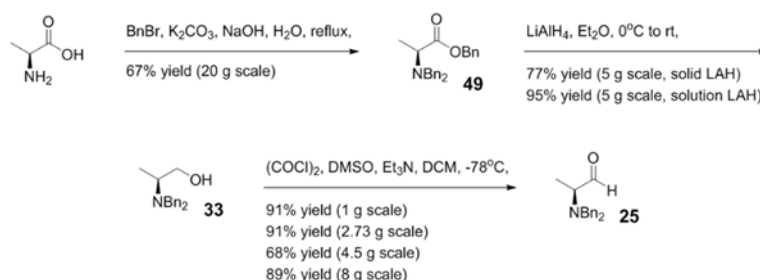
dibenzyl- α -aminoalcohol **33** via lithium aluminum hydride-mediated reduction of benzyl ester **49** would render the additional saponification step unnecessary. Notably, reduction of benzyl ester **49** to alcohol **33** with lithium aluminum hydride has been reported to proceed in 56% yield on a moderate



Scheme 15: Retrosynthetic Analyses for *N,N*-Dibenzyl- α -Amino Aldehyde **25.** Alternative retrosynthesis of aldehyde **25** involved direct reduction of ester **49** as opposed to saponification and subsequent reduction of resulting carboxylic acid **6**.

scale⁵⁷, and the analogous reduction of *N,N*-dibenzyl-*L*-phenylalanine benzyl ester was demonstrated on a larger scale to deliver the corresponding *N,N*-dibenzyl- α -aminoalcohol in 75-87% yield⁴⁵. According to the methods described in these reports, an aqueous solution of *L*-alanine (20 g scale) was treated with benzyl bromide under basic conditions at refluxing temperatures to produce *N,N*-dibenzyl- α -amino benzyl ester **49** in 67% yield after column chromatography (**Scheme 16**). Benzyl ester **49** (5 g scale) was then subjected to reduction facilitated by solid lithium aluminum hydride or by a solution of lithium aluminum hydride, which cleanly delivered *N,N*-dibenzyl- α -aminoalcohol **33** after column chromatography in 77% yield and 95% yield, respectively. Alcohol **33** was then oxidized to *N,N*-dibenzyl- α -amino aldehyde **25** under Swern conditions as previously described. Although conversion of alcohol **33** to aldehyde **25** via Swern oxidation was robust on all scales, the need for quick column chromatography via silica gel plug to prevent racemization and decomposition resulted in variable yields (68-89%) on moderate scales (4.5-8 g). Also to avoid potential racemization and decomposition, aldehyde **25** was freshly prepared shortly before subsequent aldol reaction, for which optical purity of aldehyde **25** was verified via optical rotation prior to each aldol batch. Ultimately, synthesis of alcohol **33** via lithium aluminum hydride-mediated reduction of benzyl ester **49** (95% yield)

outperformed the preparation of alcohol **33** via saponification of benzyl ester **49** and subsequent $\text{BH}_3\text{-Me}_2\text{S}$ -mediated reduction of carboxylic acid **6** (91% yield from the 1st scale up), even if the saponification of benzyl ester **49** to carboxylic acid **6** occurred in 100% yield. Overall, the production of *N,N*-dibenzyl- α -amino aldehyde **25** during the 2nd scale up proceeded in 58% yield over 3 steps from *L*-alanine, exceeding the efficiency of the 1st scale up both in terms of yield and number of synthetic steps.



Scheme 16. 2nd Scale Up Preparation of *N,N*-Dibenzyl- α -Amino Aldehyde **25**. Implementation of the new synthetic strategy for preparation of aldehyde **25** saved one synthetic step and substantially improved the overall yield.

Although the isolation of both β -hydroxy ketone diastereomers resulting from achiral borane-mediated aldol reaction between α,α -difluoro methyl ketone **26** and *N,N*-dibenzyl- α -amino aldehyde **25** was originally desirable, the total yield of CF_2 -Enigmol suffered during the 1st scale up, in part due to poor aldol diastereoselectivity (*d.r.* = 61:39 *syn/anti*), which produced desired diastereomer **35** in 43% yield. This result is consistent with the reported lack of diastereoselectivity observed during aldol reaction between *N,N*-dibenzyl- α -amino aldehydes and achiral boron enolates³³. In contrast, chlorodicyclohexylborane-mediated aldol reaction between tridecane-substituted methyl ketone and *N*-Boc-alaninal was reported to proceed with excellent substrate-directed diastereoselectivity (*d.r.* = 95:5 *syn/anti*), albeit in low isolated yield (20%) regardless of the significantly enhanced *d.r.*⁴⁷, emphasizing the importance of *N*-protecting groups in diastereoinduction. Proposed Zimmerman-Traxler chair transition states⁵⁸ (**Figure 9**, top) illustrate that the structural distinction between enolate attack of aldehyde **25** from *re* and *si* faces involves potential interaction between the cyclohexyl borane

ligands and the chiral *N,N*-dibenzylamino group (*re* transition state) or the chiral methyl group (*si* transition state). Putative steric repulsion between the enolate axial α -proton and the chiral methyl group (*re* transition state) or the chiral *N,N*-dibenzylamino group (*si* transition state) marks an additional point of differentiation. Although unfavorable steric interaction between the cyclohexyl ligands and the chiral *N,N*-dibenzylamino group (*re* transition state) would be predicted to fuel a strong preference for the *si* transition state, only very modest *syn*-diastereoselectivity was observed during aldol reaction with achiral chlorodicyclohexylborane. Alternatively, *syn*-diastereoselectivity of aldol reactions involving *N,N*-dibenzyl- α -amino aldehyde **25** and α,α -difluoro methyl ketone **26** could, in principle, be improved with the use of chiral boranes. While the original aldol-based synthesis of Enigmol utilized (-)-DiPCl for aldol reaction between *N,N*-dibenzyl- α -amino methyl ketone **7** and tridecanal, the resulting *syn*-aminoalcohol was exclusively detected with the use of either (-)-DiPCl or (+)-DiPCl²², indicating that the diastereoselectivity was surprisingly under strong substrate control. In contrast, *N,N*-dibenzyl- α -amino aldehydes derived from valine and phenylalanine were each reported to undergo aldol reactions with *R,R*- and *S,S*-2,5-diphenylborolane-stabilized enolates derived from thioacetate isopropyl ester in moderate to good yield (50-85%) with complete reagent control of diastereoselectivity (14:1 \leq *d.r.* \leq 28:1) for the matched aldehyde enantiomers⁵⁹. Similarly, aldehyde **25**, as well as *N,N*-dibenzyl- α -amino aldehydes derived from *L*-valine, *L*-leucine, *L*-isoleucine, and *L*-phenylalanine, underwent aldol reaction with a thioacetate *tert*-butyl ester-derived enolate stabilized by a chiral borane reagent prepared from either (+)-menthol or (-)-menthol, resulting in moderate to good yield (71-80%) with complete reagent control of diastereoselectivity⁵⁸ (95:5 \leq *d.r.* \leq 99:1). Unfortunately, preparation of bromo or chloroboranes linked via carbon to two chiral substituents derived from 2,5-diphenylborolane⁶⁰ or menthol⁶¹ is particularly inefficient, requiring isolation of a single bis-substituted haloborane enantiomer away from several undesired stereoisomers. Since the ultimate goal was to scale up CF₂-Enigmol, which was already successful during the 1st scale up even with poor aldol diastereoselectivity, aldol reactions between α,α -difluoro methyl ketone **26** and *N,N*-dibenzyl- α -amino aldehyde **25** were attempted with commercially available chiral boranes (-)-DiPCl

and (+)-DiPCl. While (+)-DiPCl-mediated aldol reaction (**Figure 9**, Batch 2) led to a mixture of β -hydroxy ketone diastereomers **35** and **36** that favored *anti*-stereoisomer **36** ($d.r. = 27:73$ *syn/anti*) via the *re* transition state, (-)-DiPCl (**Figure 9**, Batch 3) facilitated a slight boost in *syn*-diastereoselectivity ($d.r. = 66:34$ *syn/anti*) via the *si* transition state over that ($d.r. = 61:39$ *syn/anti*) induced by achiral chlorodicyclohexylborane (**Figure 9**, Batch 1). All diastereomeric ratios resulting from aldol reaction were determined via LC-MS analysis.

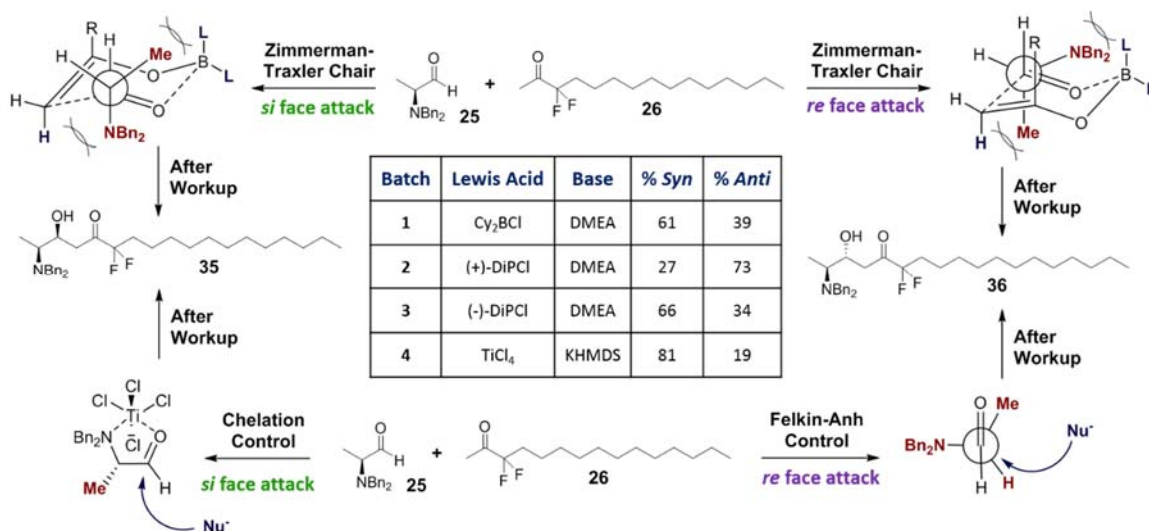
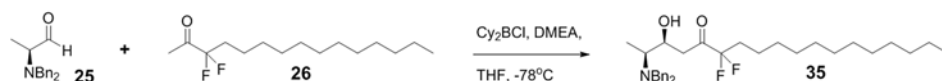


Figure 9. Diastereoselectivity of Aldol Reaction between Methyl Ketone **26** and Aldehyde **25**. Competition between borane-stabilized Zimmerman-Traxler chair transition states, or between chelation-controlled and Felkin-Anh-controlled transition states, dictate diastereoselectivity of aldol reaction between methyl ketone **26** and aldehyde **25**.

Preference for the *syn*-adduct with achiral chloroborane suggests that asymmetric induction is formally under slight chelation control as opposed to Felkin-Anh control, which preferences *anti*- versus *syn*-stereoisomers after addition of nucleophiles to *N,N*-dibenzyl- α -amino aldehydes. For instance, nucleophilic addition of achiral aryl and alkyl lithium species, aryl and alkyl Grignards, Gillman-type reagents, and alkyl zinc reagents to *N,N*-dibenzyl- α -amino aldehyde **25** was reported to proceed under Felkin-Anh control through *re* face attack (**Figure 9**, bottom), favoring the corresponding *anti*-aminoalcohols^{33,62} ($75:25 \leq d.r. \leq 97:3$). In contrast, *syn*-diastereoselectivity (*si* face attack) could only be afforded via chelation-controlled nucleophilic addition mediated by particularly

harsh reagents, such as methyltitanium trichloride (*d.r.* = 94:6) and allyltrimethylsilyl/tin tetrachloride⁶² (*d.r.* = 84:16). Furthermore, aldol reaction of *N,N*-dibenzyl- α -amino aldehyde **25** with lithium enolates derived from methyl acetate and isopropyl acetate both occurred in good yield (82% and 84%, respectively), and both strongly favored the corresponding *anti*-aminoalcohols (*d.r.* = 95:5 and 97:3, respectively) through Felkin-Anh control (*re* transition state). Alternatively, titanium tetrachloride-mediated aldol reaction between aldehyde **25** and phenyl acetate-derived trimethylsilyl ketene acetal was reported to proceed with good chelation-controlled diastereoselectivity (*d.r.* = 95:5) via *si* face attack, generating the corresponding *syn*-aminoalcohol in 25% yield. Similarly, titanium tetrachloride-mediated aldol reaction between α,α -difluoro methyl ketone **26** and *N,N*-dibenzyl- α -amino aldehyde **25** resulted in substantially improved *syn*-diastereoselectivity (*d.r.* = 81:19) as compared to that achieved with achiral chlorodicyclohexylborane (*d.r.* = 61:39), suggesting the a chelation mechanism was at play (**Figure 9**, Batch 4). Unfortunately, very little of the desired β -hydroxy ketone **35**, which was contaminated with several impurities, was isolated after column chromatography.



Batch	Scale	Quench Method	TLC Temperature	TLC Results	% Yield <i>Syn</i>
1st Scale Up	1.59 g	Dropwise at -78°C , to -10°C	-78°C (pre-quench)	High ratio of 35 to 26	43
1	2.00 g	Dropwise at -78°C , to -10°C	-78°C (pre-quench)	High ratio of 35 to 26	9
2	3.30 g	Dropwise at -78°C , to -10°C	-78°C (pre-quench)	High ratio of 35 to 26	10
			-10°C (post-quench)	Low ratio of 35 to 26	
3	847 mg	Cannula from -78°C to 0°C	-78°C (pre-quench)	High ratio of 35 to 26	19
4	200 mg	Pour from -20°C to 0°C	-78°C (pre-quench)	High ratio of 35 to 26	38
			-60°C (pre-quench)	High ratio of 35 to 26	
			-40°C (pre-quench)	High ratio of 35 to 26	
			-20°C (pre-quench)	High ratio of 35 to 26	
5	1.41 g	Pour from -20°C to 0°C	-78°C (pre-quench)	High ratio of 35 to 26	38
			-30°C (pre-quench)	High ratio of 35 to 26	
6	2.86 g	Pour from -20°C to 0°C	-78°C (pre-quench)	High ratio of 35 to 26	36
			-30°C (pre-quench)	High ratio of 35 to 26	
7	4.96 g	Pour from -20°C to 0°C	-78°C (pre-quench)	Moderate ratio of 35 to 26	30

Table 6: 2nd Scale Up of β -Hydroxy Ketone 35. Retro-aldol reaction during quench of aldol reaction between aldehyde **25** and methyl ketone **26** was overcome by altering the method of reaction quench.

Due to the low yield obtained with titanium tetrachloride, and due to the higher cost of chiral chloroboranes versus achiral chloroboranes, chlorodicyclohexylborane-mediated aldol reaction remained the most viable option for the 2nd scale up of β -hydroxy ketone **35**. During the 1st scale up of CF₂-Enigmol, aldol reaction between α,α -difluoro methyl ketone **26** (1.59 g scale) and *N,N*-dibenzyl- α -amino aldehyde **25** produced *syn*-aminoalcohol **35** in 43% yield after column chromatography (**Table 6**, 1st Scale Up Batch). In contrast, scaling the reaction up to a 2 g scale (**Table 6**, Batch 1) and a 3.3 g scale (**Table 6**, Batch 2) both resulted in substantially decreased isolation of desired product **35** (9% yield and 10% yield, respectively), as well as recovery of a significant quantity of α,α -difluoro methyl ketone **26**. Notably, the reaction was quenched in each case via dropwise addition of aqueous phosphate buffer (pH = 7) at -78°C after TLC indicated complete consumption of methyl ketone **26**, and the resulting biphasic mixtures were allowed to slowly warm to room temperature. For the 3.3 g scale aldol reaction (**Table 6**, Batch 2), TLC analysis at -10°C during the warm up period indicated a large ratio of starting methyl ketone **26** to desired *syn*-aminoalcohol **35**, suggesting that retro-aldol occurred during reaction quench. Since quenching the reaction at -78°C via dropwise addition of an aqueous solution results in a very slow quench as the reaction mixture warms up, transfer of the reaction mixture at -78°C via cannula into a large volume of aqueous phosphate buffer (pH = 7) at 0°C was applied to an 847 mg scale aldol reaction (**Table 6**, Batch 3) in order to facilitate a more rapid quench. While this method of reaction quench delivered desired β -hydroxy ketone **35** in 19% yield after column chromatography, yield still suffered due to retro-aldol reaction. It was then hypothesized that β -hydroxy ketone **35** was thermally unstable at temperatures $\leq -10^\circ\text{C}$ under the reaction conditions. Accordingly, the aldol reaction was carried out on a 200 mg scale (**Table 6**, Batch 4), and TLC analysis was conducted prior to reaction quench at -80°C, -60°C, -40°C, and -20°C, each of which demonstrated a large ratio of desired *syn*-aminoalcohol **35** to starting methyl ketone **26**. The reaction mixture at -20°C was then poured over a large volume of aqueous phosphate buffer (pH = 7) at 0°C, the biphasic mixture shaken vigorously, and the resulting aqueous layer was quickly removed, facilitating isolation of *syn*-aminoalcohol **35** in 38% yield after column chromatography. This new

workup method was subsequently applied to 1.41 g (**Table 6**, Batch 5), 2.86 g (**Table 6**, Batch 6), and 4.96 g (**Table 6**, Batch 7) scales, which facilitated production of desired product **35** in 38% yield, 36% yield, and 30% yield, respectively. Although yield trended inversely with reaction scale, this was a result of tricky separation of **35** and the closely-eluting *anti*-diastereomer **36** via silica gel chromatography, as opposed to retro-aldol during reaction quench.

While diastereoselectivity and scalability could be improved for the aldol reaction between α,α -difluoro methyl ketone **26** and *N,N*-dibenzyl- α -amino aldehyde **25**, a substantial quantity of β -hydroxy ketone **35** was available to proceed with the 2nd scale up of CF₂-Enigmol. With substantial improvements to the synthesis of α,α -difluoro ester **27** during the 2nd scale up endeavor, the non-diastereoselective reduction of β -hydroxy ketone **35** remained the least efficient step of the entire synthetic route, facilitating isolation of desired *syn*-diol **38** in only 28% yield during the 1st scale up. While the reduction of β -hydroxy ketone **35** with sodium borohydride at room temperature led to complete conversion of the starting material, a roughly equal mixture of diastereomers was rapidly generated, and the isolated yield of *syn*-diol **38** suffered from difficult chromatographic separation from the closely eluting undesired *anti*-diol **39**; thus, an improvement in *syn*-diastereoselectivity was sought. One of the most well-established methods for *syn*-reduction of β -hydroxy ketones involves the addition of sodium borohydride to preformed dialkylborane chelates, which direct hydride addition on the face opposite that of the adjacent axial hydrogen⁶³ (**Figure 10**, top). For example, a series of β -hydroxy (mono-alkyl-, aryl-, or vinyl-substituted) ketones (alkyl-, aryl-, or β -ester-substituted) premixed with diethylmethoxyborane at -78°C were reported to undergo highly diastereoselective reduction to the corresponding *syn*-1,3-diols ($98:2 \leq d.r. \leq 99:1$) upon addition of sodium borohydride in moderate to excellent yield⁶⁴ (68-99%). This led to the hypothesis that sodium borohydride-mediated reduction of an *in situ*-generated, dialkylborane chelate derived from β -hydroxy ketone **35** would diastereoselectively generate desired *syn*-diol **38**. In order to establish a baseline diastereomeric ratio, β -hydroxy ketone **35** was first subjected to sodium borohydride-mediated reduction at -78°C (**Figure 10**, Batch 1), which resulted in a 41:59 ratio between *syn*- and *anti*-diols, as indicated by LC-MS analysis. Next, starting

material **35** was premixed with diethylmethoxyborane at -78°C to generate the corresponding dialkylborane chelate *in situ*, and sodium borohydride was added at -78°C (**Figure 10**, Batch 2), resulting in a similar ratio between **38** and **39** (*d.r.* = 45:55 *syn/anti*). As the *gem*-difluoro group of **35** likely renders the adjacent alcohol poorly nucleophilic, it was hypothesized that the intermediate boron chelate did not form at -78°C after 30 min of stirring. In an attempt to improve formation of the boron chelate, reduction of β -hydroxy ketone **35** involving diethylmethoxyborane and sodium borohydride was carried out at 0°C (**Figure 10**, Batch 3), which resulted in LC-MS detection of the same diastereomeric ratio (45:55 *syn/anti*). In a final attempt to utilize an intermediate dialkylborane chelate to induce *syn*-diastereoselectivity, a solution of β -hydroxy ketone **35** was treated with diethylmethoxyborane at -78°C (**Figure 10**, Batch 4), the reaction mixture was stirred at -78°C for 30 min, and the resulting mixture was allowed to slowly warm to 0°C , at which point the solution was cooled back down to -78°C where sodium borohydride was added. Although these conditions facilitated a slight depletion in *anti*-diastereoselectivity (*d.r.* = 51:49 *syn/anti*), they suggested that sodium borohydride-mediated reduction of β -hydroxy ketone **35** via the corresponding boron chelate would not be a viable option for the diastereoselective production of desired *syn*-diol **38**.

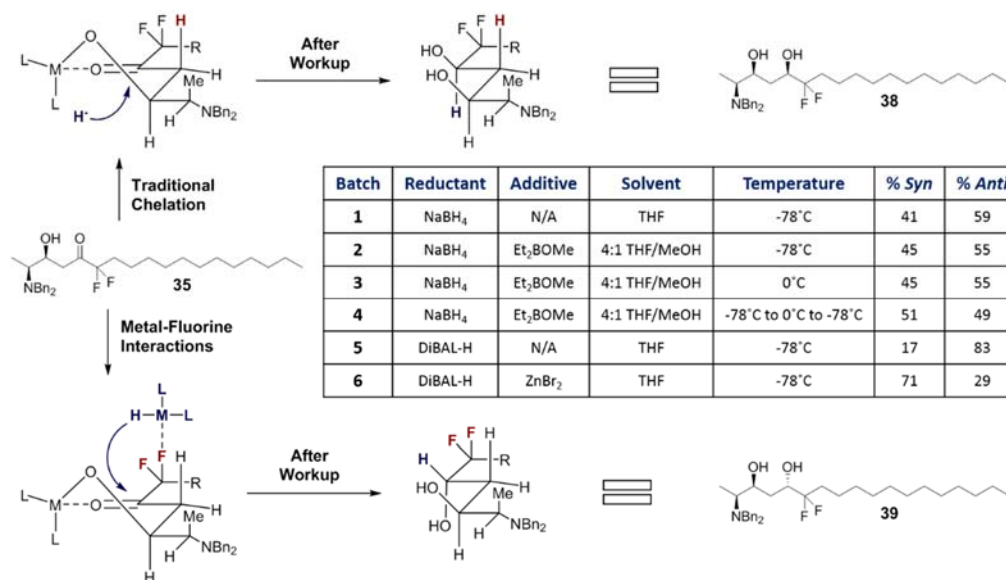
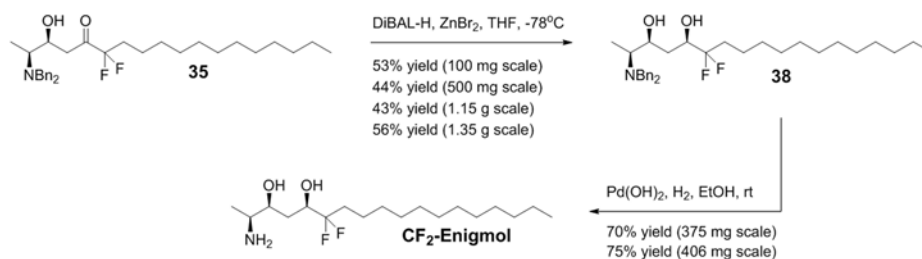


Figure 10. Diastereoselectivity of Reduction of β -Hydroxy Ketone 35. Competition between a Zimmerman-Traxler-type chair transition state and metal-fluorine interaction-controlled transition state dictates diastereoselectivity of reduction of β -hydroxy ketone 35.

An alternative approach to *syn*-reduction of β -hydroxy ketones to give the corresponding *syn*-1,3-diols was reported to involve diisobutylaluminum hydride, which similarly directed diastereoselective hydride delivery via an aluminum-chelated transition state⁶⁵. For example, diisobutylaluminum hydride-mediated reduction of β -hydroxy (mono-alkyl- vinyl-, or aryl-substituted) ketones (alkyl- or aryl-substituted) at -78°C was reported to proceed with fair to excellent degrees of *syn*-diastereinduction ($67:30 \leq d.r. \leq 95:5$), as well as good to excellent yields (81-91%). Accordingly, a solution of β -hydroxy ketone 35 was treated with diisobutylaluminum hydride at -78°C (Figure 10, Batch 5), which contrastingly led to a mixture of diols 38 and 39 that favored the *anti*-diastereomer ($d.r. = 83:17$). Consistent with this result, the reduction of α,α -difluoro- β -hydroxy (mono-alkyl- or aryl-substituted) ketones (alkyl- or aryl-substituted) with diisobutylaluminum hydride at -78°C was reported to demonstrate poor to excellent *anti*-diastereoselectivity ($53:47 \leq d.r. \leq 100:0$) for the large majority of substrates examined⁶⁶. The authors rationalized that *anti*-diastereinduction must not result from the typical diisobutylaluminum hydride-stabilized transition state, and alternatively proposed that hydride delivery was instead directed by metal-fluorine interactions between a fluorine atom and another molecule of diisobutylaluminum hydride. Therefore, the reaction was carried out in the presence of various Lewis acids in an effort to identify a reagent that could disrupt the putative fluorine-aluminum interaction, thereby allowing diastereoselective hydride direction via the typical transition state. This screen resulted in the reported discovery that diisobutylaluminum hydride-mediated reduction of a variety of substrates in the presence of zinc(II) bromide delivered the corresponding 2,2-difluoro-*syn*-1,3-diols with good to excellent diastereoselectivity ($78:22 \leq d.r. \leq 95:5$) and in excellent yield (97-100% of the mixture of diastereomers). Zinc(II) bromide likely served to coordinate the *gem*-difluoro group, preventing an interaction between fluorine and aluminum that stabilized the metal-fluorine interaction transition state and favored conversion to the *anti*-diol. Accordingly, diisobutylaluminum hydride-mediated reduction of β -hydroxy ketone 35 (100 mg scale) was carried

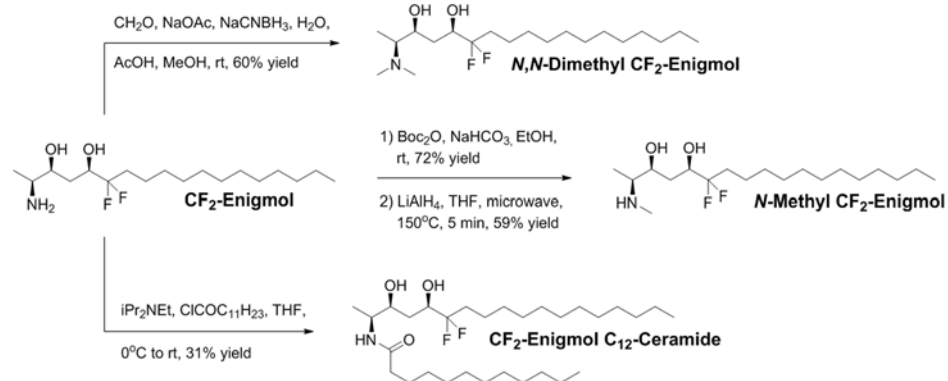
out in the presence of zinc(II) bromide at -78°C (**Figure 10**, Batch 6), which gratifyingly proceeded with moderate *syn*-diastereoselectivity (*d.r.* = 71:29), delivering the desired *syn*-1,3-diol **38** in 53% yield (**Scheme 17**). Therefore, zinc(II) bromide likely disrupted the metal-fluorine interaction transition state, causing the typical aluminum-chelated transition state to predominate. Similar metal-fluorine interactions could have been responsible for the poor diastereoselectivity observed for achiral and chiral borane-mediated aldol reactions, which may have involved competition between a Zimmerman-Traxler-type chair transition state and a metal-fluorine interaction transition state⁶⁷. Alternatively, the DiBAL-H-mediated *anti*-reduction could have resulted from an acyclic transition state, due to the poor Lewis basicity of the α,α -difluoro ketone oxygen. With this result, intermediate **35** was subjected to the same conditions for the preparation of ample quantities of *syn*-diol **38** on progressively larger scales (0.5-1.35 g), which resulted in relatively consistent isolated yields of the desired diastereomer after column chromatography (43-56% yield). Thus, synthesis of **38** via diisobutylaluminum hydride-mediated reduction of β -hydroxy ketone **35** in the presence of zinc(II) bromide during the 2nd scale up endeavor proceeded with a maximum of 56% yield, outperforming preparation of **38** via sodium borohydride-mediated reduction during the 1st scale up, which occurred in only 28% yield. Finally, *N,N*-dibenzylamino CF₂-Enigmol precursor **38** underwent palladium-catalyzed hydrogenolysis to yield CF₂-Enigmol in 70% yield and 75% yield on scales of 375 mg (x 4 batches) and 406 mg (x 3 batches), respectively. Ultimately, the synthesis of CF₂-Enigmol was improved from 0.2% yield during the 1st scale up preparation from chlorooxalate **29** and intermediate carboxylic acid **6** to a maximum of 4.5% yield during the 2nd scale up from terminal alkyne **47** and *L*-alanine.



Scheme 17: 2nd Scale Up Preparation of CF₂-Enigmol. Diastereoselective reduction of β -hydroxy ketone **35** mediated by DiBAL-H in the presence of ZnBr₂ substantially improved the scalability of CF₂-Enigmol.

1.2.f. *Synthesis and in vitro Cytotoxicity of CF₂-Enigmol Metabolites*

Although a maximum of 4.5% overall yield of CF₂-Enigmol certainly left room for further improvement, ample quantities of CF₂-Enigmol were available both for evaluation of anti-cancer activity *in vivo*, and for synthesis of CF₂-Enigmol metabolites for evaluation of cytotoxicity *in vitro*. Metabolism of Enigmol *in vivo* results in NMT-mediated generation of *N*-methyl and *N,N*-dimethyl Enigmol^{23,25}, both of which retain the cytotoxic signaling properties of Enigmol *in vitro*, as well as slow CS-mediated conversion to *N*-acyl Enigmols, which are substantially less active. As this attractive metabolic profile of Enigmol is crucial to effective inhibition of tumor growth, it was important to characterize the cytotoxic properties of *N*-methylated and *N*-acylated metabolites of CF₂-Enigmols *in vitro*, prior to comparison between Enigmol and CF₂-Enigmol anti-cancer activity *in vivo*. Accordingly, syntheses of *N*-methyl CF₂-Enigmol, *N,N*-dimethyl CF₂-Enigmol, and CF₂-Enigmol C₁₂-ceramide were initiated (**Scheme 18**). First, *N,N*-dimethyl CF₂-Enigmol was prepared in 60% yield via sodium cyanoborohydride-facilitated reductive amination between CF₂-Enigmol and formaldehyde in an acetate buffer. Next, synthesis of *N*-methyl CF₂-Enigmol was carried out over 2 steps starting with Boc protection of the CF₂-Enigmol amino group, which proceeded in 72% yield, followed by microwave-assisted reduction of the resulting *tert*-butyl carbamate with lithium aluminum hydride²⁰, which occurred in 59% yield after only 5 min at 150°C. Finally, a solution of CF₂-Enigmol was treated with dodecanoyl chloride and Hünig's base at 0°C, which delivered the desired CF₂-Enigmol C₁₂-ceramide metabolite in 31% yield.



Scheme 18: Synthesis of CF₂-Enigmol Metabolites. As mechanisms of CF₂-Enigmol metabolism were expected to match those of Enigmol metabolism, *N*-methyl CF₂-Enigmol, *N,N*-dimethyl CF₂-Enigmol, and CF₂-Enigmol C₁₂-Ceramide were synthesized from CF₂-Enigmol for evaluation of cytotoxicity against human prostate cancer cell viability *in vitro*.

Each of the CF₂-Enigmol metabolites was submitted to our collaborators in the laboratory of Dr. John Petros (Department of Urology, Emory University School of Medicine) for evaluation of cytotoxic activity against both LNCaP and PC3 human prostate cancer cells *in vitro*. In similar fashion to assays conducted for the fluorinated Enigmol analogs, cultured LNCaP and PC3 cells were treated with increasing concentrations of 1:1 complexes of drug and fatty acid-free BSA, which were freshly prepared in ethanol 1 hr prior to addition. Upon addition of the formulated drugs, cells were incubated for 24 hrs, after which the WST-1 reagent was added and luminescence was measured. Concentration response curves were generated via nonlinear regression using Graphpad Prism software, and IC₅₀ values (\pm S.E.M.) were calculated from curves fit based on a four parameter logistic equation (**Table 7**). While *N*-methyl CF₂-Enigmol and *N,N*-dimethyl CF₂-Enigmol each demonstrated concentration-dependent cytotoxicity against both LNCaP (IC₅₀ = 5 μ M and 6 μ M, respectively) and PC3 (IC₅₀ = 10 μ M and 10 μ M, respectively) human prostate cancer cells, CF₂-Enigmol C₁₂-ceramide was completely inactive up to 80 μ M in both cell lines. Thus, while methylated metabolites of CF₂-Enigmol retained the cell death signaling properties just as methylated metabolites of Enigmol, CF₂-Enigmol C₁₂-ceramide, like acylated metabolites of Enigmol, was substantially less active than the parent compound. Ultimately, verification of the similar signaling profiles of methylated and acylated metabolites of

Enigmol and CF₂-Enigmol suggested that anti-cancer efficacy of these drugs *in vivo* would not vary as a function of metabolite activity.

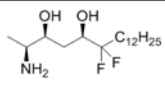
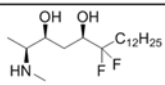
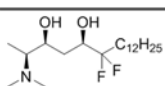
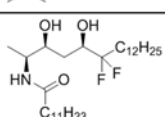
Compound	Structure	LNCaP IC ₅₀ (μM)	PC3 IC ₅₀ (μM)
CF ₂ -Enigmol		13.4 ± 1.07	11.7 ± 1.05
N-Methyl CF ₂ -Enigmol		≈ 5.2	10.2 ± 6.44
N,N-Dimethyl CF ₂ -Enigmol		5.9 ± 1.10	≈ 9.9
CF ₂ -Enigmol C ₁₂ -Ceramide		Inactive	Inactive

Table 7. Cytotoxicity of CF₂-Enigmol Metabolites against Human Prostate Cancer Cells *in vitro*. LNCaP or PC3 human prostate cancer cells were incubated with drug, and cell viability was quantified by measuring mitochondrial activity with the WST-1 reagent. Experiments were performed in triplicate, and IC₅₀ values were calculated using GraphPad Prism software from concentration-response curves that were generated via nonlinear regression using a four parameter logistic equation.

1.2.g. Anti-Tumor Activity of Fluorinated Enigmol Analogs *in vivo*

Based on the established tissue accumulation levels, both CF₃-Enigmol and CF₂-Enigmol were expected to achieve higher tumor concentrations than Enigmol, which was anticipated to enhance anti-tumor efficacy *in vivo*. To test this hypothesis, two separate *in vivo* experiments involving mouse xenograft models of prostate cancer were designed to assess anti-tumor activity of Enigmol versus CF₃-Enigmol or CF₂-Enigmol. Xenograft studies, the first of which was conducted to compare Enigmol and CF₃-Enigmol, were carried out by our collaborators in the laboratory of Dr. John Petros (Department of Urology, Emory University School of Medicine) and at the Emory Institute for Drug Development. Nude mice were injected subcutaneously between scapulae with cultured PC3 human prostate cancer cells, and tumors were established for 16 days (until palpable). Once tumors became palpable, mice were divided into five groups in such a way that tumor volumes were evenly distributed amongst the groups. Subjects in each group were then treated once daily with either vehicle (95:5 olive oil/EtOH, n = 11), 3 mg/kg Enigmol (n = 11), 10 mg/kg Enigmol (n = 11), 3 mg/kg CF₃-Enigmol

(n = 10), or 10 mg/kg CF₃-Enigmol (n = 11) via oral gavage (200 µL). Drug formulations were freshly prepared each day prior to administration. During the treatment course, tumor volume was measured every 2-3 days with digital calipers (Volume = $\frac{1}{2}$ *Length*Width²) to characterize drug-induced growth inhibition until excessive tumor burden was reached on day 33, ethically requiring animal subject sacrifice (**Figure 11a**). While 3 mg/kg dosing regimens were ineffective for both Enigmol (n = 11) and CF₃-Enigmol (n = 10), treatment with 10 mg/kg Enigmol (n = 11) resulted in significant tumor growth inhibition (p = 0.02) as compared to control. Although 10 mg/kg CF₃-Enigmol (n = 11) appeared to have some growth inhibitory effect, anti-tumor efficacy did not reach statistical significance (p = 0.17). Thus, despite the substantially elevated tissue concentrations achieved by CF₃-Enigmol versus Enigmol, this pharmacokinetic enhancement did not translate to improved anti-tumor efficacy. Furthermore, mouse body weight was measured periodically as an indication of systemic toxicity (**Figure 11b**). While no substantial weight loss was observed amongst control, 3 mg/kg Enigmol, 10 mg/kg Enigmol, or 3 mg/kg CF₃-Enigmol treatment groups, the 10 mg/kg CF₃-Enigmol treatment group lost an alarming amount of body weight ($11.6 \pm 1.32\%$) over the treatment course of 17 days (p = 0.0037). This phenomenon was not previously observed during *in vivo* studies with Enigmol or with related analogs, and thus, this result marks CF₃-Enigmol as a systemically toxic liability. A working hypothesis is that, due to the larger volume of CF₃ versus CH₃, the ω-trifluoromethyl group of CF₃-Enigmol could disrupt cell membrane lipid stacking, which could lead to membrane leakage and ultimately to systemic toxicity. If true, this would be consistent with the relatively low t_{1/2} and high Cl of CF₃-Enigmol, and accordingly, future experiments will be implemented to address this question. To evaluate the relationship between *in vivo* efficacy and drug concentrations achieved at the site of action, tumor accumulation of Enigmol and CF₃-Enigmol was measured. Tumors were harvested on the final day of treatment from xenograft-bearing mice (n = 4 per treatment group), tumors were homogenized, and drug concentrations were quantified using LC-MS/MS (**Figure 11c**). For both Enigmol and CF₃-Enigmol, tumor accumulation was dose-dependent, where 10 mg/kg Enigmol (5.2 µM) achieved 5-fold higher concentrations than 3 mg/kg Enigmol (1.1 µM) and 10 mg/kg CF₃-Enigmol (25 µM)

reached 8-fold higher levels than 3 mg/kg CF₃-Enigmol (3.2 μM). While 10 mg/kg Enigmol did not achieve IC₉₀ concentrations (14 μM) in PC3 tumors after 17 days of once daily treatment, 10 mg/kg CF₃-Enigmol did (IC₉₀ = 24 μM); a related boost in anti-tumor activity, however, was unexpectedly not observed.

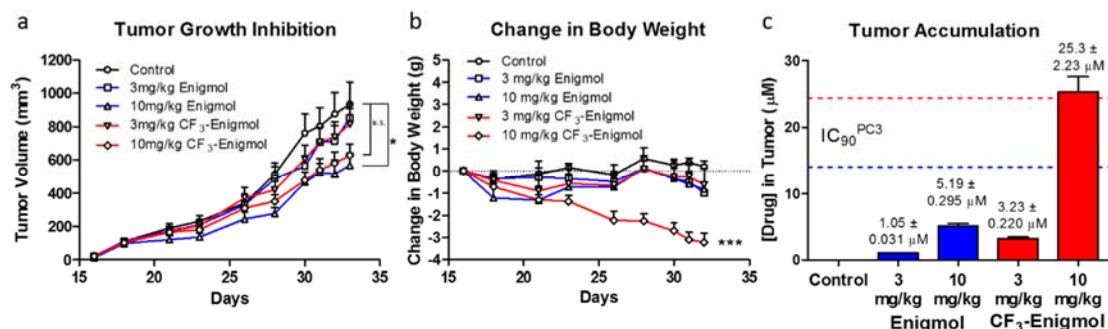


Figure 11: Enigmol vs. CF₃-Enigmol in Mouse Xenograft Model of Prostate Cancer. Nude mice (n = 10-11 per group) with palpable tumors derived from PC-3 human prostate cancer cells were treated once daily via oral gavage with either vehicle (95:5 olive oil/EtOH), Enigmol (3 or 10 mg/kg), or CF₃-Enigmol (3 or 10 mg/kg). (a) Tumor volume and (b) change in body weight were measured periodically throughout the study, until excessive tumor burden was reached, at which point, mice were sacrificed, tumors were harvested, and (c) tumor accumulation was measured using LC-MS/MS. Graphs were generated using GraphPad Prism software, and data are represented as the mean ± S.E.M. Statistical significance (*p < 0.05, **p < 0.01, or ***p < 0.001) of tumor growth inhibition between groups was assessed via linear mixed model for repeated measurement with autoregressive covariance structure using Statistical Analysis System (SAS) software. Significance of change in body mass was determined using one-way ANOVA followed by Sidak's multiple comparison test in GraphPad Prism.

Thus, focus was shifted to CF₂-Enigmol, which was similarly compared head-to-head with Enigmol in a subsequent mouse xenograft study. As CF₂-Enigmol reached higher tissue levels than Enigmol, it was hypothesized that CF₂-Enigmol would demonstrate enhanced inhibition of the rate of tumor growth *in vivo* by virtue of increased drug concentration in tumor. Accordingly, PC3 cells were subcutaneously implanted into nude mice, and tumors were established for 22 days (until palpable) before beginning once daily dosing via oral gavage with either vehicle (95:5 PEG400/Tween80, n = 9 or 10, 1 mouse died on day 32), 10 mg/kg Enigmol (n = 9 or 10, 1 mouse died on day 36), 10 mg/kg CF₂-Enigmol (n = 10) or 30 mg/kg CF₂-Enigmol (n = 10). During the treatment course, tumor volume and body weight were measured periodically until excessive tumor burden was reached on day 38,

ethically requiring animal subject sacrifice (**Figure 12a**). While 30 mg/kg CF₂-Enigmol did not demonstrate enhanced efficacy over 10 mg/kg CF₂-Enigmol, 10 mg/kg CF₂-Enigmol significantly enhanced tumor growth rate inhibition relative to both control ($p = 0.0003$) and 10 mg/kg Enigmol ($p = 0.04$). Importantly, neither 10 mg/kg nor 30 mg/kg CF₂-Enigmol caused weight loss (**Figure 12b**), suggesting that systemic toxicity associated with CF₃-Enigmol resulted from fluorine atoms specifically at the end of the lipid tail. To determine whether the improved *in vivo* performance of CF₂-Enigmol versus Enigmol was accompanied by increased tumor uptake, tumors were harvested 24 hrs after the final oral gavage from xenograft-bearing mice ($n = 4$ per treatment group), tumors were homogenized, and drug concentrations were quantified using LC-MS/MS (**Figure 12c**). Consistent with the observed tissue distribution properties, 10 mg/kg CF₂-Enigmol (24 μ M) achieved strikingly higher concentrations (15-fold) in tumor than 10 mg/kg Enigmol (1.6 μ M). Furthermore, while 10 mg/kg Enigmol did not achieve IC₉₀ concentrations (14 μ M) in tumor after 16 days of once daily treatment, both 10 mg/kg and 30 mg/kg CF₂-Enigmol did (IC₉₀ = 15 μ M). Despite the fact that 30 mg/kg CF₂-Enigmol reached extraordinary tumor levels (62 μ M), both 10 mg/kg and 30 mg/kg CF₂-Enigmol demonstrated indistinguishable *in vivo* anti-tumor efficacy, suggesting that a saturating concentration in tumor cells is achieved after two weeks of a once daily oral dosing at ≤ 10 mg/kg.

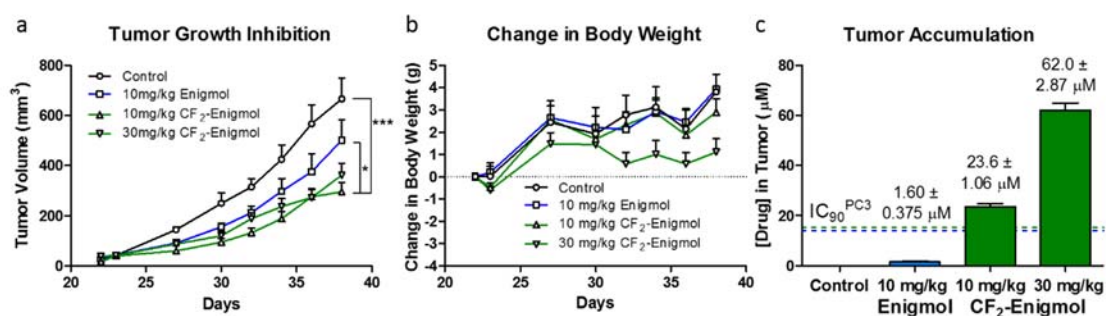


Figure 12. Enigmol vs. CF₂-Enigmol in Mouse Xenograft Model of Prostate Cancer. Nude mice ($n = 10-11$ per group) with palpable tumors derived from PC-3 human prostate cancer cells were treated once daily via oral gavage with either vehicle (95:5 PEG400/Tween80), Enigmol (10 mg/kg), or CF₂-Enigmol (10 or 30 mg/kg). (a) Tumor volume and (b) change in body weight were measured periodically throughout the study, until excessive tumor burden was reached, at which point, mice were sacrificed, tumors were harvested, and (c) tumor accumulation was measured using LC-MS/MS.

Graphs were generated using GraphPad Prism software, and data are represented as the mean \pm S.E.M. Statistical significance (* $p < 0.05$, ** $p < 0.01$, or *** $p < 0.001$) of tumor growth inhibition between groups was assessed via linear mixed model for repeated measurement with autoregressive covariance structure using Statistical Analysis System (SAS) software.

1.3. Conclusions

Ultimately, the hypothesis that flat *in vitro* and *in vivo* structure activity relationships could be overcome by increasing compound lipophilicity was examined. Enhancement in lipophilicity was accomplished by conceptually replacing aliphatic C-H bonds with C-F bonds, leading to the design of CF₃-Enigmol and CF₂-Enigmol. Each of these novel, fluorinated Enigmol analogs were synthesized via aldol methodology, and were subsequently evaluated for anti-cancer activity. As anticipated, all three compounds demonstrated very similar potency and efficacy against LNCaP and PC3 human prostate cancer cell viability *in vitro*. Subsequent plasma pharmacokinetic experiments not only confirmed the oral bioavailability of CF₃-Enigmol and CF₂-Enigmol, but also indicated that plasma exposure after oral dose trended with compound lipophilicity. In contrast, CF₂-Enigmol unexpectedly absorbed into tissue at strikingly higher concentrations than CF₃-Enigmol, suggesting that physicochemical characteristics other than lipophilicity control tissue distribution after oral administration. While Enigmol and CF₃-Enigmol did not achieve therapeutically effective concentrations (IC₉₀ value against PC3 cell viability) in any tissue compartment, CF₂-Enigmol accumulated into lung, brain, and kidney at levels \geq IC₉₀. Despite improved pharmacokinetic properties and achievement of IC₉₀ levels in tumor, CF₃-Enigmol did not demonstrate enhanced tumor growth inhibition over Enigmol *in vivo*, and furthermore, once daily oral gavage of 10 mg/kg CF₃-Enigmol proved systemically toxic. Alternatively, CF₂-Enigmol demonstrated statistically enhanced tumor growth suppression as compared to Enigmol, without signs of systemic toxicity, marking the first Enigmol analog to date with significantly improved *in vivo* efficacy. While Enigmol did not reach IC₉₀ levels in tumor, CF₂-Enigmol did achieve IC₉₀ tumor concentrations, which is consistent with elevated *in vivo* activity. CF₂-Enigmol was subsequently licensed to Que Oncology for clinical consideration.

Since Enigmol was equally efficacious to androgen-independent prostate cancer standard of care docetaxel²⁰, CF₂-Enigmol could offer therapeutic advantage over taxane-based chemotherapeutics for hormone-refractory prostate cancer. Moreover, CF₂-Enigmol is orally bioavailable, whereas docetaxel is typically administered via injection, and accordingly, prescription of CF₂-Enigmol compared to docetaxel could improve patient compliance. Additionally, the apparent absence of CF₂-Enigmol-induced systemic toxicity could further translate to a much larger therapeutic window than that exhibited by more aggressive docetaxel. Furthermore, due to enormous CF₂-Enigmol concentrations in lung, brain, and kidney, anti-tumor efficacy could prove to be even more profound for the treatment of solid tumors residing in these tissues. Finally, the remarkable tissue distribution properties of CF₂-Enigmol suggest its utility in lipid conjugation prodrug strategies for improving systemic exposure and tissue accumulation of poorly bioavailable cargo.

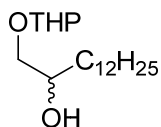
1.4. Experimental Methods

1.4.a. *Synthetic Procedures*

For water and/or air sensitive reactions, all solvents were dried and degassed by the SG Waters Glass Contour solvent purification system unless otherwise specified. Automated flash column chromatography was performed using a Teledyne ISCO CombiFlash Companion system with silica gel-packed columns (SiliCycle Inc.). Analytical thin-layer chromatography was carried out on aluminum-supported silica gel plates (Sigma, thickness = 200 μm) with fluorescent indicator (F-254). Visualization of compounds on TLC plates was accomplished with UV light (254 nm) or with phosphomolybdic acid, ninhydrin, potassium permanganate, or sulfuric acid stains. Melting points were obtained using capillary tubes and a 200 W MeTemp melting point apparatus. Optical rotation was measured with a sodium lamp using a Perkin Elmer 341 Polarimeter. Infrared absorption spectra were obtained on a Thermo Scientific Nicolet 370 FT-IR spectrophotometer via the Smart Orbit Diamond Attenuated Total Reflectance accessory, and peaks are reported in cm^{-1} . NMR spectra (¹H, ¹⁹F, and

^{13}C) were obtained using a Varian INOVA 400 MHz spectrometer in deuterated chloroform (CDCl_3) with the residual solvent peak (CDCl_3 : $^1\text{H} = 7.27$ ppm, $^{13}\text{C} = 77.23$ ppm) as an internal reference and trifluoroacetic acid (TFA) as external reference (TFA: $^{19}\text{F} = -76.55$ ppm) unless otherwise specified. NMR data is reported to include chemical shifts (δ) reported in ppm, multiplicities indicated as s (singlet), d (doublet), t (triplet), q (quartet), m (multiplet), br (broadened), or app (apparent), coupling constants (J) reported in Hz, and integration normalized to 1 atom (H, C, or F). High resolution mass spectrometry was performed by the Emory University Mass Spectrometry Center, directed by Dr. Fred Strobel. LC-MS was performed on an Agilent 1200 HPLC equipped with a 6120 Quadrupole mass spectrometer (ESI-API) using mixtures of HPLC grade MeOH/ H_2O (spiked with 0.1% formic acid) and an analytical, reverse-phase, Agilent C18 XDB eclipse column (150 x 4.6 mm or 50 x 4.6 mm). Chiral HPLC was performed on a Varian ProStar HPLC equipped with a 335 series diode array detector using mixtures of HPLC grade hexanes/*i*PrOH and an analytical, normal-phase, Daicel ChiralPak AD-H column (150 x 4.6 mm). Elemental analyses were performed by Atlantic Microlab, Inc (Norcross, GA). Compounds listed below for which full characterization is not presented were previously reported in the literature as referenced in the main text. Enigmol was synthesized by Dr. Ethel Garnier-Amblard at the Emory Institute for Drug Development, according to previously reported methods²⁰. CF_3 -Enigmol²⁷ and compound **16**²⁶ were synthesized by Dr. Mark Baillie in the Liotta Group.

1-((tetrahydro-2H-pyran-2-yl)oxy)tetradecan-2-ol (**20**): 1,2-tetradecanediol (**19**, 5.00 g, 21.7 mmol, 1.00 eq)



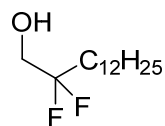
and ruthenium(III) acetylacetonate (0.173 g, 0.434 mmol, 0.02 eq) were added to a flame-dried flask with a stir bar. The solid mixture was diluted with chloroform (75.0 mL) and stirred under Ar. 3,4-Dihydro-2H-pyran (2.18 mL, 23.9 mmol, 1.10 eq) was added slowly, and the reaction mixture was warmed to 65 °C and allowed to reflux under Ar overnight. The next morning, the crude mixture was diluted with diethyl ether and evaporated under reduced pressure to yield 7.50 g crude product. The crude material was purified via column chromatography eluting with 1:8 EtOAc/hexanes, to yield a pale yellow oil as a mixture of four stereoisomers (3.62 g, 11.5 mmol, 53%

yield). $R_f = 0.22$ (1:5 EtOAc/hexanes), $R_f = 0.17$ (1:10 EtOAc/hexanes). IR (ν_{\max} , cm^{-1}) 3446, 2922, 2852, 1135, 1074, 1024. HRMS (APCI) $m/z = 315.28973$ (Theo. for $\text{C}_{19}\text{H}_{38}\text{O}_3 + \text{H}$: 315.28937). Anal. Calcd. for $\text{C}_{19}\text{H}_{38}\text{O}_3$: C, 72.56; H, 12.18. Found: C, 72.82; H, 12.45.

1-((tetrahydro-2H-pyran-2-yl)oxy)tetradecan-2-one (18): A solution of 1-(tetrahydro-2H-pyran-2-yl)oxytetradecan-2-ol (**20**, 0.248 g, 0.789 mmol, 1.00 eq) in DCM (10.0 mL) was added to a flame-dried flask with a stir bar. Pyridinium chlorochromate (0.129 g, 0.946 mmol, 1.20 eq) and celite (0.108 g) were subsequently added to the solution, which was further diluted with DCM (7.00 mL). The resulting mixture was stirred under Ar at room temperature overnight. The next day, TLC showed little progression from the night before, and accordingly, pyridinium chlorochromate (0.194 g, 1.42 mmol, 1.50 eq), celite (0.194 g), and DCM (6.00 mL) were added. Once starting material ceased to convert, as indicated by TLC, the reaction mixture was poured over a plug of silica gel and flushed with 1:5 EtOAc/hexanes. Purification was carried out using column chromatography eluting with 1:11 EtOAc/hexanes to yield a clear, pale-yellow oil (0.110 g, 0.355 mmol, 45% yield). $R_f = 0.39$ (1:5 EtOAc/hexanes), $R_f = 0.23$ (1:10 EtOAc/hexanes). IR (ν_{\max} , cm^{-1}) 2922, 2852, 1720, 1128, 1075, 1036. ^1H NMR (400 MHz, CDCl_3) δ 4.64 (t, $J = 3.2$ Hz, 1H), 4.26 (d, $J = 17.2$ Hz, 1H), 4.12 (d, $J = 17.2$ Hz, 1H), 3.80-3.85 (m, 1H), 3.49-3.54 (m, 1H), 2.45 (dt, $J = 1.6$ Hz, 7.2 Hz, 2H), 1.60-1.88 (m, 4H), 1.54-1.58 (m, 4H), 1.25-1.27 (m, 18H), 0.876 (t, $J = 6.8$ Hz, 3H). ^{13}C (100 MHz, CDCl_3) δ 208.9, 98.8, 72.1, 62.4, 39.2, 32.1, 30.4, 29.8, 29.6, 29.6, 29.5, 29.4, 25.5, 23.5, 22.8, 19.3, 14.3. HRMS (APCI) $m/z = 313.27393$ (Theo. for $\text{C}_{19}\text{H}_{36}\text{O}_3 + \text{H}$: 313.27372). Anal. Calcd. for $\text{C}_{19}\text{H}_{36}\text{O}_3$: C, 73.03; H, 11.61. Found: C, 72.84; H, 11.76.

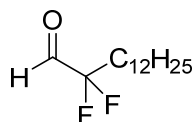
2-((2,2-difluorotetradecyl)oxy)tetrahydro-2H-pyran (21): 1-(tetrahydro-2H-pyran-2-yl)oxytetradecan-2-one (**18**, 0.100 g, 0.320 mmol, 1.00 eq) was diluted with DCM (0.700 mL) and added to a 2 mL Eppendorf tube under a funnel of Ar. The reaction vessel was cooled to 0°C , and diethylaminosulfur trifluoride (0.211 mL, 1.60 mmol, 5.00 eq) and methanol (0.004 mL, 0.096 mmol, 0.030 eq) were added dropwise in succession. The reaction vessel was sealed, and the resulting reaction mixture was allowed to warm to room temperature and to stir overnight. Reaction

progress was monitored by TLC. Upon consumption of starting material, the reaction was quenched dropwise with cold saturated aqueous sodium bicarbonate. The resulting aqueous layer was extracted with DCM, and combined organic layers were dried over MgSO₄, filtered, and evaporated under reduced pressure. Column chromatography was employed for purification, eluting with 1:1 DCM/hexanes to yield a yellow oil (0.083 g, 0.250 mmol, 78% yield). R_f = 0.59 (1:1 DCM/hexanes), R_f = 0.41 (1:2 DCM/hexanes). IR (ν_{max}, cm⁻¹) 2923, 2853, 1130, 1078, 1037. ¹H NMR (400 MHz, CDCl₃) δ 4.69 (t, *J* = 3.6 Hz, 1H), 3.81-3.90 (app dd, *J* = 11.8 Hz, 22.6 Hz, 1H), 3.80-3.86 (m, 1H), 3.55-3.64 (app dd, *J* = 11.4 Hz, 23.4 Hz, 1H), 3.52-3.57 (m, 1H), 1.80-2.00 (m, 3H), 1.46-1.79 (m, 7H), 1.24-1.31 (m, 18H), 0.883 (t, *J* = 6.8 Hz, 3H). ¹³C (100 MHz, CDCl₃) δ 123.0 (t, *J* = 960 Hz), 98.6, 67.4 (t, *J* = 120 Hz), 61.8, 33.7 (t, *J* = 93.6 Hz), 31.8, 30.1, 29.5, 29.4, 29.3, 25.2, 22.6, 21.7, 18.8, 14.0. ¹⁹F (376 MHz, CDCl₃) δ -105.3 (m, 1F), -106.2 (m, 1F). HRMS (APCI) *m/z* = 335.27562 (Theo. for C₁₉H₃₆O₂F₂ + H: 335.27561).

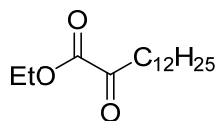


2,2-difluorotetradecan-1-ol (**22**): 2-(2,2-difluorotetradecyloxy)tetrahydro-2H-pyran (**21**,

1.85 g, 5.53 mmol, 1.00 eq) was diluted with methanol (30.0 mL), *p*-toluenesulfonic acid monohydrate (0.105 g, 0.553 mmol, 0.100 eq) was added, and the resulting reaction mixture was allowed to stir at room temperature. After 90 min, TLC indicated complete consumption of starting material. Solvent was evaporated under reduced pressure, and the crude material was purified via column chromatography eluting with 1:6 EtOAc/hexanes to yield a white solid (1.34 g, 5.36 mmol, 97% yield). R_f = 0.22 (1:8 EtOAc/hexanes), R_f = 0.28 (1:4 DCM/hexanes). Mp 50-52°C. IR (ν_{max}, cm⁻¹) 3365, 2917, 2847, 1088, 1038, 1017, 897, 806, 698. ¹H NMR (400 MHz, CDCl₃) δ 3.75 (t, *J* = 12.8 Hz, 2H), 1.84-1.97 (m, 2H), 1.83 (br s, 1H), 1.44-1.54 (p, *J* = 7.8 Hz, 2H), 1.23-1.39 (m, 18H), 0.888 (t, *J* = 6.8 Hz, 3H). ¹³C NMR (100 MHz, CDCl₃) δ 123.6 (t, *J* = 961 Hz), 64.3 (t, *J* = 126 Hz), 33.5 (t, *J* = 95.2 Hz), 32.1, 29.9, 29.7, 29.6, 22.9, 22.0, 14.3. ¹⁹F NMR (376 MHz, CDCl₃) δ -109.1 (m, 2F). HRMS (ESI) *m/z* = 249.20340 (Theo. for C₁₉H₃₆O₂F₂ - H: 249.20355). Anal. Calcd. for C₁₄H₂₈F₂O: C, 67.16; H, 11.27; F, 15.18. Found: C, 66.89; H, 11.23; F, 14.95.



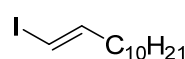
2,2-difluorotetradecanal (17): Oxalyl chloride (0.471 mL, 5.38 mmol, 3.00 eq) was added to a flame-dried flask with a stir bar, diluted with DCM (8.00 mL), cooled to -78°C , and stirred under Ar. DMSO (0.770 mL, 10.8 mmol, 6.00 eq) was added dropwise, and the resulting reaction mixture was allowed to stir at -78°C under Ar for 20 min. A solution of 2,2-difluorotetradecan-1-ol (**22**, 0.449 g, 1.79 mmol, 1.00 eq) in DCM (6.00 mL) was added dropwise, and the resulting mixture was allowed to stir at -78°C under Ar for 90 min. Finally, triethylamine (3.00 mL, 21.5 mmol, 12.0 eq) was added dropwise, and the resulting mixture was allowed to slowly warm to 0°C and stir under Ar. Once TLC indicated complete consumption of starting material, the reaction mixture was filtered over celite and washed with DCM. The resulting solution was evaporated under reduced pressure. Purification was accomplished via distillation, during which the desired product was collected at 190°C under vacuum (0.75 mm Hg) as a 1:3 ratio of desired aldehyde (0.023 g, 0.092 mmol, 5% yield) to the corresponding *gem*-diol hydrate (0.073 g, 0.275 mmol, 15% yield). $R_f = 0.14$ (1:4 EtOAc/hexanes), 0.28 (1:1 Et₂O/hexanes). Mp $52\text{--}54^{\circ}\text{C}$, $65\text{--}67^{\circ}\text{C}$. IR (ν_{max} , cm^{-1}) 2954, 2917, 2850, 1767, 1244, 1227, 1103, 1062, 1014, 911, 879, 682. ¹H NMR (400 MHz, CDCl₃) δ 9.51 (s, 0.25 H), 5.01 (app t, $J = 6.6$ Hz, 0.75 H), 1.88–2.03 (m, 2H), 1.45–1.57 (m, 2H), 1.20–1.36 (m, 18H), 0.888 (t, $J = 6.8$ Hz, 3H).

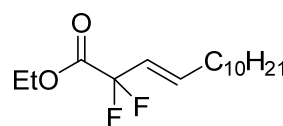


Ethyl 2-oxotetradecanoate (28): Weinreb Ketone Synthesis: *N,O*-Dimethyl hydroxylamine (5.00 g, 82.0 mmol, 1.00 eq) was added to a flame-dried flask with a stir bar. The reagent was diluted with DCM (273 mL), cooled to 0°C , and stirred under Ar. Triethylamine (22.8 mL, 164 mmol, 2.00 eq) and ethyl chlorooxoacetate (**29**, 11.0 mL, 98.0 mmol, 1.20 eq) were subsequently added, and the resulting mixture was allowed to slowly warm to room temperature while stirring under Ar. Once starting material disappeared on TLC, the reaction was quenched with MeOH, and solvent was evaporated under reduced pressure. The crude material was diluted with a small volume of THF, triethylammonium hydrochloride precipitated, and the solid was filtered and washed with THF. The mother liquor was then evaporated under reduced pressure, and the resulting crude material was purified via column chromatography to yield the desired Weinreb

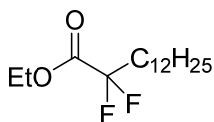
amide intermediate. ^1H NMR (400 MHz, CDCl_3) δ 4.28 (q, $J = 7.2$ Hz, 2H), 3.70 (s, 3H), 3.17 (s, 3H), 1.31 (t, $J = 7.0$ Hz, 3H). A small portion of the Weinreb amide (0.100 g, 0.621 mmol, 1.00 eq) was then added to a flame-dried flask with a stir bar. The intermediate was diluted with THF (3.6 mL), cooled to -78°C , and stirred under Ar. A freshly prepared THF solution of dodecylmagnesium bromide (0.310 mL, 0.621 mmol, 1.00 eq) was added dropwise at -78°C , and the resulting mixture was allowed to stir under Ar at -78°C . Once starting material disappeared on TLC, the reaction was quenched slowly with saturated aqueous ammonium chloride, and the resulting aqueous layer was extracted with DCM. Combined organic layers were washed with brine, dried over MgSO_4 , filtered, and evaporated under reduced pressure. The resulting crude material was purified via column chromatography to deliver the desired α -keto ester (0.030 g, 0.111 mmol, 18% yield).

Imidazole-Mediated Ketone Synthesis. Imidazole (18.3 g, 268 mmol, 2.00 eq) was added to a flame-dried flask with a stir bar, diluted with THF (244 mL), cooled to 0°C , and stirred under Ar. A solution of ethyl chlorooxoacetate (**29**, 15.0 mL, 134 mmol, 1.00 eq) in THF (61.0 mL) was added dropwise at 0°C , and the reaction mixture was stirred under Ar at 0°C for 2 hr. The mixture was then filtered to remove imidazole hydrochloride, and the resulting solution was cooled to -78°C and stirred under Ar. A freshly prepared THF solution of dodecylmagnesium bromide (74.0 mL, 147 mmol, 1.10 eq) was added dropwise at -78°C , and the resulting mixture was stirred under Ar at -78°C . Once starting material disappeared on TLC, the reaction was quenched slowly with saturated aqueous ammonium chloride. The organic layer was washed with brine, dried over MgSO_4 , filtered, and evaporated under reduced pressure. Purification was carried out via column chromatography to yield a slightly yellow oil (6.25 g, 22.7 mmol, 17% yield over 2 steps). $R_f = 0.55$ (1:8 EtOAc/Hex), $R_f = 0.42$ (1:20 EtOAc/Hex). IR (ν_{max} , cm^{-1}) 2923, 2853, 1728, 1464, 1247, 1177, 1128, 1054, 722. ^1H NMR (400 MHz, CDCl_3) δ 4.32 (q, $J = 7.2$ Hz, 2H), 2.83 (t, $J = 7.6$ Hz, 2H), 1.63 (p, $J = 7.2$ Hz, 2H), 1.37 (t, $J = 7.2$ Hz, 3H), 1.26 (m, 18H), 0.89 (t, $J = 6.8$ Hz, 3H). ^{13}C NMR (100 MHz, CDCl_3) δ 194.7, 161.3, 62.3, 39.3, 32.0, 29.7, 29.7, 29.7, 29.5, 29.4, 29.4, 29.0, 23.0, 22.8, 14.1, 14.0. HRMS (ESI) $m/z = 271.22684$ (Theo. for $\text{C}_{16}\text{H}_{30}\text{O}_3 + \text{H}$: 271.22677).


(E)-1-iodododec-1-ene (**46**): Schwartz reagent (ZrCp₂HCl, 6.92 g, 26.8 mmol, 1.60 eq) was added to a flame-dried flask with a stir bar. The solid was diluted with THF (78.0 mL), cooled to 0°C, and stirred under Ar. Dodec-1-yne (**47**, 3.59 mL, 16.8 mmol, 1.00 eq) was added dropwise at 0°C, and the resulting mixture was allowed to warm to room temperature and to stir for 3.5 hrs. The resulting very dark reaction mixture was cooled to -78°C, and a solution of iodine (5.11 g, 20.1 mmol, 1.20 eq) in THF (34.0 mL) was added via syringe pump over 50 min. The mixture was stirred for another 2 hrs at -78°C under Ar. At this point, the reaction mixture was warmed to 0°C and poured over 0.1 N aqueous HCl (78 mL). The aqueous layer was extracted with diethyl ether (3 x 50 mL). The combined organic layers were washed with saturated aqueous NaHCO₃ (50 mL), saturated aqueous Na₂S₂O₃ (50 mL), and brine (50 mL), dried over MgSO₄, filtered, and evaporated under reduced pressure. Purification was carried out via column chromatography eluting with hexanes to yield a clear oil (4.59 g, 15.6 mmol, 93% yield). R_f = 0.90 (Hex). IR (ν_{max}, cm⁻¹) 2922, 2852, 1461, 1376, 1197, 943, 721, 660. ¹H NMR (400 MHz, CDCl₃) δ 6.52 (dt, *J* = 7.6 Hz, *J* = 14.4 Hz, 1H), 5.97 (dt, *J* = 1.2 Hz, *J* = 14.4 Hz, 1H), 2.05 (dq, *J* = 1.2 Hz, *J* = 7.6 Hz, 2H), 1.39 (p, *J* = 7.2 Hz, 2H), 1.26 (m, 14H), 0.89 (t, *J* = 6.8 Hz, 3H). ¹³C NMR (100 MHz, CDCl₃) δ 146.8, 74.5, 36.3, 32.1, 29.8, 29.7, 29.6, 29.5, 29.1, 28.6, 22.9, 14.3. HRMS (ESI) *m/z* = 295.09178 (Theo. for C₁₂H₂₃I + H: 295.09173).


(E)-ethyl 2,2-difluorotetradec-3-enoate (**48**): Activated copper powder (17.0 g, 268 mmol, 3.10 eq) was added to a 1 L 3-neck flame-dried flask with a stir bar. DMSO (Dri-Solv, 292 mL) was added, and the resulting solution was stirred vigorously under Ar at room temperature. A solution of (*E*)-1-iodododec-1-ene (**46**, 25.3 g, 86.0 mmol, 1.00 eq) in DMSO (Dri-Solv, 138 mL) was added via addition funnel, and then ethyl 2-bromo-2,2-difluoroacetate (11.0 mL, 86.0 mmol, 1.00 eq) was added via syringe. The reaction flask was equipped with a reflux condenser, warmed to 60°C, and stirred overnight under Ar. In the morning, the mixture was poured over a cold 1:1 solution of saturated aqueous ammonium chloride to water. The aqueous layer was extracted with diethyl ether 4 times. The combined organic layers were washed twice with saturated aqueous ammonium chloride and twice with brine, dried over MgSO₄, filtered, and evaporated under

reduced pressure. The resulting crude oil was purified via column chromatography eluting with 1:40 EtOAc to hexanes to yield a clear oil (17.3 g, 59.6 mmol, 69% yield). $R_f = 0.40$ (1:40 EtOAc/Hex), $R_f = 0.45$ (1:20 EtOAc/Hex). IR (ν_{\max} , cm^{-1}) 2925, 2855, 1767, 1674, 1465, 1372, 1292, 1227, 1079, 969, 854, 780, 721. $^1\text{H NMR}$ (400 MHz, CDCl_3) δ 6.27 (m, 1H), 5.67 (m, 1H), 4.33 (q, $J = 7.2$ Hz, 2H), 2.14 (m, 2H), 1.42 (p, $J = 7.2$ Hz, 2H), 1.36 (t, $J = 7.2$ Hz, 3H), 1.27 (m, 14H), 0.89 (t, $J = 6.8$ Hz, 3H). $^{13}\text{C NMR}$ (100 MHz, CDCl_3) δ 164.4 (t, $J = 34.6$ Hz), 140.2 (t, $J = 8.9$ Hz), 121.1 (t, $J = 25.0$ Hz), 112.6 (t, $J = 246$ Hz), 63.0, 32.1 (2C), 29.8, 29.7, 29.6, 29.5, 29.2, 28.3, 22.9, 14.3, 14.1. $^{19}\text{F NMR}$ (376 MHz, CDCl_3) δ -103.2 (dd, $J = 3.0$ Hz, $J = 5.6$ Hz, 1F), -103.2 (dd, $J = 3.0$ Hz, $J = 5.6$ Hz, 1F). HRMS (ESI) $m/z = 291.21313$ (Theo. for $\text{C}_{16}\text{H}_{28}\text{O}_2\text{F}_2 + \text{H}$: 291.21301). Anal. Calcd. for $\text{C}_{16}\text{H}_{28}\text{O}_2\text{F}_2$: C, 66.18; H, 9.72; F, 13.08. Found: C, 65.98; H, 9.50; F, 12.84.

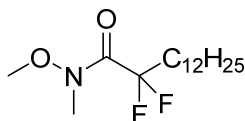


Ethyl 2,2-difluorotetradecanoate (27): Nucleophilic Difluorination. Ethyl 2-oxotetradecanoate (**28**, 0.200 g, 0.740 mmol, 1.00 eq) was added to an Eppendorf

tube with a stir bar and diluted with DCM (1.40 mL). The solution was cooled to 0°C , and diethylaminosulfur trifluoride (0.107 mL, 0.814 mmol, 1.10 eq) was added dropwise. The resulting mixture was allowed to warm to room temperature, and progress was monitored by TLC. After 5 hrs, starting material disappeared on TLC. The reaction mixture was transferred to a separatory funnel, diluted with DCM, and quenched very carefully with water. The solution was adjusted to neutral pH with dropwise addition of saturated aqueous sodium bicarbonate. The aqueous layer was extracted with DCM, and the combined organic layers were dried over MgSO_4 , filtered, and evaporated under reduced pressure. Purified via column chromatography to yield a clear oil (0.180 g, 0.616 mmol, 83% yield).

Hydrogenation: A solution of (*E*)-ethyl 2,2-difluorotetradec-3-enoate (**48**, 3.06 g, 10.5 mmol, 1.00 eq) in EtOAc (132 mL) was added to a 1 L flask with a stir bar. The solution was further diluted with EtOH (132 mL), and the resulting solution was stirred vigorously under Ar at room temperature. 10% palladium on carbon (1.12 g, 1.05 mmol, 0.100 eq) was added, and the resulting mixture was stirred vigorously under Ar at room temperature. The flask was evacuated for 5 min via low vacuum, and then filled with Ar. These 2 steps were repeated twice more. Finally, one last evacuation was carried out,

and the flask was filled with H₂ via balloon. The resulting mixture was stirred vigorously at room temperature under H₂ balloon for 24 hrs. The reaction was monitored by LC-MS. Upon consumption of starting material, the reaction mixture was filtered over celite, which was washed thoroughly with EtOAc. Solvent was evaporated under reduced pressure. The crude product was purified via column chromatography eluting with 1:40 EtOAc to hexanes to yield a slightly yellow oil (2.89 g, 9.88 mmol, 94% yield). R_f = 0.59 (1:20 EtOAc/Hex), R_f = 0.75 (1:10 EtOAc/Hex). IR (ν_{max}, cm⁻¹) 2924, 2854, 1764, 1465, 1374, 1336, 1304, 1189, 1130, 1095, 1034, 849, 778, 724, 642. ¹H NMR (400 MHz, CDCl₃) δ 4.33 (q, *J* = 6.8 Hz, 2H), 2.06 (m, 2H), 1.46 (app p, *J* = 7.6 Hz, 2H), 1.36 (t, *J* = 7.2 Hz, 3H), 1.27 (m, 18H), 0.89 (t, *J* = 6.8 Hz, 3H). ¹³C NMR (100 MHz, CDCl₃) δ 164.6 (t, *J* = 33.1 Hz), 116.6 (t, *J* = 248.6 Hz), 62.8, 34.7 (t, *J* = 23.1 Hz), 32.1, 29.8, 29.8, 29.8, 29.6, 29.6, 29.4, 29.3, 22.9, 21.6 (t, *J* = 4.1 Hz), 14.3, 14.1. ¹⁹F NMR (376 MHz, CDCl₃) δ -106.5 (t, *J* = 16.9 Hz, 2F). HRMS (ESI) *m/z* = 293.22788 (Theo. for C₁₆H₃₀O₂F₂ + H: 293.22866). Anal. Calcd. for C₁₆H₃₀O₂F₂: C, 65.72; H, 10.34; F, 12.99. Found: C, 66.31; H, 10.30; F, 12.71.



2,2-difluoro-N-methoxy-N-methyltetradecanamide

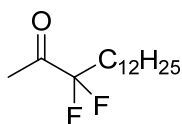
(**32**):

N,O-

dimethylhydroxylammonium chloride (8.78 g, 90.0 mmol, 3.00 eq) was added

to a 1 L 3-neck flame-dried flask equipped with an addition funnel and a stir bar. The solid was diluted with THF (159 mL), cooled to -78°C, and stirred under Ar. A solution of *n*-butyllithium in hexanes (72.0 mL, 180 mmol, 6.00 eq) was added dropwise via addition funnel at -78°C, and the resulting solution was allowed to stir at -78°C for 30 min. The dry ice-acetone bath was removed for 15 min, and the reaction mixture was subsequently re-cooled to -78°C. A solution of ethyl 2,2-difluorotetradecanoate (**27**, 8.78 g, 30.0 mmol, 1.00 eq) in THF (141 mL) was added slowly via addition funnel at -78°C, and the resulting mixture was stirred under Ar at -78°C. 15min after the addition was completed, TLC indicated consumption of starting material. The cold bath was removed for 10 min, and the reaction was quenched with saturated aqueous ammonium chloride. Once the mixture warmed to room temperature, a small volume of water was added to dissolve salts. The aqueous layer was extracted 3 times with EtOAc. Combined organic layer were washed with brine, dried over MgSO₄,

filtered, and evaporated under reduced pressure. The crude product was recrystallized from cold pentane to yield a white solid (9.09 g, 29.6 mmol, 99% yield). $R_f = 0.35$ (1:10 EtOAc/Hex), $R_f = 0.50$ (1:4 EtOAc/Hex). Mp 33-35°C. IR (ν_{\max} , cm^{-1}) 2917, 2849, 1678, 1461, 1184, 1161, 1016, 968, 876, 725, 653. ^1H NMR (400 MHz, CDCl_3) δ 3.75 (s, 3H), 3.27 (br s, 3H), 2.12 (m, 2H), 1.49 (app p, $J = 7.6\text{Hz}$, 2H), 1.26 (m, 18H), 0.89 (t, $J = 6.8\text{Hz}$, 3H). ^{13}C NMR (100 MHz, CDCl_3) δ 164.2 (t, $J = 23.1\text{ Hz}$), 118.2 (t, $J = 248.2\text{ Hz}$), 61.9, 34.5 (t, $J = 23.1\text{ Hz}$), 32.9, 32.0, 29.7, 29.7, 29.7, 29.5, 29.4, 29.4, 29.3, 22.7, 21.5, 14.1. ^{19}F (376 MHz, CDCl_3) δ -104.1 (app s, 2F). HRMS (ESI) $m/z = 308.23974$ (Theo. for $\text{C}_{16}\text{H}_{31}\text{F}_2\text{NO}_2 + \text{H}$: 308.23956). Anal. Calcd. for $\text{C}_{16}\text{H}_{31}\text{F}_2\text{NO}_2$: C, 62.51; H, 10.16; F, 12.36; N, 4.56. Found: C, 62.58; H, 10.07; F, 12.21; N, 4.56.

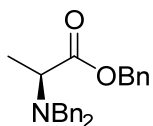


3,3-difluoropentadecan-2-one (**26**): **Grignard Addition.** Ethyl 2,2-difluorotetradecanoate (**27**, 0.150 g, 0.513 mmol, 1.00 eq) was added to a flame-dried

flask with a stir bar. The α,α -difluoro ester was diluted with THF (10.1 mL), cooled to -78°C , and stirred under Ar. A commercially available solution of methylmagnesium chloride (0.171 mL, 0.515 mmol, 1.00 eq) was added in dropwise fashion, and the resulting mixture was allowed to stir under Ar at -78°C . Once starting material disappeared on TLC, the reaction was quenched with saturated aqueous ammonium chloride, and the mixture was allowed to warm to room temperature. The resulting organic layer was washed with brine, dried over MgSO_4 , filtered, and evaporated under reduced pressure. Purification was accomplished via column chromatography to yield a pale yellow oil (0.040 g, 0.152 mmol, 30% yield).

Weinreb Ketone Synthesis. 2,2-difluoro-N-methoxy-N-methyltetradecanamide (**32**, 4.00 g, 13.0 mmol, 1.00 eq) was added to a 3-neck, 500 mL, flame-dried flask equipped with a low temperature internal thermometer and a stir bar. The solid was diluted with THF (130 mL), cooled to -78°C , and stirred vigorously under Ar. A solution of methyllithium in diethyl ether (8.13 mL, 13.0 mmol, 1.00 eq) was added via syringe pump (0.14 mL/min). Temperature was maintained below -70°C during addition. After the addition was completed, TLC indicated some remaining starting material. Another 0.300 eq methyllithium was added via syringe pump at the same rate. After addition was complete,

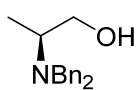
TLC still indicated remaining starting material. Another 0.300 eq methylolithium was added via syringe pump at the same rate. After the addition was completed, TLC indicated consumption of starting material. The reaction was quenched with saturated aqueous ammonium chloride, and the resulting mixture was transferred to a single neck flask. Solvent was evaporated under reduced pressure. A small volume of water was added to dissolve salts, and the resulting aqueous layer was extracted 3 times with EtOAc. The combined organic layers were washed twice with brine, dried over MgSO₄, filtered, and evaporated under reduced pressure. The crude product was purified via column chromatography eluting with 1:50 EtOAc to hexanes to yield a clear oil (2.67 g, 10.2 mmol, 78% yield). $R_f = 0.82$ (1:10 EtOAc/Hex), $R_f = 0.60$ (1:30 EtOAc/Hex), $R_f = 0.49$ (1:40 EtOAc/Hex). IR (ν_{\max} , cm⁻¹) 2924, 2854, 1747, 1465, 1361, 1206, 1137, 1034, 984. ¹H NMR (400 MHz, CDCl₃) δ 2.33 (t, $J = 1.6$ Hz, 3H), 1.97 (m, 2H), 1.44 (m, 2H), 1.26 (m, 18H), 0.89 (t, $J = 6.8$ Hz, 3H). ¹³C NMR (100 MHz, CDCl₃) δ 199.2 (t, $J = 33.1$ Hz), 118.3 (t, $J = 249.7$ Hz), 32.5 (t, $J = 22.7$ Hz), 32.1, 29.8, 29.8, 29.8, 29.6, 29.6, 29.5, 29.5, 24.1, 22.9, 21.4 (t, $J = 4.1$ Hz), 14.2. ¹⁹F (376 MHz, CDCl₃) δ -107.6 (dt, $J = 17.5$ Hz, 1.5 Hz, 2F). HRMS (APCI) $m/z = 263.21811$ (Theo. for C₁₅H₂₉F₂O + H: 263.21810). Anal. Calcd. for C₁₅H₂₈F₂O: C, 68.66; H, 10.76; F, 14.48. Found: C, 68.78; H, 10.74; F, 14.62.



(*S*)-benzyl 2-(dibenzylamino)propanoate (**49**): Sodium hydroxide (18.0 g, 449 mmol, 2.00 eq) and potassium carbonate (62.0 g, 449 mmol, 2.00 eq) were added to a 1 L 3-neck flask

equipped with a reflux condenser, an addition funnel, and a stir bar. The solids were diluted with water (374 mL) and stirred at room temperature. Added *L*-alanine (20.0 g, 224 mmol, 1.00 eq), and warmed the mixture to 115°C. Benzyl bromide (80.0 mL, 673 mmol, 3.00 eq) was added dropwise via addition funnel over 1 hr, and the resulting mixture was stirred at reflux. Reaction progress was monitored by LC-MS. The reaction mixture was allowed to cool to room temperature, and was extracted three times with diethyl ether. The combined organic layers were washed twice with brine, dried over MgSO₄, filtered, and evaporated under reduced pressure. The crude product was purified via column chromatography eluting with 1:10 EtOAc to hexanes to yield a viscous clear oil (53.7 g, 149 mmol, 67% yield). $[\alpha]_D^{20} = -78.7$ ($c = 1.00$ in CHCl₃). ¹H NMR (400 MHz, CDCl₃) δ 7.21-7.42 (m, 15H), 5.24

(d, $J = 12.0$ Hz, 1H), 5.17 (d, $J = 12.0$ Hz, 1H), 3.84 (d, $J = 14.4$ Hz, 2H), 3.64 (d, $J = 14.0$ Hz, 2H), 3.57 (q, $J = 7.2$ Hz, 1H), 1.36 (d, $J = 7.2$ Hz, 3H). ^{13}C NMR (100 MHz, CDCl_3) δ 173.6, 139.9 (2C), 136.2, 128.7 (6C), 128.3 (6C), 127.0 (3C), 66.1, 56.3, 54.5, 15.0. HRMS (APCI) $m/z = 360.19515$ (Theo. for $\text{C}_{24}\text{H}_{25}\text{N}_2\text{O}_8 + \text{H}$: 360.19581).

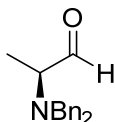


(S)-2-(dibenzylamino)propan-1-ol (**33**): **Carboxylic Acid Reduction**: A solution of *(S)*-2-(dibenzylamino)propanoic acid (**6**, 4.15 g, 15.4 mmol, 1.00 eq) in THF (77.0 mL) was

added to a flame-dried, 500 mL flask with a stir bar. The solution was further diluted with diethyl ether (77.0 mL), and was stirred vigorously under Ar at room temperature. Borane-dimethyl sulfide complex (5.11 mL, 53.9 mmol, 3.50 eq) was added dropwise via syringe pump (6.0 mL/hr) at room temperature. After the addition was completed, the flask was quickly equipped with a reflux condenser, and heated to 40°C. The reaction mixture was allowed to reflux overnight. In the morning, LC-MS indicated complete conversion of starting material to desired product. The reaction was quenched dropwise with MeOH, and solvent was evaporated under reduced pressure. The crude product was purified via automated column chromatography (CombiFlash, 80 g column, 15 min isocratic 20% EtOAc in hexanes) to yield a white solid (3.59 g, 14.1 mmol, 91% yield).

Benzyl Ester Reduction: *(S)*-Benzyl 2-(dibenzylamino)propanoate (**49**, 5.00 g, 13.9 mmol, 1.00 eq) was added to a flame-dried, 250 mL flask with a stir bar. The oil was diluted with diethyl ether (39.7 mL), cooled to 0°C, and stirred vigorously under Ar. Added a THF solution of lithium aluminum hydride (8.35 mL, 16.7 mmol, 1.20 eq) dropwise via syringe pump (10.0 mL/hr). The resulting reaction mixture was allowed to warm to room temperature and stir overnight. In the morning, a clear solution was observed, and TLC indicated almost complete conversion of starting material. The reaction mixture was cooled to 0°C, and water (0.620 mL) was carefully added dropwise. Then, 15% aqueous sodium hydroxide (0.620 mL) was carefully added dropwise, and this was followed by the careful addition of water (1.91 mL). The resulting mixture was filtered, and the precipitate was washed with diethyl ether (4 x 6 mL). The combined organic layers were dried over MgSO_4 , filtered, and evaporated under reduced pressure. The crude product was purified via automated column chromatography

(CombiFlash, 80 g column, 15 min gradient from 0-20% EtOAc in hexanes, 10 min isocratic 20% EtOAc in hexanes, and 5 min gradient to 50% EtOAc in hexanes) to yield a white solid (3.36 g, 13.2 mmol, 95% yield). $[\alpha]_{\text{D}}^{20} = +42.4$ ($c = 1.00$ in EtOAc). $^1\text{H NMR}$ (400 MHz) δ 7.23-7.35 (m, 10H), 3.83 (d, $J = 13.6$ Hz, 2H), 3.47 (app t, $J = 10.4$ Hz, 1H), 3.37 (m, 1H), 3.36 (d, $J = 13.2$ Hz, 2H), 3.16 (br s, 1H), 3.00 (m, 1H), 0.99 (d, $J = 6.8$ Hz, 3H). HRMS (APCI) $m/z = 256.16941$ (Theo. for $\text{C}_{17}\text{H}_{21}\text{NO} + \text{H}$: 256.16959).



(S)-2-(dibenzylamino)propanal (**25**): Oxalyl chloride (2.34 mL, 26.7 mmol, 2.50 eq) was added to a flame-dried, 500 mL with a stir bar. The oil was diluted with DCM (59.0 mL), cooled to -78°C , and stirred under Ar. Added dimethylsulfoxide (3.44 mL, 48.1 mmol, 4.50 eq) dropwise via syringe pump (6.9 mL/hr). The resulting mixture was allowed to stir at -78°C under Ar for 1 hr. A solution of *(S)*-2-(dibenzylamino)propan-1-ol (**33**, 2.73 g, 10.7 mmol, 1.00 eq) in DCM (48.0 mL) was added dropwise via syringe pump (24.0 mL/hr). White solid formation was observed towards the end of the addition, so DCM (24.0 mL) was added to help break up the solid. The resulting mixture was allowed to stir at -78°C under Ar for 15 min. Triethylamine (7.44 mL, 53.4 mmol, 5.00 eq) was added dropwise via syringe pump (10.0 mL/hr). The resulting mixture was allowed to stir at -78°C under Ar for 1 hr. At this point, TLC indicated complete consumption of starting material. The cold bath was removed, and the reaction was quenched with saturated aqueous sodium bicarbonate until neutral pH was achieved. Once the mixture warmed above 0°C , a small volume of water was added. The organic layer was washed twice with brine, dried over MgSO_4 , filtered, and evaporated under reduced pressure. The crude product was purified via a silica plug eluting quickly with 30% EtOAc in hexanes to yield a waxy yellow solid (2.45 g, 9.67 mmol, 91% yield). $[\alpha]_{\text{D}}^{20} = -31.9$ ($c = 1.00$ in CHCl_3). $^1\text{H NMR}$ (400 MHz) δ 9.73 (s, 1H), 7.23-7.42 (m, 10H), 3.73 (d, $J = 13.6$ Hz, 2H), 3.57 (d, $J = 13.6$ Hz, 2H), 3.33 (q, $J = 6.8$ Hz, 1H), 1.18 (d, $J = 6.8$ Hz, 3H).

Aldol Method A: *N,N*-dimethylethanamine (4.73 mL, 43.6 mmol, 4.00 eq) was added to a flame-dried 1 L 3-neck flask equipped with an internal temperature probe and a stir bar. The liquid was diluted with THF (31.0 mL), cooled to -78°C via recirculating chiller, and stirred under Ar. Added a solution

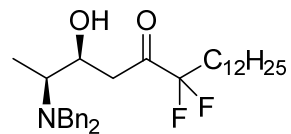
of chlorodicyclohexylborane in hexanes (14.7 mL, 14.7 mmol, 1.35 eq) dropwise via syringe pump (15.0 mL/hr). Temperature during addition was maintained below -77°C . The resulting reaction mixture was allowed to stir at -78°C for 15 min. Added a solution of 3,3-difluoropentadecan-2-one (**26**, 2.86 g, 10.9 mmol, 1.00 eq) in THF (53.0 mL) dropwise via syringe pump (35.0 mL/hr). Temperature during addition was maintained below -75°C . The resulting mixture was allowed to stir for 15 min at -78°C under Ar. The cold bath was removed, and THF (76.0 mL) was added while the solution was warming. Once the internal temperature reached -27.5°C , the cold bath was replaced, and the mixture was stirred under Ar until temperature reached -75°C . Added a solution of (*S*)-2-(dibenzylamino)propanal (**25**, 3.04 g, 12.0 mmol, 1.10 eq) in THF (31.0 mL) dropwise via syringe pump (16.0 mL/hr). Temperature during addition remained below -74°C . After the addition was completed, TLC indicated almost complete consumption of starting material, and LC-MS indicated a diastereomeric ratio of 61:39 favoring the *syn*-(2*S*,3*S*) diastereomer. The cold bath was removed, and the reaction mixture was allowed to warm to -30°C . At this point, TLC indicated complete consumption of starting material. The reaction mixture was allowed to warm to -20°C , at which point the mixture was poured over phosphate buffer (600 mL, pH = 7) in a separatory funnel. The separatory funnel was shaken until gas release ceased. The aqueous layer was quickly removed, and the organic layer was poured into a 500 mL round bottom flask equipped with a stir bar and an internal temperature probe. The organic layer was cooled to -20°C , and an aqueous solution of hydrogen peroxide (3.01 mL, 29.5 mmol, 2.70 eq) was added slowly. The resulting mixture was allowed to warm to 5°C and was poured into the separatory funnel. After sufficient shaking and gas release, the aqueous layer was removed. The organic layer was washed twice with brine, dried over MgSO_4 , filtered, and evaporated under reduced pressure. The crude product was purified via column chromatography eluting with 1:8 EtOAc to hexanes to yield separable diastereomers as clear oils: 2*S*,3*S* (2.02 g, 3.92 mmol, 36% yield) and 2*S*,3*R* (1.10 g, 2.13 mmol, 20% yield). Chiral HPLC verified that little to no racemization occurred during the reaction.

Aldol Method B: A solution of (*S*)-2-(dibenzylamino)propanal (**25**, 0.100 g, 0.395 mmol, 1.00 eq) in THF (4.00 mL) was added to a flame-dried Flask A with a stir bar. The solution was cooled to -78°C, and stirred under Ar. Added a DCM solution of titanium(IV) chloride (0.434 mL, 0.434 mmol, 1.10 eq) dropwise at -78°C, and the resulting mixture was stirred at -78°C for 1 hr. A solution of 3,3-difluoropentadecan-2-one (**26**, 0.114 g, 0.434 mmol, 1.10 eq) in THF (4.00 mL) was added to a flame-dried Flask B with a stir bar. The solution was cooled to -78°C, and stirred under Ar. Added a solution of potassium hexamethyldisilazane (0.908 mL, 0.454 mmol, 1.15 eq) in toluene dropwise at -78°C, and stirred at -78°C under Ar for 1 hr. The cold bath was removed for 10 min, and then replaced for 10 min. The resulting enolate solution was diluted with THF (4.00 mL), and transferred slowly to Flask A via cannula. The resulting reaction mixture was stirred under Ar at -78°C. Reaction progress was monitored by LC-MS. LC-MS showed a diastereomeric ratio of 81:19 favoring the desired *syn*-(2*S*,3*S*) stereoisomer. The reaction was quenched with saturated aqueous ammonium chloride. Once the mixture warmed to room temperature, a small volume of water was added to dissolve salts. The aqueous layer was extracted 3 times with diethyl ether. The combined organic layers were washed with twice with brine, dried over MgSO₄, filtered, and evaporated under reduced pressure. The small amount of isolated crude product was purified via column chromatography to yield impure and very little desired product.

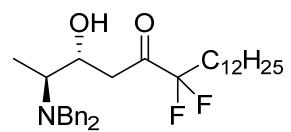
Aldol Method C: *N,N*-dimethylethanamine (0.050 mL, 0.457 mmol, 4.00 eq) was added to a flame-dried flask with a stir bar. The liquid was diluted with THF (0.500 mL), cooled to -78°C, and stirred under Ar. A solution of (+)-DiPCl or (-)-DiPCl (0.107 mL, 0.154 mmol, 1.35 eq) was added, and the resulting mixture was allowed to stir at -78°C for 15min. A solution of 3,3-difluoropentadecan-2-one (**26**, 0.030 g, 0.114 mmol, 1.00 eq) in THF (0.500 mL) was added dropwise, and the resulting mixture was stirred at -78°C for 1hr. The cold bath was removed for 10min, and then replaced. A solution of (*S*)-2-(dibenzylamino)propanal (**25**, 0.032 g, 0.126 mmol, 1.10 eq) in THF (0.500 mL) was added dropwise, and the resulting mixture was allowed to stir at -78°C. Reaction progress and

diastereoselectivity were monitored by LC-MS, which indicated the following diastereoselectivities:

(+)-DiPcI, 27:73 *syn/anti*; (-)-DiPcI, 66:34 *syn/anti*.

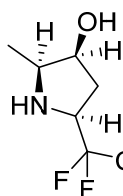


(2S,3S)-2-(dibenzylamino)-6,6-difluoro-3-hydroxyoctadecan-5-one (**35**): $R_f = 0.25$ (1:15 EtOAc/Hex), $R_f = 0.35$ (1:10 EtOAc/Hex). $[\alpha]_D^{20} = +4.3$ ($c = 1.00$ in EtOAc). IR (ν_{\max} , cm^{-1}) 3446, 2924, 2853, 1737, 1454, 1377, 1208, 1149, 1095, 1072, 1048, 1027, 746, 698. ^1H NMR (400 MHz, CDCl_3) δ 7.22-7.39 (m, 10H), 4.07 (app t, $J = 8.6$ Hz, 1H), 3.74 (d, $J = 14.0$ Hz, 2H), 3.44 (app d, $J = 18.8$ Hz, 1H), 3.41 (d, $J = 13.6$ Hz, 2H), 2.67 (dq, $J = 6.7$ Hz, 8.6 Hz, 1H), 2.52 (br s, 1H), 2.47 (dd, $J = 9.8$ Hz, 19.0 Hz, 1H), 1.93 (m, 2H), 1.43 (app p, $J = 7.6$ Hz, 2H), 1.27 (m, 18H), 1.19 (d, $J = 6.4$ Hz, 3H), 0.892 (t, $J = 6.8$ Hz, 3H). ^{13}C NMR (100 MHz, CDCl_3) δ 202.7 (t, $J = 31.7$ Hz), 139.7 (2C), 129.0 (4C), 128.5 (4C), 127.2 (2C), 118.3 (t, $J = 250.4$ Hz), 69.0, 56.8, 54.6 (2C), 42.1, 32.7 (t, $J = 22.7$ Hz), 32.1, 29.8 (3C), 29.6, 29.5, 29.4 (2C), 22.9, 21.3, 14.3, 8.4. ^{19}F NMR (376 MHz, CDCl_3) δ -107.8 (dt, $J = 17.7$ Hz, 271.8 Hz, 1F), -108.6 (dt, $J = 17.7$ Hz, 271.8 Hz, 1F). HRMS (APCI) $m/z = 516.36529$ (Theo. for $\text{C}_{32}\text{H}_{47}\text{F}_2\text{NO}_2 + \text{H}$: 516.36476). LC-MS (ES-API, + ion) 95% MeOH in H_2O isocratic, 3 min, 1.00 mL/min, C18 (Agilent Zorbax XDB-18, 50 mm x 4.6 mm, 3.5 μm), $m/z = 516.4$, $t = 1.847$ min. Chiral HPLC (254 nm) 2% iPrOH in hexane, 20 min, 1.00 mL/min, AD-H (Daicel ChiralPak, 150 mm x 4.6 mm, 5 μm), $t = 11.317$ min. Anal. Calcd. for $\text{C}_{32}\text{H}_{47}\text{F}_2\text{NO}_2$: C, 74.53; H, 9.19; N, 2.72; F, 7.37. Found: C, 74.65; H, 9.08; N, 2.88; F, 7.31.



(2S,3R)-2-(dibenzylamino)-6,6-difluoro-3-hydroxyoctadecan-5-one (**36**): $R_f = 0.38$ (1:15 EtOAc/Hex), $R_f = 0.49$ (1:10 EtOAc/Hex). $[\alpha]_D^{20} = +7.7$ ($c = 1.00$ in EtOAc). IR (ν_{\max} , cm^{-1}) 3407, 2923, 2853, 1744, 1454, 1379, 1208, 1144, 1055, 1027, 1002, 944, 747, 731, 698, 627. ^1H NMR (400 MHz, CDCl_3) δ 7.25-7.35 (m, 10H), 4.35 (br s, 1H), 4.06 (ddd, $J = 4.7$ Hz, 6.7 Hz, 9.4 Hz, 1H), 3.87 (d, $J = 13.6$ Hz, 2H), 3.33 (d, $J = 13.2$ Hz, 2H), 2.67 (m, 1H), 2.65 (m, 1H), 2.64 (m, 1H), 1.94 (m, 2H), 1.44 (app p, $J = 7.7$ Hz, 2H), 1.27 (m, 18H), 1.05 (d, $J = 6.8$ Hz, 3H), 0.898 (t, $J = 7.0$ Hz, 3H). ^{13}C NMR (100 MHz, CDCl_3) δ 199.9 (t, $J = 31.7$ Hz), 138.7 (2C), 129.2 (4C), 128.7 (4C), 127.5 (2C), 118.5 (t, $J = 250.0$ Hz), 66.9, 58.0, 53.4 (2C), 41.4, 32.5 (t, $J = 22.3$ Hz), 32.1, 29.8 (2C), 29.7, 29.6, 29.5, 29.4 (2C), 22.9, 21.2, 14.3, 8.14. ^{19}F NMR (376 MHz, CDCl_3) δ -107.9 (dt, J

= 18.0 Hz, 271.8 Hz, 1F), -108.7 (dt, $J = 17.9$ Hz, 271.8 Hz, 1F). HRMS (APCI) $m/z = 516.36540$ (Theo. for $C_{32}H_{47}F_2NO_2 + H$: 516.36476). LC-MS (ES-API, + ion) 95% MeOH in H_2O isocratic, 3 min, 1.00 mL/min, C18 (Agilent Zorbax XDB-18, 50 mm x 4.6 mm, 3.5 μ m), $m/z = 516.3$, $t = 1.035$ min. Anal. Calcd. for $C_{32}H_{47}F_2NO_2$: C, 74.53; H, 9.19; N, 2.72; F, 7.37. Found: C, 74.79; H, 9.19; N, 2.90; F, 7.21.



(2*S*,3*S*,5*S*)-5-(1,1-difluorotridecyl)-2-methylpyrrolidin-3-ol (**37**): A solution of (2*S*, 3*S*)-2-(dibenzylamino)-6,6-difluoro-3-hydroxyoctadecan-5-one (0.080 g, 0.155 mmol, 1.00 eq) in EtOH (5.20 mL) was added to a flame-dried flask with a stir bar. 10% palladium on carbon (0.017 g, 0.016 mmol, 0.100 eq) was added, and the mixture was stirred vigorously at room temperature. The flask was placed under low vacuum for 5 min, and then flushed with Ar. These two steps were repeated twice, followed by a final evacuation. Finally, the flask was placed under H_2 atmosphere via balloon, and the resulting reaction mixture was stirred vigorously overnight. In the morning, the mixture was filtered over celite, which was washed with methanol. The solvent was evaporated under reduced pressure. Impurities were dissolved in diethyl ether and pipetted off to yield pure white solid (0.032 g, 0.100 mmol, 65% yield). 1H NMR (400 MHz, CD_3OD) δ 4.30 (app s, 1H), 4.07 (m, 1H), 3.53 (m, 1H), 2.58 (m, 1H), 1.99 (m, 2H), 1.97 (m, 1H), 1.54 (m, 2H), 1.41 (d, $J = 6.6$ Hz, 3H), 1.30 (m, 18H), 0.901 (t, $J = 6.9$ Hz, 3H). NOE experiments summarized below. LC-MS (ES-API, + ion) 95% MeOH in H_2O isocratic, 3 min, 1.00 mL/min, C18 (Agilent Zorbax XDB-18, 50 mm x 4.6 mm, 3.5 μ m), $m/z = 320.2$, $t = 0.531$ min; 75-95% MeOH in H_2O , 3 min, 1.00 mL/min, C18 (Agilent Zorbax XDB-18, 50 mm x 4.6 mm, 3.5 μ m), $m/z = 320.2$, $t = 1.802$ min.

Reduction Method A: Sodium borohydride (0.135 g, 3.58 mmol, 1.50 eq) was added to a flame-dried flask with a stir bar. The solid was diluted with THF (12.0 mL). Added a solution of (2*S*,3*S*)-2-(dibenzylamino)-6,6-difluoro-3-hydroxyoctadecan-5-one (**35**, 1.23 g, 2.38 mmol, 1.00 eq) in THF (12.0 mL) via syringe pump over 30 min. Once starting material was undetectable by TLC, the reaction was quenched dropwise with water. Added 2 N aqueous HCl in dropwise fashion until neutral pH was achieved. The aqueous layer was extracted with EtOAc. The combined organic layers were washed

with brine, dried over MgSO₄, filtered, and evaporated under reduced pressure. The crude mixture of separable diastereomers was purified via column chromatography eluting with 1:4 EtOAc to hexanes to yield two yellow oils: 2*S*,3*S*,5*R* (0.350 g, 0.676 mmol, 28% yield) and 2*S*,3*S*,5*S* (0.510 g, 0.985 mmol, 41% yield).

Reduction Method B: A solution of (2*S*,3*S*)-2-(dibenzylamino)-6,6-difluoro-3-hydroxyoctadecan-5-one (**35**, 0.015 g, 0.029 mmol, 1.00 eq) in THF (0.600 mL) was added to a flame-dried vial with a stir bar. The solution was cooled to -78°C, and stirred under Ar. Added sodium borohydride (1.21 mg, 0.032 mmol, 1.10 eq), and the resulting mixture was stirred at -78°C under Ar. Reaction progress and diastereoselectivity were monitored by LC-MS. LC-MS showed a diastereomeric ratio of 41:59 disfavoring the desired *syn*-(2*S*,3*S*) stereoisomer.

Reduction Method C: A solution of (2*S*,3*S*)-2-(dibenzylamino)-6,6-difluoro-3-hydroxyoctadecan-5-one (**35**, 0.015 g, 0.029 mmol, 1.00 eq) in THF (0.500 mL) was added to a flame-dried vial with a stir bar. Added MeOH (0.120 mL), cooled to -78°C, and stirred under Ar. Added diethylmethoxyborane (4.20 µL, 0.032 mmol, 1.10 eq) via a 10 µL syringe, and the resulting mixture was stirred for 30 min at -78°C under Ar. Added sodium borohydride (1.21 mg, 0.032 mmol, 1.10 eq), and the resulting mixture was stirred at -78°C under Ar. Reaction progress and diastereoselectivity were monitored by LC-MS. LC-MS showed a diastereomeric ratio of 45:55 disfavoring the desired *syn*-(2*S*,3*S*) stereoisomer.

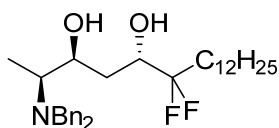
Reduction Method D: A solution of (2*S*,3*S*)-2-(dibenzylamino)-6,6-difluoro-3-hydroxyoctadecan-5-one (**35**, 0.015 g, 0.029 mmol, 1.00 eq) in THF (0.500 mL) was added to a flame-dried vial with a stir bar. Added MeOH (0.120 mL), cooled to -78°C, and stirred under Ar. Added diethylmethoxyborane (4.20 µL, 0.032 mmol, 1.10 eq) via a 10 µL syringe, and the resulting mixture was stirred at -78°C under Ar for 30 min. The resulting mixture was warmed to 0°C, and cooled back down to -78°C. Added sodium borohydride (1.21 mg, 0.032 mmol, 1.10 eq), and the resulting mixture was stirred under Ar at -78°C. Reaction progress and diastereoselectivity were monitored by LC-MS. LC-MS showed a diastereomeric ratio of 51:49 favoring the desired *syn*-(2*S*,3*S*) stereoisomer.

Reduction Method E: A solution of (2*S*,3*S*)-2-(dibenzylamino)-6,6-difluoro-3-hydroxyoctadecan-5-one (**35**, 0.015 g, 0.029 mmol, 1.00 eq) in THF (0.500 mL) was added to a flame-dried vial with a stir bar. Added MeOH (0.120 mL), cooled to 0°C, and stirred under Ar. Added diethylmethoxyborane (4.20 μ L, 0.032 mmol, 1.10 eq) via a 10 μ L syringe, and the resulting mixture was stirred for 30 min under Ar at 0°C. Added sodium borohydride (1.21 mg, 0.032 mmol, 1.10 eq), and the resulting mixture was stirred at 0°C under Ar. Reaction progress and diastereoselectivity were monitored by LC-MS. LC-MS showed a diastereomeric ratio of 45:55 disfavoring the desired *syn*-(2*S*,3*S*) stereoisomer.

Reduction Method F: A solution of (2*S*,3*S*)-2-(dibenzylamino)-6,6-difluoro-3-hydroxyoctadecan-5-one (**35**, 0.015 g, 0.029 mmol, 1.00 eq) in THF (0.600 mL) was added to a flame-dried vial with a stir bar. The solution was cooled to -78°C and stirred under Ar. Added a solution of diisobutylaluminum hydride in THF (0.087 mL, 0.087 mmol, 3.00 eq) dropwise, and the resulting mixture was stirred under Ar at -78°C. Reaction progress and diastereoselectivity were monitored by LC-MS. LC-MS showed a diastereomeric ratio of 17:83 disfavoring the desired *syn*-(2*S*,3*S*) stereoisomer.

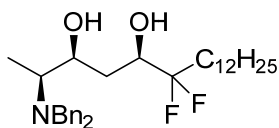
Reduction Method G: A solution of (2*S*,3*S*)-2-(dibenzylamino)-6,6-difluoro-3-hydroxyoctadecan-5-one (**35**, 1.35 g, 2.62 mmol, 1.00 eq) in THF (21.0 mL) was added to a flame-dried flask with a stir bar. Added anhydrous (dried overnight under high vacuum at 55°C) zinc(II) bromide (0.648 g, 2.88 mmol, 1.10 eq), cooled to -78°C, and stirred under Ar. Added a solution of diisobutylaluminum hydride in THF (7.85 mL, 7.85 mmol, 3.00 eq) dropwise at -78°C via syringe pump (0.13 mL/min). The resulting mixture was stirred at -78°C under Ar. Reaction progress was monitored by TLC, and diastereoselectivity was determined by LC-MS. LC-MS showed a diastereomeric ratio of 71:29 favoring the desired *syn*-(2*S*,3*S*) stereoisomer. Once starting material was undetectable by TLC, the reaction mixture was poured over of a 1:1 mixture of saturated aqueous ammonium chloride and concentrated HCl (28.0 mL). Water (8.00 mL) was added to dissolve salts. The aqueous layer was extracted 3 times with EtOAc. The combined organic layers were washed twice with brine, dried over MgSO₄, filtered, and evaporated under reduced pressure. The crude product was taken up in DCM, and an equal volume of saturated aqueous sodium potassium tartarate was added. The biphasic mixture was stirred

vigorously for 6 hrs. The resulting mixture was separated, and the aqueous layer lightly washed with DCM. The combined organic layers were washed twice with brine, dried over MgSO₄, filtered, and evaporated under reduced pressure to yield a clear yellow oil. The crude product was purified via column chromatography eluting with 1:4 EtOAc to hexanes to yield the 2*S*,3*S*,5*R* aminodiols as a clear oil (0.762 g, 1.47 mmol, 56% yield).



(2*S*,3*S*,5*R*)-2-(dibenzylamino)-6,6-difluorooctadecane-3,5-diol (**38**): $R_f = 0.41$ (1:5 EtOAc/Hex), $R_f = 0.18$ (1:10 EtOAc/Hex). $[\alpha]_D^{20} = +1.1$ ($c = 1.00$ in EtOAc).

IR (ν_{\max} , cm⁻¹) 3405, 2923, 2853, 1454, 1147, 1010, 1073, 1027, 1001, 745, 698. ¹H NMR (400 MHz, CDCl₃) δ 7.23-7.35 (m, 10H), 3.87 (m, 1H), 3.79 (d, $J = 14.0$ Hz, 2H), 3.76 (m, 1H), 3.44 (d, $J = 13.6$ Hz, 2H), 2.79 (p, $J = 6.9$ Hz, 1H), 2.25 (app d, $J = 14.4$ Hz, 1H), 1.77-1.97 (m, 2H), 1.51 (m, 2H), 1.4 (m, 1H), 1.28 (m, 18H), 1.16 (d, $J = 6.8$ Hz, 3H), 0.892 (t, $J = 6.8$ Hz, 3H). ¹³C NMR (100 MHz, CDCl₃) δ 139.7 (2C), 129.1 (4C), 128.6 (4C), 127.4 (2C), 123.8 (t, $J = 244.1$ Hz), 74.5, 74.3 (t, $J = 28.3$ Hz), 57.8, 55.2 (2C), 32.8, 32.4 (t, $J = 23.8$ Hz), 32.1, 29.8 (3C), 29.7 (2C), 29.6, 29.5, 22.9, 21.5, 14.3, 8.7. ¹⁹F NMR (376 MHz, CDCl₃) δ -111.1 (m, 1F), -114.1 (m, 1F). HRMS (APCI) $m/z = 518.38075$ (Theo. for C₃₂H₄₉F₂NO₂ + H: 518.38041). LC-MS (ES-API, + ion) 85% MeOH in H₂O isocratic, 5 min, 1.00 mL/min, C18 (Agilent Zorbax XDB-18, 50 mm x 4.6 mm, 3.5 μ m), $m/z = 518.4$, $t = 3.777$ min. Anal. Calcd. for C₃₂H₄₉F₂NO₂: C, 74.24; H, 9.54; N, 2.71; F, 7.34. Found: C, 73.49; H, 9.57; N, 2.63; F, 7.02.

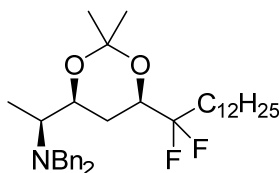


(2*S*,3*S*,5*S*)-2-(dibenzylamino)-6,6-difluorooctadecane-3,5-diol (**39**): $R_f = 0.34$ (1:5 EtOAc/Hex), $R_f = 0.13$ (1:10 EtOAc/Hex). $[\alpha]_D^{20} = +14.4$ ($c = 1.00$ in EtOAc).

IR (ν_{\max} , cm⁻¹) 3360, 2920, 2851, 1453, 1379, 1247, 1205, 1162, 1073, 1028, 1002, 976, 933, 905, 731, 697, 663. ¹H NMR (400 MHz, CDCl₃) δ 7.23-7.35 (m, 10H), 3.93 (td, $J = 2.1$ Hz, 8.0 Hz, 1H), 3.83 (m, 1H), 3.76 (d, $J = 13.6$ Hz, 2H), 3.42 (d, $J = 14.0$ Hz, 2H), 2.78 (app p, $J = 6.6$ Hz, 1H), 2.59 (br s, 1H), 2.31 (br s, 1H), 1.99 (ddd, $J = 2.7$ Hz, 10.0 Hz, 14.4 Hz, 1H), 1.76-1.92 (m, 2H), 1.70 (ddd, $J = 2.4$ Hz, 8.8 Hz, 14.4 Hz, 1H), 1.50 (app p, $J = 7.5$ Hz, 2H), 1.28 (m, 18H), 1.19 (d, $J = 6.8$ Hz, 3H), 0.891 (t, $J = 6.6$ Hz, 3H). ¹³C NMR (100 MHz, CDCl₃) δ 139.8 (2C), 129.2 (4C), 128.5 (4C),

127.3 (2C), 124.6 (t, $J = 243.3$ Hz), 70.9, 70.2 (t, $J = 28.3$ Hz), 57.2, 54.8 (2C), 33.0, 32.8 (t, $J = 23.8$ Hz), 32.1, 29.9 (3C), 29.8, 29.7, 29.6, 29.6, 22.9, 21.5, 14.3, 8.75. ^{19}F NMR (376 MHz, CDCl_3) δ -111.6 (m, 1F), -113.6 (m, 1F). HRMS (APCI) $m/z = 518.38041$ (Theo. for $\text{C}_{32}\text{H}_{49}\text{F}_2\text{NO}_2 + \text{H}$: 518.38041). LC-MS (ES-API, + ion) 85% MeOH in H_2O isocratic, 5 min, 1.00 mL/min, C18 (Agilent Zorbax XDB-18, 50 mm x 4.6 mm, 3.5 μm), $m/z = 518.4$, $t = 2.314$ min. Anal. Calcd. for $\text{C}_{32}\text{H}_{49}\text{F}_2\text{NO}_2$: C, 74.24; H, 9.54; N, 2.71; F, 7.34. Found: C, 74.38; H, 9.60; N, 2.85; F, 7.18.

Rychnovsky's Acetonide Method A: Each epimer of (2*S*,3*S*)-2-(dibenzylamino)-6,6-difluorooctadecane-3,5-diol (0.150 g, 0.290 mmol, 1.00 eq) was added to a flask with a stir bar. The oils were diluted with 2,2-dimethoxypropane (4.51 mL, 36.8 mmol, 127 eq), and *p*-toluenesulfonic acid monohydrate (0.011 g, 0.058 mmol, 0.200 eq) was added. The flasks were equipped with reflux condensers, warmed to 55°C, and stirred overnight. Progress of the reactions was monitored by LC-MS. Once LC-MS indicated almost complete conversion to desired products, the reaction mixtures were cooled to room temperature, diluted with diethyl ether, and washed with saturated aqueous sodium bicarbonate. The organic layers were dried over MgSO_4 , filtered, and evaporated under reduced pressure. The crude products were purified via column chromatography eluting with 1:80 EtOAc to hexanes to yield the desired acetonides as clear oils.

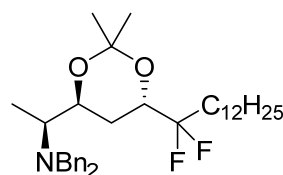


(*S*)-*N,N*-dibenzyl-1-((4*S*,6*R*)-6-(1,1-difluorotridecyl)-2,2-dimethyl-1,3-dioxan-4-

yl)ethanamine (**42**): (0.143 g, 0.256 mmol, 88% yield). $R_f = 0.41$ (1:80 EtOAc/Hex); $R_f = 0.49$ (1:40 EtOAc/Hex). $[\alpha]_{\text{D}}^{20} = -5.8$ ($c = 1.00$ in

CHCl_3). IR (ν_{max} , cm^{-1}) 2924, 2853, 1454, 1379, 1258, 1201, 1165, 1116, 1027, 1009, 969, 872, 744, 733, 698. ^1H NMR (400 MHz, CDCl_3) δ 7.22-7.37 (m, 10H), 3.95 (m, 1H), 3.88 (m, 1H), 3.77 (d, $J = 13.6$ Hz, 2H), 3.47 (d, $J = 14.0$ Hz, 2H), 2.64 (p, $J = 6.7$ Hz, 1H), 1.90 (app d, $J = 13.2$ Hz, 1H), 1.78-1.85 (m, 2H), 1.48 (m, 2H), 1.40 (s, 3H), 1.35 (s, 3H), 1.28 (m, 19H), 1.10 (d, $J = 6.8$ Hz, 3H), 0.897 (t, $J = 7.0$ Hz, 3H). ^{13}C NMR (100 MHz, CDCl_3) δ 140.4 (2C), 128.9 (4C), 128.4 (4C), 127.1 (2C), 123.2 (t, $J = 241.7$ Hz), 99.1, 71.1, 70.7 (t, $J = 29.5$ Hz), 57.4, 54.8 (2C), 32.5 (t, $J = 24.3$ Hz), 32.1, 30.0, 29.9, 29.8 (2C), 29.7, 29.6, 29.6, 29.6, 27.8, 22.9, 21.5, 19.7, 14.3, 8.1. ^{19}F NMR (376 MHz, CDCl_3) δ -110.4 (m,

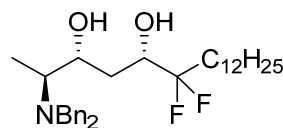
1F), -113.0 (m, 1F). HRMS (APCI) $m/z = 558.41126$ (Theo. for $C_{35}H_{53}F_2NO_2 + H$: 558.41171). Anal. Calcd. for $C_{35}H_{53}F_2NO_2$: C, 75.36; H, 9.58; N, 2.51; F, 6.81. Found: C, 75.06; H, 9.58; N, 2.44; F, 6.64.



(*S*)-*N,N*-dibenzyl-1-((4*S*,6*S*)-6-(1,1-difluorotridecyl)-2,2-dimethyl-1,3-dioxan-4-yl)ethanamine (**43**): (0.118 g, 0.212 mmol, 73% yield). $R_f = 0.30$ (1:80 EtOAc/Hex); $R_f = 0.54$ (1:40 EtOAc/Hex). $[\alpha]_D^{20} = +10.1$ ($c = 1.00$ in $CHCl_3$).

IR (ν_{max} , cm^{-1}) 2924, 2853, 1494, 1454, 1379, 1311, 1225, 1172, 1108, 1020, 942, 909, 843, 732, 698, 648. 1H NMR (400 MHz, $CDCl_3$) δ 7.22-7.37 (m, 10H), 3.89 (m, 1H), 3.81 (m, 1H), 3.75 (d, $J = 14.0$ Hz, 2H), 3.43 (d, $J = 13.6$ Hz, 2H), 2.67 (p, $J = 6.9$ Hz, 1H), 2.16 (m, 1H), 1.79-1.92 (m, 2H), 1.64 (m, 1H), 1.47 (m, 2H), 1.37 (s, 3H), 1.29 (m, 21H), 1.11 (d, $J = 6.4$ Hz, 3H), 0.899 (t, $J = 7.0$ Hz, 3H). ^{13}C NMR (100 MHz, $CDCl_3$) δ 140.2 (2C), 129.0 (4C), 128.4 (4C), 127.1 (2C), 123.7 (t, $J = 242.6$ Hz), 101.0, 69.2, 67.8 (t, $J = 30.5$ Hz), 56.7, 54.6 (2C), 33.4 (t, $J = 23.8$ Hz), 32.1, 29.9 (2C), 29.8, 29.7, 29.6, 29.6 (2C), 29.6, 24.7, 24.5, 22.9, 21.7, 14.4, 8.5. ^{19}F NMR (376 MHz, $CDCl_3$) δ -112.1 (m, 1F), -113.4 (m, 1F). HRMS (APCI) $m/z = 558.41098$ (Theo. for $C_{35}H_{53}F_2NO_2 + H$: 558.41171). Anal. Calcd. for $C_{35}H_{53}F_2NO_2$: C, 75.36; H, 9.58; N, 2.51; F, 6.81. Found: C, 75.20; H, 9.68; N, 2.49; F, 6.61.

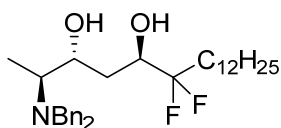
Reduction Method H: Sodium borohydride (0.041 g, 1.09 mmol, 1.50 eq) was added to a flame-dried flask with a stir bar. The solid was diluted with THF (3.65 mL). Added a solution of (2*S*,3*R*)-2-(dibenzylamino)-6,6-difluoro-3-hydroxyoctadecan-5-one (**36**, 0.375 g, 0.727 mmol, 1.00 eq) in THF (3.65 mL) via syringe pump over 30 min. Once starting material was undetectable by TLC, the reaction was quenched with water. Added 2 N aqueous HCl dropwise until neutral pH was achieved. The aqueous layer was extracted with EtOAc. The combined organic layers were washed with brine, dried over $MgSO_4$, filtered, and evaporated under reduced pressure. The crude mixture of separable diastereomers was purified via column chromatography eluting with 1:4 EtOAc to hexanes to yield two yellow oils.



(2*S*,3*R*,5*S*)-2-(dibenzylamino)-6,6-difluorooctadecane-3,5-diol (**40**): (0.150 g, 0.290 mmol, 40% yield). $R_f = 0.60$ (1:5 EtOAc/Hex), $R_f = 0.44$ (1:10

EtOAc/Hex). $[\alpha]_D^{20} = +23.5$ ($c = 1.00$ in EtOAc). IR (ν_{max} , cm^{-1}) 3475, 2924, 2852, 1454, 1143, 1110,

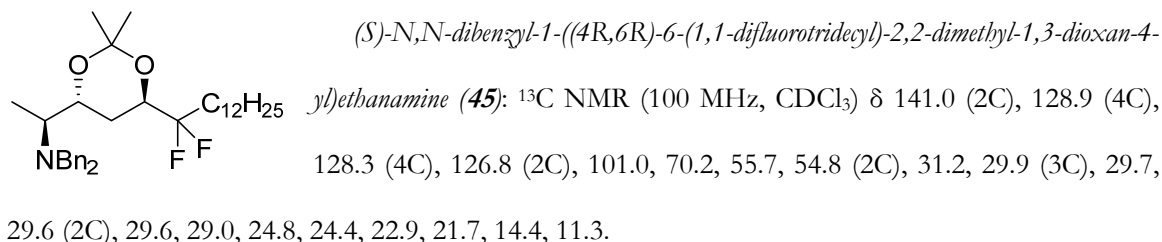
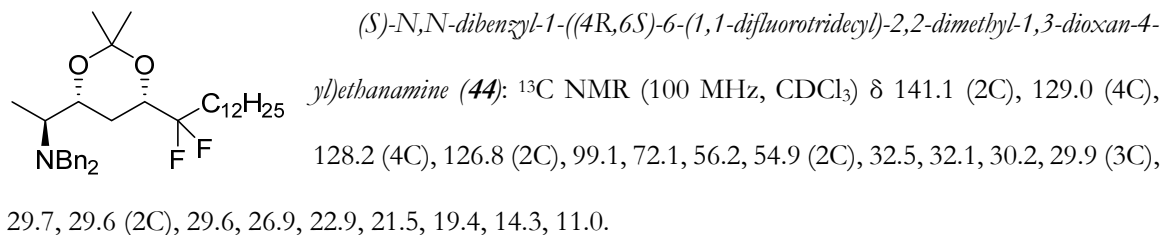
1075, 1057, 1027, 980, 748, 732, 699. ^1H NMR (400 MHz, CDCl_3) δ 7.25-7.36 (m, 10H), 4.90 (br s, 1H), 4.34 (br s, 1H), 3.98 (m, 1H), 3.83 (d, $J = 13.2$ Hz, 2H), 3.70 (m, 1H), 3.33 (d, $J = 13.2$ Hz, 2H), 2.61 (m, 1H), 1.91 (m, 2H), 1.87 (m, 2H), 1.506 (m, 2H), 1.27 (m, 18H), 1.07 (d, $J = 6.8$ Hz, 3H), 0.897 (t, $J = 6.8$ Hz, 3H). ^{13}C NMR (100 MHz, CDCl_3) δ 138.7 (2C), 129.2 (4C), 128.8 (4C), 127.6 (2C), 124.0 (t, $J = 242.6$ Hz), 73.3 (t, $J = 30.1$ Hz), 71.7, 58.9, 53.4 (2C), 32.9, 32.7 (t, $J = 23.8$ Hz), 32.1, 29.8 (3C), 29.7, 29.7, 29.6, 29.5, 22.9, 21.7, 14.3, 8.16. ^{19}F NMR (376 MHz, CDCl_3) δ -110.1 (m, 1F), -115.1 (m, 1F). HRMS (APCI) $m/z = 518.38066$ (Theo. for $\text{C}_{32}\text{H}_{49}\text{F}_2\text{NO}_2 + \text{H}$: 518.38041). Anal. Calcd. for $\text{C}_{32}\text{H}_{49}\text{F}_2\text{NO}_2$: C, 74.24; H, 9.54; N, 2.71; F, 7.34. Found: C, 73.94; H, 9.61; N, 2.70; F, 7.17.



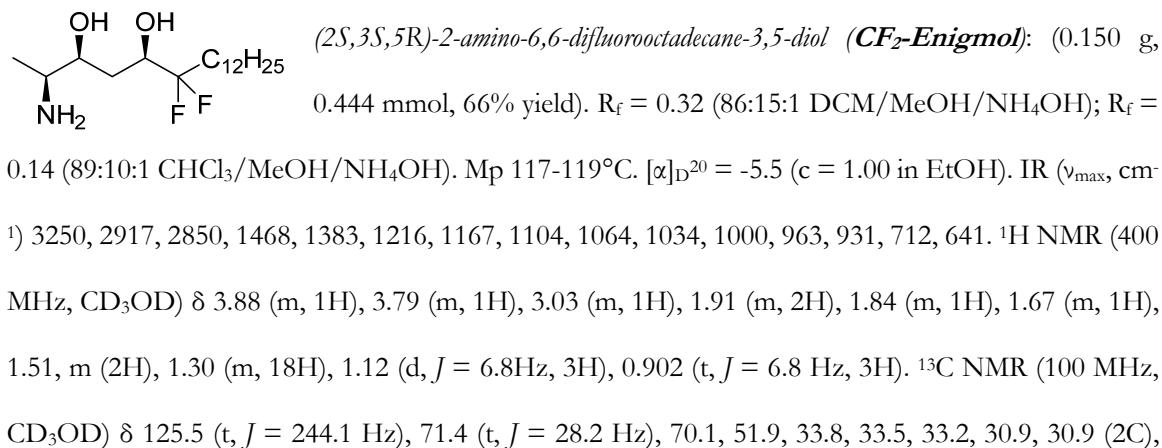
(2*S*,3*R*,5*R*)-2-(dibenzylamino)-6,6-difluorooctadecane-3,5-diol (**41**): (0.094 g, 0.182 mmol, 25% yield). $R_f = 0.43$ (1:5 EtOAc/Hex), $R_f = 0.24$ (1:10

EtOAc/Hex). $[\alpha]_{\text{D}}^{20} = +5.5$ ($c = 1.00$ in EtOAc). IR (ν_{max} , cm^{-1}) 3399, 2923, 2852, 1454, 1143, 1093, 1058, 1027, 983, 748, 732, 698, 627. ^1H NMR (400 MHz, CDCl_3) δ 7.26-7.35 (m, 10H), 4.70 (br s, 1H), 2.85 (d, $J = 13.2$ Hz, 2H), 3.82 (m, 1H), 3.34 (d, $J = 13.2$ Hz, 2H), 3.17 (app d, $J = 4.8$ Hz, 1H), 2.68 (m, 1H), 1.85 (m, 2H), 1.82 (m, 1H), 1.48 (m, 1H), 1.45 (m, 2H), 1.27 (m, 18H), 1.05 (d, $J = 6.8$ Hz, 3H), 0.890 (t, $J = 7.0$ Hz, 3H). ^{13}C NMR (100 MHz, CDCl_3) δ 138.8 (2C), 129.2 (4C), 128.8 (4C), 127.6 (2C), 124.4 (t, $J = 243.3$ Hz), 69.7 (t, $J = 29.4$ Hz), 68.1, 57.9, 53.5 (2C), 32.9 (t, $J = 23.9$ Hz), 32.5, 32.1, 29.8 (3C), 29.7, 29.7, 29.6, 29.6, 22.8, 21.6, 14.3, 8.20. ^{19}F NMR (376 MHz, CDCl_3) δ -111.3 (m, 1F), -114.3 (m, 1F). HRMS (APCI) $m/z = 518.38074$ (Theo. for $\text{C}_{32}\text{H}_{49}\text{F}_2\text{NO}_2 + \text{H}$: 518.38041). Anal. Calcd. for $\text{C}_{32}\text{H}_{49}\text{F}_2\text{NO}_2$: C, 74.24; H, 9.54; N, 2.71; F, 7.34. Found: C, 74.16; H, 9.68; N, 2.72; F, 7.10.

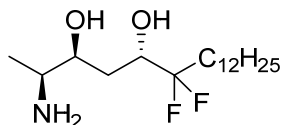
Rychnovsky's Acetonide Method B: Each epimer of (2*S*,3*R*)-2-(dibenzylamino)-6,6-difluorooctadecane-3,5-diol (0.010 g, 0.019 mmol, 1.00 eq) was added to a vial with a stir bar and diluted with 2,2-dimethoxypropane (0.300 mL, 2.45 mmol, 127 eq). *p*-Toluenesulfonic acid monohydrate (0.919 mg, 0.005 mmol, 0.250 eq) was added. The resulting reaction mixtures were warmed to 40°C and allowed to stir overnight. In the morning, the reaction mixtures were diluted with diethyl ether, washed with saturated aqueous sodium bicarbonate, dried over MgSO_4 , filtered, and evaporated under reduced pressure.



General Deprotection Procedure: A solution of each stereoisomer of (2*S*)-2-(dibenzylamino)-6,6-difluorooctadecane-3,5-diol (1.00 eq) in EtOH (0.03 M) was added to a flame-dried flask with a stir bar. Palladium(II) hydroxide (20%, 0.100 eq) was added, and the resulting mixtures were stirred vigorously under Ar at room temperature. The reaction mixtures were placed under low vacuum for 5 min, and then flushed with Ar. These two steps were repeated twice more. The reaction mixtures were placed under low vacuum again, and finally placed under H₂ atmosphere via balloons. The reaction mixtures were allowed to stir at room temperature overnight. The next day, the reaction contents were filtered over plugs of celite, which were subsequently washed with MeOH. Solvent was evaporated under reduced pressure. The crude Enigmols were purified via column chromatography eluting with mixtures of DCM (or CHCl₃), MeOH, and NH₄OH to yield enantiomerically pure C6-difluoro-Enigmols as white solids.

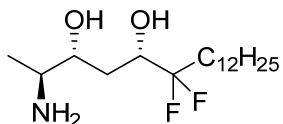


30.8, 30.8, 30.7, 30.6, 23.9, 22.6, 14.6, 12.6. ^{19}F NMR (376 MHz, CD_3OD) δ -107.0 (m, 1F), -111.0 (m, 1F). HRMS (APCI) $m/z = 338.28651$ (Theo. for $\text{C}_{18}\text{H}_{37}\text{F}_2\text{NO}_2 + \text{H}$: 338.28651). Anal. Calcd. for $\text{C}_{18}\text{H}_{37}\text{F}_2\text{NO}_2$: C, 64.06; H, 11.05; N, 4.15; F, 11.26. Found: C, 63.97; H, 10.86; N, 4.15; F, 11.08.



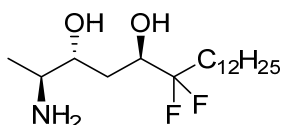
(*2S,3S,5S*)-2-amino-6,6-difluorooctadecane-3,5-diol (**2S,3S,5S-CF₂-Enigmol**):

(0.060 g, 0.178 mmol, 75% yield). $R_f = 0.21$ (62:38:2 DCM/MeOH/ NH_4OH); $R_f = 0.18$ (70:30:2 DCM/MeOH/ NH_4OH). Mp 119-122°C. $[\alpha]_{\text{D}}^{20} = +19.8$ ($c = 1.00$ in EtOH). IR (ν_{max} , cm^{-1}) 3317, 2917, 2850, 2354, 1089, 1064, 1031, 1008, 976, 962, 683, 645. ^1H NMR (400 MHz, CD_3OD) δ 3.91 (m, 1H), 3.87 (m, 1H), 3.09 (m, 1H), 1.90 (m, 2H), 1.65 (m, 1H), 1.55 (m, 1H), 1.51 (m, 2H), 1.30 (m, 18H), 1.16 (d, $J = 7.2$ Hz, 3H), 0.902 (t, $J = 6.8$ Hz, 3H). ^{13}C NMR (100 MHz, CD_3OD) δ 125.8 (t, $J = 243.3$ Hz), 69.9 (t, $J = 28.7$ Hz), 69.0, 53.3, 34.0, 33.9 (t, $J = 24.5$ Hz), 33.2, 30.9, 30.9 (2C), 30.8 (2C), 30.7, 30.6, 23.8, 22.7, 14.6, 13.6. ^{19}F NMR (376 MHz, CD_3OD) δ -107.3 (m, 1F), -110.9 (m, 1F). HRMS (APCI) $m/z = 338.28633$ (Theo. for $\text{C}_{18}\text{H}_{37}\text{F}_2\text{NO}_2 + \text{H}$: 338.28651). Anal. Calcd. for $\text{C}_{18}\text{H}_{37}\text{F}_2\text{NO}_2$: C, 64.06; H, 11.05; N, 4.15; F, 11.26. Found: C, 60.72; H, 10.50; N, 3.92; F, 10.28.



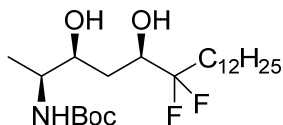
(*2S,3R,5S*)-2-amino-6,6-difluorooctadecane-3,5-diol (**2S,3R,5S-CF₂-Enigmol**):

(0.043 g, 0.127 mmol, 44% yield). $R_f = 0.44$ (86:15:1 DCM/MeOH/ NH_4OH); $R_f = 0.27$ (89:10:1 CHCl_3 /MeOH/ NH_4OH). Mp 79-82°C. $[\alpha]_{\text{D}}^{20} = +5.9$ ($c = 1.00$ in EtOH). IR (ν_{max} , cm^{-1}) 3369, 2922, 2853, 1461, 1381, 1259, 1152, 1087, 961, 858, 806, 721, 666. ^1H NMR (400 MHz, CD_3OD) δ 3.93 (m, 1H), 3.59 (m, 1H), 2.82 (m, 1H), 1.92 (m, 2H), 1.91 (m, 1H), 1.60 (m, 1H), 1.50 (m, 2H), 1.30 (m, 18H), 1.11 (d, $J = 6.4$ Hz, 3H), 0.903 (t, $J = 6.8$ Hz, 3H). ^{13}C NMR (100 MHz, CD_3OD) δ 125.7 (t, $J = 242.9$ Hz), 75.3, 71.9 (t, $J = 29.0$ Hz), 52.2, 34.8, 33.7 (t, $J = 24.6$ Hz), 33.2, 31.0, 30.9 (3C), 30.8, 30.7, 30.6, 23.9, 22.7, 19.5, 14.6. ^{19}F NMR (376 MHz, CD_3OD) δ -107.3 (m, 1F), -111.3 (m, 1F). HRMS (APCI) $m/z = 338.28622$ (Theo. for $\text{C}_{18}\text{H}_{37}\text{F}_2\text{NO}_2 + \text{H}$: 338.28651). Anal. Calcd. for $\text{C}_{18}\text{H}_{37}\text{F}_2\text{NO}_2$: C, 64.06; H, 11.05; N, 4.15; F, 11.26. Found: C, 64.72; H, 11.00; N, 3.92; F, 10.29.



(2*S*,3*R*,5*R*)-2-amino-6,6-difluorooctadecane-3,5-diol (**2*S*,3*R*,5*R*-CF₂-Enigmol**):

(0.050 g, 0.148 mmol, 82% yield). $R_f = 0.47$ (86:15:1 DCM/MeOH/NH₄OH); $R_f = 0.22$ (89:10:1 CHCl₃/MeOH/NH₄OH). Mp 69-72°C. $[\alpha]_D^{20} = -21.2$ ($c = 1.00$ in EtOH). IR (ν_{\max} , cm⁻¹) 3405, 2916, 2850, 2361, 1469, 1090, 1072, 1053, 1008, 974, 950, 932, 717, 699, 654. ¹H NMR (400 MHz, CD₃OD) δ 3.92 (m, 1H), 3.57 (m, 1H), 3.35 (s, 1H), 2.84 (app p, $J = 6.2$ Hz, 1H), 1.91 (m, 2H), 1.63 (app t, $J = 6.4$ Hz, 1H), 1.51 (m, 2H), 1.30 (m, 18H), 1.13 (d, $J = 6.0$ Hz, 3H), 0.902 (t, $J = 6.8$ Hz, 3H). ¹³C NMR (100 MHz, CD₃OD) δ 125.9 (t, $J = 243.3$ Hz), 72.4, 70.1 (t, $J = 29.0$ Hz), 53.2, 35.0, 33.9 (t, $J = 24.5$ Hz), 33.2, 31.0, 30.9 (2C), 30.8 (2C), 30.7, 30.6, 23.9, 22.8, 18.6, 14.6. ¹⁹F NMR (376 MHz, CD₃OD) δ -108.0 (m, 1F), -111.4 (m, 1F). HRMS (APCI) $m/z = 338.28616$ (Theo. for C₁₈H₃₇F₂NO₂ + H: 338.28651). Anal. Calcd. for C₁₈H₃₇F₂NO₂: C, 64.06; H, 11.05; N, 4.15; F, 11.26. Found: C, 62.58; H, 10.70; N, 4.09; F, 10.10.

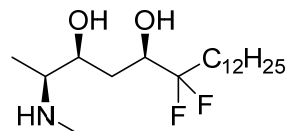


tert-butyl ((2*S*,3*S*,5*R*)-6,6-difluoro-3,5-dihydroxyoctadecan-2-yl)carbamate (**N-Boc**

CF₂-Engimol): Sodium bicarbonate (0.015 g, 0.181 mmol, 1.00 eq) was

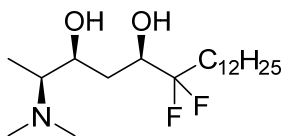
added to a flame-dried flask with a stir bar. A solution of CF₂-Enigmol (0.061 g, 0.181 mmol, 1.00 eq) in ethanol (3.61 mL) was added, and the resulting mixture was allowed to stir at room temperature under Ar. Added di-*tert*-butyl dicarbonate (0.039 g, 0.181 mmol, 1.00 eq), and the resulting mixture was allowed to stir under Ar at room temperature. After 1 hr, TLC indicated complete consumption of starting material to one major product. The reaction mixture was filtered over a fine fritted funnel, which was subsequently washed with thoroughly with MeOH. Solvent was evaporated under reduced pressure. The crude solid was purified via column chromatography eluting with 40:1 DCM/MeOH to yield a white solid (0.057 g, 0.130 mmol, 72% yield). $R_f = 0.40$ (40:1 DCM/MeOH); $R_f = 0.60$ (20:1 DCM/MeOH). Mp 80-82°C. $[\alpha]_D^{20} = -16.2$ ($c = 1.00$ in CHCl₃). IR (ν_{\max} , cm⁻¹) 3342, 2915, 2849, 2360, 1682, 1527, 1465, 1390, 1367, 1327, 1297, 1273, 1239, 1212, 1166, 1105, 1047, 1023, 976, 855, 808, 781, 761, 718, 657. ¹H NMR (300 MHz, CDCl₃) δ 4.65 (br s, 1H), 4.00 (m, 1H), 3.93 (m, 1H), 3.79 (m, 1H), 1.93 (m, 2H), 1.72 (m, 1H), 1.66 (m, 1H), 1.51 (m, 2H), 1.46 (s, 9H), 1.27 (m, 18H), 1.15 (d, $J = 7.2$ Hz, 3H), 0.888 (t, $J = 6.8$ Hz, 3H). ¹³C NMR (75 MHz, CDCl₃) δ 157.0, 123.9 (t, $J = 242.4$ Hz),

80.5, 75.7, 73.2 (t, $J = 29.0$ Hz), 51.6, 32.6 (t, $J = 23.6$ Hz), 32.1, 30.7, 29.8 (2C), 29.6 (4C), 29.6, 29.0, 28.5 (3C), 22.9, 21.6, 14.3. ^{19}F NMR (376 MHz, CDCl_3) δ -111.1 (m, 1F), -115.1 (m, 1F). HRMS (NSI) $m/z = 438.33858$ (Theo. for $\text{C}_{23}\text{H}_{45}\text{O}_4\text{NF}_2 + \text{H}$: 438.33894).



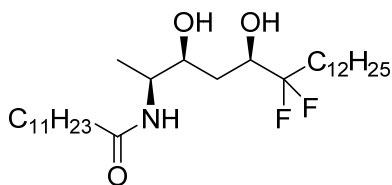
(2*S*,3*S*,5*R*)-6,6-difluoro-2-(methylamino)octadecane-3,5-diol (***N*-methyl CF_2 -**

Enigmol): A solution of *N*-Boc CF_2 -*Enigmol* (0.057 g, 0.130 mmol, 1.00 eq) in THF (11.84 mL) was added to a flame-dried microwave vial with a stir bar, and was stirred under Ar at room temperature. Added a solution of lithium aluminum hydride in THF (0.195 mL, 0.391 mmol, 3.00 eq) dropwise, and the resulting mixture was allowed to stir at room temperature under Ar for 15 min. The microwave vial cap was replaced with a fresh cap before placing the vial in the microwave for 5 min at 150°C. LC-MS (utilizing mini-workup) indicated complete conversion to the desired product. The reaction mixture was quenched very slowly at room temperature via dropwise addition of water, followed by the slow addition of dilute aqueous NaOH, followed by the slow addition of water. This mixture was extracted 3 times with EtOAc. Combined organic layers were washed once with brine, dried over Na_2SO_4 , filtered, and evaporated under reduced pressure to yield 65 mg of a white solid. The crude solid was purified via column chromatography eluting with 20:1:0.3 DCM/MeOH/ NEt_3 to yield a yellowish white solid, which was triturated with hexanes and Et_2O to yield pure white solid (0.027 g, 0.077 mmol, 59% yield). $R_f = 0.25$ (30:1:0.3 DCM/MeOH/ NEt_3); $R_f = 0.32$ (20:1:0.3 DCM/MeOH/ NEt_3). Mp 60-62°C. $[\alpha]_{\text{D}}^{20} = +18.7$ ($c = 0.500$ in CHCl_3). IR (ν_{max} , cm^{-1}) 3456, 3285, 2964, 2919, 2851, 1465, 1372, 1349, 1280, 1225, 1185, 1154, 104, 1079, 1040, 1007, 983, 968, 930, 885, 824, 790, 723, 702, 656. ^1H NMR (400 MHz, CDCl_3) δ 4.13 (m, 1H), 3.97 (m, 1H), 3.56 (m, 1H), 2.87 (m, 1H), 2.53 (s, 3H), 1.95 (m, 2H), 1.77 (m, 2H), 1.50 (m, 2H), 1.27 (m, 18H), 1.16 (m, 3H), 0.890 (t, $J = 6.4$ Hz, 3H). ^{13}C NMR (75 MHz, CDCl_3) δ 124.4 (t, $J = 242.7$ Hz), 71.4, 71.2 (t, $J = 29.6$ Hz), 62.7, 58.8, 33.2, 32.9, 32.1, 31.6, 29.8 (2C), 29.7 (3C), 29.6 (2C), 22.9, 21.6, 13.6. ^{19}F NMR (376 MHz, CDCl_3) δ -110.1 (m, 1F), -115.1 (m, 1F). HRMS (NSI) $m/z = 352.30209$ (Theo. for $\text{C}_{19}\text{H}_{39}\text{O}_2\text{NF}_2 + \text{H}$: 352.30216).



(2*S*,3*S*,5*R*)-2-(dimethylamino)-6,6-difluorooctadecane-3,5-diol (*N,N*-dimethyl

CF₂-Enigmol): CF₂-Enigmol (0.075 g, 0.222 mmol, 1.00 eq) was added to a flask with a stir bar, diluted with a solution of sodium acetate (0.576 g, 7.02 mmol, 31.6 eq) in water (4.12 mL) and acetic acid (0.412 mL), and stirred at room temperature until maximum solubility was achieved. Formaldehyde (37% wt. in H₂O, 0.830 g, 10.22 mmol, 46.0 eq) was added, and the resulting mixture was allowed to stir at room temperature for 30 min. Sodium cyanoborohydride (0.102 g, 1.62 mmol, 7.30 eq) and MeOH (1.03 mL, 25.5 mmol, 113 eq) were added in succession, and the resulting mixture was allowed to stir at room temperature for 2 hrs. Once starting material was undetectable by LC-MS, the reaction mixture was diluted with diethyl ether and basified with saturated aqueous sodium bicarbonate (to pH = 8-9). This aqueous layer was subsequently extracted once with diethyl ether. Combined organic layers were washed once with saturated aqueous sodium bicarbonate, washed once with brine, dried over MgSO₄, filtered, and evaporated under reduced pressure. The crude material was purified via column chromatography eluting with 40:1:0.3 DCM/MeOH/NEt₃ to yield a clear oil/white solid (0.049 g, 0.134 mmol, 60% yield). R_f = 0.30 (50:1:0.3 DCM/MeOH/NEt₃); R_f = 0.39 (40:1:0.3 DCM/MeOH/NEt₃). Mp 38-40°C. [α]_D²⁰ = +4.4 (c = 1.00 in CHCl₃). IR (ν_{max}, cm⁻¹) 3425, 2957, 2920, 2851, 2692, 1468, 1376, 1338, 1272, 1212, 1132, 1099, 1035, 1008, 971, 942, 930, 881, 803, 771, 720, 689, 640. ¹H NMR (400 MHz, CDCl₃) δ 4.03 (app dd, *J* = 6.2 Hz, *J* = 10.4 Hz, 1H), 3.95 (m, 1H), 2.63 (p, *J* = 6.6 Hz, 1H), 2.36 (s, 6H), 1.95 (m, 2H), 1.87 (m, 1H), 1.84 (m, 1H), 1.52 (m, 2H), 1.26 (m, 18H), 1.11 (d, *J* = 6.8 Hz, 3H), 0.885 (t, *J* = 6.6 Hz, 3H). ¹³C NMR (75 MHz, CDCl₃) δ 124.3 (t, *J* = 243.0 Hz), 71.8, 70.6 (t, *J* = 29.6 Hz), 63.3, 41.4 (2C), 34.1, 32.8 (t, *J* = 24.2 Hz), 32.1, 29.8 (4C), 29.7 (3C), 29.5, 22.9, 21.7, 14.3. ¹⁹F NMR (376 MHz, CDCl₃) δ -111.0 (m, 1F), -115.2 (m, 1F). HRMS (NSI) *m/z* = 366.31764 (Theo. for C₂₀H₄₁O₂NF₂ + H: 366.31781).



N-((2*S*,3*S*,5*R*)-6,6-difluoro-3,5-dihydroxyoctadecan-2-yl)dodecanamide

(CF₂-Enigmol C₁₂-Ceramide): CF₂-Enigmol (0.050 g, 0.148 mmol, 1.00 eq) was added to a flame-dried flask with a stir bar.

The solid was diluted with THF (3.53 mL), cooled to 0°C, and stirred under Ar. *N*-ethyl-*N*-isopropylpropan-2-amine (0.020 g, 0.156 mmol, 1.05 eq) was added, and was followed by the dropwise addition of dodecanoyl chloride (0.03 g, 0.156 mmol, 1.05 eq). The resulting mixture was stirred under Ar at 0°C for 5 min, and subsequently allowed to warm to room temperature. After 1 hr, the starting material was not visible by TLC. The reaction mixture was diluted with DCM and washed twice with H₂O. The resulting organic layer was washed twice with brine, dried over MgSO₄, filtered, and evaporated under reduced pressure. The crude material was purified via column chromatography eluting with 1:30 DCM/MeOH, followed by precipitation with Et₂O and hexanes to yield a white solid (0.024 g, 0.046 mmol, 31% yield). $R_f = 0.11$ (1:6 EtOAc/Hex); $R_f = 0.23$ (1:4 EtOAc/Hex); Mp 63-65°C. $[\alpha]_D^{20} = -15.7$ ($c = 1.00$ in CHCl₃). IR (ν_{\max} , cm⁻¹) 3260, 3089, 2955, 3916, 2847, 2360, 1739, 1627, 1579, 1468, 1438, 1384, 1266, 1237, 1205, 1171, 1145, 1084, 1042, 1024, 1011, 976, 931, 797, 721, 632. ¹H NMR (400 MHz, CDCl₃) δ 5.62 (d, $J = 8.4$ Hz, 1H), 4.90 (app q, $J = 4.4$ Hz, 1H), 4.38 (app q, $J = 7.6$ Hz, 1H), 3.88 (m, 1H), 2.35 (t, $J = 7.6$ Hz, 2H), 2.18 (m, 2H), 2.03 (app dd, $J = 4.4$ Hz, $J = 14.4$ Hz, 1H), 1.94 (m, 2H), 1.78 (m, 1H), 1.63 (m, 3H), 1.50 (m, 2H), 1.27 (m, 31H), 1.14 (d, $J = 6.4$ Hz, 3H), 0.887 (t, $J = 6.6$ Hz, 6H). ¹³C NMR (75 MHz, CDCl₃) δ 173.9, 127.6 (t, $J = 244.2$ Hz), 74.5, 73.2, 69.7 (t, $J = 27.9$ Hz), 46.9, 37.1, 34.7, 32.8, 32.1, 30.3, 29.8 (4C), 29.7 (4C), 29.5 (4C), 29.4, 25.9, 25.2, 22.9, 21.7, 16.3, 14.3. ¹⁹F NMR (376 MHz, CDCl₃) δ -110.6 (m, 1F), -115.7 (m, 1F). HRMS (APCI) $m/z = 520.45569$ (Theo. for C₃₀H₅₉O₃NF₂ + H: 520.45358).

1.4.b. *cLogP Calculations*

cLogP calculations were performed using Maestro³⁰ within the 2015 Schrödinger Small Molecule Drug Discovery Suite. Each chemical structure was built in ChemDraw, saved as a .sdf file, and imported into Maestro as a two-dimensional compound lacking nonpolar hydrogen atoms. Each compound was then prepared using the LigPrep⁶⁸ application, which added nonpolar hydrogens, added charges where appropriate at pH = 7.4 ± 0.2 (protonated amine), and generated all possible

stereoisomers. Once the proper stereoisomers were selected, physicochemical properties, including $d\text{LogP}$ values, were computed using the QikProp²⁹ application.

1.4.c. Human Prostate Cancer Cell Viability Assays

LNCAp and PC3 human prostate cancer cells (American Type Culture Collection, Rockville, MD) were cultured in RPMI-1640 medium (Cellgro, Manassas, VA) supplemented with 10% fetal bovine serum (FBS, Atlanta Biologics). Each cell line tested negative for mycoplasma prior to use in these studies. Sphingoid base analogs were formulated as 1:1 molar complexes with fatty-acid free BSA, as previously described⁹. Briefly, stock solutions of analogs in ethanol (50 mM) were diluted with a 2 mM solution of fatty-acid free BSA in phosphate-buffered saline (PBS) that had been sterile-filtered and pre-warmed to 37°C. BSA-drug complexes were vortexed and incubated at 37°C for 1 hr before use. PC3 or LNCAp cells were seeded in 96-well culture plates at densities that yielded 70% confluence the next day (10,000 cells/well and 15,000 cells/well, respectively). After adhering overnight, cells were treated with increasing concentrations of BSA-drug complexes (or the same concentrations of BSA + ethanol) for 24 hrs. Treatments were performed in triplicate, and each compound was assayed three times with each cell type. After 24 hr incubation, 10 μL WST-1 reagent (Roche) was added to each well, and plates were incubated at 37°C for 1 hr. Absorbance was measured at 450 nm with a reference wavelength of 690 nm. Baseline luminescence was measured before assay and subtracted from these data, which were subsequently normalized to BSA treatment. Concentration response curves were generated using Graphpad Prism software, and IC_{50} and IC_{90} values were calculated via nonlinear regression using a four parameter logistic equation.

1.4.d. Rat Plasma Pharmacokinetic Assays (*i.v.*)

All animal studies were performed in accordance with the guidelines of the Institutional Animal Care and Use Committee at Emory University. Male jugular pre-cannulated SD rats (250-300 g, Charles River Laboratories or Harlan Laboratories) were acclimated for at least 2 days upon receipt

before experiments were conducted. Rats were weighed the day before dosing to determine the dose and volume for each subject. Each animal was infused intravenously with 2 mg/kg (1 mg/mL) Enigmol (n = 3), CF₃-Enigmol (n = 4), or CF₂-Enigmol (n = 4) at a rate of 50 μ L/s in a vehicle comprised of PEG400/EtOH/Tween80/H₂O (40:10:3:47). During experiments, ample food was left in each cage. Blood samples (0.3 mL) were removed at 8 or 9 time points up until 8 hrs after administration, and these samples were immediately transferred to either K EDTA or Li-Heparin tubes and stored in ice water for a maximum of 1 hr. Plasma was then isolated from each blood sample via refrigerated centrifugation at 2000 g for 10 min, followed by transfer of 200 μ L supernatant to an Eppendorf tube in ice water, freezing on dry ice, and storage at -80°C until LC-MS/MS analysis. Bioanalytical LC-MS/MS assay protocol and specifications are described in a separate methods section. The pharmacokinetic parameters (T_{max} , C_{max} , $t_{1/2}$, AUC_{0-t} , and Cl) represent the mean (\pm S.E.M.) values for all subjects in a particular group. For each rat, T_{max} and C_{max} were directly extracted from the raw data, AUC_{0-t} was calculated using GraphPad Prism software, and Cl was calculated using the following equation: $Cl = Dose / AUC_{0-t}$. Additionally for each rat, terminal $t_{1/2}$ was calculated ($t_{1/2} = \ln 2/k$) using Excel by finding the slope (-k) of a linear fit to the semi natural logarithmic plot ($\ln[Drug]$ in plasma vs. time) of data points after T_{max} . For each rat, decisions concerning the number of terminal phase data points to use for each linear fit and subsequent $t_{1/2}$ calculation were based on the best obtained fits (R^2 values, # points ≥ 3 , negative slope).

1.4.e. Rat Plasma Pharmacokinetic Assays (p.o.)

Male jugular pre-cannulated SD rats (250-300 g, Harlan Laboratories) were acclimated for at least 2 days upon receipt before experiments commenced. Rats were weighed the day before dosing to determine the exact dose and volume for each subject. Each animal was dosed via oral gavage with 10 mg/kg (2 mg/mL) Enigmol (n = 4), CF₃-Enigmol (n = 4), or CF₂-Enigmol (n = 4) in a vehicle comprised of either 90:10 olive oil/EtOH or 95:5 PEG400/Tween80. During experiments, ample food was left in each cage, and blood samples (0.3 mL) were removed at 10 time points up until 24 hrs

after administration. Blood samples were immediately transferred to Li-Heparin tubes and stored in ice water for a maximum of 1 hr. Plasma was then isolated from each blood sample via refrigerated centrifugation at 2000 g for 10 min, followed by transfer of 200 μ L supernatant to an Eppendorf tube in ice water, freezing on dry ice, and storage at -80°C until LC-MS/MS analysis. Bioanalytical LC-MS/MS assay protocol and specifications are described in a separate section. The pharmacokinetic parameters (T_{max} , C_{max} , AUC_{0-t} , and %F) represent the mean (\pm S.E.M.) values for all subjects in a particular group. For each rat, T_{max} and C_{max} were directly extracted from the raw data, and AUC_{0-t} was calculated using GraphPad Prism software. With AUC_{0-t} determined after both 10 mg/kg p.o. ($\text{AUC}_{0-t}^{\text{p.o.}}$) and 2 mg/kg i.v. ($\text{AUC}_{0-t}^{\text{i.v.}}$) administration, %F was calculated using the following equation: $\%F = 100 * [\text{AUC}_{0-t}^{\text{p.o.}} / (5 * \text{AUC}_{0-t}^{\text{i.v.}})]$. Additionally for each rat, terminal $t_{1/2}$ was calculated ($t_{1/2} = \ln 2 / k$) using Excel by finding the slope ($-k$) of a linear fit to the semi natural logarithmic plot ($\ln[\text{Drug}]$ in plasma vs. time) of data points after T_{max} . For each rat, decisions concerning the number of terminal phase data points to use for each linear fit and subsequent $t_{1/2}$ calculation were based on the best obtained fits (R^2 values, # points ≥ 2 , negative slope). Due to long absorption phases, clean exponential decay of drug concentration in plasma was not observed for every subject, making $t_{1/2}$ calculations more cumbersome than they were after i.v. administration. The $t_{1/2}$ values reported were calculated with the exclusion of one rat from the CF₂-Enigmol group because linear fits to the last 2 or 3 points exhibited positive slopes. While the linear fit to the last 4 points displayed a negative slope, the fit was particularly poor ($R^2 = 0.038$).

1.4.f. Rat Tissue Distribution Assays (p.o.)

Male jugular pre-cannulated SD rats (250-300 g, Harlan Laboratories) that were dosed via oral gavage with either 10 mg/kg Enigmol ($n = 4$), CF₃-Enigmol ($n = 4$), or CF₂-Enigmol ($n = 4$) for plasma pharmacokinetic experiments were euthanized 24 hrs after dosing via CO₂ asphyxiation. Red blood cells (RBC), brain, lung, liver, kidney, and prostate were harvested from each subject, transferred to culture tubes, frozen on dry ice, and stored at -80°C until LC-MS/MS analysis. Bioanalytical LC-

MS/MS assay protocol and specifications are described in a separate section. Reported drug concentrations in tissue represent the mean (\pm S.E.M.) values for all subjects in a particular group.

1.4.g. Mouse Xenograft Studies

Male nude mice (Athymic NCr-*nu/nu*, 5 weeks old) were purchased from the NCI and acclimated for at least 2 days upon receipt before experiments commenced. PC3 cells were plated on 10 cm tissue culture dishes and grown in 10% FBS-supplemented RPMI-1640 medium until 90% confluency was achieved. Cultured cells were then detached from tissue culture dishes via addition of trypsin, suspensions from all dishes were combined into a 50 mL centrifuge tube, and cells were counted using a hemocytometer. Harvested cells were spun down and resuspended in 20 mL serum-free RPMI-1640. Each mouse was anesthetized via intraperitoneal injection (100-150 μ L depending on body mass) of a mixture of ketamine (0.045 M) and xylazine (0.0078 M). Tumors were then initiated via subcutaneous injection of suspended PC3 cells (2×10^6 cells per mouse in 200 μ L) between the scapulae of each mouse. Once tumors were established (16 days or 22 days for CF₃-Enigmol and CF₂-Enigmol xenograft studies, respectively), mice were divided into 5 groups such that mean and standard deviation of tumor volumes were as evenly distributed as possible ($n = 10$ or 11 mice per group). During the CF₃-Enigmol xenograft study, mice were treated once daily via oral gavage (200 μ L) with either vehicle (95:5 olive oil/EtOH), Enigmol (3 mg/kg or 10 mg/kg) or CF₃-Enigmol (3 mg/kg or 10 mg/kg); for the xenograft study involving CF₂-Enigmol, mice were administered either vehicle (95:5 PEG400/Tween80), Enigmol (10 mg/kg), or CF₂-Enigmol (10 mg/kg or 30 mg/kg) via once daily oral gavage (200 μ L). For both experiments, drug formulations were freshly prepared each day prior to dosing. During the treatment period, tumor volumes were measured in two dimensions (Volume = $\frac{1}{2} \times \text{Length} \times \text{Width}^2$) every 2-3 days with digital calipers. Changes in body masses were also measured every 2-3 days ($\Delta \text{Mass} = \text{Mass} - \text{Mass}_{\text{initial}}$) both to ensure accurate dosing amounts and as an indication of systemic toxicity. Notably, two mice died before the end of the CF₂-Enigmol xenograft study, one from the control group (day 32) and one from the 10 mg/kg Enigmol group (day 36). All mice were

sacrificed via CO₂ asphyxiation once excessive tumor burden was reached (17 days or 16 days after dosing initiation for CF₃-Enigmol and CF₂-Enigmol xenograft studies, respectively). Significance of tumor growth inhibition between groups was determined using linear mixed models for repeated measurements with autoregressive covariance structure, conducted with Statistical Analysis System (SAS) software. Significance of weight change between control and treatment groups was determined by one-way ANOVA followed by Sidak's multiple comparison test (GraphPad Prism software). $P < 0.05$ was considered statistically significant. Finally, tumors were harvested 24 hrs after the last oral gavage from 4 mice in each treatment group, and the harvested tumors were stored at -80°C until LC-MS/MS analysis.

1.4.h. Bioanalytical LC-MS/MS Assay

Plasma samples (collected after i.v. or p.o. drug administration) or tissue samples (collected from RBC, brain, lung, liver, kidney, prostate, or tumor after p.o. drug administration) were allowed to thaw and equilibrate to room temperature before beginning LC-MS/MS sample preparation. Plasma samples (50 µL) or tissue samples (50 mg) were diluted with 930 µL or 900 µL methanol, respectively (for protein precipitation), and combined with 20 µL internal standard solution containing either *D*-erythro-C₁₇-sphinganine (for Enigmol and CF₃-Enigmol) or CF₃-Enigmol (for CF₂-Enigmol). Resulting plasma samples were vortexed for 5 min and refrigeration-centrifuged at 3000 rpm for 10 min; resulting tissue samples were homogenized and refrigeration-centrifuged at 13200 rpm for 10-15 min until supernatants were clear. Supernatants were then pipetted into HPLC vials, and drug concentrations were subsequently determined via LC-MS/MS analysis using an Agilent 1200 Series HPLC (binary pump) equipped with a Dionex Polar Advantage II column (50 mm x 3.0 mm, 3 µm) and either an AB SCIEX API5500 QTRAP mass spectrometer (for Enigmol and CF₃-Enigmol, spray voltage ≈ 4000 V, 10-1000 ng/mL detection limit) or with an AB SCIEX API4000 mass spectrometer (for CF₂-Enigmol, spray voltage ≈ 2200 V, 10-10000 ng/mL detection limit). Threshold ionization (TIS) mass spectrometry was utilized to detect the corresponding ammonium ions (M + H) for

Enigmol ($m/z = 302.3$), CF₃-Enigmol ($m/z = 356.3$), and CF₂-Enigmol ($m/z = 338.2$). Samples containing Enigmol (rt = 2.5 min) and CF₃-Enigmol (rt = 1.5 min) were evaluated using an isocratic method (70:30 MeOH/H₂O, 0.1% formic acid, 5 min, 30°C, 0.6 mL/min, 3 µL injection volume), while those containing CF₂-Enigmol were analyzed using a slightly different isocratic method (70:30 MeOH/H₂O, 0.1% formic acid, 5 min, 30°C, 0.5 mL/min, 4 µL injection volume). Finally, extracted ion counts were converted to drug concentrations using Analyst software package, based on calibration curves generated to correlate ion count and drug concentration.

Part 2. Preferential Activation of Metabotropic Glutamate Receptor 3 over Metabotropic Glutamate Receptor 2

2.1. Introduction

2.1.a. Seven-Transmembrane Receptors and G Protein Coupling

Roughly one third of all FDA-approved drugs target seven-transmembrane receptors (7TMRs), the largest class of integral membrane proteins, which initiate intracellular signaling cascades in response to extracellular stimuli. Each type of these membrane-bound receptors selectively detects and functionally reacts to specific endogenous ligands⁶⁹, including proteins, peptides, nucleotides, amino acids, and photons, and 7TMRs are consequently essential to many aspects of human physiology. Particularly notable are the roles of 7TMRs in neurological function⁷⁰, by which information in the form of neurotransmitters, such as dopamine, serotonin, epinephrine, acetylcholine, and glutamate, is processed. According to the currently accepted model of 7TMR activation (**Figure 13**), an extracellular agonist binds to a receptor (**1**), thereby stabilizing an active 7TMR conformation⁷¹, which initiates intracellular signal transduction at the inner leaflet of the plasma membrane mediated by heterotrimeric G proteins. The activated 7TMR then undergoes (**2**) desensitization via G protein-coupled receptor kinase-mediated phosphorylation⁷² of several serine, threonine, and/or tyrosine residues located on intracellular portions of the receptor. Next, β -arrestin binds to the phosphorylated regions of the desensitized receptor⁷³, and the agonist-7TMR- β -arrestin complex (**3**) clusters into clathrin-coated pits (CCPs), where β -arrestin-mediated signaling events have been reported to occur after activation of several 7TMR subtypes⁷⁴. Endocytosis subsequently commences with dynamin-facilitated vesicle fission, by which the receptor is fully internalized (**4**) into a clathrin-coated endosome⁷⁵. Once the endosome is uncoated (**5**), the receptor becomes resensitized via G protein-coupled receptor phosphatase activity⁷⁶, and uncoated endosomes either (**6**) recycle the receptor back to the plasma membrane or (**7**) traffic the receptor to the lysosome for degradation. Interestingly,

intracellular signaling events initiating from endosomal membranes after agonist-mediated activation of several 7TMR subtypes have additionally been reported recently⁷⁷.

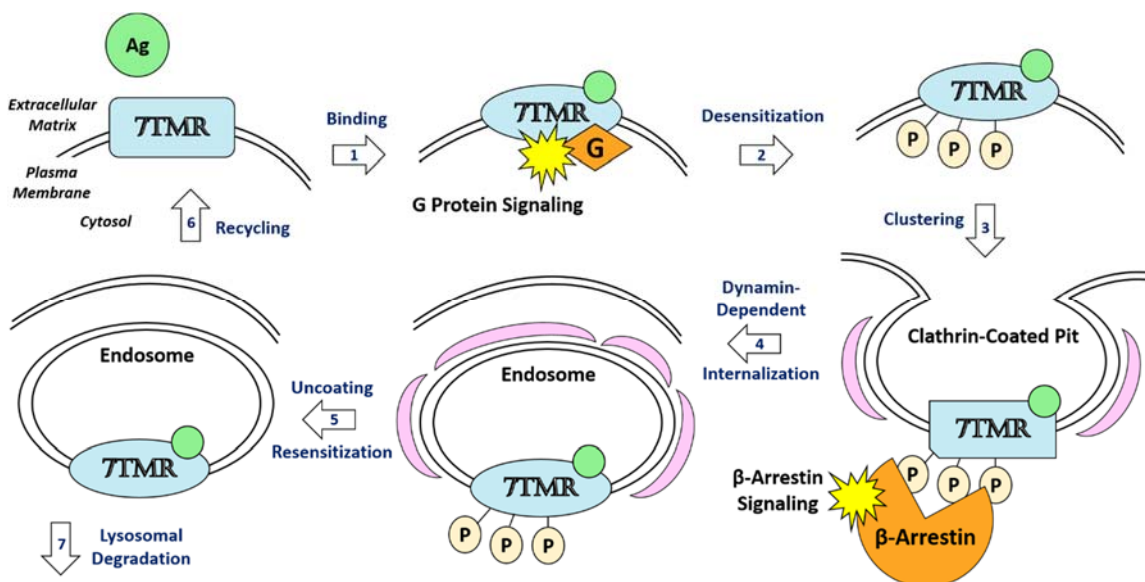


Figure 13: Current Model of 7TMR Activation. The seven-transmembrane receptor (7TMR) activation cycle involves (1) agonist (Ag) binding and subsequent G protein (G) signaling, (2) receptor desensitization via phosphorylation (P), (3) clustering into clathrin-coated pits where β -Arrestin signaling can occur, (4) internalization into endosomes, (5) endosome uncoating and receptor resensitization, and either (6) receptor recycling or (7) receptor degradation.

While agonist stabilization of active 7TMR conformations can also lead to signaling events facilitated by intracellular effector proteins other than G proteins or β -arrestin⁷⁸, G protein coupling is the primary and most well-characterized mechanism of 7TMR-mediated signal transduction. G proteins are heterotrimeric guanine nucleotide-binding GTPases that consist of α , β , and γ subunits, as illustrated by the G protein structure extracted from the first resolved x-ray crystal structure of a 7TMR-G protein complex⁷⁹ (**Figure 14a**). G protein activity is regulated (1) via interaction of intracellular 7TMR motifs with $G\alpha$ subunits, of which there are four principal isoforms⁷⁸ ($G\alpha_q$, $G\alpha_{i/o}$, $G\alpha_s$, and $G\alpha_{12/13}$), and (2) by enzyme-mediated exchange of guanosine diphosphate (GDP) and guanosine triphosphate (GTP), both of which bind at the cleft between $G\alpha$ subunit helical bundles⁷⁹. When GDP is bound, the G protein rests in an inactive state until a guanine nucleotide exchange factor

(GEF) catalyzes the displacement of GDP and replacement with GTP (**Figure 14b**). G protein activation then occurs via dissociation of the GTP-bound $G\alpha$ subunit from the $G\beta\gamma$ complex, after which both $G\alpha$ -GTP and $G\beta\gamma$ transduce intracellular signals to various downstream proteins, including kinases, lipases, and ion channels. G protein signaling ensues until GTPase-activating protein (GAP)-catalyzed hydrolysis of GTP to GDP, which not only deactivates the $G\alpha$ subunit, but also accelerates the reassociation of $G\alpha$ -GDP and $G\beta\gamma$. This guanine nucleotide exchange cycle, which is modulated by the specific interaction of each 7TMR type with predominantly $G\alpha_q$, $G\alpha_{i/o}$, $G\alpha_s$, or $G\alpha_{12/13}$ subunits, serves as a switch by which to turn G protein activity on and off.

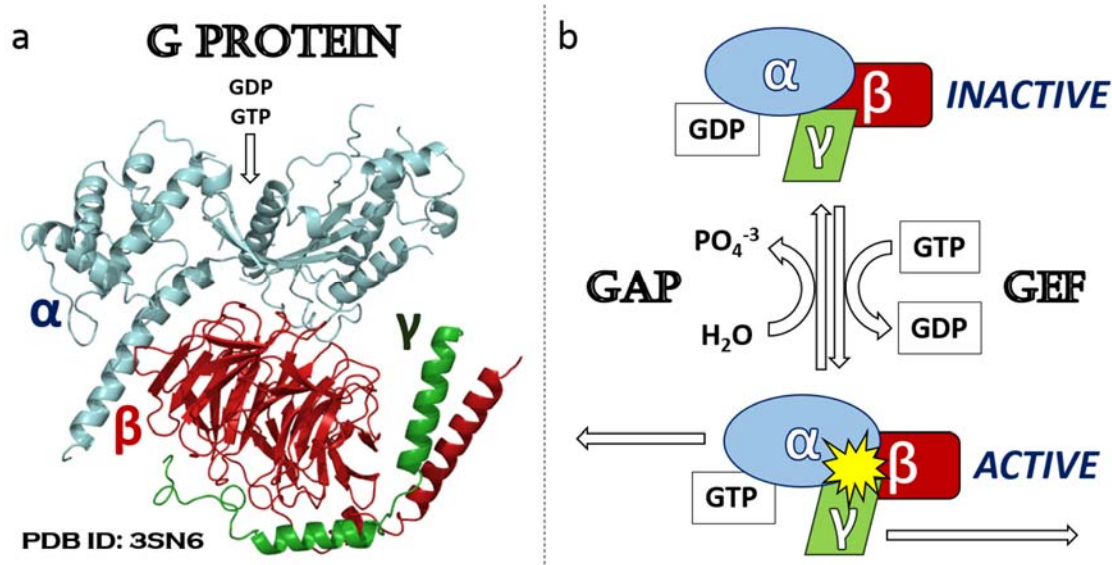


Figure 14: G Protein Activation Cycle. (a) Depiction of a heterotrimeric G protein, which contains α (red), β (blue), and γ (green) subunits, as extracted from the first x-ray structure of a 7TMR-G protein complex⁷⁹. PyMOL⁸⁰ was employed for figure generation. (b) Schematic representation of the G protein activation cycle, which is regulated not only by interaction with 7TMRs, but also by guanine nucleotide exchange factor (GEF)-mediated and GTPase-activating protein (GAP)-mediated activity.

Although the majority of the > 800 members of the 7TMR family identified in the human genome⁷⁴ all couple to G proteins with specificity for one of four $G\alpha$ subunits, 7TMRs are organized into three major classes based on sequence homology and structural similarity⁸¹. Class A 7TMRs are the most thoroughly characterized class, which comprises rhodopsin-like receptors such as dopamine,

serotonin, adrenergic, muscarinic, sphingosine-1-phosphate, and chemokine receptors. Secondly, class B is known as the secretin family of receptors, which contains glucagon receptors, parathyroid hormone receptors, calcitonin receptors, etc. Thirdly, class C 7TMRs include GABA_B, Ca⁺²-sensing, and taste receptors, as well as metabotropic glutamate receptors (mGluRs). While each 7TMR type exhibits a transmembrane domain that consists of seven α -helices connected by three intracellular loops and three extracellular loops (**Figure 15**), structures of extracellular *N*-terminal domains (NTDs), intracellular *C*-terminal domains (CTDs), and orthosteric ligand binding domains vary substantially between classes. For example, x-ray crystallographic analysis of the β_2 -adrenergic receptor⁸² (β_2 AR), a prototypical class A 7TMR, illustrated a relatively short and simple NTD (**Figure 15a**), as compared to the particularly large and complex NTD exhibited by mGluR3⁸³ (**Figure 15c**), a representative class C 7TMR. Similarly, class A CTDs, as exemplified by the β_2 AR CTD (**Figure 15a**), are also quite small compared to class C CTDs (**Figure 15c**). Class C 7TMRs are also uniquely equipped with a cysteine-rich domain (CRD) that includes several intramolecular disulfide bridges (**Figure 15c**). Orthosteric ligand binding domains also differ significantly between 7TMR classes. For instance, while endogenous class A 7TMR ligands, such as epinephrine, bind to class A 7TMRs, such as β_2 AR, within the 7TMD amidst the heptahelical bundle (**Figure 15b**), physiological class C ligands, such as glutamate, bind to class C 7TMRs, such as mGluR3, at the hinge region of the clamshell-like NTD between the top and bottom lobes (**Figure 15c**). Thus, agonist binding to class A 7TMRs directly induces a conformational change in the 7TMD during receptor activation, whereas agonist binding to the clamshell-like class C NTD causes the top and bottom lobes to clamp down, which mechanically translates to a conformational change in the 7TMD via rearrangement of the CRD.

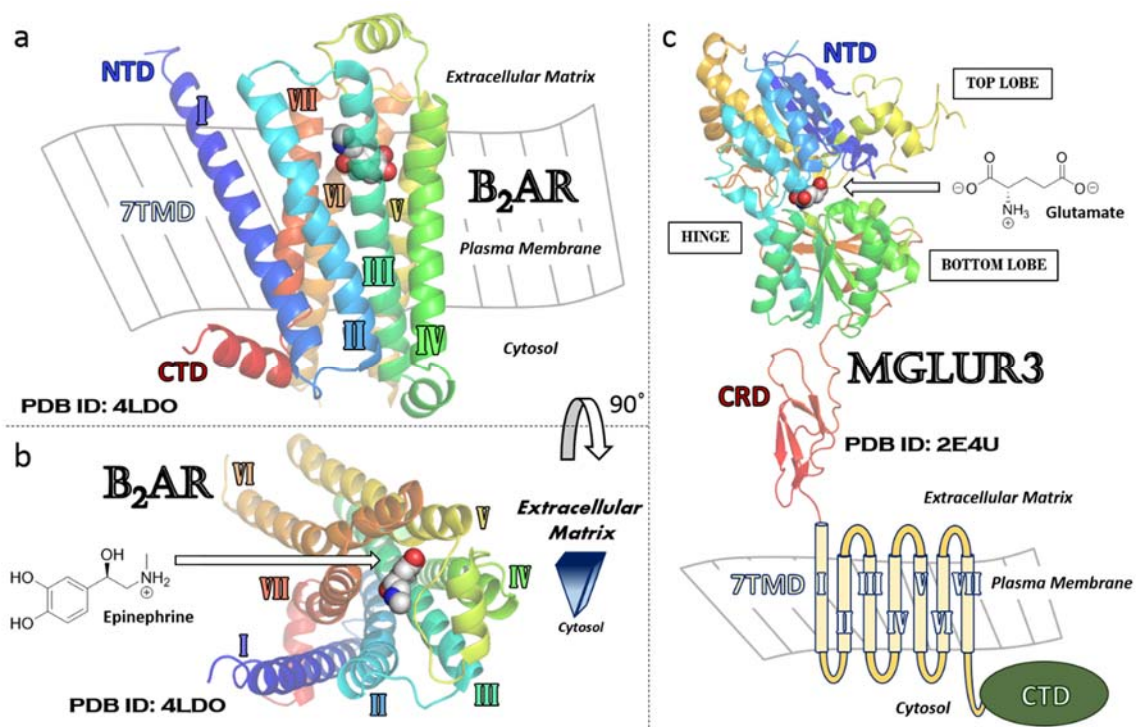


Figure 15: Structural Comparison of Class A (β_2 AR) and Class C (mGluR3) 7TMRs. (a) Depiction of an x-ray crystal structure of the β_2 -adrenergic receptor (β_2 AR) illustrates small class A 7TMR N-terminal and C-terminal domains (NTD and CTD, respectively) that are connected by a heptahelical seven-transmembrane domain (7TMD). (b) While endogenous class A 7TMR agonists, such as epinephrine, bind in the 7TMD, (c) class C 7TMRs, such as metabotropic glutamate receptor 3 (mGluR3) bind agonists, such as glutamate, in the clamshell-like NTD, as represented by x-ray crystal structure of the mGluR3 NTD⁸³. Although class C 7TMRs exhibit 7TMDs similar to those of class A 7TMRs, class C 7TMRs exhibit large NTDs and CTDs, and additionally incorporate an extracellular cysteine-rich domain (CRD). PyMOL⁸⁰ was employed for figure generation.

2.1.b. Metabotropic Glutamate Receptors

While the earliest 7TMR to be isolated, the β_1 -adrenergic receptor, was purified in the early 1980s⁸⁴, the first mGluR was discovered in the mid to late 1980s with the observation that glutamate stimulated phosphatidylinositol hydrolysis in oocytes injected with mRNA that was isolated from rat brain⁸⁵. To date, eight mGluR subtypes, which are organized into three groups according to sequence

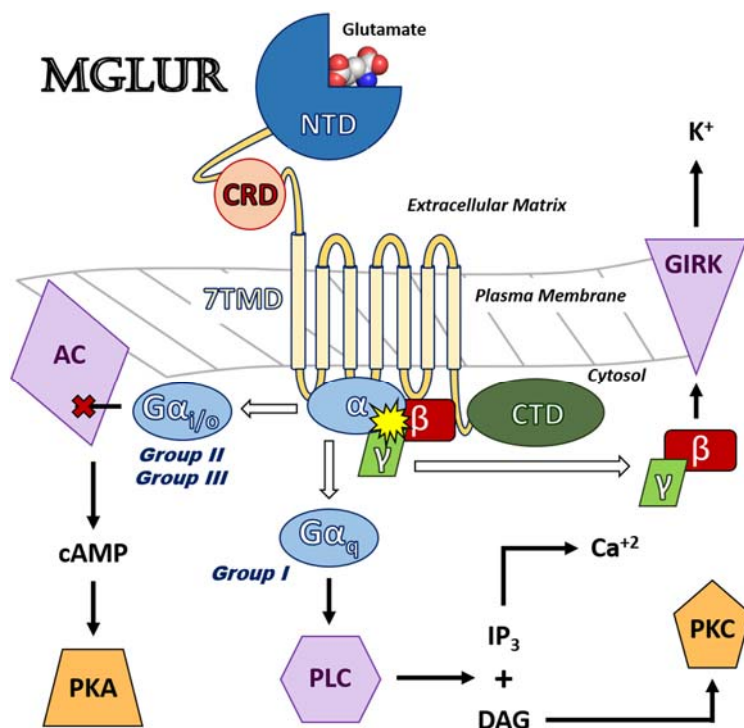


Figure 16: mGluR-Mediated G Protein Signaling. G α_q proteins stimulate phospholipase C (PLC) activity leading to generation of phosphatidylinositol 4,5-bisphosphate (IP₃), which causes release of intracellular calcium stores, and diacyl glycerol (DAG), which activates protein kinase C (PKC). G $\alpha_{i/o}$ proteins inhibit adenylyl cyclase (AC) leading to reduction of intracellular cAMP levels and protein kinase A (PKA) activity. G $\beta\gamma$ stimulates G protein-regulated inwardly rectifying potassium channel (GIRK)-mediated potassium efflux.

homology, pharmacology, and signal transduction, have been characterized⁸⁶. Group I includes mGluR1 and mGluR5, group II encompasses mGluR2 and mGluR3, and group III contains mGluR4, mGluR6, mGluR7, and mGluR8. Group I mGluRs predominantly couple to G α_q subunit-containing G proteins (**Figure 16**), which results in the stimulation of phospholipase C (PLC)-mediated hydrolysis of phosphatidylinositol 4,5-bisphosphate, generating diacyl glycerol (DAG) and inositol 1,4,5-trisphosphate (IP₃). While water-soluble IP₃ then translocates to the endoplasmic reticulum where it binds to the IP₃ receptor causing the release of intracellular calcium stores, highly lipophilic DAG remains within the plasma membrane and activates PKC. In contrast, group II and group III mGluRs selectively couple to G proteins equipped with the G $\alpha_{i/o}$ subunit, which, upon dissociation from the G $\beta\gamma$ complex, inhibits adenylyl cyclase (AC). This, in turn, reduces intracellular concentrations of cyclic

adenosine monophosphate (cAMP), and protein kinase A (PKA) activity consequently decreases. Although $G\beta\gamma$ -mediated signaling is less well-characterized than $G\alpha$ -mediated signaling, activation of mGluRs has been demonstrated to result in $G\beta\gamma$ -dependent efflux of potassium via G protein-regulated inwardly rectifying potassium channel⁸⁷ (GIRK) stimulation.

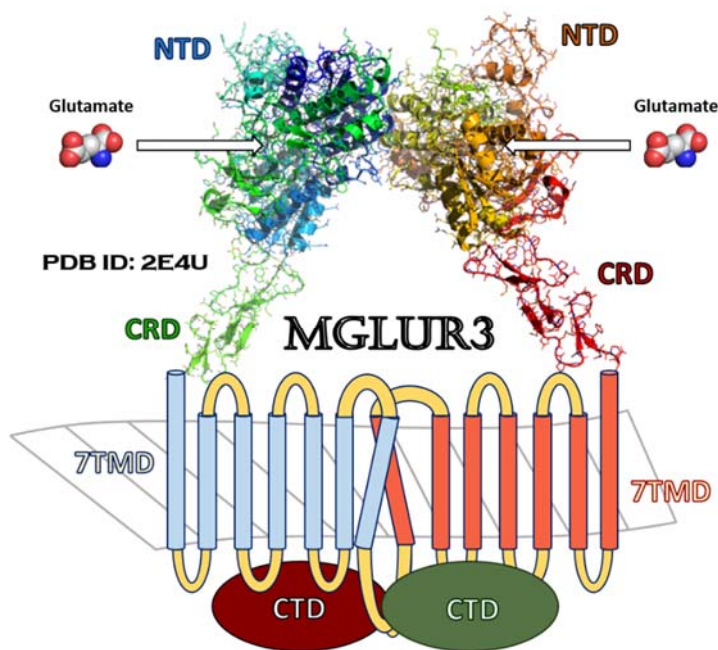


Figure 17: Homodimeric Arrangement of mGluRs. mGluRs signal through G proteins via a homodimeric organization that exhibits maximal activation when glutamate is bound to each NTD. PyMOL⁸⁰ was employed for figure generation.

In addition, all mGluR subtypes are thought to function predominantly as homodimers⁸³ (**Figure 17**), which achieve full G protein activation potential upon orthosteric binding of one glutamate molecule, or one molecule of another competitive agonist, to each protomer⁸⁸. Although glutamate and cyclopropyl analog CCG (**Table 8**) are relatively nonselective between mGluR isoforms, numerous group-selective, competitive agonists and antagonists have been discovered. For instance, mGluR1, mGluR2, and mGluR4 were originally distinguished based on selective activation by heterocyclic analog quisqualate⁸⁵, tricarboxylate DCG-IV⁸⁹, and phosphonate AP4⁹⁰, respectively, each of which is more potent than glutamate at the corresponding subgroup of receptors. The next

generation of group-selective agonists included 3,5-DHPG⁹¹, LY354740⁹², and LSP1-3081⁹³ for group I, group II, and group III mGluRs, respectively. While the α -amino carboxylate motif is common to all of these pharmacological agents, glutamate is the only full mGluR agonist amongst the twenty essential amino acids, with the exception of aspartate and cysteine, which are functional in some cases

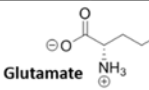
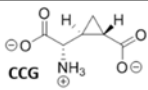
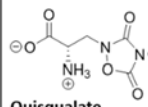
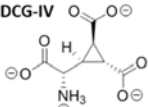
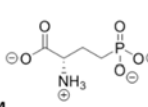
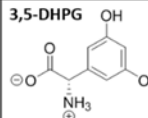
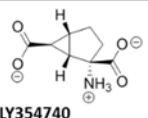
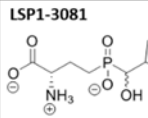
Ligand Type	Group I	Group II	Group III
Nonselective Agonists	 Glutamate	 CCG	
Original Selective Agonists	 Quisqualate	 DCG-IV	 AP4
Newer Selective Agonists	 3,5-DHPG	 LY354740	 LSP1-3081

Table 8: Group-Selectivity of Competitive mGluR Agonists. Rigidification of glutamate or bioisosteric replacement of the glutamate γ -carboxylate led to group-selective mGluR agonists.

but demonstrate poor potency⁹⁴. This indicates (1) the impressive receptor specificity for glutamate amidst the pool of endogenous amino acids, and (2) the requirement of a negatively ionizable functional group extending from the glutamate backbone. As the structural arrangement of the orthosteric binding site is highly conserved between mGluR subtypes, achieving group-selective mGluR activation has typically required the fine-tuning of ligand-receptor interactions by making small changes to the orientation of glutamate functional groups⁹⁵. This is further emphasized via structural comparison (**Table 9**) of the relatively nonselective antagonist LY341495⁹⁶ and LY367366, EGlu, and CPPG, which are group-selective, competitive antagonists for group I, group II, and group III, respectively⁹⁷. Although the bulky, lipophilic motifs extending from the α carbon vary substantially, the distal carboxylate or phosphonate motifs bind selectively to the appropriate mGluR orthosteric binding pockets with subtly different functional group orientations, in similar fashion to the corresponding group-selective agonists.

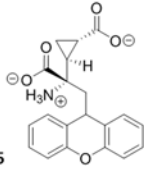
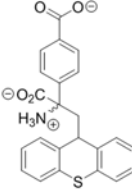
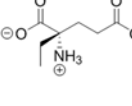
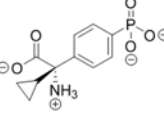
Ligand Type	Group I	Group II	Group III
Nonselective Antagonists	 LY341495		
Selective Antagonists	 LY367366	 EGlu	 CPPG

Table 9. Group-Selectivity of Competitive mGluR Antagonists. Group-selective mGluR antagonists resemble the corresponding group-selective mGluR agonists.

Discovery of these group-selective agents enabled not only pharmacological, but also physiological characterization of each mGluR group, all of which are expressed in the central nervous system. According to the tripartite synapse model of neurotransmission (**Figure 18**), which comprises a presynaptic neuron, a postsynaptic neuron, and a glial cell, the presynaptic neuron releases neurotransmitters from prepackaged vesicles into the cleft between synaptic neurons, thereby leading to the activation of receptors expressed on the postsynaptic neuron. Receptors expressed on glial cells can then respond to neurotransmitters that spill out of the synaptic cleft. Glial cells also secrete second messengers that regulate the packaging and release of neurotransmitters into presynaptic vesicles. For example, mGluR-mediated glutamatergic synaptic transmission is regulated in part by glial cell-localized cysteine-glutamate antiporter proteins that exchange extracellular cysteine for intracellular glutamate⁹⁸. The release of glutamate into extracellular space facilitates activation of group II mGluRs expressed on pre-terminal portions of presynaptic neuronal axons that are distal from the synaptic cleft⁹⁹. This signaling event results in the inhibition of neurotransmitter release from the presynaptic neuron into the synaptic cleft, and thus, represents a feedback mechanism for sensing and controlling the amount of synaptic glutamate⁹⁸. A similar feedback loop also holds for group III mGluRs expressed on terminal portions of the presynaptic neuron. Upon the release of presynaptic vesicles prepackaged with glutamate into the synaptic cleft, group I mGluRs localized on postsynaptic neuronal terminals undergo

glutamate-induced activation, which allows glutamatergic signals to propagate from the presynaptic neuron to the postsynaptic neuron⁹⁹. Notably, ionotropic glutamate receptors¹⁰⁰ (iGluRs) expressed on postsynaptic neurons compete for the same pool of synaptically-released glutamate as postsynaptic group I mGluRs. Glutamate that is not sequestered by postsynaptically-localized glutamate receptors can spill out of the synaptic cleft towards glial cells, which predominantly express mGluR3 and mGluR5¹⁰¹. Thus, mGluRs are important players in the maintenance of normal neurophysiological function.

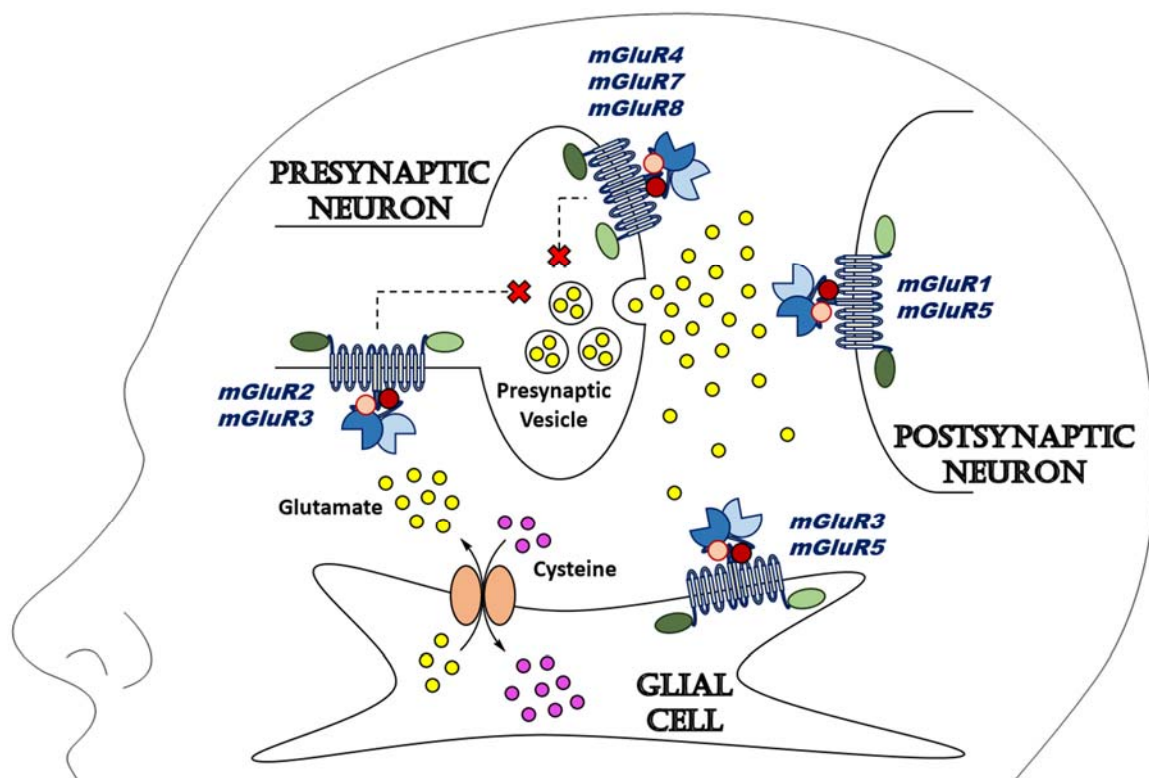


Figure 18: mGluR-Mediated Glutamatergic Synaptic Transmission. Group I, group II, and group III mGluRs all participate in glutamatergic synaptic transmission according to the tripartite synapse model. While group II and III mGluR neuronal expression is predominantly presynaptic, group I mGluR expression in neurons is largely postsynaptic. mGluR3 and mGluR5 are also expressed by glia.

Accordingly, mGluRs have been implicated as potential drug targets for a wide array of neurological disorders, such as anxiety and stress disorders¹⁰², diabetic neuropathy¹⁰³, schizophrenia¹⁰⁴, pain¹⁰⁵, fragile X syndrome¹⁰⁶, and addiction¹⁰⁷, as well several neurodegenerative disorders, including

Parkinson's disease¹⁰⁸, Huntington's disease¹⁰⁹, cerebral ischemia¹¹⁰, and Alzheimer's disease¹¹¹. While a large body of literature supports the therapeutic potential of targeting group I¹¹² or group III¹¹³ mGluRs (specifically mGluR4) for the treatment of various neurodegenerative diseases, evidence advocating the activation of group II mGluRs as a neuroprotective strategy is increasingly promising. Selective activation of group II mGluRs has been demonstrated not only to inhibit synaptic release of glutamate from prepackaged, presynaptic vesicles, which combats glutamate-mediated excitotoxicity that is associated with some conditions, but also to increase expression of a variety of growth factors, including brain-derived neurotrophic factor¹¹⁴, nerve growth factor¹¹⁵, glial-derived neurotrophic factor¹¹⁶, and transforming growth factor β ¹¹⁷ (TGF- β); upregulation of glutamate transporters and subsequent reuptake of glutamate out of the synaptic cleft has also been reported¹¹⁸. The combination of these neuroprotective signaling mechanisms has empowered selective group II mGluR agonists to protect cultured neurons from *N*-methyl-*D*-aspartate¹¹⁹ (NMDA)-, kainic acid-, or staurosporine-induced toxicity¹²⁰, as well as to defend cultured astrocytes from apoptosis induced by nitric oxide¹²¹ or by oxygen/glucose deprivation¹²². Selective group II mGluR agonists have also demonstrated neuroprotective activity *in vivo*, decreasing MPTP-induced toxicity in mice¹¹⁶, reducing neuronal death after treatment with MK-801 in adult rats¹²³, and promoting neuroprotection in gerbil models of global ischemia¹²⁴.

2.1.c. Subtype-Selective mGluR3 Activation and Neuroprotection

Despite the implication of both mGluR2 and mGluR3 as potential therapeutic targets for treatment of neurodegeneration, each of these receptors plays distinct roles in processes relating to neuronal death and neuroprotection, which is predominantly a result of differences in synaptic expression. While both mGluR2 and mGluR3 are expressed on presynaptic neurons, only mGluR3 is expressed on macroglial cells, such as astrocytes, which are the brain's first line of defense, contributing to neuronal survival during development, blood-brain barrier permeability, homeostatic blood flow, regulation of synaptic transmission, trophic support for neuronal injury, and perhaps even

synaptogenesis¹¹⁸. Although mGluR2 and mGluR3 share several common intracellular signaling mechanisms, neurons comprise an entirely different set of cellular machinery than astrocytes, which are likely responsible for the selective group II mGluR agonist-mediated release of growth factors and associated neuroprotection. For example, mGluR3 becomes upregulated on reactive astrocytes after cerebral insult, and abnormally high levels of astrocytic mGluR3 has been observed in animal models of multiple sclerosis, persistent inflammation, and epilepsy¹¹⁸. Additionally, treating co-cultures of neurons and astrocytes isolated from wild-type, mGluR2^{-/-} knockout, or mGluR3^{-/-} knockout mice with a selective group II mGluR agonist revealed that neuroprotection against NMDA- or MPTP-mediated neuronal death was controlled exclusively by astrocytic mGluR3¹²⁵. Similarly, a selective group II mGluR agonist protected rat co-cultures against toxic β -amyloid fragments, which are putatively associated with the pathology of Alzheimer's disease, via a paracrine mechanism involving glial mGluR3-dependent astrocytic release of TGF- β , which is thought to combat the progression of Alzheimer's disease¹²⁶; in contrast, subtype-selective potentiation of mGluR2 was reported to exacerbate β -amyloid toxicity¹²⁷. Furthermore, treatment of primary cultures of rat astrocytes with a selective group II mGluR agonist promoted proper α -secretase-mediated processing of amyloid precursor protein (APP) into soluble cleavage products, which is an aberrant process in the Alzheimer's brain¹²⁸. Each of these pharmacological and pathophysiological results, including the sustained astrocytic expression of mGluR3 from development through adulthood¹²⁹, implicate the therapeutic potential of a subtype-selective mGluR3 agonist for the treatment of Alzheimer's disease.

Despite this strong rationale for targeting mGluR3 selectively, pharmacological differentiation between mGluR2 and mGluR3 has proven challenging, and as a result, ligands exhibiting subtype-selectivity are sparse. The classic selective group II mGluR agonist DCG-IV demonstrated no subtype-selectivity between mGluR2 and mGluR3 in transfected CHO cells, as indicated by functional inhibition of forskolin-stimulated cAMP production¹³⁰ (**Table 10**), nor did it bind in a subtype-selective manner to membranes harvested from transfected baby hamster kidney (BHK) cells, as determined by competition experiments with [³H]-LY354740¹³¹. While the parent bicyclic glutamate analog of Eli

Lilly's group II mGluR agonist program, LY354740, exhibited 4-5-fold subtype-selectivity for mGluR2 over mGluR3 both in radioligand binding assays quantitating displacement of [³H]-LY354740¹³¹, and in functional assays measuring inhibition of forskolin-stimulated cAMP production¹³², oxygen- and sulfur-containing analogs LY379268 and LY389795, respectively, each demonstrated reduced functional subtype-selectivity under the same conditions¹³³. In contrast to these heterocyclic analogs, methyl substituted derivative LY395756 and the corresponding epimer (*epi*-LY395756) were each reported to achieve improved subtype-selectivity as compared to unsubstituted LY354740 in the same functional assay¹³². While *epi*-LY395756 demonstrated agonist activity at both mGluR2 and mGluR3 with a 5-6-fold subtype-selectivity for mGluR2, LY395756 exhibited potent agonist activity at mGluR2, and interestingly, moderate antagonist activity at mGluR3. Although LY395756 can uniquely distinguish between mGluR2 and mGluR3 functionally, it preferentially activates mGluR2, rendering it a suboptimal tool with which to explore the neuroprotective properties of subtype-selective mGluR3 activation. Aside from Eli Lilly's group II mGluR agonist program, little success has been achieved towards the discovery of subtype-selective group II mGluR agonists. One minor success involves quisqualate, the classic selective group I mGluR agonist. While quisqualate is much more potent at mGluR1 and mGluR5, it has been shown to weakly inhibit forskolin-stimulated cAMP production via mGluR3 activation in transfected CHO cells¹³⁴, but not via mGluR2 activation under similar assay conditions¹³⁵. Although quisqualate subtype-selectivity for mGluR3 over mGluR2 was 5-6-fold using radioligand binding assays measuring the displacement of [³H]-LY354740¹³¹, potent activity at group I mGluRs would convolute studies in native systems aimed at characterizing neuroprotection mediated by subtype-selective activation of mGluR3.

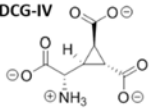
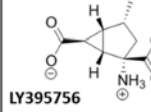
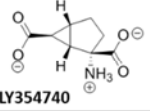
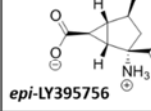
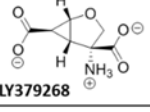
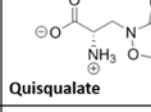
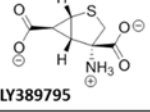
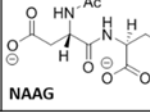
Drug	EC ₅₀ (nM) K _i (nM)		Drug	EC ₅₀ or IC ₅₀ (nM) K _i (nM)	
	mGluR2	mGluR3		mGluR2	mGluR3
DCG-IV 	910 <i>111</i>	870 <i>150</i>	LY395756 	63.6	<u>3,420</u>
LY354740 	5.60 <i>13.0</i>	27.1 <i>51.0</i>	<i>epi</i> -LY395756 	28.6	166
LY379268 	2.69	4.58	Quisqualate 	> 1,000,000 <i>113</i>	4,000 <i>22.0</i>
LY389795 	3.91	7.63	NAAG 	> 1,000,000 <i>236</i>	65,000 <i>19.0</i>

Table 10. Potency and Subtype-Selectivity of Competitive Group II mGluR Agonists. Potencies of DCG-IV¹³⁰, LY354740¹³², LY395756, *epi*-LY395756, LY279268¹³³, LY389795, quisqualate^{134,135}, and NAAG¹³⁶ were measured via inhibition of forskolin-stimulated cAMP production. All K_i values¹³¹ were measured via displacement of [³H]-LY354740 and are italicized. IC₅₀ values are underlined.

Alternatively, structurally distinct *N*-acetylaspartylglutamate (NAAG), the most prevalent peptide neurotransmitter in the mammalian central nervous system¹³⁷, has been reported not only to exhibit TGF- β -dependent¹³⁸ neuroprotective properties endogenously¹³⁹, but also to subtype-selectively activate mGluR3 over mGluR2. NAAG was identified in the mammalian brain in the mid-1960s¹⁴⁰, and in the mid-1980s, it was reported to interact with a portion of [³H]-glutamate-sensitized binding sites in rat brain¹⁴¹, suggesting that NAAG is a second endogenous ligand for a subset of glutamate receptors. Subsequent studies conducted by Wroblewska et al., established that NAAG inhibited forskolin-stimulated cAMP production in rat cerebellar granule cells¹⁴², as well as in transfected CHO cells expressing mGluR3¹³⁶, but not in transfected CHO cells expressing mGluR1, mGluR2, mGluR4, mGluR5, or mGluR6. NAAG additionally stimulated both Ca⁺² flux and phosphatidylinositol hydrolysis in human embryonic kidney (HEK293) cells expressing mGluR3/mGluR1 chimeric receptors, which signal through G α_q proteins instead of G $\alpha_{i/o}$ proteins; in contrast, NAAG did not elicit G α_q protein activity in HEK293 cells expressing mGluR2/mGluR1

chimeric receptors. NAAG-mediated inhibition of forskolin-stimulated cAMP production was also observed in primary cultures of rat cerebellar astrocytes, where mRNA corresponding to all mGluRs except for mGluR2 was detected¹⁴³. While AP4 had little effect on cAMP levels, indicating low expression levels of group III mGluRs, cAMP levels were unaffected by NAAG in the presence of nonselective mGluR antagonists, as well as selective group II mGluR antagonist EGlu, indicating that NAAG was functioning through group II mGluRs. Validating this interaction, NAAG subtype-selectively displaced [³H]-LY354740 from isolated BHK cell membranes containing mGluR3 in 12-13-fold preference to membranes containing mGluR2¹³¹. Furthermore, this subtype-selectivity translated into neuroprotection of rat neuronal-glia co-cultures against insult with high glucose¹⁴⁴, or with 2-deoxyglucose and potassium cyanide¹⁴⁵. Under both of these conditions, NAAG-mediated neuroprotection was (1) blocked by EGlu, (2) not inhibited by selective group I or selective group III antagonists, and (3) drastically desensitized in the absence of glial cells, further implicating mGluR3 as the endogenous protein target of NAAG. Although NAAG did not activate mGluR3-mediated K⁺ flux through GIRK channels in HEK cells transfected with mGluR2 or mGluR3¹⁴⁶, or in oocytes injected with both mGluR3 and GIRK channel mRNA¹⁴⁷, activation of K⁺ flux is a Gβγ complex-dependent process, as opposed to inhibition of forskolin-stimulated cAMP, which is a Gα_{i/o}-dependent process. As the multifaceted signaling profiles of 7TMRs continue to complexify, it is becoming clear that all agonists, even orthosteric agonists for the same receptor subtype, do not interact and function in an equal manner¹⁴⁸. Thus, the fact that glutamate endogenously stimulates both Gα_{i/o}-mediated and Gβγ-mediated signaling events does not necessarily mean that NAAG should be expected to activate the Gβγ complex in addition to Gα_{i/o}. Ultimately, the few reports of NAAG inactivity towards mGluR3-mediated K⁺ flux is not inconsistent with the body of literature supporting NAAG-mediated neuroprotection via stimulation of mGluR3-dependent Gα_{i/o} activity¹⁴⁹.

2.2. Results and Discussion

2.2.a. *Design of NAAG Analogs*

Despite the relatively poor potency of NAAG at mGluR3¹³⁶, the remarkable selectivity for mGluR3 versus mGluR2, coupled with the established neuroprotective properties¹⁵⁰, inspired our laboratory to deem NAAG an attractive lead compound with which to commence the search for a more potent mGluR3-selective agonist with therapeutic potential against Alzheimer's disease. Although quisqualate, which exhibits similar mGluR3 versus mGluR2 selectivity, would have been a reasonable option as well, potent activity at other mGluRs and iGluRs renders quisqualate a suboptimal starting point. The unique chemical structure of NAAG, as compared to structures of all other established orthosteric group II mGluR agonists, was further intriguing. Although NAAG analogs would eventually need to be modified to slow or obviate peptidase-mediated metabolism, the preliminary priority was to predict the active conformation of NAAG at mGluR3 via computational molecular modeling, which would be followed by synthesis and pharmacological evaluation of a series of NAAG analogs designed to probe the predicted conformations. With support for a putative active conformation, subsequent reduction of the number of rotatable bonds via design and synthesis of cyclic NAAG analogs that rigidify the active pharmacophore was anticipated to substantially increase both potency and affinity by virtue of lowering the entropic penalty of binding. Improved mGluR3 activity would not likely be accompanied by increased mGluR2 activity because the active NAAG conformation naturally discriminates between these receptors, and because cyclic analogs would reinforce and robustify this active conformation. Ultimately, the expected outcome was a NAAG analog with elevated agonist activity at mGluR3, as well as increased selectivity for mGluR3 over mGluR2.

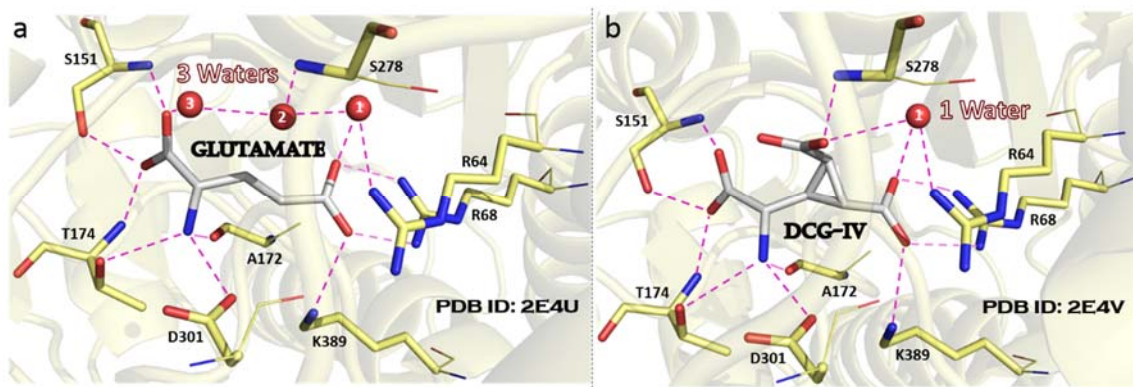


Figure 19. mGluR3 Orthosteric Binding Pocket Interactions with Glutamate and DCG-IV. Comparison of x-ray crystal structures of mGluR3⁸³ bound to (a) glutamate and (b) DCG-IV illustrates that these agonists interact with many common mGluR3 residues, but also that they bind with different arrangements of structural water molecules. PyMOL⁸⁰ was employed for figure generation.

Preliminarily, it was necessary to predict the conformation by which NAAG selectively activates mGluR3. While structures of the mGluR3 NTD bound to several orthosteric agonists, including glutamate and DCG-IV (**Figure 19**), have been elucidated using x-ray crystallography⁸³, the structure of an mGluR3-NAAG complex has been published. Accordingly, molecular modeling was employed (1) to analyze and compare the resolved agonist-bound mGluR3 structures, (2) to virtually dock NAAG into the orthosteric ligand binding pocket, and (3) to computationally explore the lowest energy conformation(s) of NAAG when bound to the mGluR3 NTD *in silico*. Examination of the glutamate-bound (**Figure 19a**) and DCG-IV-bound (**Figure 19b**) mGluR3 NTD crystal structures reveals that the agonist amino group is stabilized via salt bridge interaction with the D301 side chain carboxylic acid, as well as by hydrogen bonding interactions with the T174 side chain hydroxyl group and the A172 backbone carbonyl oxygen. Additionally, agonist α -carboxylic acids interact via hydrogen bond with both the side chain hydroxyl group and the backbone amide nitrogen of S151, whereas agonist γ -carboxylic acids engage in electrostatic interactions with the cationic side chains of R68 and K389. Alternative to these common binding motifs, the binding mode of DCG-IV differs from that of glutamate due to distinct arrangements of structural water molecules. While three water molecules remain bound while glutamate occupies the pocket, only one structural water molecule is present during DCG-IV binding, a difference that stems from displacement of two water molecules by the

extra carboxylic acid of DCG-IV. Although the guanidine side chain of R64 and the agonist γ -carboxylic acids form hydrogen bonds with the only common water molecule, this water molecule engages in an additional hydrogen bond with a second water molecule when glutamate is bound, and alternatively, with the extra agonist carboxylic acid when DCG-IV is bound. The glutamate-bound structure additionally conveys electrostatic interactions between this second water molecule and both the backbone amide nitrogen of S278 and the third water molecule, which further stabilizes the α -carboxylic acid of glutamate with an additional hydrogen bond. In contrast, the absence of the second and third water molecules at the DCG-IV-bound structure is somewhat energetically offset by hydrogen bonding interaction between the backbone amide nitrogen of S278 and the extra DCG-IV carboxylic acid. Interestingly, [^3H]-DCG-IV affinity was reported to be virtually absent at mGluR3 R64A, R68A, K389A, S151A, T174A, and D301A mutant receptors¹⁵¹, indicating that agonist interaction with each of these residues is essential for ligand binding.

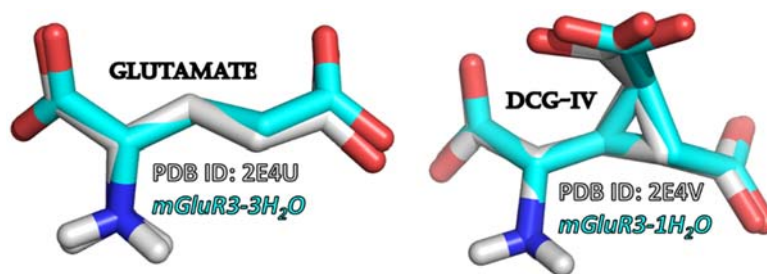


Figure 20. Control Docking Experiments at mGluR3 *in silico* Models. Glutamate and DCG-IV were computationally docked using the Glide application¹⁵² in Maestro³⁰ into molecular models of mGluR3 containing three (*mGluR3-3H₂O*) and one (*mGluR3-1H₂O*) structural water molecule(s) that were based on glutamate- and DCG-IV-bound mGluR3 x-ray structures⁸³, respectively. PyMOL⁸⁰ was employed for figure generation.

Although glutamate and DCG-IV share several common binding motifs at mGluR3, larger and structurally unique NAAG likely interacts with distinct amino acid residues upon binding to mGluR3. To enable computational prediction of the active conformation of NAAG, all agonist-bound structures of mGluR3 were subjected to visual inspection, which indicated that orientations of the amino acid residues essential for ligand binding were exquisitely conserved between structures.

Accordingly, the highest resolution agonist-bound mGluR3 NTD x-ray structure⁸³ available on the protein data bank (PDB ID: 2E4W, agonist = 1*S*,3*S*-ACPD) was imported into Maestro³⁰ within the Schrödinger Small-Molecule Drug Discovery software suite. This structure was subsequently prepared¹⁵³ for ligand docking via (1) addition of hydrogen atoms to satisfy valence requirements, (2) adjustment of amino acid residue ionization to represent physiological pH, and (3) removal of all water molecules except for the aforementioned structural water molecules. This resulted in two mGluR3 models, one with one structural water molecule (*mGluR3-1H₂O*) in the ligand binding pocket as in the DCG-IV-bound structure, and one with three structural water molecules (*mGluR3-3H₂O*) as in the glutamate-bound structure. Using the Glide application¹⁵² in Maestro, an identical ligand binding region was subsequently defined for each of these models to encompass a relatively large volume beyond that occupied by 1*S*,3*S*-ACPD, a rigidified glutamate analog, in order to accommodate larger NAAG. To ensure that molecular modifications made to the original crystal structure did not deleteriously affect any of the essential ligand binding pocket residues, control docking experiments were conducted using the Glide application, with which glutamate was docked into *mGluR3-3H₂O* and DCG-IV was docked into *mGluR1-1H₂O*. Comparison of the resulting agonist conformations that were predicted computationally (**Figure 20**, blue carbons) with those from crystal structures that were resolved empirically (**Figure 20**, gray carbons) revealed highly accurate and reproducible results.

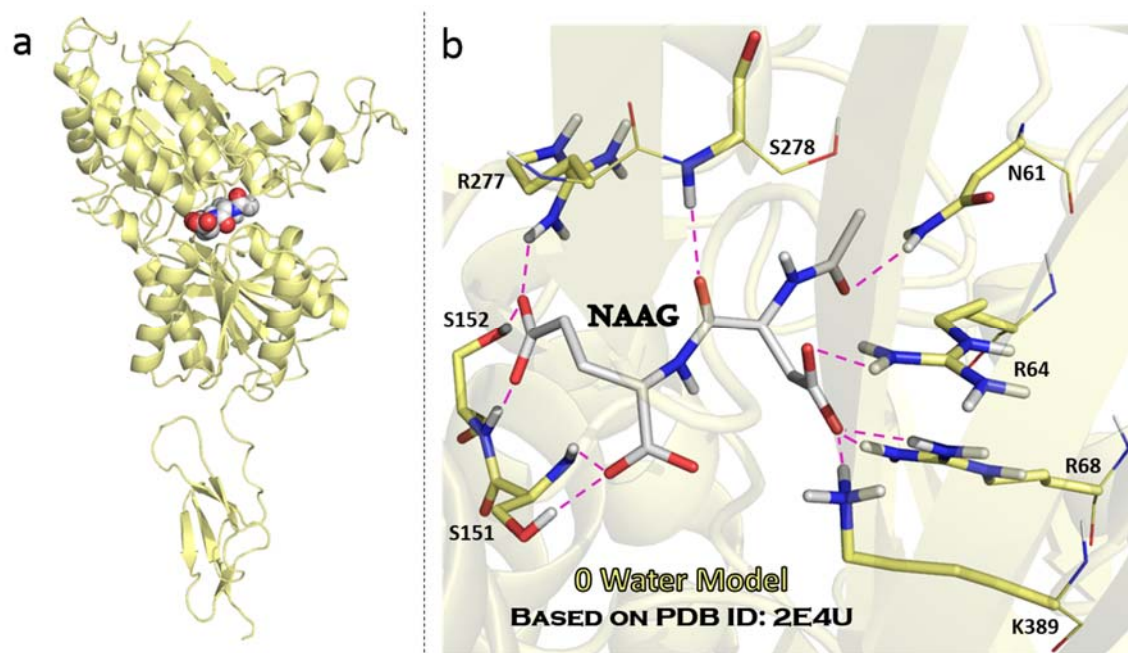
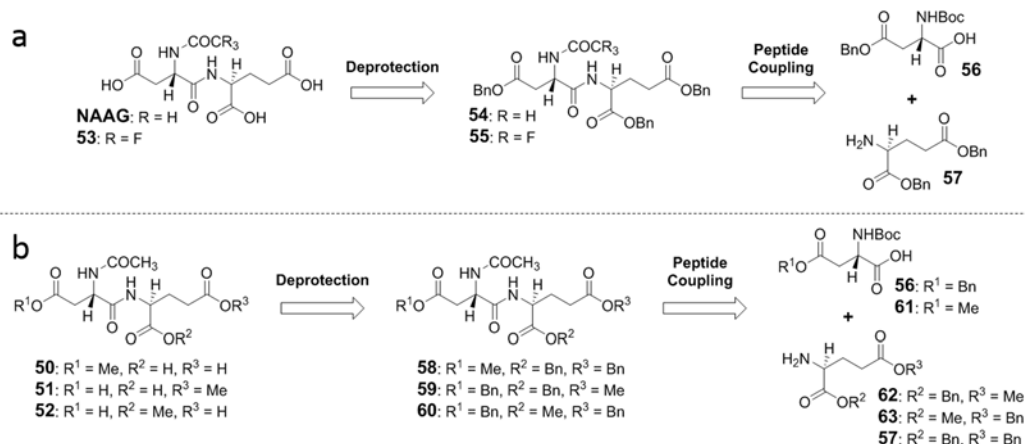


Figure 21: Predicted NAAG Docking Poses at mGluR3. (a) NAAG was computationally docked using the Glide application¹⁵² in Maestro³⁰ into a molecular model of mGluR3 without any structural water molecules (*mGluR3-0H₂O*). (b) A representative NAAG conformation illustrates several interactions common to multiple NAAG poses. PyMOL⁸⁰ was employed for figure generation.

The conformational accuracy exhibited by these control experiments indicated that both mGluR3 models, *mGluR1-1H₂O* and *mGluR3-3H₂O*, were appropriate for docking experiments involving NAAG. However, despite all attempts to dock NAAG with the Glide application into each of these models using varying levels of stringency, not one NAAG binding pose was predicted at either mGluR3 model. Since DCG-IV displaces two more structural water molecules than glutamate, and because NAAG is larger than both DCG-IV and glutamate, it is possible that NAAG binding does not involve any structural water molecules. Accordingly, a third mGluR3 model, which was prepared in similar fashion to the first two mGluR3 models except for the incorporation of 0 water molecules (*mGluR3-0H₂O*), was generated in Maestro. Subsequent utilization of the Glide application enabled docking of NAAG into *mGluR3-0H₂O*, which resulted in several different predicted NAAG conformations within the ligand binding pocket (**Figure 21a**). A representative orientation (**Figure 21b**) illustratively facilitates description of the two commonalities amongst the pool of lowest energy NAAG conformations: (1) one NAAG carboxylate residing in the cationic sub-pocket composed of

and the backbone amide hydrogen of S151. It was further hypothesized that hydrogen bonding interactions of the *N*-acetyl group with mGluR3 was important for NAAG activity. There are two ways in which the *N*-acetyl group can participate in hydrogen bonding: (1) hydrogen bond donation from the amide hydrogen and/or (2) hydrogen bond acceptance from the amide oxygen. Accordingly, compound **53** was designed to probe the electrostatic requirements of the *N*-acetyl group. While the *N*-acetyl group of analog **53** would be a better hydrogen bond donor than the corresponding NAAG moiety, it would be a worse hydrogen bond acceptor, due in each case to the inductively electron-withdrawing character of the trifluoromethyl group. Therefore, if the *N*-acetyl group acts as a hydrogen bond donor at mGluR3, compound **53** would be more potent than NAAG, and on the contrary, if the *N*-acetyl group acts as a hydrogen bond acceptor, NAAG would be more potent than analog **53**.

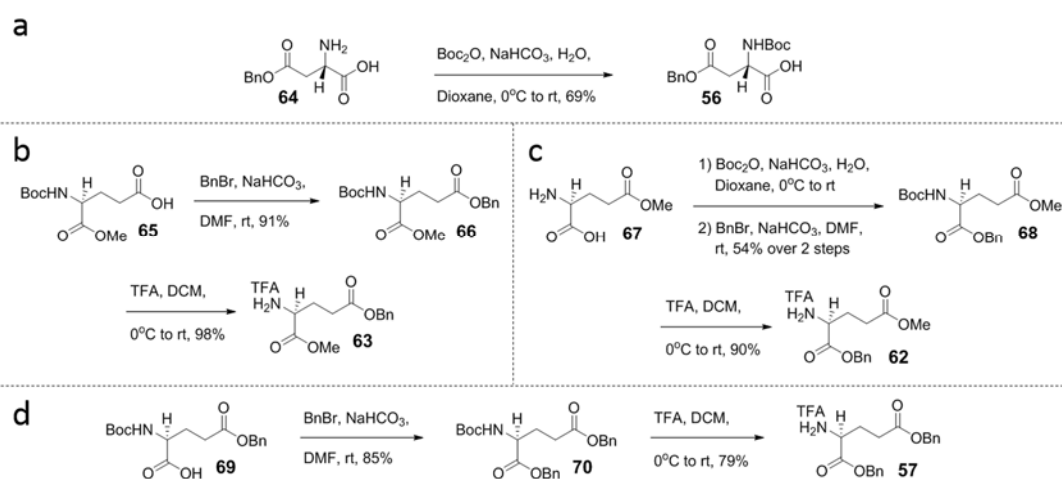
2.2.b. Synthesis of NAAG Analogs



Scheme 20: Retrosynthetic Analyses of NAAG Analogs. Retrosynthesis of (a) NAAG and trifluoroacetyl analog **53**, as well as of (b) methyl ester analogs **50**, **51**, and **52**, involved peptide coupling and the use of easily removable benzyl ester protecting groups.

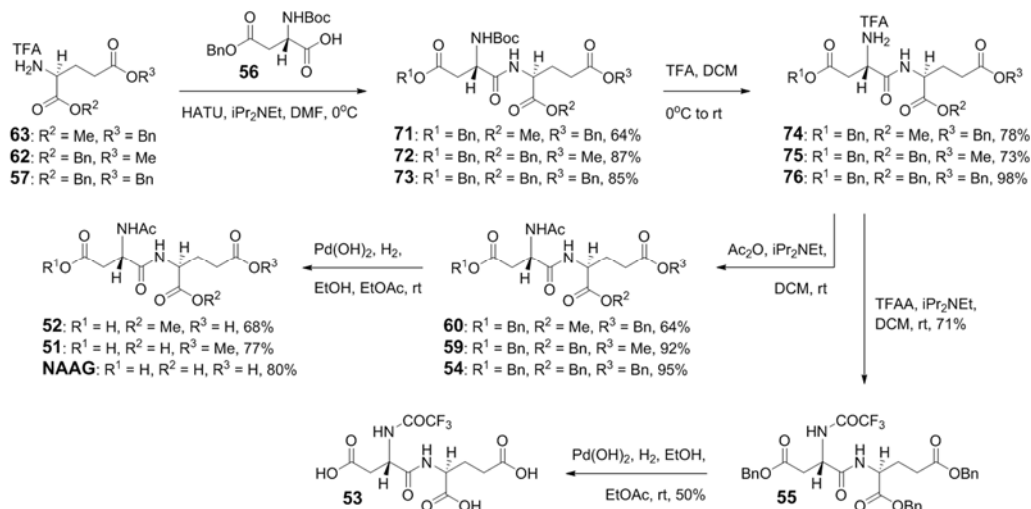
Retrosynthetic analysis of NAAG and trifluoroacetyl analog **53** (*Scheme 20a*) illustrates that these compounds were envisioned to be produced via deprotection of benzyl esters **54** and **55**, respectively, which were expected to form via peptide coupling between carboxylic acid-bearing

aspartate derivative **56** and amine-bearing dibenzyl glutamate **57**, followed by amine deprotection and subsequent *N*-acetylation with either acetic anhydride or trifluoroacetic anhydride. Similarly, retrosynthetic analysis of methyl ester analogs **50**, **51**, and **52** (*Scheme 20b*) began with deprotection of dibenzyl ester intermediates **58**, **59**, and **60**, respectively. Preparation of these compounds was expected to proceed through peptide coupling between carboxylic acid **56** and amine **62** or **63**, as well as between carboxylic acid **61** and amine **57**, followed by successive amine deprotection and *N*-acetylation with acetic anhydride. Because four of the five final compounds contain *N*-acetyl groups, it would obviously be advantageous to use acetyl instead of Boc protecting groups for the amines of synthons **56** and **61**. However, *N*-acetyl groups, which are more electron-withdrawing than *N*-Boc groups, were preliminarily observed to undergo epimerization during peptide coupling with amine **57**. Alternatively, Boc-protected **56** was resistant to racemization when exposed to 0.1 eq potassium *tert*-butoxide in *tert*-butanol for 24 hrs at room temperature, as well as when dissolved in pyridine for 24 hrs at room temperature, and therefore, Boc protecting groups were installed before peptide coupling and removed afterward.



Scheme 21: Preparation of Amino Acid Synthons for Synthesis of NAAG Analogs. Syntheses of NAAG and all four proposed analogs were enabled via preparation of only five total amino acid synthons, including (a) carboxylic acid **56**, as well as ammonium salts (b) **63**, (c) **62**, and (d) **57**.

Accordingly, synthesis of the required protected amino acid building blocks began with Boc protection of commercially available aspartyl β -benzyl ester **64** (*Scheme 21a*), which yielded desired carbamate **56** in 69% yield. Additionally, commercially available glutamyl methyl ester **65** was subjected to benzyl protection of the γ -carboxylic acid with benzyl bromide under mildly basic conditions (*Scheme 21b*), producing in 91% yield the diester intermediate **66**¹⁵⁴, which was subsequently exposed to TFA to facilitate amine deprotection, yielding the corresponding trifluoroacetate salt **63**¹⁵⁵ in 98%. Similarly, commercially available glutamate γ -methyl ester **67** was Boc-protected (*Scheme 21c*), and the resulting carbamate¹⁵⁶ was then treated with benzyl bromide to protect the α -carboxylic acid as a benzyl ester. This two-step reaction sequence produced in 54% yield the diester intermediate **68**¹⁵⁷, which was subsequently exposed to TFA to facilitate Boc-deprotection, generating the corresponding trifluoroacetate salt **62**. In similar fashion, commercially available carboxylic acid **69** was treated with benzyl bromide under mildly basic conditions to yield in 85% yield benzyl ester **70**¹⁵⁸ (*Scheme 21d*), which was then subjected to acid-mediated amine deprotection, producing the corresponding trifluoroacetate salt **57**¹⁵⁹ in 79% yield. Next, trifluoroacetate salts **63**, **62**, and **57** were desalted *in situ* with *N,N*-diisopropylethylamine (DiPEA), and each resulting free amine underwent peptide coupling with carboxylic acid **56** (*Scheme 22*), which was pre-mixed with DiPEA and HATU in order to activate the carboxylic acid for peptide bond formation¹⁶⁰; HATU-mediated peptide couplings produced protected dipeptides **71**, **72**, and **73** in 64%, 87%, and 85% yields, respectively, without epimerization



Scheme 22. Synthesis of NAAG Analogs. Preparation of NAAG and three analogs with only four amino acid synthons for evaluation of mGluR3 agonist activity *in vitro*.

of the aspartyl chiral center. Boc protecting groups were subsequently removed with TFA, which yielded corresponding trifluoroacetate salts **74**, **75**, and **76** in 78%, 73%, and 98%, respectively. Each of these three intermediates was then treated with acetic anhydride and DiPEA to facilitate preparation of *N*-acetylation products **60**, **59**, and **54**, which proceeded in 64%, 92%, and 95% yields, respectively. Subsequent palladium-catalyzed hydrogenolysis of all benzyl-protected carboxylic acids produced methyl esterified NAAG analogs **52** and **51**, as well as **NAAG**¹⁶¹ itself, in 68%, 77%, and 80% yields, respectively. Additionally, tribenzyl ester **76** was treated with trifluoroacetic anhydride in the presence of DiPEA, generating in 71% yield the corresponding trifluoroacetamide **55**, which was finally subjected to palladium-catalyzed hydrogenolysis for benzyl ester cleavage, affording desired trifluoroacetamide analog **53** in 50% yield.

2.2.c. GloSensor Assay Measures Group II and III mGluR Activity. Some of the information presented in the section is reprinted¹³⁰ with permission of the American Society for Pharmacology and Experimental Therapeutics. All rights reserved. Copyright © 2014 by the American Society for Pharmacology and Experimental Therapeutics.

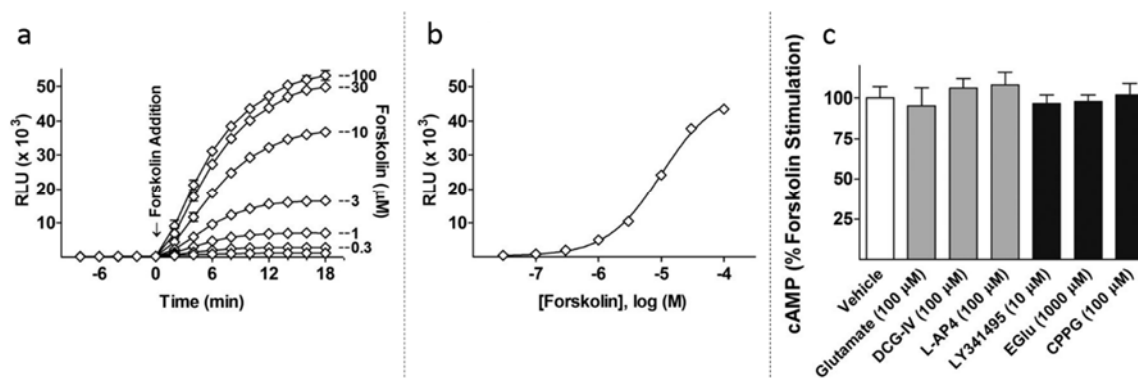


Figure 22. Forskolin-Stimulated cAMP Production in CHO-Glo Cells¹³⁰. (a) CHO cells, stably transfected with the GloSensor cAMP biosensor (CHO-Glo), showed concentration-dependent increases in relative light units (RLU) over time when treated with increasing concentrations of the AC activator forskolin. The reading from each well was normalized to its own basal luminescence, determined before forskolin addition. (b) The forskolin concentration-response curve was generated from data obtained 16 min after forskolin treatment. (c) Group II and group III mGluR agonists and antagonists do not affect forskolin-mediated cAMP production in CHO-Glo cells (lacking a transfected receptor). Data are presented as the mean \pm S.E.M. of three individual experiments performed in triplicate.

Preparation of aspartyl methyl ester analog **50** was underway when these five compounds, including NAAG, were submitted to colleagues in the laboratory of Dr. Jarda Wroblewski (Department of Pharmacology and Physiology, Georgetown University) as we collaborated to design and implement a real-time assay paradigm¹³⁰ with which to compare the pharmacological properties of group II and group III mGluRs. This assay utilized the GloSensor cAMP Biosensor¹⁶² (Promega), a recombinant firefly luciferase conjugated to a cAMP binding domain. cAMP binding promotes a conformational shift within the GloSensor protein, which induces luciferase activity. cAMP levels, which are modulated by group II and group III mGluR activation, are positively correlated with light output resulting from the luciferase-mediated breakdown of D-luciferin. Accordingly, CHO cells were transfected with the

GloSensor plasmid, and multiple clones were tested for maximal luminescence in response to the AC activator forskolin (10 μM). The clone with the largest increase in luminescence in response to forskolin was selected, and a single cell line (CHO-Glo) was established. Untransfected CHO cells lacking the GloSensor construct did not produce a detectable signal, whereas treatment of CHO-Glo cells with forskolin caused a concentration-dependent increase in relative light units (RLU) over time (*Figure 22a*). The concentration dependence of cAMP production is shown using data measured 16 min after the addition of forskolin (*Figure 22b*). The EC_{50} for forskolin was calculated in this system to be $9.44 \pm 0.60 \mu\text{M}$, which is comparable to the reported forskolin EC_{50} of 5-10 μM ¹⁶³. From these data, 1 μM forskolin was chosen as a concentration sufficient to stimulate cAMP production with minimal potential for substrate depletion and a reliable signal-to-noise ratio. As a control, common group II and group III mGluR ligands were tested on CHO-Glo cells to ensure that these compounds would not affect cAMP levels in the absence of transfected mGluRs (*Figure 22c*). Several group II and/or group III mGluR agonists (glutamate, DCG-IV, and AP4) and antagonists (LY341945, EGlu, and CPPG) were assayed at saturating concentrations. As expected, none of these drugs significantly altered cAMP production in CHO-Glo cells, indicating not only the lack of endogenous mGluRs in CHO cells, but also that measurement of ligand-mediated mGluR activity would not be confounded by mGluR-independent signaling mechanisms.

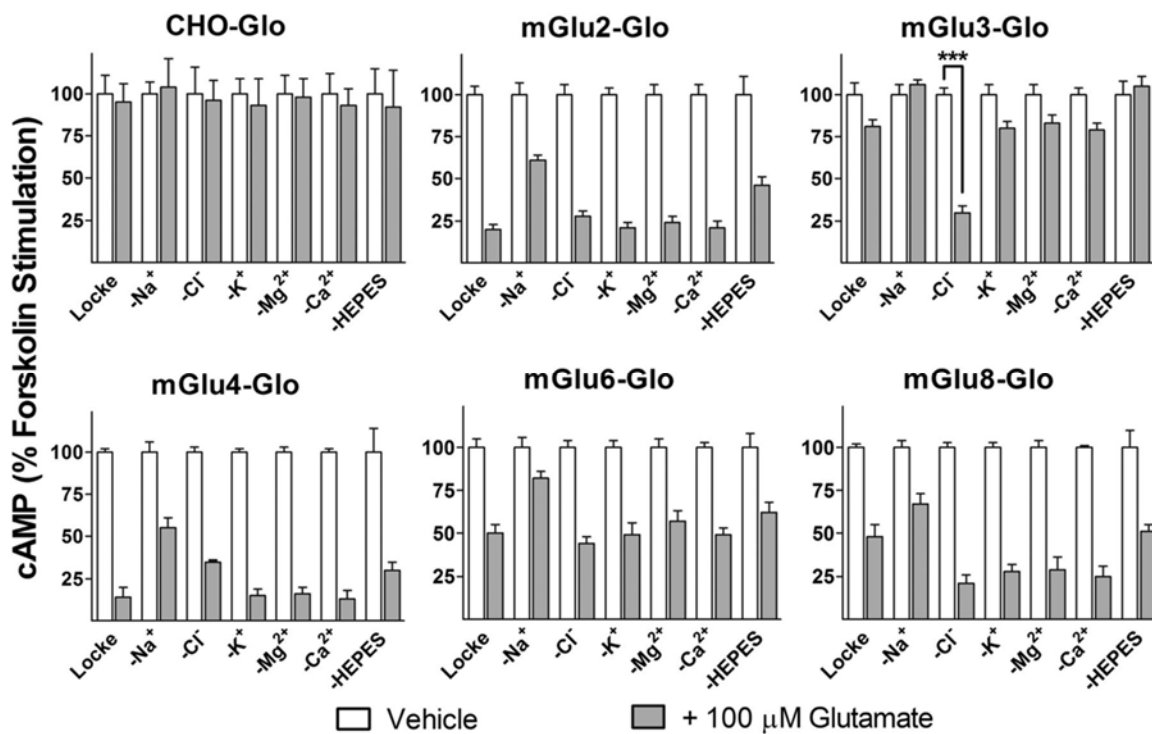


Figure 23: Ion Sensitivity of Glutamate-Mediated Group II and III mGluR Activation¹³⁰. CHO-Glo or mGlu-Glo cells were treated with vehicle (white bars) or 100 μ M glutamate (gray bars) in a series of modified Locke's buffers (**Table 11**). In each buffer, data were normalized as a percent of vehicle treatment. Glutamate-mediated decreases in cAMP production were statistically significant ($P < 0.01$) at all mGlu-Glo cell lines, with the exception of mGlu3-Glo. Glutamate activation of mGluR3 was significant only when Locke-Cl⁻ was used as the assay buffer. Statistical differences in the data were assessed by a Student's t test. Data are presented as the mean \pm S.E.M. of three individual experiments performed in triplicate. *** $P < 0.001$.

Next, CHO-Glo cells were transfected with individual group II or III mGluR cDNAs, previously cloned into pIRES2-AcGFP1. Stable clones of CHO-Glo cells expressing individual mGluR types (mGlu2-Glo, mGlu3-Glo, mGlu4-Glo, mGlu6-Glo, mGlu7-Glo, and mGlu8-Glo) were selected based on AcGFP fluorescence and maximal light output in response to forskolin treatment. In Locke's buffer, all mGlu-Glo cell lines, except for mGlu3-Glo, showed significant decreases in forskolin-stimulated cAMP production in response to 100 μ M glutamate (**Figure 23**). Since several studies demonstrated that mGluR activation is sensitive to ions^{164,165}, it was hypothesized that a buffer constituent precluded mGlu3-Glo cells from inhibiting forskolin-stimulated cAMP production in response to glutamate treatment. To test this hypothesis, each buffer constituent was individually replaced with a structurally distinct ion of like charge (**Table 11**). Sodium was replaced with choline

(Locke-Na⁺). Potassium, magnesium, or calcium was replaced with sodium (Locke-K⁺, Locke-Mg⁺², and Locke-Ca⁺², respectively). Chloride, replaced with gluconate, was reduced from 164.2 to 4.6 mM (Locke and Locke-Cl⁻, respectively). HEPES was replaced with Tris, and the pH was adjusted to 7.4 with gluconic acid (Locke-HEPES). The removal of K⁺, Mg⁺², or Ca⁺² had no significant effect on cAMP production in any mGlu-Glo cell line (**Figure 23**). Locke-Na⁺ or Locke-HEPES showed nonspecific decreases in cAMP inhibition at all mGlu-Glo cells. In low chloride buffer (Locke-Cl⁻),

Component	Concentration (mM)						
	Locke	Locke-Na ⁺	Locke-Cl ⁻	Locke-K ⁺	Locke-Ca ⁺²	Locke-Mg ⁺²	Locke-HEPES
NaCl	154	-	-	154	156.6	156	154
KCl	5.6	5.6	-	-	5.6	5.6	5.6
CaCl ₂	1.3	1.3	1.3	1.3	-	1.3	1.3
MgCl ₂	1.0	1.0	1.0	1.0	1.0	-	1.0
NaHCO ₃	3.6	-	3.6	3.6	3.6	3.6	3.6
Glucose	5.6	5.6	5.6	5.6	5.6	5.6	5.6
HEPES	20	20	20	20	20	20	-
CholineCl	-	154	-	5.6	-	-	-
CholineHCO ₃	-	3.6	-	-	-	-	-
NaGluconate	-	-	154	-	-	-	-
KGluconate	-	-	5.6	-	-	-	-
Tris	-	-	-	-	-	-	20

Table 11: Composition of Buffers Used to Examine Group II and III mGluR Ion Sensitivity¹³⁰.

glutamate significantly inhibited forskolin-stimulated cAMP production in mGlu3-Glo cells. In contrast, the removal of chloride decreased glutamate efficacy at mGlu4-Glo cells, a result consistent with previously reported work¹⁶⁵. Chloride removal showed no significant effect at any other mGlu-Glo cell line. Because this finding allowed reliable measurements of mGluR3 activation, all subsequent GloSensor assays involving mGluR3 were performed in Locke's buffer containing 4.6 mM chloride (Locke-Cl⁻), whereas all GloSensor assays involving mGluR2, mGluR4, mGluR6, and mGluR8 were performed using traditional Locke's buffer. Unfortunately, mGlu7-Glo cells did not respond to glutamate under any of the conditions described.

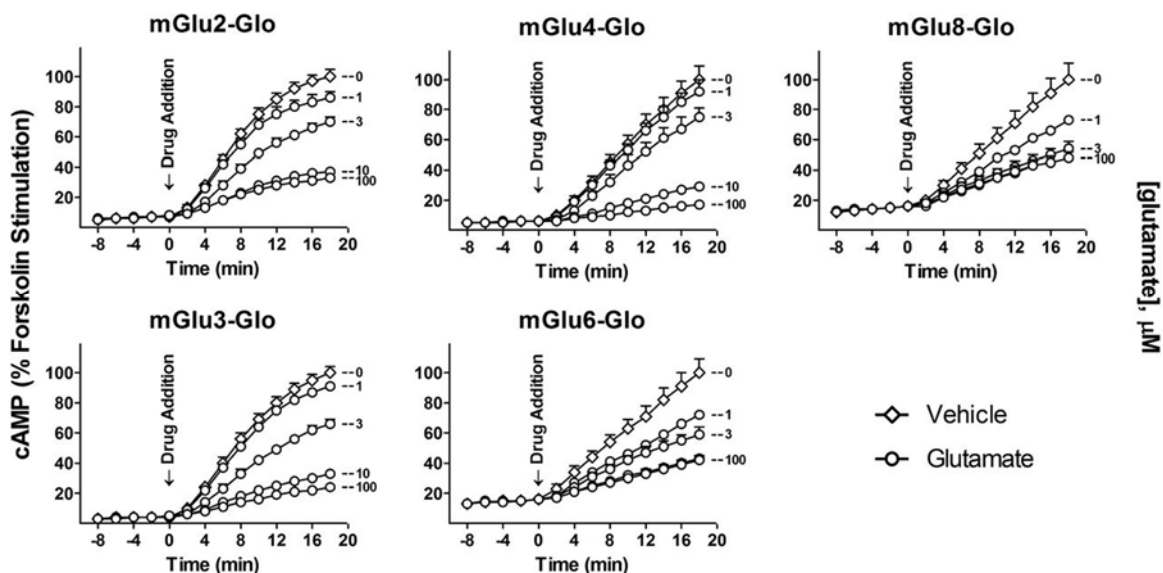


Figure 24: Group II and III mGluR-Mediated Inhibition of cAMP Production¹³⁰. mGlu-Glo cell lines were treated with 1 μ M forskolin and increasing concentrations of glutamate. Concentration-dependent decreases in RLU were observed at all mGlu-Glo cell lines. Data from each treatment was normalized to its own basal luminescence. Data are presented as the mean \pm S.E.M. of three individual experiments performed in triplicate.

When assayed in normal Locke's buffer at mGlu2-, mGlu4-, mGlu6-, and mGlu8-Glo and Locke-Cl⁻ at mGlu3-Glo cells, all cell lines showed glutamate-mediated, concentration-dependent decreases in forskolin-stimulated cAMP production in real time (**Figure 24**). By 8 min after drug addition, glutamate-mediated decreases in cAMP production were proportional at all subsequent time points. Data from the 16 min time point showed the best signal-to-noise ratio and were therefore used for all concentration-response curves (**Figure 25**). To ensure that effects on cAMP levels were entirely mediated by mGluR activation of $G\alpha_{i/o}$ proteins, the ability of glutamate to inhibit cAMP production

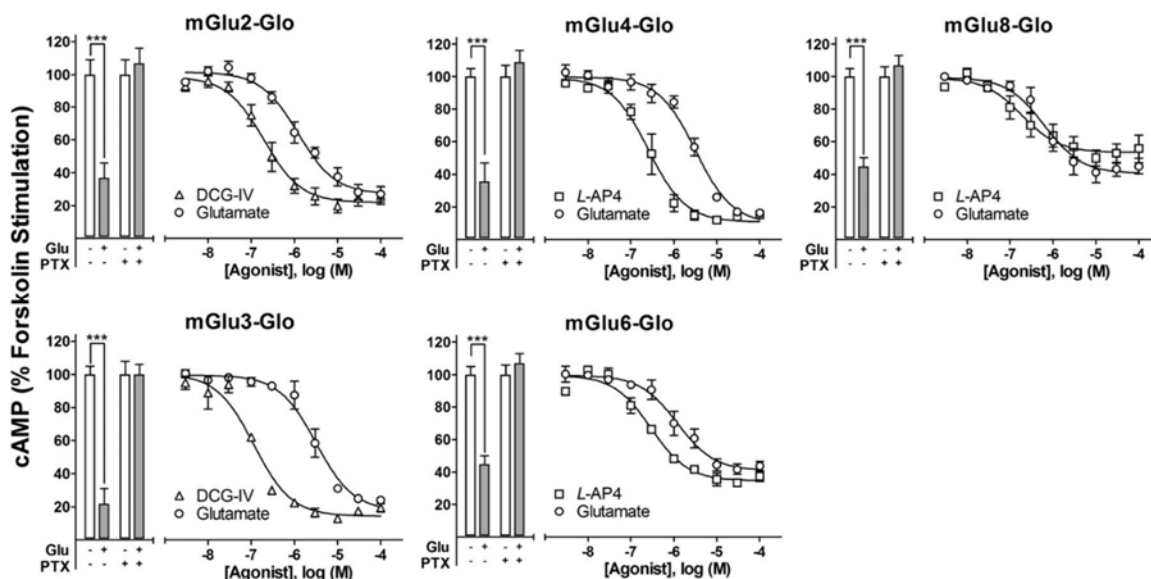


Figure 25: Concentration-Dependent, PTX-Sensitive, Agonist-Mediated mGluR Activation¹³⁰. mGlu-Glo cells were pretreated with (or without) PTX before each assay. Vehicle (white bars) or 100 μ M glutamate (gray bars), \pm PTX, were normalized to their respective vehicle-treated values. mGlu-Glo cell lines were treated with vehicle or increasing concentrations of mGluR agonists, glutamate, or either DCG-IV or AP4. Statistical significance was assessed by a Student's t test. Data for concentration-response curves were normalized to vehicle-treated values. Data are presented as the mean \pm S.E.M. of three individual experiments performed in triplicate. *** $P < 0.001$.

was measured in the presence of pertussis toxin (PTX). PTX, which alone had no effect on forskolin-stimulated cAMP production in CHO-Glo cells, is a bacterial exotoxin that inactivates $G\alpha_{i/o}$ proteins via ADP-ribosylation of $G\alpha_{i/o}$ subunits. As previously demonstrated, 100 μ M glutamate was sufficient to significantly reduce cAMP levels at all mGlu-Glo cell lines (**Figure 23**). However, in cells pretreated overnight with 1 mg/mL PTX, glutamate failed to inhibit cAMP production (**Figure 25**, bars). These results indicate that inhibition of cAMP production in mGlu-Glo cell lines is receptor-mediated and entirely modulated by $G\alpha_{i/o}$ proteins. To further characterize these cell lines, the potencies of two agonists were determined at each receptor. All cell lines were assayed with the endogenous mGluR agonist glutamate. Additionally, mGlu2- and mGlu3-Glo cell lines were assayed with the group II mGluR-selective agonist DCG-IV; mGlu4-, mGlu6-, and mGlu8-Glo cell lines were assayed with the group III mGluR-selective agonist AP4 (Fig. 4). As expected, both DCG-IV and AP4 were more potent than glutamate at their respective receptors, as indicated by EC_{50} values calculated for glutamate, DCG-IV, and AP4 (**Table 12**). Additionally, DCG-IV and AP4 were inactive up to 100 μ M at group

III and group II mGluRs, respectively, and agonist potencies measured via GloSensor assay were comparable to EC₅₀ values reported in the literature⁸⁶.

Receptor	Glutamate (μM)			DCG-IV (μM)			AP4 (μM)		
	EC ₅₀	95% CI	Reported	EC ₅₀	95% CI	Reported	EC ₅₀	95% CI	Reported
mGluR2	2.9	1.8-4.7	4-20	0.91	0.50-1.7	0.3	> 100	-	> 100
mGluR3	3.2	2.4-4.3	4-5	0.87	0.79-0.96	0.2	> 100	-	> 100
mGluR4	3.9	2.2-6.9	3-20	> 100	-	> 100	0.26	0.16-0.42	0.4-1.2
mGluR6	1.2	0.67-2.1	16	> 100	-	> 100	0.28	0.19-0.42	0.9
mGluR8	0.62	0.35-1.1	0.02	> 100	-	> 100	0.19	0.06-0.56	0.4

Table 12: Comparison of Previously Reported Agonist Potencies with those from GloSensor¹³⁰. Ranges of glutamate, DCG-IV, and AP4 of EC₅₀ values were reviewed in the literature⁹⁷.

To ensure that decreases in cAMP mediated by agonists were attributed to receptor-specific, orthosteric interactions, competition assays were performed to determine whether the competitive antagonist LY341495 would reverse glutamate-mediated inhibition of cAMP production. Vehicle, glutamate (100 μM), or LY341495 (1 μM) was added to mGlu-Glo cells, and light output was measured every 2 min for 18 min (**Figure 26**). A second drug treatment (vehicle, 1 mM glutamate, or 10 μM LY341495) was applied 18 min after the first addition, and light output was measured every 2 min for 18 min. Ten-fold higher concentrations of drug were used during the second treatment to ensure full competition with the prior treatment. During the first addition (time = 0-18 min), glutamate prevented cAMP production in all mGlu-Glo cell lines, but not in CHO-Glo cells. Notably, treatment with the antagonist LY341495 showed inverse efficacy during the first addition, increasing cAMP production above vehicle treatment in mGlu4-, mGlu6-, and mGlu8-Glo cell lines, suggesting its action as an inverse agonist. After the second addition (time = 18-36 min), glutamate inhibited cAMP production in all vehicle-treated and LY341495-treated mGlu-Glo cells, but not in CHO-Glo cells. Additionally after the second addition, glutamate-treated mGlu-Glo cells challenged with LY341495 not only reversed glutamate-mediated inhibition of cAMP production, but also showed inverse agonism at all

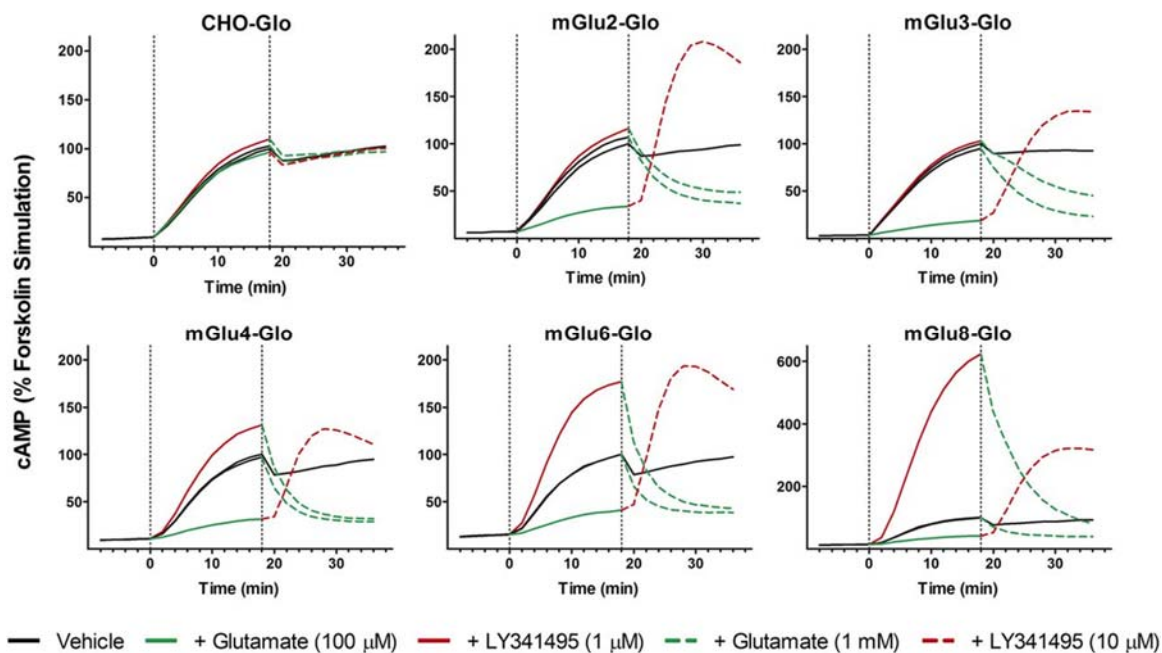


Figure 26. Real-Time Reversibility of Agonist and Antagonist Effects on cAMP Production¹³⁰. CHO-Glo or mGlu-Glo cells were pre-equilibrated with the substrate in Locke's buffer (Locke 4.6 at mGlu3-Glo), and basal luminescence was measured as before. Vehicle (black line), glutamate (100 μ M, green dashed line), or LY341495 (1 μ M, red dashed line) was added first. A second treatment of vehicle (black line), glutamate (1 mM, green, solid line), or LY341495 (10 μ M, red solid line) was added at 18 min. For the sake of clarity, S.E.M. is not shown, but averaged 8% through the experiment. Data are presented as the means of three individual experiments performed in triplicate.

cell lines. Interestingly, inverse agonism was present in mGlu2- and mGlu3-Glo cell lines only when LY341495 was added to agonist treated cells, whereas mGlu4-, mGlu6-, and mGlu8- Glo cell lines showed inverse agonism both in the presence and in the absence of agonist. After the second treatment, nonspecific, transient decreases in RLU signal, probably due to volume change in the wells, were observed at all cell lines, including the control CHO-Glo cell line. Decreases in luminescence were also observed after 30 min for all mGlu-Glo cell lines, a phenomenon that was likely due to phosphodiesterase activity. To further examine the behavior of antagonists, LY341495 was used at increasing concentrations to shift the concentration-response curve of glutamate at mGluR3 (**Figure 27**). As expected for this competitive antagonist, a rightward shift in the glutamate concentration-response curve was observed with increasing concentrations of LY341495. Each curve was normalized to its own maximal RLU in the absence of glutamate, and glutamate EC_{50} values were determined at

each concentration of LY341495. On the basis of these calculations, a Schild plot was constructed, yielding a K_b of LY341495 at rat mGluR3 of 1.8 nM, which is comparable to the LY341495 affinity¹⁶⁶ (0.75 nM) determined empirically using transfected human mGluR3.

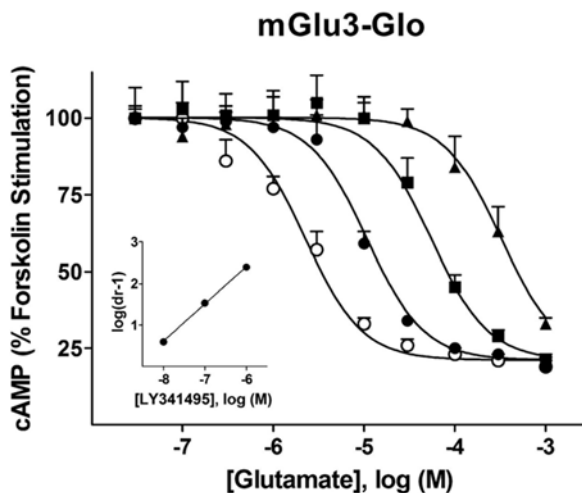


Figure 27: Quantitation of mGluR Antagonist Potency Using GloSensor¹³⁰. mGlu3-Glo cells were pre-equilibrated with substrate in Locke-Cl⁻. Increasing concentrations of glutamate were added, without or with several concentrations of LY341495 (0 M, white circles; 10⁻⁸ M, black circles; 10⁻⁷ M, black squares; 10⁻⁶ M, black triangles). The K_b values were calculated using GraphPad Prism software. (Inset) A Schild plot is shown where dr indicates dose ratio and the values of dr-1 are plotted versus antagonist concentration. Data are mean presented as the mean \pm S.E.M. of three individual experiments performed in triplicate.

The GloSensor cAMP assay, which is represented schematically in **Figure 28**, provides several advantages over other methods for measuring mGluR activation: (1) every assay that has measured mGluR-mediated $G\alpha_{i/o}$ activity has been an endpoint assay, requiring phosphodiesterase inhibitors to facilitate quantitation of total cAMP produced. In contrast, the GloSensor method measures cAMP production in real time. This novelty enables pharmacological stimulation and inhibition of receptor activity on the same cells in the same assay, demonstrating the competitive and reversible nature of orthosteric ligands acting at group II and III mGluRs. (2) The GloSensor method allows direct, functional measurements of the classic signaling pathway modulated by group II and group III mGluRs. Although competition binding assays allow for measurements of ligand affinity, they do not address any functional properties associated with the ligand, thereby disallowing definition of a ligand

as an agonist, partial agonist, antagonist, or inverse-agonist. Furthermore, alternative methods focus on measurement of noncanonical $G\beta\gamma$ -mediated potassium flux as a substitute indicator for receptor activation. (3) In contrast to many electrophysiological and biophysical methods, the GloSensor method does not require expensive equipment, as all measurements can be performed with any luminescence detector. The substrate D-luciferin is inexpensive, and experiments were performed using several luciferin salts, all of which produced similar results. Additionally, setup and assay times are particularly short, making GloSensor an efficient assay paradigm that can facilitate rapid and reliable measurements of ligand activity in a high-throughput screening format.

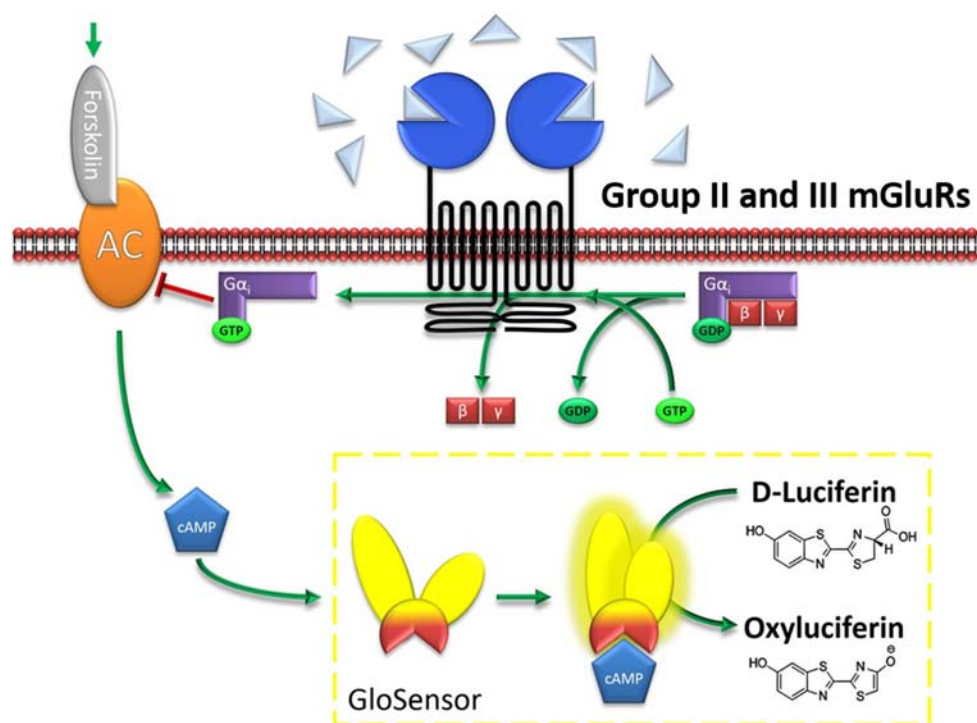


Figure 28. Schematic Representation of the GloSensor Assay¹³⁰. Forskolin stimulates cAMP production via AC. cAMP binding to the GloSensor construct causes a conformational shift that increases luciferase activity, whereby the D-luciferin substrate is oxidized to produce oxyluciferin and light. Agonist stimulation of group II or group III mGluRs activates heterotrimeric $G_{i/o}$ proteins, where the liberated α -subunit then inhibits AC activation. Agonist activity is measured as decreased light output relative to vehicle treatment.

2.2.d. *mGluR3* Activity of NAAG and Analogs

With the GloSensor assay established, NAAG and analogs **51**, **52**, and **53** were evaluated for activity at mGluR3. Although full mGluR3 activation resulted from treating mGlu3-Glo cells with a saturating concentration (100 μ M) of glutamate (**Figure 29**), none of the synthetic dipeptides, including NAAG, decreased forskolin-stimulated cAMP levels at 1 mM drug concentrations. Additionally, a robust inverse agonist response resulted from treatment with a saturating concentration of LY341495 (1 μ M), indicating that NAAG, **51**, **52**, or **53** did not inhibit mGluR3 activity. Notably, addition of high concentrations of NAAG to mGlu3-Glo cells that were incubated in either normal Locke's buffer or in Locke's buffer with low chloride concentration did not lead to mGluR3 activation in either case. Despite the large body of literature describing measurements of $G\alpha_{i/o}$ -mediated AC inhibition that supports NAAG as a selective agonist of mGluR3¹⁴⁹, several alternative reports involving measurement

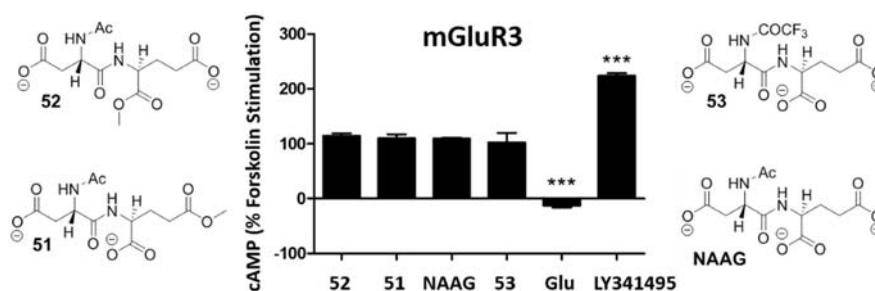


Figure 29. Activity of NAAG and Analogs and mGluR3. mGlu3-Glo cells were treated with 100 μ M glutamate, 1 μ M LY341495, 1 mM NAAG, or 1 mM NAAG analog, and inhibition of forskolin-stimulated cAMP production was evaluated using the GloSensor assay. Glutamate-mediated decrease and LY341495-mediated increase in cAMP production were statistically significant ($P < 0.01$). NAAG and analogs did not stimulate mGluR3-mediated AC inhibition like glutamate, nor did they act as inverse agonists at mGluR3 like LY341495. Statistical differences in the data were assessed by a Student's *t* test. Data are presented as the mean \pm S.E.M. of three individual experiments performed in triplicate. *** $P < 0.001$.

of $G\beta\gamma$ signaling claim that NAAG does not activate mGluR3¹⁶⁷. As the multifaceted signaling profiles of 7TMRs continue to complexify, it is becoming clear that all agonists, even orthosteric agonists for the same receptor subtype, do not interact and function in an equal manner¹⁴⁸. Thus, while these results

are not inconsistent per se, the NAAG controversy has pervaded the literature for over two decades, and unfortunately, preliminary evaluation using the newly implemented GloSensor assay was unable to rectify these issues. However, as NAAG-mediated mGluR3 activity has been measured inconsistently using different cell types and different assay systems, it is possible that NAAG successfully activates mGluR3 in some settings but not others. For instance, this discrepancy could be explained with the requirement of some sort of cofactor, an endogenous small molecule, peptide, or protein that exists in some cell types but not others. One provocative hypothesis was reported to involve colocalization and association of mGluR3 with endogenous NAAG peptidase, both of which have been shown on astrocytic membranes¹⁶⁸. It was further proposed by the same author that endogenous NAAG is actually a protected glutamate that does not signal through post-synaptic neurons, but rather survives long enough to translocate outside of the synaptic cleft to astrocytes¹⁶⁹. Here, NAAG could interact with the putative mGluR3-NAAG peptidase complex, and then be cleaved by NAAG peptidase into *N*-acetylaspartate and glutamate, which could then stimulate proximal mGluR3. While this would be quite an interesting hypothesis to examine, the inactivity of NAAG at mGluR3 in the GloSensor assay ultimately rendered it a poor lead compound with which to discover novel mGluR3-selective agonists with neuroprotective properties, at least until a more detailed understanding of endogenous NAAG activity is achieved.

2.2.e. Group II mGluR Antagonist-Mediated Inverse Agonism. Some of the information presented in the section is reprinted¹⁷⁰ with permission of the American Society for Pharmacology and Experimental Therapeutics. All rights reserved. Copyright © 2015 by the American Society for Pharmacology and Experimental Therapeutics.

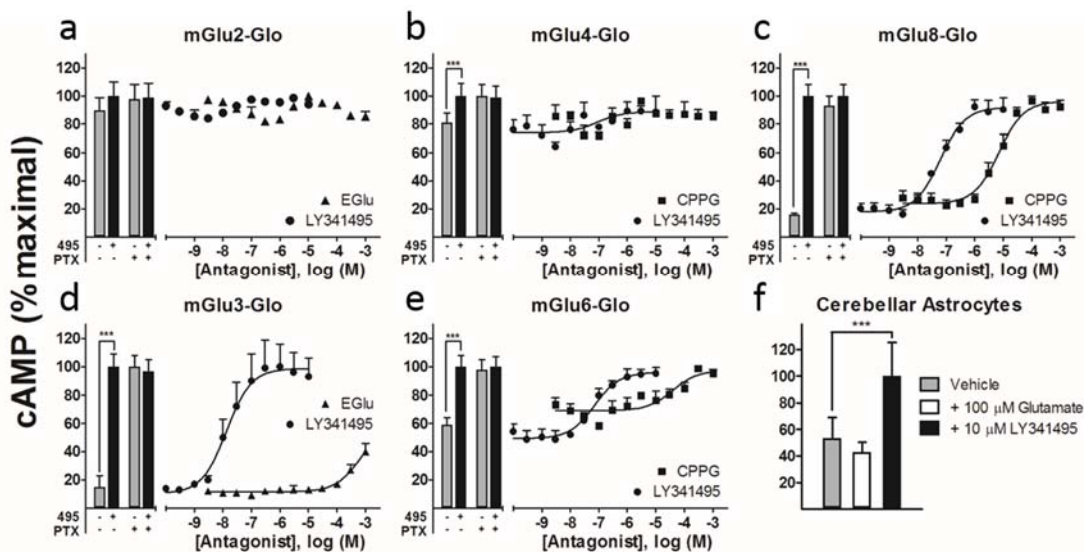
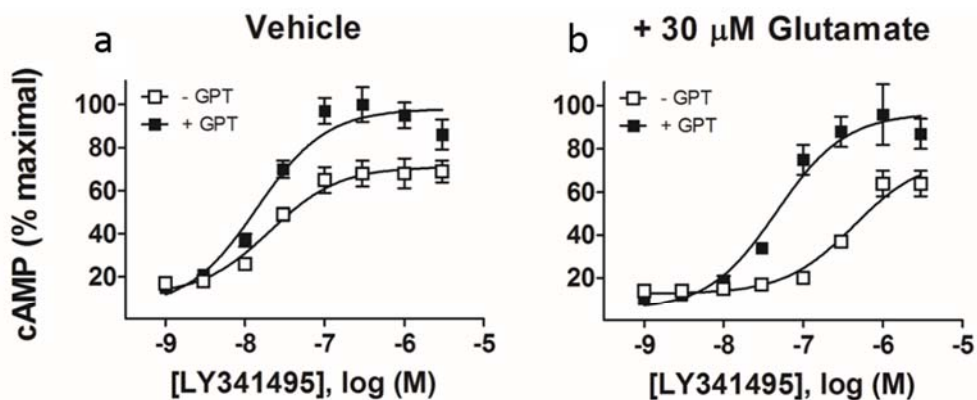


Figure 30. Group II and III mGluR Antagonist-Mediated, PTX-Sensitive Inverse Agonism¹⁷⁰. (a-e, bars) The nonselective, competitive antagonist LY341495 (10 μ M), significantly increased forskolin-stimulated cAMP levels in mGlu3-, mGlu4-, mGlu6-, and mGlu8-, but not mGlu2-, Glo cell lines. When these cell lines were pretreated with PTX however, this apparent inverse agonism was absent. Maximal cAMP production was independently normalized in the absence of or presence of PTX. (a-e, curves) Concentration-response curves of LY341495 demonstrate dose-dependence, and concentration-response curves of either EGlu or CPPG demonstrate specificity for group II and III mGluRs, respectively. cAMP levels, stimulated with 1 μ M forskolin, were measured by the GloSensor method. (f) In primary cultures of rat cerebellar astrocytes, treatment with 10 μ M LY341495 significantly increased cAMP levels, indicating a similar disinhibition of AC as observed in mGlu-Glo cells. cAMP levels, stimulated with 1 μ M forskolin were measured by the LANCE method and calculated relative to a cAMP standard curve. Data are normalized to maximal cAMP levels and are presented as the mean \pm S.E.M. of three individual experiments performed in triplicate. Statistical significance was assessed using a two-tailed Student's *t*-test. *** $P < 0.001$.

Despite this negative result, the fact that chloride effected mGluR3 activity but not mGluR2 activity was quite intriguing. If this difference stemmed from direct interaction between chloride and mGluR3 but not mGluR2, identification of the structural determinants of chloride selectivity could translate into a strategy for achieving selective mGluR3 activation. Therefore, the effect of chloride on mGluR3 but not mGluR2 activity, which appeared to be related to LY341495-mediated inverse agonism, became the subject of subsequent evaluation. During GloSensor assay development¹³⁰, group II and III mGluR competitive antagonist LY341495 was observed to significantly increase forskolin-stimulated cAMP production, relative to vehicle treatment, in mGlu3-, mGlu4-, mGlu6-, and mGlu8-, but not mGlu2-, Glo cell lines¹⁷⁰ (Figure 30a-e, bars). Pretreatment with PTX completely eliminated

the effect of LY341495, indicating that this antagonist-mediated increase in cAMP was due to $G\alpha_{i/o}$ signaling, and resulted from a disinhibition of AC. Concentration-response curves of LY341495, EGlu, and CPPG demonstrated dose-dependence (*Figure 30a-e*, curves), confirming that inverse agonism was mGluR-mediated and was not unique to LY341495. These results encouraged the determination of whether LY341495 could disinhibit cAMP production in a native system. Indeed, in primary cultures of cerebellar astrocytes, LY341495 increased forskolin-stimulated cAMP levels (*Figure 30f*), and furthermore, glutamate did not significantly inhibit cAMP production. These results are consistent with those in transfected cells, which could indicate that antagonists of mGluR3, mGluR4, mGluR6, and mGluR8 are actually inverse agonists of high constitutive GPCR activity ($\approx 80\%$ at mGluR3 and mGluR8).



Vehicle				Vehicle + 30 μ M Glutamate			
Treatment	EC_{50} (nM)	95% C.I.	P Value	Treatment	EC_{50} (nM)	95% C.I.	P Value
- GPT	20.6	10.5-40.2	0.38	- GPT	431	239-778	0.00015
+ GPT	14.1	7.70-25.8		+ GPT	46.4	24.3-88.7	

Figure 31: Antagonist-Mediated, Glutamate-Independent Inverse Agonism at mGluR3¹⁷⁰. (a) Concentration-response curves of LY341495 in the absence or presence of GPT show no statistical difference in antagonist potency in mGlu3-Glo cells. (b) When spiked with 30 μ M glutamate, concentration-response curves of LY341495 in the absence of GPT show a 9-fold rightward shift in antagonist potency, relative to the presence of GPT. EC_{50} values of LY341495 were statistically different in the absence versus in the presence of GPT. For experiments represented in both panels, relative increases in LY341495 efficacy were observed in the presence of GPT. Cells were incubated in DMEM buffer in the absence or presence of GPT for 4 hrs prior to assay. EC_{50} values were calculated using the four parameter logistic equation. Statistical significance was assessed using a two-

tailed Student's *t*-test. Data are presented as the mean \pm S.E.M. of three individual experiments performed in triplicate.

Alternatively, antagonists could have been competing with residual glutamate. Therefore, experiments were performed using glutamate-pyruvate transaminase (GPT), an enzyme that converts glutamate to an inactive metabolite, α -ketoglutarate. Concentration-response curves of LY341495 at mGluR3 showed statistically indistinguishable potencies in the absence ($EC_{50} = 21$ nM) and presence ($EC_{50} = 14$ nM) of GPT (**Figure 31a**). In the presence of 30 μ M glutamate, however, the concentration-response curve of LY341495 was shifted 9-fold to the right ($EC_{50} = 420$ nM) without GPT, relative to the control ($EC_{50} = 47$ nM) with GPT (**Figure 31b**). If antagonist-mediated efficacy were due to competition with residual glutamate, LY341495 potency would be statistically different in the presence of GPT, or LY341495 efficacy would be absent. In contrast, no statistical change in potency or efficacy was observed. These results indicate that the antagonist-mediated efficacy was not due to competition with glutamate; rather, it represents either true inverse agonism of constitutive group II and III mGluR activity, or competition with an unidentified agonist.

2.2.f. Pharmacological Characterization of Chloride. Some of the information presented in the section is reprinted¹⁷⁰ with permission of the American Society for Pharmacology and Experimental Therapeutics. All rights reserved. Copyright © 2015 by the American Society for Pharmacology and Experimental Therapeutics.

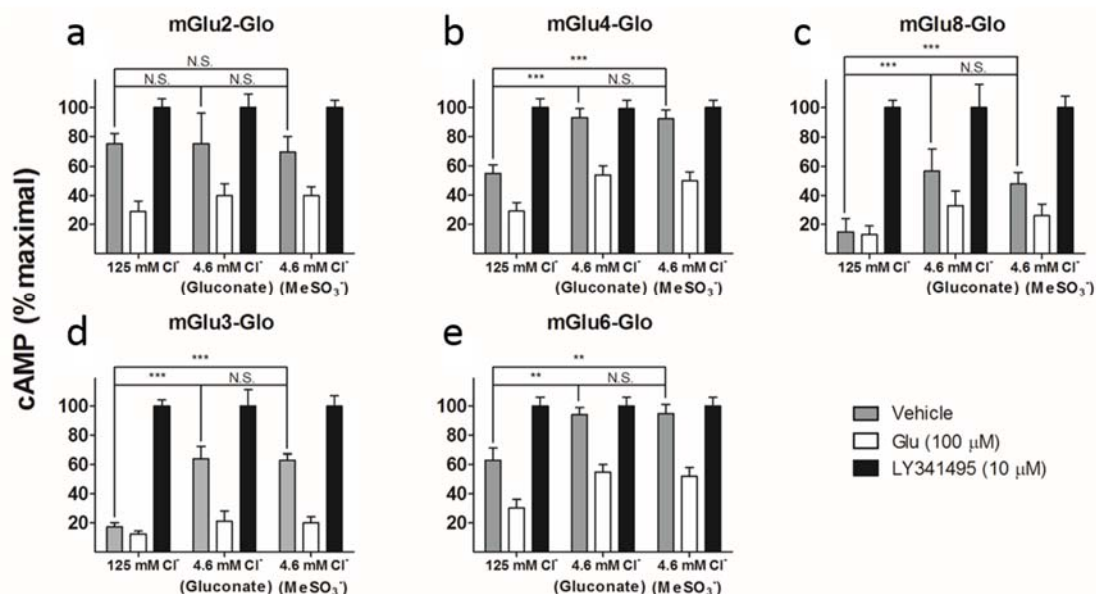


Figure 32. Chloride-Specific Activity at Group II and III mGluRs¹⁷⁰. (a) cAMP levels modulated by 100 μM glutamate or 10 μM LY341495 in mGlu2-Glo cells are unaffected by chloride, gluconate, or methanesulfonate. (b) cAMP levels modulated by glutamate or LY341495 in mGlu3-Glo cells are identical in 4.6 mM chloride, whether chloride is replaced with gluconate, methanesulfonate, or bicarbonate. (c-e) cAMP levels modulated by 100 μM glutamate or 10 μM LY341495 in mGlu3-, mGlu4-, mGlu6-, and mGlu8-Glo cells are significantly different in 125 mM vs. 4.6 mM chloride. However, cAMP levels modulated by glutamate or LY341495 in mGlu4-, mGlu6-, and mGlu8-Glo cells are identical in 4.6 mM chloride, whether chloride is replaced with gluconate, or methanesulfonate. All data are normalized to maximal forskolin-stimulated cAMP levels, for each buffer condition. Data are presented as the mean ± S.E.M. of three individual experiments performed in triplicate. Statistical significance was assessed using a two-tailed Student's *t*-test. ** *P* < 0.01, *** *P* < 0.001.

Replacement of chloride with gluconate was previously described to improve agonist efficacy at mGluR3¹³⁰ (Figure 23). To determine that this effect was, in fact, due to chloride removal as opposed to gluconate addition, experiments were performed using structurally distinct anion substitutions. Substitution of chloride with gluconate or methanesulfonate at all receptors, as well as bicarbonate at mGluR3, revealed statistically indistinguishable results at each group II and III mGluR

type examined (*Figure 32*), confirming that this effect was chloride-specific. To investigate the effects of chloride on the activation of these receptors, buffers containing increasing concentrations of chloride (replaced with gluconate) were employed. To compare chloride concentration-response curves between different cell lines, data were normalized to maximal cAMP production at each chloride concentration. As a negative control, a saturating concentration (10 μ M) of the competitive antagonist LY341495 was employed to measure receptor-independent cAMP production. Additionally, a saturating concentration of glutamate (1 mM) was used as a positive control to establish the maximal

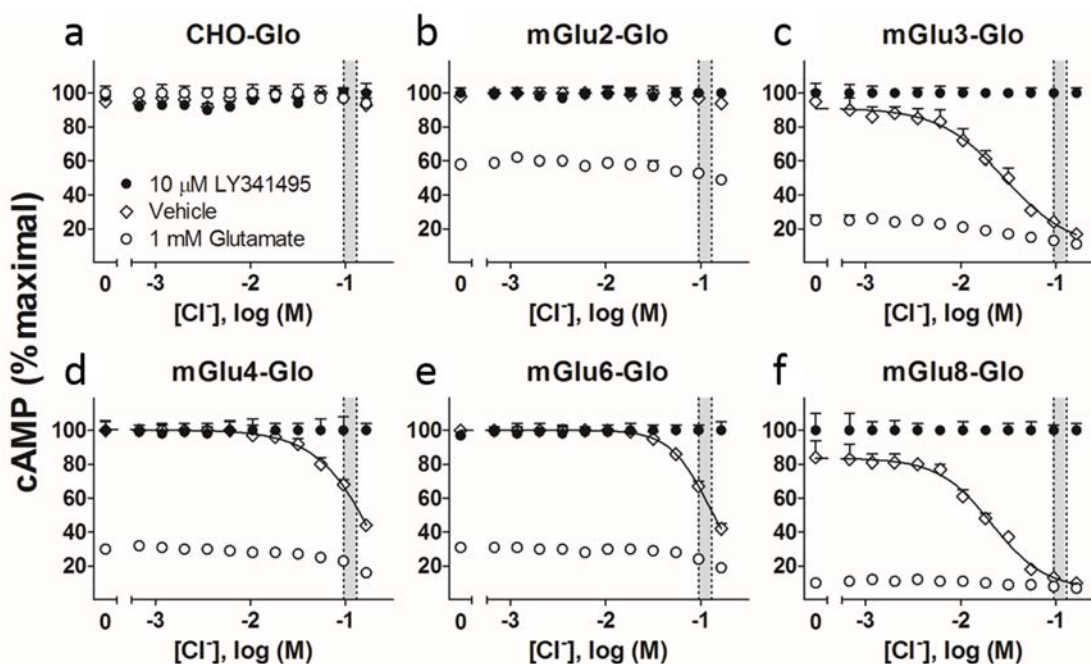


Figure 33. Chloride Activation of mGluR3, mGluR4, mGluR6, and mGluR8, but not mGluR2¹⁷⁰. (a) cAMP levels in CHO-Glo cells were unaffected by 10 μ M LY341495 or 1 mM glutamate, regardless of chloride concentration. (b) cAMP levels in mGlu2-Glo cells were reduced by glutamate, but unaffected by LY341495 or chloride. (c-f) cAMP levels in mGlu3-, mGlu4-, mGlu6-, and mGlu8-Glo cells were reduced by 1 mM glutamate, and by chloride in a concentration-dependent manner. Chloride EC_{50} values were calculated to be 29.0 mM, \sim 275 mM, \sim 120 mM, and 21.1 mM at mGluR3, mGluR4, mGluR6, and mGluR8, respectively. Data were normalized independently at each chloride concentration to the maximal cAMP resulting from either LY341495, vehicle, or glutamate treatment. Gray bars represent the physiological range of chloride, from 95 to 125 mM. EC_{50} values were calculated using the four parameter logistic equation. Data are presented as the mean \pm S.E.M. of three individual experiments performed in triplicate and are summarized in *Table 13*.

level of mGluR-mediated inhibition of cAMP production. Using this experimental paradigm, increasing chloride concentrations revealed a concentration-dependent, chloride-mediated activation of mGluR3 ($EC_{50} = 29$ mM), mGluR4 ($EC_{50} \approx 280$ mM), mGluR6 ($EC_{50} \approx 120$ mM), and mGluR8 ($EC_{50} = 21$ mM), but not mGluR2 (**Figure 33b-f**). A summary of EC_{50} values, standard errors, and hill slopes are reported in **Table 13**. Importantly, cAMP levels in CHO-Glo cells were unaffected by 10 μ M LY341495 or by 1 mM glutamate, regardless of chloride concentration (**Figure 33a**). Maximal cAMP inhibition by glutamate was variable between receptor subtypes, possibly due to different transfection or $G_{i/o}$ -coupling efficiencies between cell lines or receptor subtypes, respectively. At mGluR3 and mGluR8, these data indicate that chloride and glutamate inhibit cAMP production with the same degree of efficacy, and that high chloride concentrations produce maximal receptor activation that is neither additive with nor affected by glutamate. Therefore, it was concluded that chloride independently activates mGluR3, mGluR4, mGluR6, and mGluR8, but not mGluR2.

Receptor	Chloride EC_{50} (mM)	Hill Slope
mGluR2	Inactive	Inactive
mGluR3	28.9	-1.26
mGluR4	≈ 275	-1.29
mGluR6	≈ 120	-2.13
mGluR8	21.1	-1.56

Table 13: Quantitation of Chloride-Mediated Group II and III mGluR Activity¹⁷⁰. Chloride EC_{50} values and Hill slopes were calculated from concentration-response curves displayed in **Figure 33**.

It was subsequently hypothesized that the previously reported “putative chloride binding site¹⁷¹” is, in fact, the orthosteric pocket for chloride. Although no crystal structures of mGluR2, mGluR4, mGluR6, or mGluR8 NTDs are available on the PDB, several agonist-bound mGluR3 NTD crystal structures have been published⁸³. Unfortunately, the corresponding x-ray structures do not show chloride occupation of the putative site; rather, this pocket is occupied by a water molecule. In contrast, an unpublished crystal structure of the mGluR3 NTD bound to LY341495 (PDB ID: 3SM9)

does contain a chloride ion in the “putative chloride binding site.” Comparison between the agonist-bound and antagonist-bound structures revealed that the residues comprising this site were identically aligned, and furthermore, that the respective water molecule and chloride ion were oriented precisely. To illustrate the proximity of the “putative chloride binding site” and orthosteric glutamate, **Figure 34a** displays the glutamate-bound crystal structure of the mGluR3 NTD (PDB ID: 2E4U) where the water molecule is colored green to represent chloride. Although it has been proposed that the “putative chloride binding site” may exist at all group II and III mGluRs^{171,172}, data presented in **Figure 34b** indicate that mGluR2 is not activated by chloride. Thus, it was hypothesized that the “putative chloride binding site” present at mGluR3 is disrupted at mGluR2. To preliminarily evaluate this hypothesis, *in silico* mGluR3 model *mGluR3-0H₂O* previously generated using Maestro³⁰ was utilized as a three-dimensional template with which to build a corresponding homology model of mGluR2 (*mGluR2-0H₂O*) using the Prime application¹⁷³ in Maestro. The mGluR3 model lacking all water molecules was

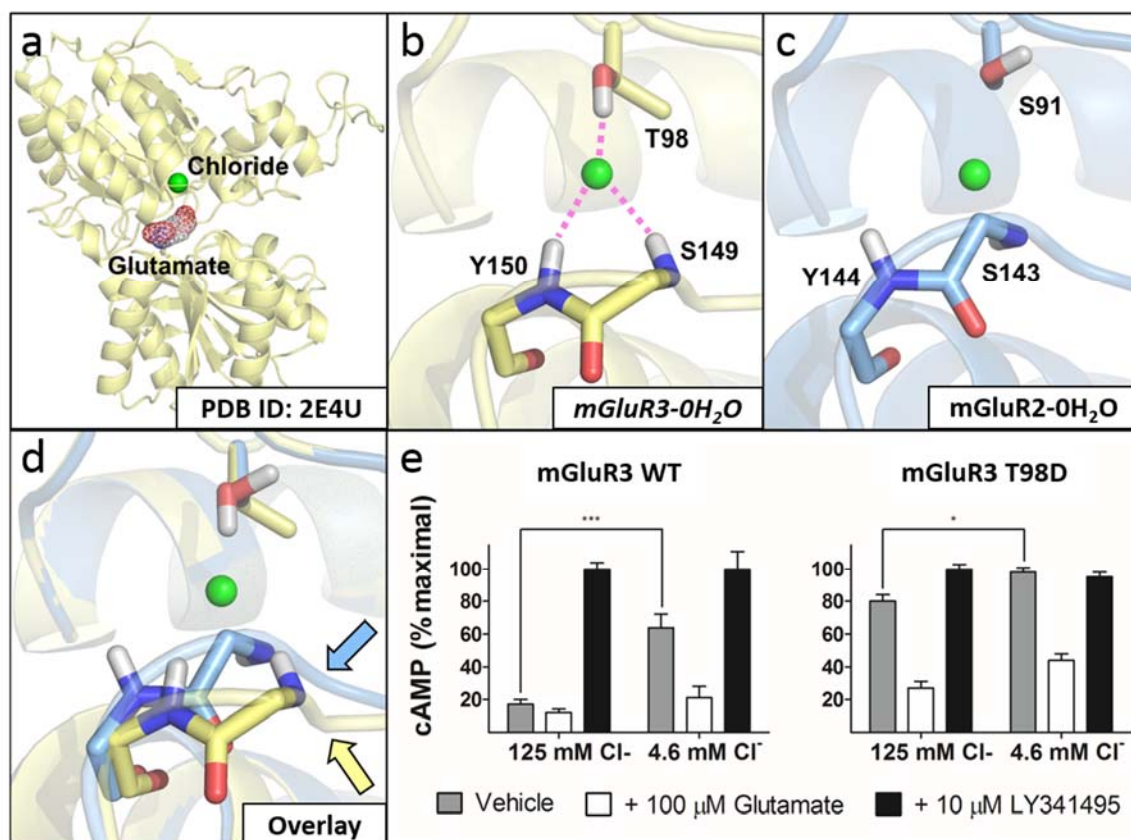


Figure 34. Disruption of the mGluR3 Chloride Binding Pocket at mGluR2¹⁷⁰. (a-d) mGluR3 and mGluR2 are represented in pale-yellow and pale-blue, respectively. Glutamate is displayed as a mesh surface with gray carbons, and chloride (actually a water molecule from agonist-bound structures) is green. (a) The glutamate-bound crystal structure of the mGluR3 NTD⁸³ illustrates the proximity of the orthosteric glutamate and chloride sites. (b) An *in silico* mGluR3 model (*mGluR3-0H₂O*), built from the 1*S*,3*S*-ACPD-bound mGluR3 crystal structure⁸³, is displayed, focusing on the chloride binding pocket. Predicted interactions between chloride and T98, S149, and Y150 are magenta. (c) An *in silico* mGluR2 homology model (*mGluR2-0H₂O*), generated from *mGluR3-0H₂O*, shows no predicted interactions between chloride and S91, S143, and Y144. (d) An overlay of these models demonstrates a backbone shift at mGluR2 (pale-blue arrow), versus mGluR3 (pale-yellow arrow), which disrupts the chloride site at mGluR2. (e) cAMP levels modulated by 100 μ M glutamate or 10 μ M LY341495 in wild-type mGlu3-Glo cells were significantly different in 125 mM versus 4.6 mM chloride, relative to vehicle treatment. However, cAMP levels modulated by glutamate or LY341495 at the mGluR3 T98D mutant were less affected by chloride. Data are presented as the mean \pm S.E.M. of three individual experiments performed in triplicate. Statistical significance was assessed using a two-tailed Student's *t*-test. * $P < 0.05$, *** $P < 0.001$. Modeling figures were generated using PyMOL⁸⁰.

selected over water-containing models to allow maximum flexibility in the binding pocket during homology model construction. Superposition of *mGluR3-0H₂O* with the water molecule (colored green to represent chloride) from PDB ID: 2E4U shows that chloride is appropriately positioned for hydrogen bonding interactions with the polar hydrogen of the T98 side chain, as well as with the polar hydrogens of the Y150 and S149 backbone nitrogens (**Figure 34b**). Alternatively, the corresponding *mGluR2-0H₂O* homology model shows substantial differences in the conformations of analogous residues S91, Y144, and S143 (**Figure 34c**), all of which are improperly aligned for hydrogen bonding interactions with chloride. An overlay of these models (**Figure 34d**) suggests that a backbone shift (indicated with arrows) is responsible for these conformational differences, and ultimately for mGluR2 chloride-insensitivity.

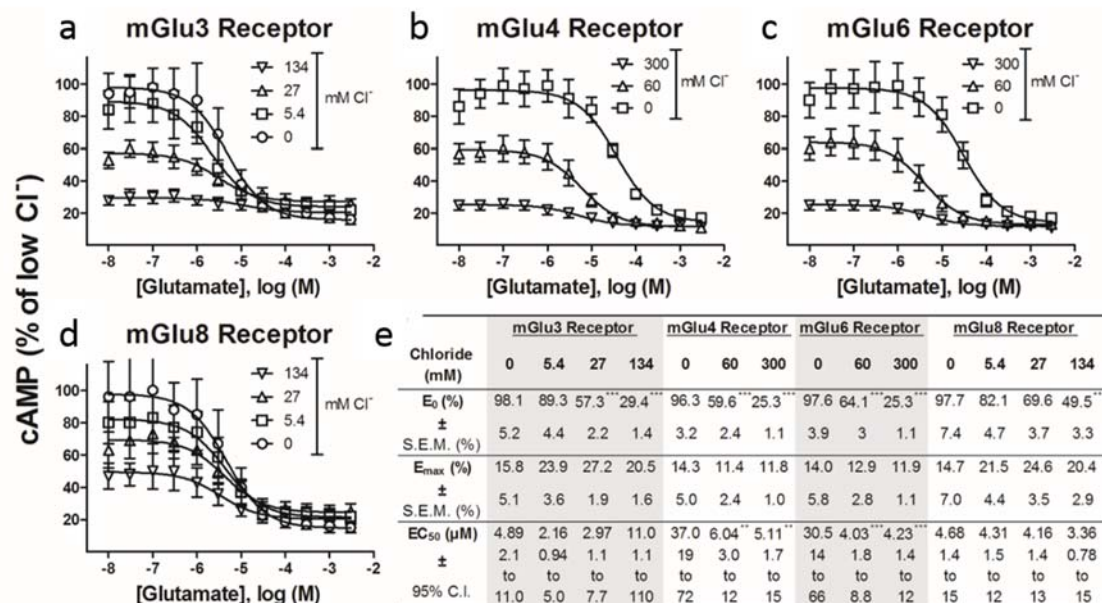


Figure 35: Definition of Chloride as Both an Agonist and a PAM at Group II and III mGluRs¹⁷⁰. (a-d) Concentration-response curves of glutamate in the presence of increasing chloride concentrations (determined for each receptor based on chloride EC_{50} values from **Figure 31**) show an increase in basal cAMP inhibition (E_0) at low glutamate concentrations, but no change in maximal cAMP inhibition (E_{max}) at high glutamate concentrations. The EC_{50} of glutamate was significantly decreased in the absence of chloride at mGluR4 and mGluR6, but was statistically unaffected by chloride at mGluR3 and mGluR8. (e) A table of E_0 , E_{max} , and EC_{50} values highlights statistical differences. All data were normalized as a percent of maximal cAMP levels in the absence of chloride. E_0 , E_{max} , and EC_{50} values were calculated using the four parameter logistic equation. Statistics were calculated using a one-way ANOVA with a Bonferroni post-hoc test, where statistical significance was defined at $P < 0.05$. Data are presented as the mean \pm S.E.M. of three individual experiments performed in triplicate. ** $P < 0.01$, *** $P < 0.001$.

Although the “putative chloride binding site” is strongly implicated as the orthosteric chloride pocket, chloride interaction at this site has never been validated empirically. In principle, mutation of T98 to a larger and negatively charged aspartate residue should sterically and electrostatically preclude chloride function. Accordingly, an mGluR3 T98D mutant, which, unlike wild-type mGluR3, showed considerably less LY341495-mediated inverse agonism ($p = 0.048$) in the presence of 125 mM chloride (**Figure 34e**), as well as a strong response to glutamate treatment, was constructed. Also in contrast to the wild-type receptor, the mutant receptor responded to both drugs in a chloride-independent manner. This not only demonstrates that T98 is critical for chloride binding, but ultimately supports the hypothesis that the “putative chloride binding site” is, in fact, the orthosteric binding pocket for

chloride. Because T98 is conserved as either a threonine or serine at all group II and III mGluRs¹⁷⁰, it is probable that chloride-mediated activation of mGluR4, mGluR6, and mGluR8 also results from chloride binding in this orthosteric region. To further investigate the relationship between the two agonists, glutamate and chloride, concentration-response curves of glutamate at several chloride concentrations were generated (**Figure 35a-d**). The parameters E_{max} , E_0 , and EC_{50} were analyzed for statistically significant differences (**Figure 35e**). The results show no significant difference in the E_{max} of glutamate at mGluR3, mGluR4, mGluR6, or mGluR8, suggesting that glutamate efficacy is unaffected by chloride. However, E_0 increased in response to increasing concentrations of chloride. These data further support that chloride activates mGluR3, mGluR4, mGluR6, and mGluR8 in the absence of glutamate, and that both ligands are agonists of these receptors. Finally, EC_{50} values for glutamate at mGluR4 and mGluR6 were statistically different with increasing chloride, suggesting that chloride acts as a positive allosteric modulator (PAM) of glutamate activity at these receptors. In contrast, the EC_{50} values of glutamate at mGluR3 and mGluR8 were statistically unaffected.

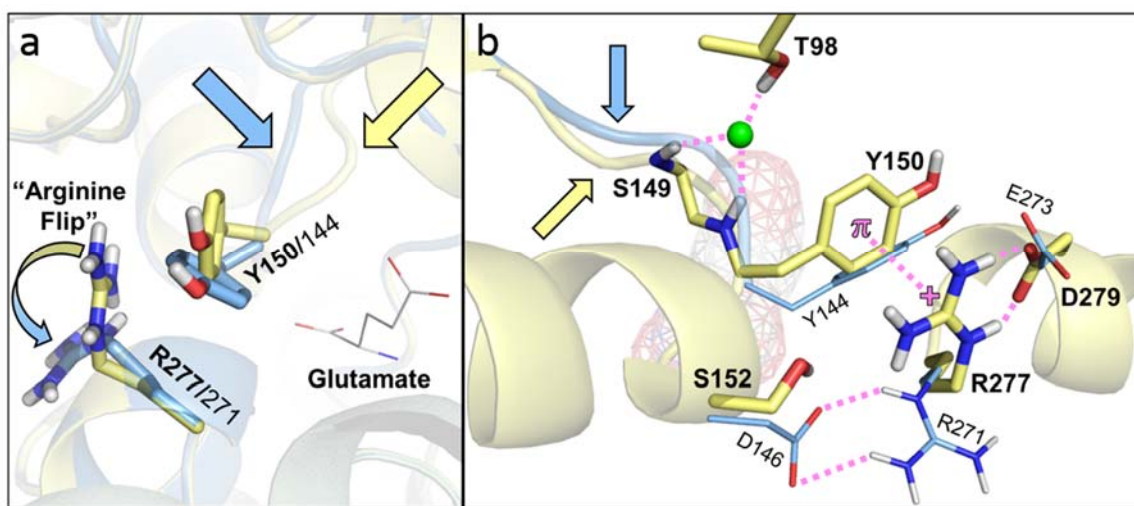


Figure 36. “Arginine Flip”-Mediated Chloride Discrimination between mGluR3 and mGluR2¹⁷⁰. (a) Overlay of *mGluR3-0H₂O* (pale-yellow) and *mGluR2-0H₂O* (pale-blue) *in silico* models reveals strikingly different conformations of R277/R271. This “Arginine Flip” (curved arrow) alters the conformation of Y150/Y144, which causes a backbone to diverge between mGluR2 (pale-blue arrow) and mGluR3 (pale-yellow arrow). Glutamate (gray carbons) illustrates proximity to the orthosteric glutamate site. (b) The mGluR3 model (pale-yellow) shows a π -cation interaction between R277 and Y150, and that D279 (E273 at mGluR2) stabilizes the conformation of R277 via a salt bridge.

The mGluR2 homology model (pale-blue) shows that the “Arginine Flip” precludes a π -cation interaction with Y144 because R271 is stabilized by a salt bridge with D146 (S152 at mGluR3). Furthermore, this overlay of glutamate, chloride, *mGluR3-0H₂O* (pale-yellow), and *mGluR2-0H₂O* (pale-blue) illustrates the structural differences that chloride exploits to selectively activate mGluR3, but not mGluR2. At mGluR3, the orientation of Y150 aligns S149 and T98 appropriately to bind chloride. At mGluR2 however, the conformation of Y144 facilitates a backbone shift (pale-blue arrow), relative to mGluR3 (pale-yellow arrow), which disrupts the chloride binding site. Glutamate is displayed as a mesh surface (gray carbons) to convey proximity to the orthosteric glutamate site, and molecular interactions are colored magenta. Modeling figures were generated using PyMOL⁸⁰.

Preliminary comparison *mGluR3-0H₂O* with the corresponding *mGluR2-0H₂O* homology model illustrated a change in backbone conformation that appears to preclude chloride binding at mGluR2 (**Figure 34d**). Further analysis revealed that this backbone shift stems from a stark conformational difference between corresponding arginine and tyrosine residues, R277/Y150 and R271/Y144, at *mGluR3-0H₂O* and *mGluR2-0H₂O*, respectively (**Figure 36a**). The mGluR3 model shows that R277 interacts with Y150, one of the key residues in the orthosteric chloride pocket, via a π -cation interaction (**Figure 36b**). At the mGluR2 model however, R271 adopts a conformation that precludes a π -cation interaction, causing Y144 to adopt a different orientation that leads to the aforementioned backbone shift. Consequently, this “Arginine Flip,” which appears to be mediated by two homologous amino acids that are different between mGluR2 and mGluR3, disrupts the orthosteric chloride site at mGluR2. While the conformation of R277 at mGluR3 is stabilized by a salt bridge with D279 (E273 at mGluR2), the orientation of R271 at mGluR2 is stabilized by a salt bridge with D146 (S152 at mGluR3). As D146 is a unique residue of mGluR2 (a conserved serine at all other mGluRs¹³⁰), it was hypothesized that D146 and S152 are responsible for chloride discrimination between mGluR2 and mGluR3. To test this hypothesis empirically, an mGluR2 D146S mutant and the corresponding mGluR3 S152D mutant were constructed. In support of the hypothesis, and in contrast to wild-type mGluR2 (**Figure 37a**), the D146S mutant, was activated by chloride (**Figure 37c**). The converse mutation at mGluR3 (S152D) however, resulted in a chloride-insensitive, constitutively active mutant receptor (**Figure 37d**). Based on this unexpected constitutive activity, the hypothesis was broadened to include E273 and D279 as residues responsible for chloride discrimination between mGluR2 and mGluR3, respectively. Accordingly, a new series of mGluR2 mutants (E273D and D146S/E273D)

and corresponding mGluR3 mutants (D279E and S152D/D279E) were constructed. The mGluR2 E273D mutant was chloride-insensitive (**Figure 38a**), similar to the wild-type mGluR2. The mGluR3 D279E mutant however, showed a rightward shift in chloride potency (**Figure 38b**), suggesting that the larger glutamate residue partially destabilizes the π -cation interaction between Y150 and R277, relative to wild-type mGluR3. The mGluR2 D146S/E273D mutant (**Figure 38c**) showed similar chloride-sensitivity to that observed at the mGluR2 D146S mutant, suggesting that E273 does not participate in stabilizing the conformation of R271. Conversely, the mGluR3 S152D/D279E mutant was neither chloride-sensitive nor constitutively active (**Figure 37e**), effectively resulting in a singly-mutated mGluR3 that behaved like wild-type mGluR2. These results demonstrate that the sole structural determinant of chloride-insensitivity at mGluR2 is D146, which facilitates the R271 “Arginine Flip,” thereby precluding a π -cation interaction with Y144. These findings strongly suggest that the π -cation interaction between R277 and Y150 structurally rigidifies the orthosteric chloride site at mGluR3, and that the absence of a similar interaction at mGluR2 prevents chloride-mediated activation.

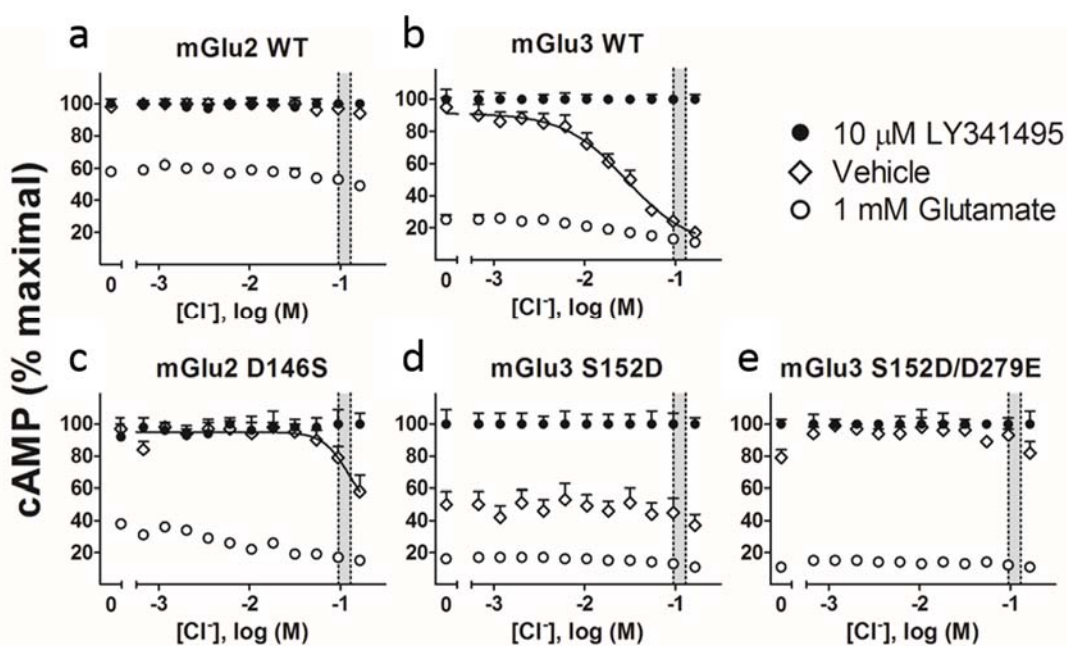


Figure 37: Molecular Switch-Controlled Chloride Sensitivity at mGluR3 and mGluR2¹⁷⁰. (a-b) Chloride concentration-response curves for wild-type mGluR2 and mGluR3 are reproduced from **Figure 31** for comparison. Remaining panels show chloride concentration-response curves at (c) the mGluR2 D146S mutant, (d) the mGluR3 S152D mutant, and (e) the mGluR3 S152D/D279E mutant. All mutant receptors responded to 1 mM glutamate. Data were normalized independently at each chloride concentration to the maximal cAMP resulting from either LY341495, vehicle, or glutamate treatment. Gray bars represent the physiological range of chloride (95 to 125 mM). Curves were fit using the four parameter logistic equation. Data are the mean \pm S.E.M. of three experiments performed in triplicate.

Other laboratories have reported antagonist-mediated increases in cAMP production at group II and III mGluRs as well¹⁷⁴. In agreement with Suzuki et al.¹⁷⁵ data described above demonstrate that antagonist-mediated efficacy is PTX-sensitive, indicating an already engaged $G\alpha_{i/o}$ -coupled signaling mechanism. Furthermore, LY341495-mediated inverse agonism was observed in primary cultures of cerebellar astrocytes, suggesting that, even in the absence of glutamate, group II and III mGluRs are highly active *in vivo*. Furthermore, results displayed above indicate that high basal receptor activity is not due to glutamate contamination, but is rather due to the presence of the endogenous agonist, chloride. Before the mGluRs were cloned, several studies reported that chloride enhanced [³H]-glutamate binding in rat brain¹⁷⁶, and also in astrocytes at binding sites that were unaffected by kainic acid and NMDA¹⁷⁷. Since, it has been reported that radioligand binding to truncated mGluR3 and mGluR4 was improved by physiologically relevant chloride concentrations¹⁶⁵. Alternatively, while other research groups have suggested that cations affect group II mGluRs¹³¹, one report concludes with the claim that increasing concentrations of Ca^{+2} activated mGluR3, but not mGluR2, although the counterion was not specified, nor was the concurrent increase in anion concentration controlled for. Somewhat surprisingly, there appears to be no reported functional studies that have controlled for chloride concentration while measuring activation of group II and III mGluRs. Because nearly all physiological buffers contain chloride, it is likely that chloride has been a confounding variable in many reports of group II and III mGluR, perhaps including claims that NAAG selectively activates mGluR3. While results displayed in **Figure 23** indicated that Ca^{+2} does not modulate glutamate-mediated group II or III mGluR activity, much of the data described above supports that chloride activates mGluR3, mGluR4, mGluR6, and mGluR8, but not mGluR2. Because receptor activation results from direct

interaction of the endogenous ion chloride with its own binding site, chloride is, by definition, an orthosteric agonist of these mGluRs. Chloride also potentiates glutamate potency at mGluR4 and mGluR6, and therefore, chloride is a PAM with respect to glutamate activity at these receptors. Future experiments will clarify not only whether glutamate is a PAM with respect to chloride, but also how chloride modulates the potency of other orthosteric ligands. Ultimately, our data show that, with the exception of mGluR2, the group II and III mGluRs are as much chloride receptors as they are glutamate receptors.

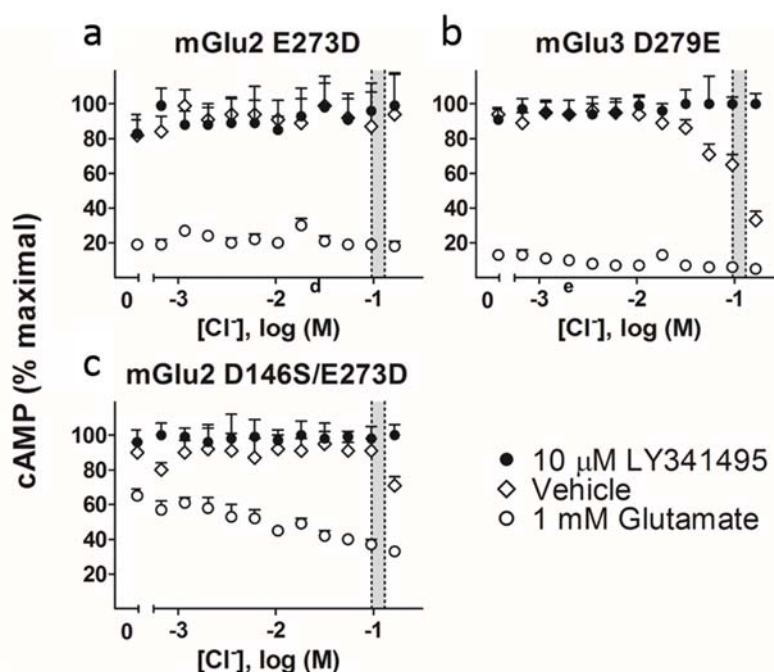


Figure 38. Chloride Sensitivity Unaffected by Mutation of D279 or E273¹⁷⁰. Chloride-response curves for (a) the mGluR2 E273D mutant, (b) the mGluR2 D146S/E273D dual mutant, and (c) the mGluR3 D279E mutant. All mutant receptors responded to 1 mM glutamate. Data were normalized independently at each chloride concentration to the maximal cAMP resulting from either LY341495, vehicle, or glutamate treatment. Gray bars represent the physiological range of chloride (95 to 125 mM). Curves were fit using the four parameter logistic equation. Data are the mean \pm S.E.M. of three independent experiments performed in triplicate.

Interestingly, the chloride binding site at group II and III mGluRs is structurally conserved at atrial natriuretic peptide receptors^{171,178} (ANPRs). While chloride is not an ANPR agonist, chloride has been shown to modulate ANPR oligomerization¹⁷². In the absence of chloride, ANPRs exist exclusively

as homodimers, regardless of receptor number. In the presence of 150 mM chloride however, free monomers predominate, but shift towards the dimeric state as a function of increasing receptor expression. While preliminary competition binding experiments using [³H]-LY341494 and membranes harvested from mGlu3-Glo cells revealed complex, chloride-dependent effects on both ligand potency and the number of glutamate binding sites, further investigation will determine if a similar phenomenon underscores a dynamic interplay between monomeric, homodimeric, and heterodimeric mGluR states, regulated by both chloride concentration and receptor expression.

Because mGluR2 is the only group II and III mGluR subtype not activated by chloride, it can reasonably be proposed that chloride-sensitivity is a fundamental property of these receptors, and that mGluR2 chloride-insensitivity is exceptional. Results described above suggest that this chloride-insensitivity stems from the absence of a π -cation interaction between R271 and Y144, which is present between R277 and Y150 at mGluR3. While this π -cation interaction has been previously described as a structural motif of both mGluR2 and mGluR3^{83,179}, it is not absolutely required for glutamate-mediated activation^{151,179,180}, and results described above support that it is only present at mGluR3. Instead, it is proposed that D146 at mGluR2 (a conserved serine at all other mGluRs¹⁷⁰) precludes a π -cation interaction by facilitating an “Arginine Flip,” relative to mGluR3, which consequently disrupts the orthosteric chloride site. Supporting this claim are the chloride-sensitive mGluR2 D146S and D146S/E273D mutants, as well as the chloride-insensitive mGluR3 S152D and S152D/D279E mutants. This swap of chloride-sensitivity by site-directed mutagenesis is consistent with other studies, where the differential ion-sensitivities of the wild-type receptors were reversed by D146S mutation at mGluR2 and corresponding S152D mutation at mGluR3^{164,180}. These results are in accord with a scenario under which the “Arginine Flip” is induced by mutation of a single amino acid, which acts as a chloride switch between mGluR2 and mGluR3. Because the arginine and tyrosine residues are not conserved through the group III mGluRs¹⁷⁰, this chloride switch marks a unique structural divergence between mGluR3 and mGluR2, which share 80% sequence homology, and are largely thought to activate and signal in the same fashion.

2.2.g. Implications for Selective mGluR3 Agonist Design

Despite a shared $G_{i/o}$ -coupled signaling mechanism, recent studies demonstrate that activation of mGluR2 and mGluR3 can elicit opposing neurotrophic and cognitive effects^{113,125,181}, thus highlighting the need for subtype-selective agonists to evaluate the therapeutic potential of each mGluR subtype individually. Unfortunately, selective activation of mGluR3 or mGluR2 has been difficult to achieve due to the lack of identified structural differences. Results described above, however, demonstrate a subtle difference in tyrosine conformation that may be exploitable for drug selectivity. In support of this claim, a previous study showed that a 4-fold difference in [³H]-LY354740 affinity between mGluR2 and mGluR3 was reversed at the D146S and S152D mutants, respectively¹⁸⁰. Because S152 and D146 do not directly interact with agonists⁸³, it is proposed that this affinity reversal was due to an “Arginine Flip” that alters the conformation of more proximal tyrosine. Furthermore, a new, selective mGluR2 agonist has been proposed to bind near S278/S272¹³², which are directly adjacent to R277/R271 at mGluR3 and mGluR2, respectively. As *mGluR3-0H₂O* and *mGluR2-0H₂O* models do not predict different conformations of S278 and S272, the selective mGluR2 agonist may actually exploit different conformations of the neighboring tyrosine and/or arginine residues.

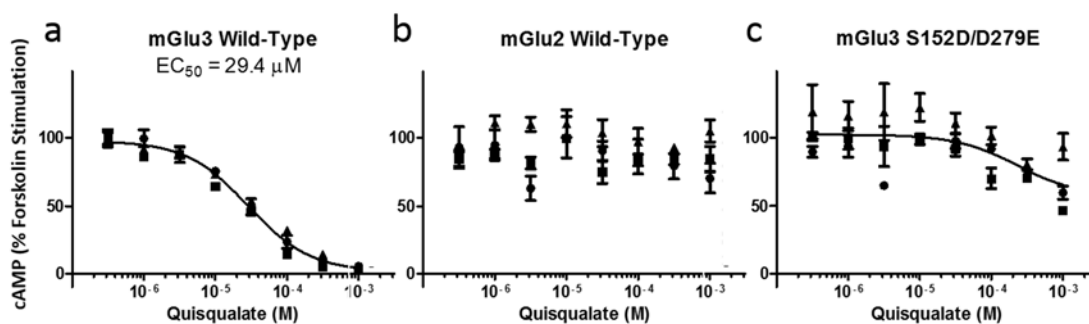
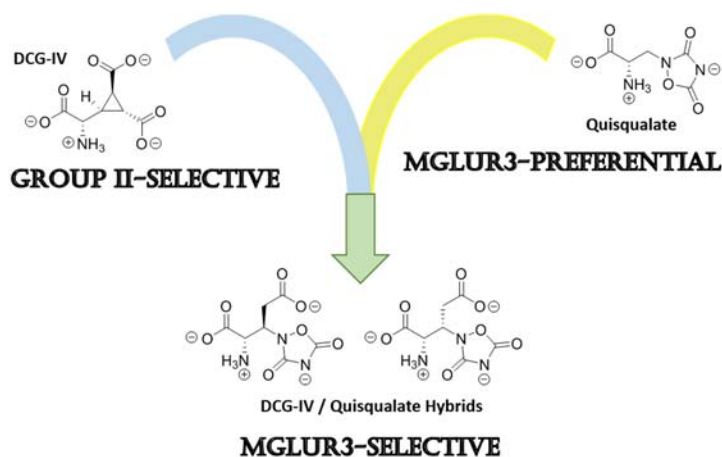


Figure 39. Preferential Activation of mGluR3 over mGluR2 by Quisqualate. Concentration-response curves of quisqualate at (a) mGluR3, (b) mGluR2, and (c) the mGluR3 S152D/D279E dual mutant were generated via nonlinear regression with a four parameter logistic equation using GraphPad Prism software. Data are the mean \pm S.E.M. of three independent experiments performed in triplicate.

Results described above also reveal a second region of dissimilarity between mGluR3 and mGluR2: the orthosteric chloride site. While targeting this region has already been proposed as a strategy for the design of subtype-selective group III mGluR agonists^{171,182}, mGluR4, mGluR6, and mGluR8 all contain functional chloride sites. In contrast to the claim that all mGluRs share the “putative chloride binding site¹⁷¹,” functional assays indicated that this site is not conserved at mGluR2. Thus, the opportunity for subtype-selectivity between group II mGluRs by targeting the orthosteric chloride site (or lack thereof) is much more pronounced than for group III mGluRs, where this strategy may have already had some success¹⁸². Ultimately, the close proximity of chloride and glutamate binding sites, as well as the effects of chloride on glutamate potency at mGluR4 and mGluR6, renders selective orthosteric drug design inextricably intertwined with chloride function. In fact, quisqualate may discriminate between mGluR3 and mGluR2 based on some of the same structural motifs that differ between the two receptors. While the EC₅₀ of quisqualate was determined to be 29.4 μM at mGluR3 using the GloSensor assay (*Figure 39a*), treatment of mGlu2-Glo cells with increasing concentrations of quisqualate did not robustly inhibit forskolin-stimulated cAMP production (*Figure 39b*), even at 1 mM drug concentrations, obviating calculation of an EC₅₀ value at mGluR2. Interestingly, concentration-response curve of quisqualate at the mGluR3 S152D/D279E dual mutant (*Figure 39c*) demonstrates a substantial decrease in both potency and efficacy, acting more like wild-type mGluR2 than wild-type mGluR3. The fact that this dual mutant mGluR3 also responded to chloride like wild-type mGluR2 (*Figure 37e*), it is likely that quisqualate interaction is similarly quite sensitive to the “Arginine Flip.” Even if quisqualate does not differentiate between mGluR3 and mGluR2 based on this proposed mechanism, the quisqualate heterocycle is a structural motif that could be incorporated into nonselective group II mGluR agonist scaffolds, such as that of DCG-IV, to induce mGluR3 subtype-selectivity (*Scheme 23*). Such DCG-IV / quisqualate hybrids not only could represent new chemical tools with which to study pharmacological differences between mGluR3 and mGluR2, but could also exhibit therapeutic value against neurodegenerative diseases such as Alzheimer’s disease by virtue of selective activation of astrocytic mGluR3.



Scheme 23: New Design Principles for mGluR3 Selectivity. A molecule with the group II mGluR selectivity of DCG-IV, as well as the mGluR3 versus mGluR2 preference of quisqualate, could achieve subtype-selective mGluR3 activation.

2.3. Conclusions

Although design, synthesis, and biological evaluation of NAAG analogs **51**, **52**, and **53** did not result in the achievement of selective mGluR3 activation, it was discovered that chloride, an endogenous anion generally deemed a passive participant in neuronal excitability, preferentially activates mGluR3 over mGluR2 via interaction with its own binding site. Chloride was also determined to be an agonist of mGluR8 and an ago-PAM of mGluR4 and mGluR6. Therefore, it can be concluded that these mGluRs have two, distinct orthosteric sites¹⁸³, one for glutamate and one for chloride, making group II and III mGluRs, with the exception of mGluR2, as much chloride receptors as they are glutamate receptors. Furthermore, chloride-insensitivity of mGluR2 results from a single amino acid difference, highlighting a molecular switch for chloride-insensitivity that is proposed to be transduced through an “Arginine Flip.” These structural differences between mGluR2 and mGluR3 mark a new strategy for the design of subtype-selective group II mGluR agonists, which must necessarily be considered within the context of chloride function. Ultimately, these findings underscore a scenario in which either (1) mGluR3, mGluR4, mGluR6, and mGluR8 are highly active *in vivo* due to

static extracellular chloride concentrations, or (2) chloride microdomains exist throughout the CNS, rendering local, extracellular chloride levels far more tightly regulated, both spatially and temporally, than currently accepted.

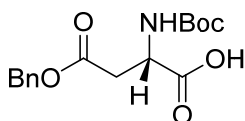
2.4. Experimental Methods

2.4.a. Synthetic Procedures

All solvents were dried and degassed by the SG Waters Glass Contour System unless otherwise specified. Automated flash column chromatography was performed using a Teledyne ISCO CombiFlash Companion system with silica gel-packed columns (SiliCycle Inc.). Analytical thin-layer chromatography was carried out on aluminum-supported silica gel plates (Sigma, thickness = 200 μm) with fluorescent indicator (F-254). Visualization of compounds on TLC plates was accomplished UV light (254 nm) or with phosphomolybdic acid, ninhydrin, Seebach's stain, or bromocresol green. Melting points were obtained using capillary tubes and a 200 W MelTemp melting point apparatus. Optical rotation was measured using a Perkin Elmer 341 Polarimeter. Infrared absorption spectra were obtained on a Thermo Scientific Nicolet 370 FT-IR spectrophotometer via the Smart Orbit Diamond Attenuated Total Reflectance accessory, and peaks are reported in cm^{-1} . NMR spectra (^1H , ^{19}F , and ^{13}C) were obtained using a Varian INOVA 400 MHz spectrometer in deuterated chloroform (CDCl_3) with the residual solvent peak (CDCl_3 : ^1H = 7.27 ppm, ^{13}C = 77.23 ppm) as an internal reference and trifluoroacetic acid (TFA) as external reference (TFA: ^{19}F = -76.55 ppm) unless otherwise specified. NMR data is reported to include chemical shifts (δ) reported in ppm, multiplicities indicated as s (singlet), d (doublet), t (triplet), q (quartet), m (multiplet), br (broadened), or app (apparent), coupling constants (J) reported in Hz, and integration normalized to 1 atom (H, C, or F). High resolution mass spectrometry was performed by the Emory University Mass Spectrometry Center, directed by Dr. Fred Strobel. HPLC and LC-MS analysis was performed on an Agilent 1200 HPLC equipped with a 6120 Quadrupole mass spectrometer (ESI-API) using mixtures of HPLC grade MeOH/ H_2O (spiked with

0.1% formic acid) and an analytical, reverse-phase, Agilent C18 XDB eclipse column (150 x 4.6 mm or 50 x 4.6 mm). Elemental analyses were performed by Atlantic Microlab, Inc (Norcross, GA). Compounds listed below for which full characterization is not presented were previously reported in the literature as referenced in the main text.

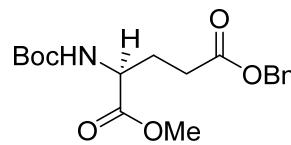
General Procedure for Boc-Protecting Amines: Protected glutamic or aspartic acid (1.00 eq) was added to a flask with a stir bar. The starting material was diluted with 1:2 water/dioxane (0.20 M). Sodium bicarbonate (2.00 eq) was added, and the resulting mixture was cooled to 0°C. Added di-tert-butyl dicarbonate (1.30 eq), and the resulting reaction mixture was allowed to warm to room temperature and stir overnight. Reaction progress was monitored by LC-MS. In the morning, solvent was evaporated under reduced pressure. The crude product was dissolved in 10% aqueous sodium bicarbonate (2/3 reaction volume), and then washed once with diethyl ether. Solid citric acid was added to adjust the pH to 4. The resulting aqueous layer was extracted 6 times with EtOAc. The combined organic layers were washed twice with water and twice with brine, dried over MgSO₄, filtered, and evaporated under reduced pressure.

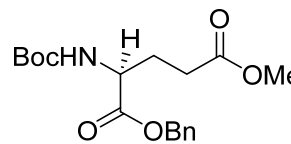


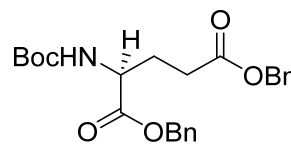
(S)-4-(benzyloxy)-2-((tert-butoxycarbonyl)amino)-4-oxobutanoic acid (**56**): The crude material was recrystallized from EtOAc and hexanes to yield white solid (5.02 g, 15.5 mmol, 69% yield). $[\alpha]_D^{20} = +25.6$ (c = 1.00 in 1 N HCl). ¹H NMR (400 MHz, CDCl₃) δ 7.32-7.40 (m, 5H), 5.56 (d, *J* = 8.0 Hz, 1H), 5.17 (d, *J* = 15.2 Hz, 1H), 5.14 (d, *J* = 15.6 Hz, 1H), 4.64 (m, 1H), 3.10 (dd, *J* = 17.2 Hz, *J* = 4.0 Hz, 1H), 2.90 (dd, *J* = 17.2 Hz, *J* = 4.8 Hz, 1H), 1.46 (s, 9H). HRMS (APCI) *m/z* = 322.13013 (Theo. for C₁₆H₂₁NO₆ - H: 322.12961). LC-MS (ES-API, - ion) 95% MeOH in H₂O isocratic, 3 min, 1.00 mL/min, C18 (Agilent Zorbax XDB-18, 50 mm x 4.6 mm, 3.5 μm), *m/z* = 322.0, *rt* = 0.577 min; 75-95% MeOH in H₂O, 3 min, 1.00 mL/min, C18 (Agilent Zorbax XDB-18, 50 mm x 4.6 mm, 3.5 μm), *m/z* = 322.0, *rt* = 1.002 min.

General Procedure for Benzyl-Esterifying Carboxylic Acids: Protected glutamic acid (1.00 eq) and sodium bicarbonate (3.00 eq) were added to a flask with a stir bar. The solids were diluted with DMF (0.22 M) and stirred at room temperature. Added benzyl bromide (3.00 eq), and the resulting mixture

was allowed to stir at room temperature. Reaction progress was monitored by LC-MS. Once starting material was undetectable by LC-MS, the reaction mixture was diluted with EtOAc, and was washed 3 times with 10% aqueous sodium bicarbonate and twice with water. The organic layer was dried over MgSO₄, filtered, and evaporated under reduced pressure.

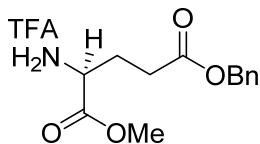

5-benzyl 1-methyl (tert-butoxycarbonyl)-L-glutamate (66): The crude product was purified by column chromatography to yield a white solid (0.854 g, 2.43 mmol, 91% yield). ¹H NMR (400 MHz, CDCl₃) 7.32-7.40 (m, 5H), 5.13 (m, 3H), 4.36 (dd, *J* = 8.4 Hz, *J* = 13.2 Hz, 1H), 3.74 (s, 3H), 2.47 (m, 2H), 2.20 (m, 1H), 1.98 (m, 1H), 1.44 (s, 9H). ¹³C NMR (100 MHz, CDCl₃) δ 173.1, 172.7, 155.6, 135.9, 128.8 (2C), 128.5, 128.5 (2C), 80.3, 66.7, 53.0, 52.7, 30.5, 28.5 (3C), 28.0. HRMS (ESI) *m/z* = 374.15749 (Theo. for C₁₈H₂₅NO₆ + Na: 374.15741).


1-benzyl 5-methyl (tert-butoxycarbonyl)-L-glutamate (68): The crude material was recrystallized from diethyl ether and hexanes to yield white solid (3.12 g, 8.87 mmol, 54% yield). [α]_D²⁰ = -16 (c = 0.16 in MeOH). ¹H NMR (400 MHz, CDCl₃) δ 7.32-7.39 (m, 5H), 5.16 (m, 3H), 4.38 (app dd, *J* = 8.0 Hz, *J* = 12.8 Hz, 1H), 3.67 (s, 3H), 2.39 (m, 2H), 2.20 (m, 1H), 1.98 (m, 1H), 1.44 (s, 9H). HRMS (ESI) *m/z* = 352.17498 (Theo. for C₁₈H₂₅NO₆ + H: 352.17546).


Dibenzyl (tert-butoxycarbonyl)-L-glutamate (70): The crude material was recrystallized from diethyl ether and hexanes to yield white solid (5.39 g, 12.6 mmol, 85% yield). Mp 68-71°C. IR (ν_{max}, cm⁻¹) 3336, 2974, 1723, 1678, 1514, 1346, 1263, 1250, 1204, 1170, 1102, 1057, 1012, 748, 726, 696. ¹H NMR (400 MHz, CDCl₃) δ 7.28-7.43 (m, 10H), 5.08-5.23 (m, 5H), 4.39 (m, 1H), 2.38-2.52 (m, 2H), 2.18-2.28 (m, 1H), 1.92-2.03 (m, 1H), 1.43 (s, 9H). ¹³C NMR (100 MHz, CDCl₃) δ 172.7, 172.3, 155.5, 135.9, 135.4, 128.8, 128.8 (4C), 128.7, 128.4 (4C), 80.2, 67.4, 66.7, 53.1, 30.4, 28.5 (3C), 27.9. HRMS (APCI) *m/z* = 428.20752 (Theo. for C₂₄H₂₉NO₆ + H: 428.20676).

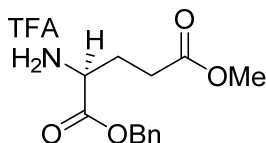
General Procedure for Boc-Deprotection: Boc-protected amine (1.00 eq) was added to a flask with a stir bar, and diluted with DCM (0.08 M). The resulting solution was cooled to 0°C, and 2,2,2-trifluoroacetic acid (43.5 eq) was added. The resulting mixture was allowed to warm to room

temperature, and reaction progress was monitored by TLC. Once starting material disappeared on TLC, solvent was evaporated under reduced pressure.



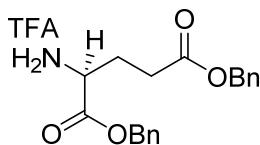
5-benzyl 1-methyl L-glutamate trifluoroacetic acid salt (63): No further purification was required (1.12 g, 3.07 mmol, 98% yield). $[\alpha]_{\text{D}}^{20} = +8.0$ (c = 1.00 in DCM).

$^1\text{H NMR}$ (400 MHz, CDCl_3) δ 7.80-8.70 (br s, 3H), 7.32- 7.38 (m, 5H), 5.11 (s, 2H), 4.21 (app t, $J = 5.6$ Hz, 1H), 3.77 (s, 3H), 2.65 (t, $J = 6.4$ Hz, 2H), 2.30 (m, 2H). HRMS (APCI) $m/z = 252.12309$ (Theo. for $\text{C}_{13}\text{H}_{18}\text{NO}_4 + \text{H}$: 252.12303).



1-benzyl 5-methyl L-glutamate trifluoroacetic acid salt (62): The crude material was purified via column chromatography to yield a pale yellow oil (2.93 g, 8.02

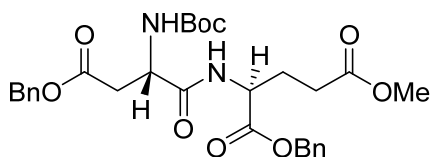
mmol, 90% yield). $^1\text{H NMR}$ (400 MHz, CDCl_3) δ 7.34-7.38 (m, 5H), 5.19 (m, 2H), 4.20 (m, 1H), 3.61 (s, 3H), 2.53 (m, 2H), 2.28 (m, 2H). HRMS (APCI) $m/z = 252.12293$ (Theo. for $\text{C}_{13}\text{H}_{17}\text{NO}_4 + \text{H}$: 252.12303).



Dibenzyll L-glutamate trifluoroacetic acid salt (57): The crude material was purified via recrystallization from diethyl ether and hexanes at 0°C to yield a white

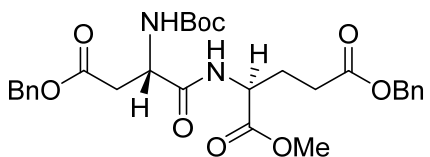
solid (4.40 g, 9.96 mmol, 79% yield). $[\alpha]_{\text{D}}^{20} = -3.3$ (c = 1.00 in DCM). $^1\text{H NMR}$ (400 MHz, CDCl_3) δ 7.22-7.40 (m, 10H), 5.16 (m, 2H), 5.04 (m, 2H), 4.20 (t, $J = 6.0$ Hz, 1H), 2.55 (m, 2H), 2.28 (m, 2H). HRMS (ESI) $m/z = 328.15400$ (Theo. for $\text{C}_{19}\text{H}_{21}\text{NO}_4 + \text{H}$: 328.15433).

General Procedure for Peptide Coupling: Carboxylic acid (1.10 eq) was added to a flask with a stir bar, and diluted with DMF (60% of volume for 0.10 M reaction). Hünig's base (1.00 eq) was added, and the resulting mixture was cooled to 0°C . HATU (1.00 eq) was added, and the resulting mixture was stirred at 0°C for 15 min. Added a solution of trifluoroacetate salt (1.00 eq) in DMF (40% of volume for 0.10 M reaction) and Hünig's base (1.00 eq) dropwise via syringe pump over 1 hr at 0°C . Reaction progress was monitored by LC-MS. Once reaction progress ceased, the reaction mixture was diluted with EtOAc, and was washed once with 10% aqueous citric acid, once with water, once with saturated aqueous sodium bicarbonate, once again with water, and finally once with brine. The organic layer was dried over MgSO_4 , filtered, and evaporated under reduced pressure.



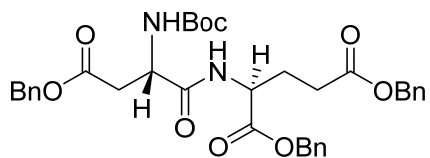
1-benzyl 5-methyl ((S)-4-(benzyloxy)-2-((tert-butoxycarbonyl)amino)-4-oxobutanoyl)-L-glutamate (72): The crude material was purified via column chromatography to yield a pale yellow oil (0.544 g,

0.977 mmol, 87% yield). $[\alpha]_{\text{D}}^{20} = +6.5$ ($c = 1.00$ in DCM). IR (ν_{max} , cm^{-1}) 3347, 2977, 1733, 1678, 1498, 1453, 1367, 1249, 1163, 1050, 1025, 910, 858, 730, 697, 648. ^1H NMR (400 MHz, CDCl_3) δ 7.31-7.39 (m, 10H), 7.18 (d, $J = 7.6$ Hz, 1H), 5.68 (d, $J = 8.8$ Hz, 1H), 5.16 (s, 2H), 5.13 (s, 2H), 4.64 (dt, $J = 8.0$ Hz, $J = 5.2$ Hz, 1H), 4.55 (m, 1H), 3.66 (s, 3H), 3.08 (dd, $J = 4.4$ Hz, $J = 17.2$ Hz, 1H), 2.71 (dd, $J = 6.0$ Hz, $J = 17.2$ Hz, 1H), 2.36 (m, 2H), 2.25 (m, 1H), 2.00 (m, 1H), 1.46 (s, 9H). ^{13}C NMR (100 MHz, CDCl_3) δ 173.1, 171.7, 171.2, 170.7, 155.4, 135.4, 135.2, 128.6 (2C), 128.6 (3C), 128.5, 128.3, 128.2 (3C), 80.5, 67.3, 66.8, 51.8 (2C), 50.6, 36.1, 29.7, 28.2 (3C), 27.2. HRMS (ESI) $m/z = 557.24999$ (Theo. for $\text{C}_{29}\text{H}_{36}\text{N}_2\text{O}_9 + \text{H}$: 557.24936). HPLC Method A (75-95% MeOH in H_2O , 3 min, 1.00 mL/min, C18) $\text{rt} = 2.128$ min; Method B (95% MeOH in H_2O isocratic, 3 min, 1.00 mL/min, C18) $\text{rt} = 0.620$ min.



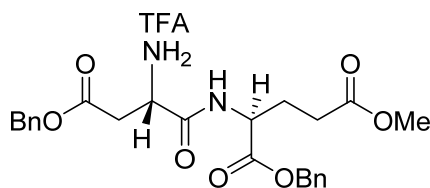
5-benzyl 1-methyl ((S)-4-(benzyloxy)-2-((tert-butoxycarbonyl)amino)-4-oxobutanoyl)-L-glutamate (71): The crude material was purified

via column chromatography to yield a pale yellow oil (0.400 g, 0.719 mmol, 64% yield). $[\alpha]_{\text{D}}^{20} = +9.2$ ($c = 1.00$ in DCM). IR (ν_{max} , cm^{-1}) 3346, 2976, 1732, 1498, 1453, 1389, 1366, 1211, 1160, 1050, 1025, 970, 911, 858, 738, 697. ^1H NMR (400 MHz, CDCl_3) δ 7.31-7.38 (m, 10H), 7.13 (d, $J = 8.0$ Hz, 1H), 5.66 (d, $J = 8.8$ Hz, 1H), 5.11 (m, 4H), 4.61 (dt, $J = 8.0$ Hz, $J = 5.0$ Hz, 1H), 4.55 (m, 1H), 3.72 (m, 3H), 3.10 (dd, $J = 4.4$ Hz, $J = 17.6$ Hz, 1H), 2.72 (dd, $J = 6.0$ Hz, $J = 17.2$ Hz, 1H), 2.44 (m, 2H), 2.25 (m, 1H), 2.00 (m, 1H), 1.45 (s, 9H). ^{13}C NMR (100 MHz, CDCl_3) δ 172.7, 171.9 (2C), 170.9, 155.6, 135.9, 135.5, 128.7 (4C), 128.5 (2C), 128.4 (4C), 80.7, 67.0, 66.6, 52.7, 51.8, 50.7, 36.2, 30.1, 28.4 (3C), 27.4. HRMS (ESI) $m/z = 579.23184$ (Theo. for $\text{C}_{29}\text{H}_{36}\text{N}_2\text{O}_9 + \text{Na}$: 579.23130). HPLC Method A (75-95% MeOH in H_2O , 3 min, 1.00 mL/min, C18) $\text{rt} = 2.231$ min; Method B (95% MeOH in H_2O isocratic, 3 min, 1.00 mL/min, C18) $\text{rt} = 0.629$ min.



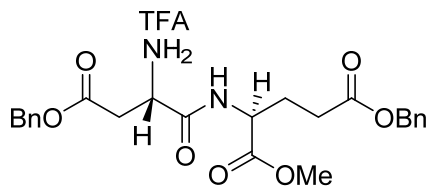
Dibenzyloxy ((*S*)-4-(benzyloxy)-2-((*tert*-butoxycarbonyl)amino)-4-oxobutanoyl)-*L*-glutamate (**73**): The crude material was purified via column chromatography to yield a pale yellow oil (0.604 g,

0.955 mmol, 85% yield). $[\alpha]_{\text{D}}^{20} = +5.3$ ($c = 1.00$ in DCM). $^1\text{H NMR}$ (400 MHz, CDCl_3) δ 7.31-7.37 (m, 15H), 7.16 (d, $J = 8.0$ Hz, 1H), 5.64 (d, $J = 8.0$ Hz, 1H), 5.11 (m, 6H), 4.66 (dt, $J = 8.0$ Hz, $J = 5.2$ Hz, 1H), 4.54 (m, 1H), 3.08 (dd, $J = 4.4$ Hz, $J = 17.2$ Hz, 1H), 2.70 (dd, $J = 6.0$ Hz, $J = 17.2$ Hz, 1H), 2.41 (m, 2H), 2.27 (m, 1H), 2.01 (m, 1H), 1.45 (s, 9H). HRMS (ESI) $m/z = 633.28107$ (Theo. for $\text{C}_{35}\text{H}_{40}\text{N}_2\text{O}_9 + \text{H}$: 633.28066).



1-benzyl 5-methyl ((*S*)-2-amino-4-(benzyloxy)-4-oxobutanoyl)-*L*-glutamate trifluoroacetic acid salt (**75**): The crude material was purified via column chromatography to yield a pale yellow oil

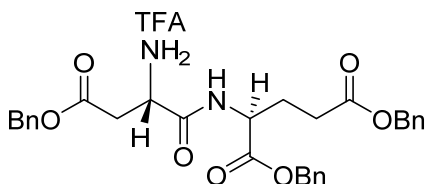
(0.459 g, 0.805 mmol, 73% yield). $[\alpha]_{\text{D}}^{20} = -1.6$ ($c = 1.00$ in DCM). IR (ν_{max} , cm^{-1}) 3036, 2954, 1730, 1668, 1554, 1439, 1393, 1177, 1131, 1003, 910, 836, 799, 742, 722, 697. $^1\text{H NMR}$ (400 MHz, CDCl_3) δ 8.17 (d, $J = 7.2$ Hz, 1H), 7.28-7.31 (m, 10H), 5.09 (m, 4H), 4.55 (m, 2H), 3.57 (s, 3H), 2.99 (app t, $J = 6.8$ Hz, 2H), 2.34 (app t, $J = 6.0$ Hz, 2H), 2.16 (m, 1H), 1.98 (m, 1H). $^{13}\text{C NMR}$ (100 MHz, CDCl_3) δ 173.5, 170.8 (2C), 168.3, 161.9, 135.2, 135.0, 128.7 (2C), 128.6 (2C), 128.5, 128.5, 128.4 (2C), 128.3 (2C), 116.6 (q, $J = 383.2$ Hz), 67.5, 67.4, 52.2, 51.8, 49.7, 34.9, 29.8, 26.4. $^{19}\text{F NMR}$ (376 MHz, CDCl_3) δ -76.0 (s, 3F). HRMS (ESI) $m/z = 457.19737$ (Theo. for $\text{C}_{24}\text{H}_{28}\text{N}_2\text{O}_7 + \text{H}$: 457.19693). HPLC Method A (50-95% MeOH in H_2O , 3 min, 1.00 mL/min, C18) $\text{rt} = 2.716$ min; Method B (95% MeOH in H_2O isocratic, 3 min, 1.00 mL/min, C18) $\text{rt} = 0.533$ min.



5-benzyl 1-methyl ((*S*)-2-amino-4-(benzyloxy)-4-oxobutanoyl)-*L*-glutamate trifluoroacetic acid salt (**74**): The crude material was purified via column chromatography to yield a pale yellow oil

(0.321 g, 0.563 mmol, 78% yield). $[\alpha]_{\text{D}}^{20} = +7.2$ ($c = 1.00$ in DCM). IR (ν_{max} , cm^{-1}) 3036, 2955, 1731, 1668, 1499, 1453, 1393, 1361, 1176, 1131, 1002, 835, 799, 737, 722, 697. $^1\text{H NMR}$ (400 MHz, CDCl_3) δ 8.15 (d, $J = 7.2$ Hz, 1H), 7.28-7.32 (m, 10H), 5.10 (m, 4H), 4.54 (m, 2H), 3.61 (s, 3H), 3.06 (app t, J

= 7.8 Hz, 2H), 2.42 (app t, $J = 7.4$ Hz, 2H), 2.16 (m, 1H), 1.99 (m, 1H). ^{13}C NMR (100 MHz, CDCl_3) δ 173.0, 171.5, 170.9, 168.3, 162.4, 135.8, 135.0, 128.6 (3C), 128.5, 128.4 (2C), 128.3, 128.3 (3C), 116.6 (q, $J = 381.3$ Hz), 67.6, 66.7, 52.6, 52.3, 49.8, 35.0, 30.2, 26.5. ^{19}F NMR (376 MHz, CDCl_3) δ -76.0 (s, 3F). HRMS (ESI) $m/z = 457.19702$ (Theo. for $\text{C}_{24}\text{H}_{28}\text{N}_2\text{O}_7 + \text{H}$: 457.19693). HPLC Method A (50-95% MeOH in H_2O , 3 min, 1.00 mL/min, C18) $rt = 2.715$ min; Method B (75-95% MeOH in H_2O , 3 min, 1.00 mL/min, C18) $rt = 0.738$ min.

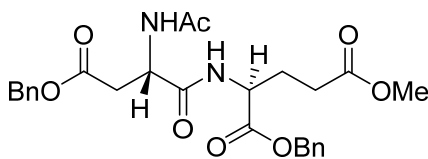


Dibenzyl ((S)-2-amino-4-(benzyloxy)-4-oxobutanoyl)-L-glutamate

trifluoroacetate salt (76): The crude material was recrystallized from diethyl ether and hexanes to yield a white solid (0.604 g,

0.934 mmol, 98% yield). Mp 101-103°C. $[\alpha]_{\text{D}}^{20} = +1.2$ ($c = 1.00$ in DCM). ^1H NMR (400 MHz, CDCl_3) δ 8.08 (m, 4H), 7.24-7.33 (m, 15H), 5.07 (m, 6H), 4.57 (m, 2H), 3.13 (m, 1H), 3.00 (m, 1H), 2.38 (app t, $J = 7.6$ Hz, 2H), 2.17 (m, 1H), 2.00 (m, 1H). HRMS (APCI) $m/z = 533.22829$ (Theo. for $\text{C}_{30}\text{H}_{32}\text{N}_2\text{O}_7 + \text{H}$: 533.22823).

General Procedure for Acetyl-Protecting Amines. A solution of trifluoroacetate salt (1.00 eq) in DCM (0.13 M) was added to a flask with a stir bar. Added Hünig's base (1.00 eq), and then added acetic anhydride (1.20 eq). The resulting reaction mixture was allowed to stir at room temperature, and reaction progress was monitored by TLC. Once starting material disappeared on TLC, solvent was evaporated under reduced pressure. The crude product was diluted with DCM, washed twice with water, dried over MgSO_4 , filtered, and evaporated under reduced pressure.

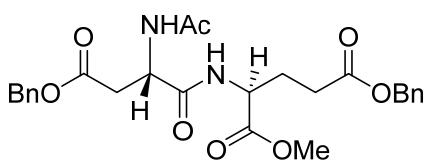


1-benzyl 5-methyl ((S)-2-acetamido-4-(benzyloxy)-4-oxobutanoyl)-L-

glutamate (59): The crude material was purified via column chromatography to yield a white solid (0.370 g, 0.742 mmol,

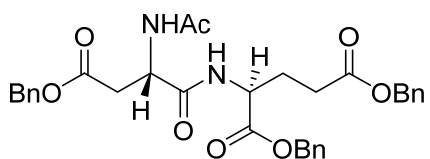
92% yield). Mp = 133-135°C. $[\alpha]_{\text{D}}^{20} = -24.5$ ($c = 1.00$ in MeOH). IR (ν_{max} , cm^{-1}) 3297, 1747, 1723, 1677, 1647, 1537, 1383, 1238, 1211, 1168, 1138, 752, 698, 670. ^1H NMR (400 MHz, CDCl_3) δ 7.33-7.39 (m, 10H), 7.29 (d, $J = 7.6$ Hz, 1H), 6.76 (d, $J = 8.4$ Hz, 1H), 5.15 (m, 4H), 4.86 (m, 1H), 4.59 (m, 1H), 3.66 (s, 3H), 3.05 (dd, $J = 4.0$ Hz, $J = 16.8$ Hz, 1H), 2.66 (d, $J = 6.8$ Hz, $J = 17.2$ Hz, 1H), 2.36

(m, 2H), 2.21 (m, 1H), 2.03 (m, 4H). ^{13}C NMR (100 MHz, CDCl_3) δ 173.4, 172.0, 171.2, 170.6, 170.4, 135.5, 135.3, 128.8 (2C), 128.7 (2C), 128.6, 128.5, 128.4 (4C), 67.4, 67.1, 52.2, 52.0, 49.3, 36.1, 30.0, 26.9, 23.3. HRMS (APCI) $m/z = 499.20758$ (Theo. for $\text{C}_{26}\text{H}_{30}\text{N}_2\text{O}_8 + \text{H}$: 499.20749). HPLC Method A (75-95% MeOH in H_2O , 3 min, 1.00 mL/min, C18) $rt = 1.035$ min; Method B (95% MeOH in H_2O isocratic, 3 min, 1.00 mL/min, C18) $rt = 0.555$ min.



5-benzyl 1-methyl ((S)-2-acetamido-4-(benzyloxy)-4-oxobutanoyl)-L-

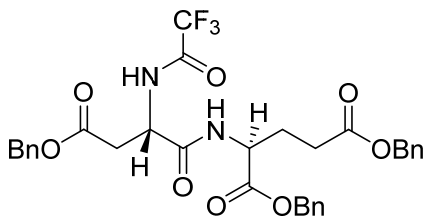
glutamate (60): The crude material was purified via column chromatography to yield a white solid (0.173 g, 0.347 mmol, 64% yield). $\text{Mp} = 107\text{-}109^\circ\text{C}$. $[\alpha]_{\text{D}}^{20} = -17.2$ ($c = 1.00$ in MeOH). IR (ν_{max} , cm^{-1}) 3293, 1753, 1728, 1640, 1539, 1381, 1306, 1211, 1162, 1131, 966, 753, 698, 612. ^1H NMR (400 MHz, CDCl_3) δ 7.32-7.36 (m, 10H), 7.25 (m, 1H), 6.74 (m, 1H), 5.13 (m, 4H), 4.87 (m, 1H), 4.56 (m, 1H), 3.71 (s, 3H), 3.06 (dt, $J = 3.4$ Hz, $J = 17.2$ Hz, 1H), 2.68 (dd, $J = 6.4$ Hz, $J = 17.2$ Hz, 1H), 2.45 (m, 2H), 2.23 (m, 1H), 2.02 (m, 4H). ^{13}C NMR (100 MHz, CDCl_3) δ 172.8, 171.7, 170.6, 170.4, 135.8, 135.4, 128.7 (3C), 128.5, 128.4, 128.3 (3C), 128.3 (2C), 67.0, 66.7, 52.6, 52.0, 49.2, 36.1, 30.2, 26.9, 23.2. HRMS (APCI) $m/z = 499.20752$ (Theo. for $\text{C}_{26}\text{H}_{30}\text{N}_2\text{O}_8 + \text{H}$: 499.20749). HPLC Method A (75-95% MeOH in H_2O , 3 min, 1.00 mL/min, C18) $rt = 1.040$ min; Method B (95% MeOH in H_2O isocratic, 3 min, 1.00 mL/min, C18) $rt = 0.606$ min.



Dibenzyl ((S)-2-acetamido-4-(benzyloxy)-4-oxobutanoyl)-L-glutamate

(54): The crude material was recrystallized from diethyl ether to yield a white solid (4.88 g, 8.49 mmol, 95% yield). $[\alpha]_{\text{D}}^{20} = -$

18.7 ($c = 1.00$ in MeOH). ^1H NMR (400 MHz, CDCl_3) δ 7.30-7.40 (m, 15H), 7.26 (br d, $J = 7.6$ Hz, 1H), 6.71 (br d, $J = 8.0$ Hz, 1H), 5.11-5.19 (m, 6H), 4.86 (m, 1H), 4.61 (m, 1H), 3.05 (dd, $J = 17.2$ Hz, $J = 3.6$ Hz, 1H), 2.65 (dd, $J = 17.4$ Hz, $J = 6.8$ Hz, 1H), 2.41 (m, 2H), 2.24 (m, 1H), 2.01 (m, 1H), 2.00 (s, 3H). HRMS (ESI) $m/z = 597.22103$ (Theo. for $\text{C}_{32}\text{H}_{34}\text{N}_2\text{O}_8 + \text{Na}$: 597.22074).



Dibenzyloxy

((S)-4-(benzyloxy)-4-oxo-2-(2,2,2-

trifluoroacetamido)butanoyl)-L-glutamate (55): (S)-4-(benzyloxy)-1-

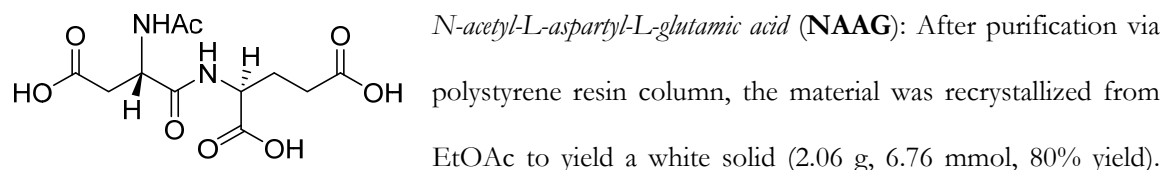
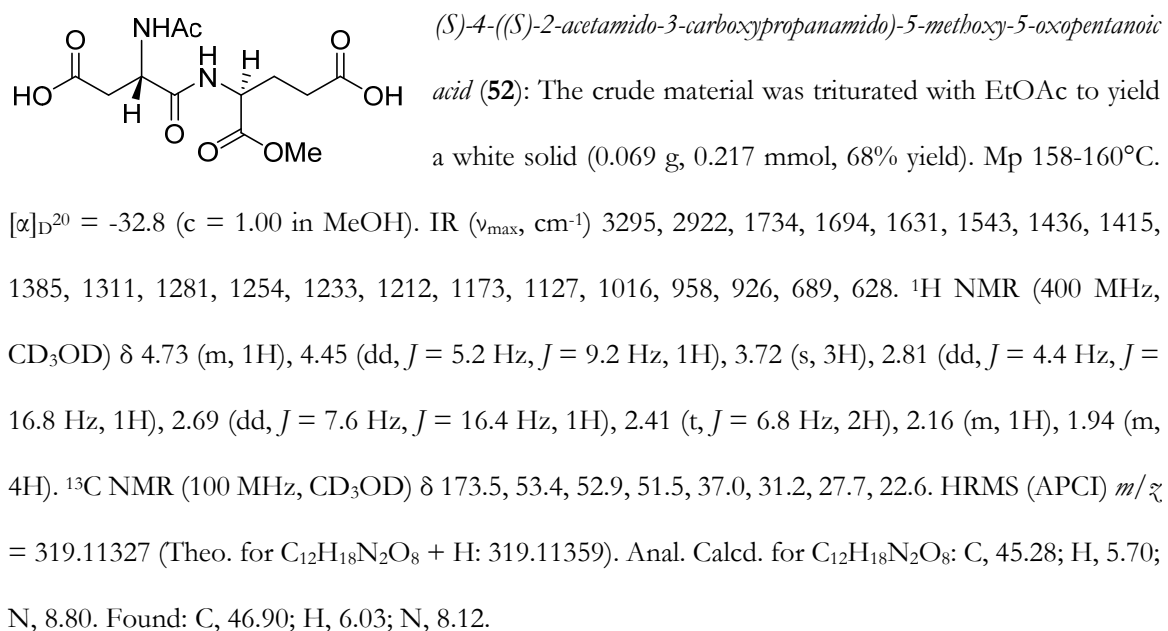
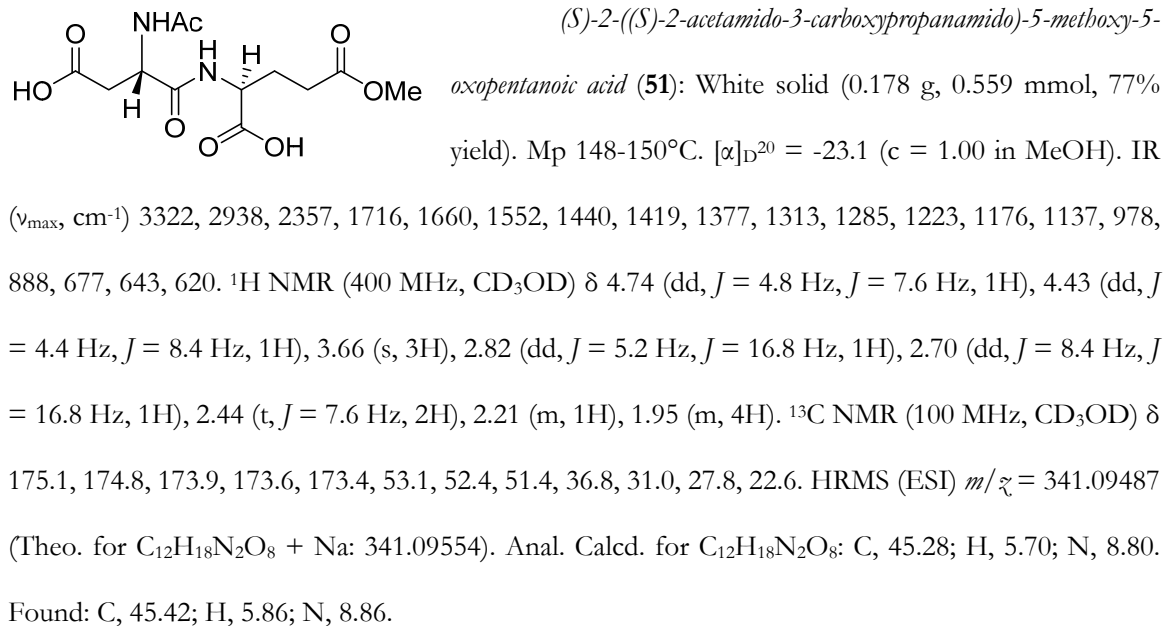
(((S)-1,5-bis(benzyloxy)-1,5-dioxopentan-2-yl)amino)-1,4-

dioxobutan-2-aminium 2,2,2-trifluoroacetate (76, 1.00 g, 1.55

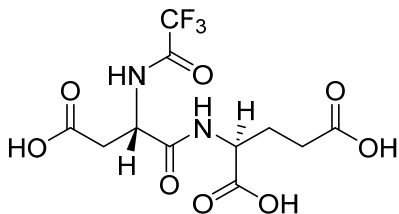
mmol, 1.00 eq) was added to flask with a stir bar, and was diluted with DCM (11.90 mL). Added Hünig's base (0.540 mL, 3.09 mmol, 2.00 eq), followed by 2,2,2-trifluoroacetic anhydride (0.262 mL, 1.86 mmol, 1.20 eq), and the resulting mixture was stirred at room temperature. Reaction progress was monitored by TLC, and disappearance of starting material was observed after about 45 min. Solvent was evaporated under reduced pressure. The crude material was diluted with DCM, washed twice with water, dried over MgSO₄, filtered, and evaporated under reduced pressure. The crude material was recrystallized from diethyl ether to yield a white solid (0.690 g, 1.10 mmol, 71% yield). Mp 92-95°C. $[\alpha]_{\text{D}}^{20} = +11.4$ (c = 1.00 in DCM). IR (ν_{max} , cm⁻¹) 3312, 3277, 1747, 1728, 1708, 1660, 1543, 1341, 1169, 1126, 941, 751, 728, 696. ¹H NMR (400 MHz, CDCl₃) δ 7.67 (d, *J* = 5.2 Hz, 1H), 7.26-7.35 (m, 16H), 5.07 (m, 6H), 4.78 (m, 1H), 4.54 (m, 1H), 2.99 (dd, *J* = 3.6 Hz, *J* = 17.2 Hz, 1H), 2.66 (dd, *J* = 8.0 Hz, *J* = 17.6 Hz, 1H), 2.34 (m, 2H), 2.17 (m, 1H), 1.98 (m, 1H). ¹³C NMR (100 MHz, CDCl₃) δ 172.8, 171.3, 170.9, 169.0, 157.0 (q, *J* = 50.1 Hz), 135.7, 135.1, 135.1, 128.7 (2C), 128.7 (2C), 128.7 (3C), 128.6, 128.5 (3C), 128.4 (4C), 115.7 (q, *J* = 381.0 Hz), 67.5, 67.4, 66.8, 52.4, 49.4, 36.1, 30.2, 26.6. ¹⁹F NMR (376 MHz, CDCl₃) δ -76.6 (s, 3F). HRMS (ESI) $m/z = 651.19211$ (Theo. for C₃₂H₃₁N₂O₈ + H: 651.19247). HPLC Method A (75-95% MeOH in H₂O, 3 min, 1.00 mL/min, C18) *rt* = 2.535 min; Method B (95% MeOH in H₂O isocratic, 3 min, 1.00 mL/min, C18) *rt* = 0.596 min.

General Procedure for Benzyl Ester Deprotection: Benzyl ester (1.00 eq) was added to a flask with a stir bar, and diluted with ethanol (0.05 M). Added 20% palladium(II) hydroxide on carbon (0.100 eq), and the resulting mixture was stirred vigorously under Ar. The flask was evacuated via low vacuum for 5 min, and then flushed with Ar. These 2 steps were repeated twice more, followed by a final evacuation and final flush with H₂ via balloon. The reaction mixture was stirred vigorously overnight at room temperature under H₂. Reaction progress was monitored by LC-MS. Once starting material was

undetectable by LC-MS, the reaction mixture was filtered over a plug of celite, which was subsequently washed thoroughly with MeOH. Solvent was evaporated under reduced pressure. The crude product was purified via a polystyrene resin, eluting with combinations of water and methanol.



$[\alpha]_{\text{D}}^{20} = -30.0$ ($c = 1.00$ in H_2O). ^1H NMR (400 MHz, CD_3OD) δ 4.75 (dd, $J = 8.0$ Hz, $J = 4.8$ Hz, 1H), 4.43 (dd, $J = 8.8$ Hz, $J = 4.8$ Hz, 1H), 2.83 (dd, $J = 16.8$ Hz, $J = 5.2$ Hz, 1H), 2.71 (dd, $J = 17.2$ Hz, $J = 8.4$ Hz, 1H), 2.41 (t, $J = 7.6$ Hz, 2H), 2.20 (m, 1H), 2.03 (s, 3H), 1.95 (m, 1H).



(2,2,2-trifluoroacetyl)-L-aspartyl-L-glutamic acid (**53**): After purification via polystyrene resin column, the material was recrystallized from EtOAc to yield a white solid (0.156 g, 0.435

mmol, 50% yield). Mp 154-156°C. $[\alpha]_{\text{D}}^{20} = -26.8$ ($c = 1.00$ in MeOH). IR (ν_{max} , cm^{-1}) 3291, 3097, 1725, 1697, 1569, 1446, 1417, 1278, 1226, 1173, 1157, 1085, 906, 863, 810, 758, 730, 685, 665, 624. ^1H NMR (400 MHz, CD_3OD) δ 4.82 (dd, $J = 4.8$ Hz, $J = 9.6$ Hz, 1H), 4.43 (dd, $J = 4.8$ Hz, $J = 8.8$ Hz, 1H), 2.93 (dd, $J = 4.8$ Hz, $J = 17.2$ Hz, 1H), 2.79 (dd, $J = 9.2$ Hz, $J = 17.2$ Hz, 1H), 2.42 (t, $J = 7.6$ Hz, 2H), 2.02 (m, 1H), 1.96 (m, 1H). ^{13}C NMR (100 MHz, CDCl_3) δ 176.6, 174.7, 173.6, 172.0, 159.1 (q, $J = 36.7$ Hz), 117.5 (q, $J = 285.0$ Hz), 53.3, 51.9, 36.4, 31.2, 27.8. ^{19}F NMR (376 MHz, CD_3OD) δ -73.9 (s, 3F). HRMS (APCI) $m/z_{\text{c}} = 359.06957$ (Theo. for $\text{C}_{11}\text{H}_{13}\text{N}_2\text{O}_8\text{F}_3 + \text{H}$: 359.06968). Anal. Calcd. for $\text{C}_{11}\text{H}_{13}\text{F}_3\text{N}_2\text{O}_8$: C, 36.88; H, 3.66; N, 7.82; F, 15.91. Found: C, 37.52; H, 3.73; N, 7.58; F, 15.32.

2.4.b. Molecular Modeling

X-ray crystal structures of mGluR3 NTDs⁸³ bound to glutamate (and three orthosteric water molecules) or DCG-IV (and one orthosteric water molecule) were downloaded from the PDB and imported into Maestro³⁰ within the Schrödinger 2011 software suite. One of the monomers of each of these symmetrical homodimeric structures was removed along with its bound ligand and all associated water molecules. Using the ProteinPrep workflow¹⁵³ within Maestro, the remaining monomer-ligand complexes were preliminarily prepared for molecular modeling via (1) addition of hydrogen atoms to satisfy valence requirements, (2) adjustment of amino acid residue ionization to represent physiological pH (7.4 ± 0.2), and (3) removal of all water molecules except for three or one structural orthosteric water molecule(s) for glutamate-bound and DCG-IV-bound structures, respectively. This resulted in two mGluR3 models, one with three structural water molecules (*mGluR3-3H₂O*) in the ligand binding

pocket, as in the glutamate-bound structure, and one with one structural water molecule (*mGluR3-1H₂O*), as in the DCG-IV-bound structure. Using the Glide application¹⁵² in Maestro, an identical ligand binding region was subsequently defined for each of these models according to the following specifications: use input partial charges, centroid of workspace ligand, dock ligands similar in size to workspace ligand, and allow rotation of receptor hydroxyl groups. To ensure that modifications made to the original structures did not deleteriously affect any of the essential ligand binding pocket residues, control docking experiments were conducted prior to NAAG docking. Accordingly, glutamate and DCG-IV were imported into Maestro from ChemDraw in .sdf format, and the agonists were subsequently prepared with the LigPrep application⁶⁸. LigPrep was used (1) to add hydrogens to the appropriate valence, (2) to adjust ligand ionization to represent physiological pH, and (3) to select the desired stereoisomers according to the following parameters: OPLS_2005 force field, pH = 7.4 ± 0.2, and Epik ionization. With each agonist prepared appropriately, glutamate was docked into *mGluR3-3H₂O* and DCG-IV was docked into *mGluR1-1H₂O* using standard precision Glide docking according to the following parameters: dock flexibly, sample N inversions, sample ring conformations, include input ring conformations, penalize nonplanar amide conformations, add Epik state penalties, use enhanced planarity force field, and perform post-docking minimization. Each of these control docking studies resulted in highly accurate agonist binding conformations as compared to the crystal structure agonist orientations. Therefore, NAAG was prepared using LigPrep in similar fashion to glutamate and DCG-IV, and subsequent standard precision Glide docking was attempted at each model. Although the conformational accuracy exhibited by control experiments indicated that the both mGluR3 models, *mGluR1-1H₂O* and *mGluR3-3H₂O*, were appropriate for docking experiments involving NAAG. However, despite all attempts to dock NAAG with the Glide application into each of these models using varying levels of stringency, not one NAAG binding pose was predicted at either mGluR3 model. Accordingly, a third mGluR3 model excluding all structural water molecules (*mGluR3-0H₂O*) to give NAAG ample space to bind was prepared in Maestro using more advanced computational techniques for protein optimization. X-ray structure of the homodimeric mGluR3 NTD

complexed with 1*S*,3*S*-ACPD⁸³ (PDB ID: 2E4W), which was chosen over the other agonist-bound mGluR3 structures for best resolution (2.40 Å) and fewest unresolved loops, was downloaded from the PDB and imported into Maestro. As performed for the other mGluR3 models, one of the monomers was removed along with its bound ligand and all water molecules. Using the ProteinPrep workflow¹⁵³ within Maestro, the remaining monomer-ligand complex was preliminarily prepared for molecular modeling. With the Prime application¹⁷³ in Maestro, the resulting structure was further subjected to a series of loop refinements and energy minimizations to optimize side chain geometries and orientations, which were subsequently analyzed using web-based ProCheck¹⁸⁴. With the *mGluR3-1H₂O* model prepared and optimized, utilization of the Glide application enabled standard precision docking of NAAG into *mGluR3-0H₂O*, resulting in several predicted NAAG conformations within the ligand binding pocket, the lowest energy conformation being represented in **Figure 21**. Due to the absence of water molecules in the orthosteric binding pocket of *mGluR3-0H₂O*, this mGluR3 model was also employed for generation of a corresponding mGluR2 homology model (*mGluR2-0H₂O*) in order to allow maximum flexibility of residues in the orthosteric binding region. Using the Prime application, *mGluR3-0H₂O* was used as a three-dimensional template on which to base *mGluR2-0H₂O*. A web-based version of Protein BLAST was used for multiple sequence alignment of all 8 mGluRs, resulting in an mGluR3 and mGluR2 sequence alignment that was 66% identical and 80% homologous. This alignment was imported into Prime, where all sequence gaps were left untreated, except for a three residue gap in the mGluR3 sequence. Secondary structure prediction indicated α -helical character spanning this gap, and accordingly, the single displaced α -helical residue (S503 at mGluR3) was moved to the other side of the gap. Using Prime, the resulting mGluR2 structure was subjected to a series of loop refinements, energy minimizations, and side chain predictions. Model specifications were again analyzed with web-based ProCheck, and optimized mGluR2 homology model *mGluR2-0H₂O* was generated. Finally, *mGluR3-0H₂O* and *mGluR2-0H₂O* were exported from Maestro as .pdb files and subsequently imported into PyMOL⁸⁰ for figure preparation.

2.4.c. *GloSensor Assays*

cDNA encoding rat mGluR2, mGluR3, mGluR4, mGluR6, or mGluR8 were cloned into the pIRES2-AcGFP1 vector, digested with EcoRI (New England Biolabs, Ipswich, MA) using the In-Fusion cloning method (Clontech, Mountain View, CA). Polymerase chain reactions (PCR) to amplify mGluR cDNAs for insertion into the pIRES2-AcGFP1 vector were performed using the Phusion High-Fidelity DNA Polymerase Kit (New England Biolabs). The entire sequence of each mGluR construct was confirmed by sequence analysis (Genewiz, South Plainfield, NJ). The pGloSensor-22F cAMP plasmid was purchased from the Promega Corporation. Dulbecco's modified Eagle's medium (DMEM), proline, FBS, hygromycin, Lipofectamine LTX, and dialyzed FBS for cell culture were purchased from Invitrogen (Carlsbad, CA). G-418 was purchased from Research Products International (Mount Prospect, IL). Forskolin and PTX, as well as receptor agonists glutamate, DCG-IV, AP4, and quisqualate and receptor antagonists LY341495, EGlu, and CPPG, were obtained from Tocris Bioscience (Ellisville, MO). D-Luciferin potassium salt was purchased from Gold Biotechnology (St. Louis, MO). Pyruvate, sodium chloride, potassium chloride, calcium chloride, magnesium chloride, sodium bicarbonate, HEPES, sodium gluconate, potassium gluconate, calcium gluconate, magnesium gluconate, sodium methanesulfonate, potassium methanesulfonate, gluconic acid, and TPP tissue culture plasticware were purchased from Sigma-Aldrich (St. Louis, MO). GPT was purchased from Roche Diagnostics (Indianapolis, IN). All buffers were prepared using ultrapure H₂O from a Milli-Q water purification system (EMD Millipore, Billerica, MA).

Cell Culture: Cell culture was performed as described previously^{130,170}. CHO-K1 cells were transfected with the pGloSensor-22F plasmid using Lipofectamine LTX, and cells were subsequently selected using 200 µg/mL hygromycin. CHO cells stably expressing the pGloSensor-22F construct (CHO-Glo) were then transfected with pIRES-AcGFP1 encoding mGluR2, mGluR3, mGluR4, mGluR6, or mGluR8, and cells were selected using 200 µg/mL G-418. Stable cell lines were maintained with 0.8 µg/mL hygromycin and 0.8 µg/mL G-418. All cells were cultured in 6% CO₂ at 37°C in DMEM (high glucose) containing 10% FBS, 300 µM proline, 2 mM glutamine, and antibiotic-antimycotic

(Invitrogen) and in the presence of G-418 and/or hygromycin. Cell lines were maintained in 6 cm polystyrene dishes. Cells for assay were plated on 96-well, white-walled, clear-bottom plates (Corning Life Sciences, Tewksbury, MA) and grown to confluence without G-418 or hygromycin. Rat cerebellar astrocyte cultures were prepared as previously described¹⁴³. Briefly, dissociated cerebellar cells from 7 day old female rat pups were trypsin-digested and grown in DMEM containing 10% FBS on 60 mm TPP dishes, where the medium was exchanged every 3-5 days. Cells were assayed after 9-12 days *in vitro*. Animal use was reviewed and approved by Georgetown IACUC.

Buffers: With the exception of assays involving GPT, all assays were performed in either Locke's buffer or a modified Locke's buffer to replace specific ions (**Table 11**). To substitute for sodium (Locke-Na⁺), sodium chloride and sodium bicarbonate were replaced with choline chloride and choline bicarbonate, respectively. To substitute for chloride (Locke-Cl⁻), sodium chloride, potassium chloride, magnesium chloride, and calcium chloride were replaced with (1) sodium gluconate, potassium gluconate, magnesium gluconate, and calcium gluconate, respectively, (2) sodium bicarbonate, potassium bicarbonate, magnesium bicarbonate, and calcium bicarbonate, respectively, or (3) sodium methanesulfonate and potassium methanesulfonate. Potassium (Locke-K⁺), magnesium (Locke-Mg⁺²), or calcium (Locke-Ca⁺²) was replaced with sodium chloride. HEPES (Locke-HEPES) was replaced with Tris and adjusted to pH 7.4 with gluconic acid.

cAMP Measurements: All GloSensor assays were performed using live cells, in a 96-well format on sterile white-walled, clear-bottom plates. Culture medium was aspirated and replaced with 100 μ L of the appropriate Locke's buffer containing 0.45 mg/mL or 1.8 mg/mL D-luciferin (Locke-Luc). To equilibrate the cells with substrate, plates were preincubated in the dark at room temperature for 1 hr. Bioluminescence was quantified using the EnVision Multilabel Plate Reader (PerkinElmer Life and Analytical Sciences, Waltham, MA) using a 1 s integration time. Before drug addition, each plate was read five times at 2 min intervals to establish basal bioluminescence levels from each well. The average of these five pre readings was used to normalize each well's response to account for differences in GloSensor expression and cell density. After the five pre readings, a final concentration of 1 μ M

forskolin with the appropriate final concentration of agonist, and/or antagonist was added in 50 μ L Locke-Luc buffer (150 μ L final volume). Measurements were taken every 2 min for 18 min after drug addition. The bioluminescence measured at 16 min was used for generation of bar graphs and concentration-response curves. For real-time competition experiments, a second treatment (vehicle, agonist, or antagonist) was applied at 18 min in 50 μ L Locke-Luc buffer (200 μ L final volume). To account for the volume increase, forskolin and the first treatment drug were also added to maintain initial concentrations. For experiments involving PTX, 1 μ g/mL PTX was added to each well 24 hrs prior to assay. The GPT assay protocol was similar to all other GloSensor assays, with the exception that the assay was performed in DMEM buffer containing 10% dialyzed FBS, 1.8 mg/mL *D*-Luciferin, 10 mM pyruvate, and either vehicle or 33 μ g/mL GPT in DMEM. The medium on confluent cells was replaced with DMEM buffer with or without GPT, and plates were subsequently returned to the incubator for 3 hrs. These plates were then removed from the incubator and incubated in the dark at room temperature for 1 hr. Drugs were added in DMEM buffer after baseline readings, and luminescence was quantified as described above.

Site-Directed Mutagenesis: Mutations to mGluR cDNAs were performed by PCR-based mutagenesis using the In-Fusion HD cloning system (Clontech). Briefly, for each point mutation, two PCR products were produced with 15 bp complementary at both the 3' end of the first PCR product and at the 5' end of the second PCR product. Each point mutation was engineered into the complementary 15 bp overhangs. PCR reactions were performed using the Phusion High-Fidelity DNA Polymerase Kit (New England Biolabs, Ipswich, MA), and products were cloned into an EcoRI cut-site using the In-Fusion cloning method. Each mutation was confirmed by sequence analysis (Genewiz, South Plainfield, NJ). Vectors expressing mutant mGluRs were individually transfected into CHO-Glo cells using Lipofectamine LTX.

Statistical Analysis: Statistical significance was assessed using either a two-tailed Student's t test, or a one-way ANOVA with a Bonferroni post-hoc test, as appropriate. Concentration-response curves

were calculated by nonlinear regression using a four parameter logistic equation. All calculations were performed using GraphPad Prism software.

2.4.d. LANCE cAMP Assays

cAMP production from astrocytes was measured using the LANCE cAMP kit (PerkinElmer) according to the manufacturer's instructions. Concisely, the media on cerebellar astrocytes that were grown on 60 mm TPP plates was exchanged for Locke's buffer, and plates were equilibrated to room temperature for 1 hr. Cells were scraped from the dishes, centrifuged at 1000 x g for 1 min, and washed once with Locke's buffer. The cells were then resuspended in Stimulation buffer (containing a 1:100 dilution of the Alexa-Fluor 647 antibody), and subsequently mixed with drug dilutions in a ProxiPlate-384 microplate (PerkinElmer). Cells were stimulated for 30 min at room temperature, Detection Mix was added, and the plates were further incubated for 1 hr at room temperature. Fluorescence was stimulated with an excitation wavelength of 340 nm, and emission was read at 615 nm and 665 nm. Data were normalized to the readings from the control emission wavelength (615 nm).

Part 3. Overall Conclusions

3.1. Crossover between Sphingolipids and mGluRs

Although the projects described in Part 1 and Part 2 were considered, designed, and implemented separately, the respective topics in biochemistry and pharmacology may actually be more intertwined than originally appreciated. Since sphingolipids and 7TMRs are both localized predominantly within lipid bilayers, 7TMR structure and function could, in principle, be modulated via sphingolipid interaction. While this is, of course, highlighted by the class of S1PRs, there are a few alternative reports in the literature of such phenomena. For instance, addition of fumonisin B₁ to CHO cells stably expressing serotonin_{1A} 7TMRs (5-HT_{1A}R), decreased membrane levels of sphingomyelin in a concentration-dependent manner, which translated not only into reduced 5-HT_{1A}R orthosteric agonist binding, but also into diminished G protein-dependent signaling¹⁸⁵. In contrast, addition of sphingosine to cells treated with fumonisin B₁ replenished membrane sphingolipid concentrations and reverted agonist binding back to control levels. Importantly, receptor expression remained unaffected after addition of fumonisin B₁, both with and without sphingosine, suggesting that membrane-associated sphingolipids regulate agonist binding, 5-HT_{1A}R conformation, and ultimately, G protein-dependent signaling. Additionally, reduction of intracellular levels of glycosphingolipids via addition of glycosyltransferase inhibitor PDMP to cultured human cervical cancer (HeLa) cells expressing 5-HT₇R resulted in decreased maximal serotonin binding, but did not affect serotonin binding affinity or 5-HT₇R expression¹⁸⁶. PDMP also reduced orthosteric agonist binding to 5-HT_{1A}R in transfected CHO cells *in vitro*, but did not alter binding affinity or coupling to G proteins¹⁸⁷. Furthermore, monosialotetrahexosylganglioside (GM1) was reported to alter both the K_D and B_{max} of orthosteric antagonist [³H]-spiperone to membranes containing 5-HTR that were harvested from rat dorsal cerebral cortex¹⁸⁸. Interestingly, putative sphingolipid binding motifs have been detected computationally in various 5-HTR across several species¹⁸⁵, as well in the 6th transmembrane helix of human mGluR2¹⁸⁹, which bound to radiolabeled sphingolipid precursors and/or metabolites in

transiently transfected HeLa cells. Furthermore, elevation of intracellular GM1 in F11 cells or in transfected CHO cells modulated δ -opioid receptor G protein coupling and intracellular concentrations of cAMP *in vitro*, which likely stemmed from changes in receptor conformation¹⁹⁰. Overall, these results suggest that various sphingolipid species naturally bind to and modulate the activity of several 7TMR subtypes, and future developments relating to these interactions will not only enhance our understanding of 7TMR conformational dynamics within the plasma membrane, but could also present powerful opportunities for the discovery of novel therapeutic agents.

In turn, identification of novel sphingolipid analogs that selectively modulate the activity of 5-HT_{1A} could represent an opportunity to develop therapeutic agents with novel mechanisms of action. Such a project will be used as a platform to discuss important considerations, including lessons learned from the trenches during the implementation of the projects described in Part 1 and Part 2, for each stage of the drug discovery process. Drug discovery typically begins with identification of a biological target (protein, oligonucleotide, biochemical pathway, etc.) that has been therapeutically validated for some disease state. For example, inhibition of certain isoforms of 5-HT_{1A} clinically attenuates symptoms associated with the psychotic symptoms of schizophrenia¹⁹¹. 5-HT_{1A} was validated as a viable target for atypical anti-psychotics by preclinical biological studies¹⁹², just as mGluR3 was validated as a therapeutic target for Alzheimer's disease through preclinical biological experiments involving mGluR3^{-/-} and mGluR2^{-/-} KO mice¹²⁵. While these studies certainly point towards mGluR3 as the group II mGluR to target for neuroprotection, it has been argued that the results are perhaps confounded by compensatory mechanisms whereby, in the absence of mGluR2 *in vivo*, mGluR3 adopts several roles normally specific to mGluR2. In the case of 5-HT_{1A}, the successful clinical evaluation of 5-HT_{1A} antagonism directly supports inhibition of 5-HT_{1A} as a viable strategy with which to treat the psychotic symptoms of schizophrenia¹⁹¹. However, because several 5-HT_{1A} inhibitors have been FDA-approved, the barrier to approval for second generation 5-HT_{1A} inhibitor anti-psychotics is much higher than for those with novel mechanisms of action. Perhaps sphingolipid pathway modulators lie somewhere between these two extremes. While pathway modulator and S1PR agonist prodrug

fingolimod has been FDA-approved for treatment of multiple sclerosis, no other pathway modulator has been approved for any other indication, emphasizing an opportunity to develop sphingolipid pathway modulators for other disease states with novel mechanisms of action¹⁹³. Whatever the disease state of interest, it is imperative not only to pursue therapeutic targets that have been appropriately validated, but also to evaluate the potential risks versus the potential rewards, especially if the major research goal is an approved clinical agent. While both industrial and academic researchers obviously value high reward discoveries, academia is generally more tolerant of high risk projects, especially if the research involves validation of a novel mechanism of action. In contrast to industrial research, which is generally corporately structured, academic research typically facilitates more seamlessly the pursuit of discoveries made while examining something else for a different purpose, such as chloride activity and mGluR3, which was discovered while searching for selective mGluR3 agonists. In this case, discovery of chloride activity at mGluR3 but not mGluR2 actually highlights a new opportunity for selective mGluR3 agonist design, bringing full circle this synergistic serendipity.

The next stage of the drug discovery process involves the identification of hit compounds, which are typically discovered via high throughput screening and/or computational molecular modeling, or in contrast, via slight modification of endogenous small molecules. The latter is exemplified by the conceptual removal of the sphingosine primary hydroxyl group to prevent metabolic phosphorylation to S1P, which resulted in the identification of 1-deoxysphingosine as a hit compound²². In general, a hit compound demonstrates proof-of-concept activity, even if the potency and/or efficacy is weak; in the case of sphingosine analogs with anti-cancer potential, the desired activity profile constituted an improvement in cytotoxic signaling and an attenuation of sphingosine kinase-mediated phosphorylation, as compared to the parent compound sphingosine. Similarly, a DCG-IV/quisqualate hybrid would mark a hit compound if it demonstrated selectivity for mGluR3. As exemplified by the apparent inactivity of NAAG at mGluR3 in the GloSensor assay, it is extremely important to verify the measurable activity of both hit and parent compounds in the desired assay paradigm so as to avoid wasting valuable time and resources on the synthetic preparation of analogs

(e.g. NAAG analogs) of invalidated parent compounds (e.g. NAAG). These considerations could also be applied to the discovery of sphingolipid analogs with anti-psychotic properties by virtue of inhibition of 5-HT_{1R}. For example, suppose that sphingomyelin acts as either a PAM or a cofactor of 5-HT_{1R}. It would follow that the sphingomyelin binding site, which must be occupied by sphingomyelin for maximal receptor activity, could be accessed by sphingomyelin analogs exhibiting bulky and lipophilic structural modifications, which could inhibit receptor function. Because sphingolipids undergo rapid interconversion inside the cell to a vast number of metabolites however, it would be of utmost importance to verify that the active species responsible for PAM and/or cofactor activity is actually sphingomyelin. This could be accomplished using a variety of methods including but not limited to appropriately designed binding experiments, cell-based assays utilizing enzyme inhibitors, and lipidomics analyses. Sphingomyelin analog selectivity between 5-HT_{1R} subtypes must also be considered, and a true hit compound would inhibit selectively the desired isoform(s), even if analog potency and/or efficacy is weak at this stage.

Traditional medicinal chemistry comes into play during both the hit-to-lead optimization stage, as well as the lead refinement stage, of the drug discovery process. Drug design at these stages is highly enabled by computational molecular modeling, either with ligand-based (e.g. pharmacophore mapping) or structure-based techniques (e.g. ligand docking). The major goals during the hit-to-lead optimization stage and the lead refinement stage are to maximize on-target potency, attenuate off-target activity, and optimize solubility, metabolism, and bioavailability. Falling into this category is incorporation of the C-5 hydroxyl group of Enigmol to retain sphingosine-like solubility, as well as utilization of the unnatural C-3 hydroxyl group stereocenter of Enigmol to slow CS-mediated *N*-acylation. As described herein, the lead compound Enigmol was further refined via fluorination of the lipid tail to improve bioavailability. Notably, lead compounds and refined lead compounds alike typically need to be prepared on large scale to provide ample material for rigorous biological characterization. Comparison of Enigmol and its fluorinated analogs for example, could not be conducted with the use of cell-based assays, but rather required whole animals for analysis of pharmacokinetic properties. As exemplified

by the assessment of Enigmol, CF₃-Enigmol, and CF₂-Enigmol in mouse xenograft models of prostate cancer, the final stage of the drug discovery process involves preclinical evaluation of efficacy in various animal models of the desired disease state. Accordingly, launching CF₂-Enigmol from the drug discovery process into the drug development process would likely require 1) significant efficacy in alternative animal models of prostate cancer and/or lung cancer, 2) successful toxicity results at high doses (e.g. 100 mg/kg) in multiple mammalian species (e.g. mice, rats, and dogs), and 3) an improved synthetic process to enable more efficient preparation of CF₂-Enigmol in ≥ 10 g batches. Although most of these points concerning the discovery of CF₂-Enigmol within the context of the drug discovery process would apply to the discovery of sphingolipid-derived 5-HT_{2A} inhibitors with anti-psychotic properties, one exception is emphasized by the need to further optimize the CF₂-Enigmol scale up process. While this perhaps would not have been an ideal graduate student project, preclinical development of CF₂-Enigmol would have profoundly benefited from early improvements to the corresponding synthetic route. Although many improvements were made, process optimization was not the focus, and most of the enhancements were marginal. This highlights that organic synthesis is often the bottleneck of the drug discovery process, and that it doesn't matter how many appropriate animal models of a disease state are available if sufficient quantities of the experimental drug cannot be produced. Therefore, consideration of synthetic accessibility early on in the drug discovery process is advantageous to the successful development of clinical candidates, such as sphingolipid-derived 5-HT_{2A} inhibitors designed to treat the psychotic symptoms of schizophrenia. For such a class of neuroactive compounds, it would also be imperative to ensure that lead compounds and refined lead compounds alike penetrate the blood-brain barrier by either passive or active transport. If the lead compound demonstrates poor absorption into the brain, a series of refined leads would be designed with the goal of either 1) increasing compound lipophilicity to enhance passive transport or 2) discovering prodrugs to target active transport mechanisms. Overall, the drug discovery process is much less linear than it is typically depicted, and it more accurately involves numerous, interdisciplinary, simultaneously moving parts that must work in concert towards the common goal of clinical

development, without which discoveries made in the laboratory can never reach the bedside of the patient in need.

3.2. References

- (1) Pruett, S. T.; Bushnev, A.; Hagedorn, K.; Adiga, M.; Haynes, C. A.; Sullards, M. C.; Liotta, D. C.; Merrill, A. H. Biodiversity of Sphingoid Bases (“Sphingosines”) and Related Amino Alcohols. *J. Lipid Res.* **2008**, *49*, 1621–1639.
- (2) Zheng, W.; Kollmeyer, J.; Symolon, H.; Momin, A.; Munter, E.; Wang, E.; Kelly, S.; Allegood, J. C.; Liu, Y.; Peng, Q.; Ramaraju, H.; Sullards, M. C.; Cabot, M.; Merrill, A. H. Ceramides and Other Bioactive Sphingolipid Backbones in Health and Disease: Lipidomic Analysis, Metabolism, and Roles in Membrane Structure, Dynamics, Signaling and Autophagy. *Biochim. Biophys. Acta* **2006**, *1758*, 1864–1884.
- (3) Nussbaumer, P. Medicinal Chemistry Aspects of Drug Targets in Sphingolipid Metabolism. *ChemMedChem* **2008**, *3*, 543–551.
- (4) Spiegel, S.; Milstien, S. Sphingosine-1-Phosphate: An Enigmatic Signalling Lipid. *Nat. Rev. Mol. Cell Biol.* **2003**, *4*, 397–407.
- (5) Merrill, A. H. Sphingolipid and Glycosphingolipid Metabolic Pathways in the Era of Sphingolipidomics. *Chem. Rev.* **2011**, *111*, 6387–6422.
- (6) Merrill, A. H.; Liotta, D. C.; Riley, R. T. Fumonisin: Fungal Toxins That Shed Light on Sphingolipid Function. *Trends Cell Biol.* **1996**, *6*, 218–223.
- (7) Nava, V. E.; Hobson, J. P.; Murthy, S.; Milstien, S.; Spiegel, S. Sphingosine Kinase Type 1 Promotes Estrogen-Dependent Tumorigenesis of Breast Cancer MCF-7 Cells. *Exp. Cell Res.* **2002**, *281*, 115–127.
- (8) Kohno, M.; Momoi, M.; Oo, M. L.; Paik, J.-H.; Lee, Y.-M.; Venkataraman, K.; Ai, Y.; Ristimaki, A. P.; Fyrst, H.; Sano, H.; Rosenberg, D.; Saba, J. D.; Proia, R. L.; Hla, T. Intracellular Role for Sphingosine Kinase 1 in Intestinal Adenoma Cell Proliferation. *Mol. Cell. Biol.* **2006**, *26*, 7211–7223.
- (9) Merrill, A. H.; Nimkar, S.; Menaldino, D.; Hannun, Y. A.; Loomis, C.; Bell, R. M.; Tyagi, S. R.; Lambeth, J. D.; Stevens, V. L.; Hunter, R.; Liotta, D. C. Structural Requirements for Long-Chain (Sphingoid) Base Inhibition of Protein Kinase C in Vitro and for the Cellular Effects of These Compounds. *Biochemistry* **1989**, *28*, 3138–3145.
- (10) Olivera, A.; Kohama, T.; Edsall, L.; Nava, V.; Cuvillier, O.; Poulton, S.; Spiegel, S. Sphingosine Kinase Expression Increases Intracellular Sphingosine-1-Phosphate and Promotes Cell Growth and Survival. *J. Cell Biol.* **1999**, *147*, 545–557.
- (11) Xia, P.; Gamble, J. R.; Wang, L.; Pitson, S. M.; Moretti, P. A. B.; Wattenberg, B. W.; D’Andrea, R. J.; Vadas, M. A. An Oncogenic Role of Sphingosine Kinase. *Curr. Biol.* **2000**, *10*, 1527–1530.

- (12) Johnson, K. R.; Johnson, K. Y.; Crellin, H. G.; Ogretmen, B.; Boylan, A. M.; Harley, R. A.; Obeid, L. M. Immunohistochemical Distribution of Sphingosine Kinase 1 in Normal and Tumor Lung Tissue. *J. Histochem. Cytochem.* **2005**, *53*, 1159–1166.
- (13) Mandala, S. M.; Thornton, R.; Galve-Roperh, I.; Poulton, S.; Peterson, C.; Olivera, A.; Bergstrom, J.; Kurtz, M. B.; Spiegel, S. Molecular Cloning and Characterization of a Lipid Phosphohydrolase That Degrades Sphingosine-1- Phosphate and Induces Cell Death. *Proc. Natl. Acad. Sci. U. S. A.* **2000**, *97*, 7859–7864.
- (14) Sweeney, E. A.; Sakakura, C.; Shirahama, T.; Masamune, A.; Ohta, H.; Hakomori, S.; Igarashi, Y. Sphingosine and Its Methylated Derivative N,N-Dimethylsphingosine (DMS) Induce Apoptosis in a Variety of Human Cancer Cell Lines. *Int. J. Cancer* **1996**, *66*, 358–366.
- (15) Auzenne, E.; Leroux, M. E.; Hu, M.; Pollock, R. E.; Feig, B.; Klostergaard, J. Cytotoxic Effects of Sphingolipids as Single or Multi-Modality Agents on Human Melanoma and Soft Tissue Sarcoma in Vitro. *Melanoma Res.* **1998**, *8*, 227–239.
- (16) French, K. J.; Upson, J. J.; Keller, S. N.; Zhuang, Y.; Yun, J. K.; Smith, C. D. Antitumor Activity of Sphingosine Kinase Inhibitors. *J. Pharmacol. Exp. Ther.* **2006**, *318*, 596–603.
- (17) Plano, D.; Amin, S.; Sharma, A. K. Importance of Sphingosine Kinase (SphK) as a Target in Developing Cancer Therapeutics and Recent Developments in the Synthesis of Novel SphK Inhibitors. *J. Med. Chem.* **2014**, *57*, 5509–5524.
- (18) Desai, K.; Sullards, M. C.; Allegood, J.; Wang, E.; Schmelz, E. M.; Hartl, M.; Humpf, H.-U.; Liotta, D. C.; Peng, Q.; Merrill, A. H. Fumonisin and Fumonisin Analogs as Inhibitors of Ceramide Synthase and Inducers of Apoptosis. *Biochim. Biophys. Acta* **2002**, *1585*, 188–192.
- (19) Esteve, J.; Lorente, A.; Romea, P.; Urpi, F.; Rios-Luci, C.; Padron, J. M. Synthesis and Biological Evaluation of 1-Deoxy-5-Hydroxysphingosine Derivatives. *European J. Org. Chem.* **2011**, 960–967.
- (20) Garnier-Amblard, E. C.; Mays, S. G.; Arrendale, R. F.; Baillie, M. T.; Bushnev, A. S.; Culver, D. G.; Evers, T. J.; Holt, J. J.; Howard, R. B.; Liebeskind, L. S.; Menaldino, D. S.; Natchus, M. G.; Petros, J. A.; Ramaraju, H.; Reddy, G. P.; Liotta, D. C. Novel Synthesis and Biological Evaluation of Enigmols as Therapeutic Agents for Treating Prostate Cancer. *ACS Med. Chem. Lett.* **2011**, *2*, 438–443.
- (21) Humpf, H.-U.; Schmelz, E.-M.; Meredith, F. I.; Vesper, H.; Vales, T. R.; Wang, E.; Menaldino, D. S.; Liotta, D. C.; Merrill, A. H. Acylation of Naturally Occurring and Synthetic 1-Deoxysphinganine by Ceramide Synthase. *J. Biol. Chem.* **1998**, *273*, 19060–19064.
- (22) Bushnev, A. S.; Baillie, M. T.; Holt, J. J.; Menaldino, D. S.; Merrill, A. H.; Liotta, D. C. An Efficient Asymmetric Synthesis of Enigmols (1-Deoxy-5-Hydroxysphingoid Bases), an Important Class of Bioactive Lipid Modulators. *ARKIVOC* **2010**, *viii*, 263–277.
- (23) Symolon, H.; Bushnev, A.; Peng, Q.; Ramaraju, H.; Mays, S. G.; Allegood, J. C.; Pruett, S. T.; Sullards, M. C.; Dillehay, D. L.; Liotta, D. C.; Merrill, A. H. Enigmol: A Novel Sphingolipid Analogue with Anticancer Activity against Cancer Cell Lines and In Vivo Models for Intestinal and Prostate Cancer. *Mol. Cancer Ther.* **2011**, *10*, 648–657.
- (24) Menaldino, D. S.; Bushnev, A.; Sun, A.; Liotta, D. C.; Symolon, H.; Desai, K.; Dillehay, D. L.; Peng, Q.; Wang, E.; Allegood, J.; Trotman-Pruett, S.; Sullards, M. C.; Merrill, A. H. Sphingoid

- Bases and de Novo Ceramide Synthesis: Enzymes Involved, Pharmacology and Mechanisms of Action. *Pharmacol. Res.* **2003**, *47*, 373–381.
- (25) Pruett, S. T. Biological Mass Spectrometry of Sphingolipids in Drug Discovery and Development Chemistry. Ph.D. Thesis, Emory University, Atlanta, GA, 2006.
- (26) Meyer, E. V. S.; Holt, J. J.; Girard, K. R.; Ballie, M. T.; Bushnev, A. S.; Lapp, S.; Menaldino, D. S.; Arrendale, R. F.; Reddy, G. P.; Evers, T. J.; Howard, R. B.; Culver, D. G.; Liotta, D. C.; Galinski, M. R.; Natchus, M. G. Sphingolipid Analogues Inhibit Development of Malaria Parasites. *ACS Med. Chem. Lett.* **2012**, *3*, 43–47.
- (27) Liotta, D. C.; Holt, J. J.; Natchus, M. G.; Galinski, M. R.; Baillie, M. T.; Miller, E. J. Sphingosine Analogs, Compositions, and Methods Related Thereto. WO 2013/049280 A2, 2013.
- (28) Pulukuri, S. M. K.; Gondi, C. S.; Lakka, S. S.; Jutla, A.; Estes, N.; Gujrati, M.; Rao, J. S. RNA Interference-Directed Knockdown of Urokinase Plasminogen Activator and Urokinase Plasminogen Activator Receptor Inhibits Prostate Cancer Cell Invasion, Survival, and Tumorigenicity in Vivo. *J. Biol. Chem.* **2005**, *280*, 36529–36540.
- (29) QikProp, Version 4.4, Schrödinger, LLC., New York, NY, 2015.
- (30) Maestro, Version 10.2, Schrödinger, LLC., New York, NY, 2015.
- (31) Dalvi, V. H.; Rossky, P. J. Molecular Origins of Fluorocarbon Hydrophobicity. *Proc. Natl. Acad. Sci. U. S. A.* **2010**, *107*, 13603–13607.
- (32) Kirk, K. L. Fluorination in Medicinal Chemistry: Methods, Strategies, and Recent Developments. *Org. Process Res. Dev.* **2008**, *12*, 305–321.
- (33) Reetz, M. T. Synthesis and Diastereoselective Reactions of N,N-Dibenzylamino Aldehydes and Related Compounds. *Chem. Rev.* **1999**, *99*, 1121–1162.
- (34) Varala, R.; Adapa, S. R. Ruthenium(III) Acetylacetonate [Ru(acac)₃] - An Efficient Chemoselective Catalyst for the Tetrahydropyranylation (THP) of Alcohols and Phenols under Solvent-Free Conditions. *Can. J. Chem.* **2006**, *84*, 1174–1179.
- (35) Linderman, R. J.; Graves, D. M. Oxidation of Fluoroalkyl-Substituted Carbinols by the Dess-Martin Reagent. *J. Org. Chem.* **1989**, *54*, 661–668.
- (36) Meyer, S. D.; Schreiber, S. L. Acceleration of the Dess-Martin Oxidation by Water. *J. Org. Chem.* **1994**, *59*, 7549–7552.
- (37) Ley, S. V.; Norman, J.; Griffith, W. P.; Marsden, S. P. Tetrapropylammonium Perruthenate, Pr₄N⁺RuO₄⁻, TPAP: A Catalytic Oxidant for Organic Synthesis. *Synthesis (Stuttg.)* **1994**, *7*, 639–666.
- (38) Quero, C.; Rosell, G.; Jimenez, O.; Rodriguez, S.; Bosch, M. P.; Guerrero, A. New Fluorinated Derivatives as Esterase Inhibitors. Synthesis, Hydration, and Crossed Specificity Studies. *Bioorg. Med. Chem.* **2003**, *11*, 1047–1055.
- (39) Chiu, C. C.; Jordan, F. Novel Synthesis of 2-Oxo-4-Phenyl-3-Butanoic Acid, a New Inhibitor and Alternate Substrate of Pyruvate Decarboxylase. *J. Org. Chem.* **1994**, *59*, 5763–5766.

- (40) Nimitz, J. S.; Mosher, H. S. A New Synthesis of α -Keto Esters and Acids. *J. Org. Chem.* **1981**, *42*, 211–213.
- (41) Cochi, A.; Métro, T.-X.; Pardo, D. G.; Cossy, J. Enantioselective Synthesis of SSR 241586 by Using an Organo-Catalyzed Henry Reaction. *Org. Lett.* **2010**, *12*, 3693–3695.
- (42) Dubowchik, G. M.; Padilla, L.; Edinger, K.; Firestone, R. A. Amines That Transport Protons across Bilayer Membranes: Synthesis, Lysosomal Neutralization, and Two-Phase pK_a Values by NMR. *J. Org. Chem.* **1996**, *61*, 4676–4684.
- (43) Lemonnier, G.; Zoute, L.; Quirion, J.-C.; Jubault, P. First Efficient Synthesis of Fluorinated Glycidic Esters from Ketones. *Org. Lett.* **2010**, *12*, 844–846.
- (44) Iseki, K.; Asada, D.; Kuroki, Y. Preparation of Optically Active α,α -Difluoro- β -Hydroxyketones. *J. Fluor. Chem.* **1999**, *97*, 85–89.
- (45) Reetz, M. T.; Drewes, M. W.; Schwickardi, R. Preparation of Enantiomerically Pure α -N,N-Dibenzylamino Aldehydes: S-2-(N,N-Dibenzylamino)-3-Phenylpropanol. *Org. Synth.* **1999**, *76*, 110–116.
- (46) Stanway, S. J.; Thomas, E. J. 1,5-Stereocontrol in Tin(IV) Halide Mediated Reactions between N- and S-Substituted Pent-2-Enylstannanes and Aldehydes or Imines. *Tetrahedron* **2012**, *68*, 5998–6009.
- (47) Dias, L. C.; Fattori, J.; Perez, C. C.; de Oliveira, V. M.; Aguilar, A. M. An Efficient Procedure for the Synthesis of 2-N-Boc-Amino-3,5-Diols. *Tetrahedron* **2008**, *64*, 5891–5903.
- (48) Pan, Q.; Zou, B.; Wang, Y.; Ma, D. Diastereoselective Aldol Reaction of N,N-Dibenzyl- α -Amino Aldehydes with Ketones Catalyzed by Proline. *Org. Lett.* **2004**, *6*, 1009–1012.
- (49) Rychnovsky, S. D.; Skalitzky, D. J. Stereochemistry of Alternating Polyol Chains: ¹³C NMR Analysis of 1,3-Diol Acetonides. *Tetrahedron Lett.* **1990**, *31*, 945–948.
- (50) Zaidlewicz, M.; Baum, O.; Srebnik, M. Borane Dimethyl Sulfide. *e-EROS: Encyclopedia of Reagents for Organic Synthesis*, 1–9.
- (51) Konas, D. W.; Coward, J. K. Ethyl Bromodifluoroacetate. *e-EROS: Encyclopedia of Reagents for Organic Synthesis*, 1–5.
- (52) Sato, K.; Omote, M.; Ando, A.; Kumadaki, I. Reactions of Ethyl Bromodifluoroacetate in the Presence of Copper Powder. *J. Fluor. Chem.* **2004**, *125*, 509–515.
- (53) Sato, K.; Kawata, R.; Ama, F.; Omote, M.; Ando, A.; Kumadaki, I. Synthesis of Alkenyl- and Aryldifluoroacetate Using a Copper Complex from Ethyl Bromodifluoroacetate. *Chem. Pharm. Bull. (Tokyo)*. **1999**, *47*, 1013–1016.
- (54) Moreno, M.; Murruzzu, C.; Riera, A. Enantioselective Synthesis of Sphingadienines and Aromatic Ceramide Analogs. *Org. Lett.* **2011**, *13*, 5184–5187.
- (55) Kleiderer, E. C.; Adams, R. Stereochemistry of Diphenyls. XXXI. Preparation and Properties of 2,2',6,6'-Tetrafluoro-3,3'-Dicarboxy-5,5'-Dichlorodiphenyl. *J. Am. Chem. Soc.* **1933**, *55*, 4219–4225.
- (56) Xu, J.; Zhang, X.; Qiu, X.-L.; Qing, F.-L. Synthesis of 2,3,4-Trideoxy-4,4-Difluoro-D-Ribohexopyranose Adenosines. *Synthesis (Stuttg.)*. **2009**, *4*, 602–608.

- (57) Dix, D.; Imming, P. New Benzyl-Protected Derivatives of Glycine, Alanine, and Serine: Easily Accessible Building-Blocks for Synthesis. *Arch. Pharm. (Weinheim)*. **1995**, *328*, 203–205.
- (58) Gennari, C.; Moresca, D.; Vulpetti, A.; Pain, G. Reagent Control in the Aldol Addition Reaction of Chiral Boron Enolates with Chiral Aldehydes. Total Synthesis of (3S,4S)-Statine. *Tetrahedron* **1997**, *53*, 5593–5608.
- (59) Reetz, M. T.; Rivadeneira, E.; Niemeyer, C. Reagent Control in the Aldol Addition of Chiral Boron Enolates Based on the 2,5-Diphenylborolane Ligand System. *Tetrahedron Lett.* **1990**, *31*, 3863–3866.
- (60) Reetz, M. T.; Kunisch, F.; Heitmann, P. Chiral Lewis Acids for Enantioselective C-C Bond Formation. *Tetrahedron Lett.* **1986**, *27*, 4721–4724.
- (61) Gennari, C.; Carcano, M.; Donghi, M.; Mongelli, N.; Vanotti, E.; Vulpetti, A. Taxol Semisynthesis: A Highly Enantio- and Diastereoselective Synthesis of the Side Chain and a New Method for Ester Formation at C-13 Using Thioesters. *J. Org. Chem.* **1997**, *62*, 4746–4755.
- (62) Reetz, M. T.; Drewes, M. W.; Schmitz, A. Stereoselective Synthesis of β -Amino Alcohols from Optically Active α -Amino Acids. *Angew. Chemie Int. Ed.* **1987**, *26*, 1141–1143.
- (63) Narasaka, K.; Pai, F.-C. Stereoselective Reduction of β -Hydroxyketones to 1,3-Diols. *Tetrahedron* **1984**, *40*, 2233–2238.
- (64) Chen, K.-M.; Hardtman, G. E.; Prasad, K.; Repic, O.; Shapiro, M. J. 1,3-Syn Diastereoselective Reduction of β -Hydroxyketones Utilizing Alkoxydialkylboranes. *Tetrahedron Lett.* **1987**, *28*, 155–158.
- (65) Kiyooka, S.; Kuroda, H.; Shimasaki, Y. 1,3-Syn Diastereoselective Reduction of β -Hydroxyketones with Diisobutylaluminum Hydride and Tributyltin Hydride. *Tetrahedron Lett.* **1986**, *27*, 3009–3012.
- (66) Kuroboshi, M.; Ishihara, T. Diastereoselective Reduction of α,α -Difluoro β -Hydroxy Ketones to Syn- and Anti-2,2-Difluoro-1,3-Diols. *Bull. Chem. Soc. Jpn.* **1990**, *63*, 1185–1190.
- (67) Morizawa, Y.; Yasuda, A.; Uchida, K. Trifluoromethyl Group Induced Highly Stereoselective Synthesis of α -Hydroxy Carbonyl Compounds. *Tetrahedron Lett.* **1986**, *27*, 1833–1836.
- (68) LigPrep, Version 3.3, Schrödinger, LLC., New York, NY, 2015.
- (69) Bockaert, J.; Pin, J.-P. Molecular Tinkering of G Protein-Coupled Receptors: An Evolutionary Success. *EMBO J.* **1999**, *18*, 1723–1729.
- (70) Krishnan, A.; Schioth, H. B. The Role of G Protein-Coupled Receptors in the Early Evolution of Neurotransmission and the Nervous System. *J. Exp. Biol.* **2015**, *218*, 562–571.
- (71) Gether, U.; Kobilka, B. K. G Protein-Coupled Receptors II. Mechanism of Agonist Activation. *J. Biol. Chem.* **1998**, *273*, 17979–17982.
- (72) Tesmer, J. J. G. Activation of G Protein-Coupled Receptor (GPCR) Kinases by GPCRs. In *G Protein-Coupled Receptors: From Structure to Function*; Royal Society of Chemistry, 2011; pp. 297–315.

- (73) Gurevich, V. V.; Gurevich, E. V. The Mechanics of Arrestin–Receptor Interaction: How GPCRs and Arrestins Talk to Each Other. In *G Protein-Coupled Receptors: From Structure to Function*; Royal Society of Chemistry, 2011; pp. 335–356.
- (74) Rajagopal, S.; Rajagopal, K.; Lefkowitz, R. J. Teaching Old Receptors New Tricks: Biasing Seven-Transmembrane Receptors. *Nat. Rev. Drug Discov.* **2010**, *9*, 373–386.
- (75) Wolfe, B. L.; Trejo, J. Clathrin-Dependent Mechanisms of G Protein-Coupled Receptor Endocytosis. *Traffic* **2007**, *8*, 462–470.
- (76) Pitcher, J. A.; Payne, E. S.; Csontos, C.; DePaoli-Roach, A. A.; Lefkowitz, R. J. The G Protein-Coupled Receptor Phosphatase: A Protein Phosphatase Type 2A with a Distinct Subcellular Distribution and Substrate Specificity. *Proc. Natl. Acad. Sci. U. S. A.* **1995**, *92*, 8343–8347.
- (77) Calebiro, D.; Nikolaev, V. O.; Persani, L.; Lohse, M. J. Signaling by Internalized G Protein-Coupled Receptors. *Trends Pharmacol. Sci.* **2010**, *31*, 221–228.
- (78) Ritter, S. L.; Hall, R. A. Fine-Tuning of GPCR Activity by Receptor-Interacting Proteins. *Nat. Rev. Mol. Cell Biol.* **2009**, *10*, 819–830.
- (79) Rasmussen, S. G. F.; DeVree, B. T.; Zou, Y.; Kruse, A. C.; Chung, K. Y.; Kobilka, T. S.; Thian, F. S.; Chae, P. S.; Pardon, E.; Calinski, D.; Mathiesen, J. M.; Shah, S. T. a; Lyons, J. a; Caffrey, M.; Gellman, S. H.; Steyaert, J.; Skiniotis, G.; Weis, W. I.; Sunahara, R. K.; Kobilka, B. K. Crystal Structure of the β_2 Adrenergic Receptor-Gs Protein Complex. *Nature* **2011**, *477*, 549–557.
- (80) The PyMOL Molecular Graphics System, Version 1.7.4, Schrödinger, LLC., New York, NY.
- (81) Gether, U. Uncovering Molecular Mechanisms Involved in Activation of G Protein-Coupled Receptors. *Endocr. Rev.* **2000**, *21*, 90–113.
- (82) Ring, A. M.; Manglik, A.; Kruse, A. C.; Enos, M. D.; Weis, W. I.; Garcia, K. C.; Kobilka, B. K. Adrenaline-Activated Structure of β_2 -Adrenoceptor Stabilized by an Engineered Nanobody. *Nature* **2013**, *502*, 575–581.
- (83) Muto, T.; Tsuchiya, D.; Morikawa, K.; Jingami, H. Structures of the Extracellular Regions of the Group II/III Metabotropic Glutamate Receptors. *Proc. Natl. Acad. Sci. U. S. A.* **2007**, *104*, 3759–3764.
- (84) Shorr, R. G. L.; Lefkowitz, R. J.; Caron, M. G. Purification of the B-Adrenergic Receptor. *J. Biol. Chem.* **1981**, *256*, 5820–5826.
- (85) Sugiyama, H.; Ito, I.; Hirono, C. A New Type of Glutamate Receptor Linked to Inositol Phosphate Metabolism. *Nature* **1987**, *325*, 531–533.
- (86) Conn, P. J.; Pin, J.-P. Pharmacology and Functions of Metabotropic Glutamate Receptors. *Annu. Rev. Pharmacol. Toxicol.* **1997**, *37*, 205–237.
- (87) Niswender, C. M.; Johnson, K. A.; Luo, Q.; Ayala, J. E.; Kim, C.; Conn, P. J.; Weaver, C. D. A Novel Assay of Gi/o-Linked G Protein-Coupled Receptor Coupling to Potassium Channels Provides New Insights into the Pharmacology of the Group III Metabotropic Glutamate Receptors. *Mol. Pharmacol.* **2008**, *73*, 1213–1224.

- (88) Yanagawa, M.; Yamashita, T.; Shichida, Y. Comparative Fluorescence Resonance Energy Transfer Analysis of Metabotropic Glutamate Receptors: Implications About the Dimeric Arrangement and Rearrangement upon Ligand Bindings. *J. Biol. Chem.* **2011**, *286*, 22971–22981.
- (89) Ishida, M.; Saitoh, T.; Shimamoto, K.; Ohfune, Y.; Shinozaki, H. A Novel Metabotropic Glutamate Receptor Agonist: Marked Depression of Monosynaptic Excitation in the Newborn Rat Isolated Spinal Cord. *Br. J. Pharmacol.* **1993**, *109*, 1169–1177.
- (90) Trombley, P. Q.; Westbrook, G. L. L-AP4 Inhibits Calcium Currents and Synaptic Transmission via a G Protein-Coupled Glutamate Receptor. *J. Neurosci.* **1992**, *12*, 2043–2050.
- (91) Schoepp, D. D.; Goldsworthy, J.; Johnson, B. G.; Salhoff, C. R.; Baker, S. R. 3,5-Dihydroxyphenylglycine Is a Highly Selective Agonist for Phosphoinositide-Linked Metabotropic Glutamate Receptors in the Rat Hippocampus. *J. Neurochem.* **1994**, *63*, 769–772.
- (92) Monn, J. A.; Valli, M. J.; Massey, S. M.; Wright, R. A.; Salhoff, C. R.; Johnson, B. G.; Howe, T.; Alt, C. A.; Rhodes, G. A.; Robey, R. L.; Griffey, K. R.; Tizzano, J. P.; Kallman, M. J.; Helton, D. R.; Schoepp, D. D. Design, Synthesis, and Pharmacological Characterization of (+)-2-Aminobicyclo[3.1.0]hexane-2,6-Dicarboxylic Acid (LY354740): A Potent, Selective, and Orally Active Group 2 Metabotropic Glutamate Receptor Agonist Possessing Anticonvulsant and Anxiolytic Pr. *J. Med. Chem.* **1997**, *40*, 528–537.
- (93) Cuomo, D.; Martella, G.; Barabino, E.; Platania, P.; Vita, D.; Madeo, G.; Selvam, C.; Goudet, C.; Oueslati, N.; Pin, J. P.; Acher, F.; Pisani, A.; Beurrier, C.; Melon, C.; Kerkerian-Le Goff, L.; Gubellini, P. Metabotropic Glutamate Receptor Subtype 4 Selectively Modulates Both Glutamate and GABA Transmission in the Striatum: Implications for Parkinson's Disease Treatment. *J. Neurochem.* **2009**, *109*, 1096–1105.
- (94) Frauli, M.; Neuville, P.; Vol, C.; Pin, J.-P.; Prézeau, L. Among the Twenty Classical L-Amino Acids, Only Glutamate Directly Activates Metabotropic Glutamate Receptors. *Neuropharmacology* **2006**, *50*, 245–253.
- (95) Bertrand, H. O.; Bessis, A.-S.; Pin, J.-P.; Acher, F. C. Common and Selective Molecular Determinants Involved in Metabotropic Glutamate Receptor Agonist Activity. *J. Med. Chem.* **2002**, *45*, 3171–3183.
- (96) Kingston, A. E.; Ornstein, P. L.; Wright, R. A.; Johnson, B. G.; Mayne, N. G.; Burnett, J. P.; Belagaje, R.; Wu, S.; Schoepp, D. D. LY341495 Is a Nanomolar Potent and Selective Antagonist of Group II Metabotropic Glutamate Receptors. *Neuropharmacology* **1998**, *37*, 1–12.
- (97) Schoepp, D. D.; Jane, D. E.; Monn, J. A. Pharmacological Agents Acting at Subtypes of Metabotropic Glutamate Receptors. *Neuropharmacology* **1999**, *38*, 1431–1476.
- (98) Nicoletti, F.; Bockaert, J.; Collingridge, G. L.; Conn, P. J.; Ferraguti, F.; Schoepp, D. D.; Wroblewski, J. T.; Pin, J.-P. Metabotropic Glutamate Receptors: From the Workbench to the Bedside. *Neuropharmacology* **2011**, *60*, 1017–1041.
- (99) Shigemoto, R.; Kinoshita, A.; Wada, E.; Nomura, S.; Ohishi, H.; Takada, M.; Flor, P. J.; Neki, A.; Abe, T.; Nakanishi, S.; Mizuno, N. Differential Presynaptic Localization of Metabotropic Glutamate Receptor Subtypes in the Rat Hippocampus. *J. Neurosci.* **1997**, *17*, 7503–7522.

- (100) Traynelis, S. F.; Wollmuth, L. P.; McBain, C. J.; Menniti, F. S.; Vance, K. M.; Ogden, K. K.; Hansen, K. B.; Yuan, H.; Myers, S. J.; Dingledine, R. Glutamate Receptor Ion Channels: Structure, Regulation, and Function. *Pharmacol. Rev.* **2010**, *62*, 405–496.
- (101) D'Antoni, S.; Berretta, A.; Bonaccorso, C. M.; Bruno, V.; Aronica, E.; Nicoletti, F.; Catania, M. V. Metabotropic Glutamate Receptors in Glial Cells. *Neurochem. Res.* **2008**, *33*, 2436–2443.
- (102) Swanson, C. J.; Bures, M.; Johnson, M. P.; Linden, A.-M.; Monn, J. A.; Schoepp, D. D. Metabotropic Glutamate Receptors as Novel Targets for Anxiety and Stress Disorders. *Nat. Rev. Drug Discov.* **2005**, *4*, 131–144.
- (103) Anjaneyulu, M.; Berent-Spillson, A.; Russel, J. W. Metabotropic Glutamate Receptors (mGluRs) and Diabetic Neuropathy. *Curr. Drug Targets* **2008**, *9*, 85–93.
- (104) Conn, P. J.; Lindsley, C. W.; Jones, C. K. Activation of Metabotropic Glutamate Receptors as a Novel Approach for the Treatment of Schizophrenia. *Trends Pharmacol. Sci.* **2009**, *30*, 25–31.
- (105) Neugebauer, V. Metabotropic Glutamate Receptors - Important Modulators of Nociception and Pain Behavior. *Pain* **2002**, *98*, 1–8.
- (106) Niswender, C. M.; Conn, P. J. Metabotropic Glutamate Receptors: Physiology, Pharmacology, and Disease. *Annu. Rev. Pharmacol. Toxicol.* **2010**, *50*, 295–322.
- (107) Hovelso, N.; Sotty, F.; Montezinho, L. P.; Pinheiro, P. S.; Herrik, K. F.; Mork, A. Therapeutic Potential of Metabotropic Glutamate Receptor Modulators. *Curr. Neuropharmacol.* **2012**, *10*, 12–48.
- (108) Johnson, K. A.; Conn, P. J.; Niswender, C. M. Glutamate Receptors as Therapeutic Targets for Parkinson's Disease. *CNS Neurol. Disord. Drug Targets* **2009**, *8*, 475–491.
- (109) Calabresi, P.; Centonze, D.; Pisani, A.; Bernardi, G. Metabotropic Glutamate Receptors and Cell-Type-Specific Vulnerability in the Striatum: Implications for Ischemia and Huntington's Disease. *Exp. Neurol.* **1999**, *158*, 97–108.
- (110) Makarewicz, D.; Gadamski, R.; Ziembowicz, A.; Kozikowski, A. P.; Wroblewski, J. T.; Lazarewicz, J. W. Neuroprotective Effects of the Agonist of Metabotropic Glutamate Receptors ABHxD-I in Two Animal Models of Cerebral Ischaemia. *Resuscitation* **2006**, *68*, 119–126.
- (111) Gravius, A.; Pietraszek, M.; Dekundy, A.; Danysz, W. Metabotropic Glutamate Receptors as Therapeutic Targets for Cognitive Disorders. *Curr. Top. Med. Chem.* **2010**, *10*, 187–206.
- (112) Bruno, V.; Battaglia, G.; Copani, A.; D'Onofrio, M.; Di Iorio, P.; De Blasi, A.; Melchiorri, D.; Flor, P. J.; Nicoletti, F. Metabotropic Glutamate Receptor Subtypes as Targets for Neuroprotective Drugs. *J. Cereb. Blood Flow Metab.* **2001**, *21*, 1013–1033.
- (113) Caraci, F.; Battaglia, G.; Sortino, M. A.; Spampinato, S.; Molinaro, G.; Copani, A.; Nicoletti, F.; Bruno, V. Metabotropic Glutamate Receptors in Neurodegeneration/Neuroprotection: Still a Hot Topic? *Neurochem. Int.* **2012**, *61*, 559–565.
- (114) Di Liberto, V.; Bonomo, A.; Frinchi, M.; Belluardo, N.; Mudò, G. Group II Metabotropic Glutamate Receptor Activation By Agonist LY379268 Treatment Increases the Expression of Brain Derived Neurotrophic Factor in the Mouse Brain. *Neuroscience* **2010**, *165*, 863–873.

- (115) Ciccarelli, R.; Di Iorio, P.; Bruno, V.; Battaglia, G.; D'Alimonte, I.; D'Onofrio, M.; Nicoletti, F.; Caciagli, F. Activation of A1 Adenosine or mGlu3 Metabotropic Glutamate Receptors Enhances the Release of Nerve Growth Factor and S-100 β Protein From Cultured Astrocytes. *Glia* **1999**, *27*, 275–281.
- (116) Battaglia, G.; Molinaro, G.; Riozzi, B.; Storto, M.; Busceti, C. L.; Spinsanti, P.; Bucci, D.; Di Liberto, V.; Mudo, G.; Corti, C.; Corsi, M.; Nicoletti, F.; Belluardo, N.; Bruno, V. Activation of mGlu3 Receptors Stimulates the Production of GDNF in Striatal Neurons. *PLoS One* **2009**, *4*, e6591.
- (117) Bruno, V.; Battaglia, G.; Casabona, G.; Copani, A.; Caciagli, F.; Nicoletti, F. Neuroprotection by Glial Metabotropic Glutamate Receptors Is Mediated by Transforming Growth Factor-B. *J. Neurosci.* **1998**, *18*, 9594–9600.
- (118) Durand, D.; Carniglia, L.; Caruso, C.; Lasaga, M. mGlu3 Receptor and Astrocytes: Partners in Neuroprotection. *Neuropharmacology* **2013**, *66*, 1–11.
- (119) Battaglia, G.; Bruno, V.; Ngomba, R. T.; Di Grezia, R.; Copani, A.; Nicoletti, F. Selective Activation of Group II Metabotropic Glutamate Receptors Is Protective against Excitotoxic Neuronal Death. *Eur. J. Pharmacol.* **1998**, *356*, 271–274.
- (120) Kingston, A. E.; O'Neill, M. J.; Lam, A.; Bales, K. R.; Monn, J. A.; Schoepp, D. D. Neuroprotection by Metabotropic Glutamate Receptor Agonists: LY354740, LY379268 and LY389795. *Eur. J. Pharmacol.* **1999**, *377*, 155–165.
- (121) Durand, D.; Caruso, C.; Carniglia, L.; Lasaga, M. Metabotropic Glutamate Receptor 3 Activation Prevents Nitric Oxide-Induced Death in Cultured Rat Astrocytes. *J. Neurochem.* **2010**, *112*, 420–433.
- (122) Ciccarelli, R.; D'Alimonte, I.; Ballerini, P.; D'Auro, M.; Nargi, E.; Buccella, S.; Di Iorio, P.; Bruno, V.; Nicoletti, F.; Caciagli, F. Molecular Signalling Mediating the Protective Effect of A1 Adenosine and mGlu3 Metabotropic Glutamate Receptor Activation against Apoptosis by Oxygen/Glucose Deprivation in Cultured Astrocytes. *Mol. Pharmacol.* **2007**, *71*, 1369–1380.
- (123) Carter, K.; Dickerson, J.; Schoepp, D. D.; Reilly, M.; Herring, N.; Williams, J.; Sallee, F. R.; Sharp, J. W.; Sharp, F. R. The mGlu2/3 Receptor Agonist LY379268 Injected into Cortex or Thalamus Decreases Neuronal Injury in Retrosplenial Cortex Produced by NMDA Receptor Antagonist MK-801: Possible Implications for Psychosis. *Neuropharmacology* **2004**, *47*, 1135–1145.
- (124) Bond, A.; Jones, N. M.; Hicks, C. A.; Whiffin, G. M.; Ward, M. A.; O'Neill, M. F.; Kingston, A. E.; Monn, J. A.; Ornstein, P. L.; Schoepp, D. D.; Lodge, D.; O'Neill, M. J. Neuroprotective Effects of LY379268, a Selective mGlu2/3 Receptor Agonist: Investigations into Possible Mechanism of Action in Vivo. *J. Pharmacol. Exp. Ther.* **2000**, *294*, 800–809.
- (125) Corti, C.; Battaglia, G.; Molinaro, G.; Riozzi, B.; Pittaluga, A.; Corsi, M.; Mugnaini, M.; Nicoletti, F.; Bruno, V. The Use of Knock-Out Mice Unravels Distinct Roles for mGlu2 and mGlu3 Metabotropic Glutamate Receptors in Mechanisms of Neurodegeneration/Neuroprotection. *J. Neurosci.* **2007**, *27*, 8297–8308.
- (126) Tesseur, I.; Zou, K.; Esposito, L.; Bard, F.; Berber, E.; van Can, J.; Lin, A. H.; Crews, L.; Tremblay, P.; Mathews, P.; Mucke, L.; Masliah, E.; Wyss-Coray, T. Deficiency in Neuronal

- TGF- β Signaling Promotes Neurodegeneration and Alzheimer's Pathology. *J. Clin. Invest.* **2006**, *116*, 3060–3069.
- (127) Caraci, F.; Molinaro, G.; Battaglia, G.; Giuffrida, M. L.; Rizzo, B.; Traficante, A.; Bruno, V.; Cannella, M.; Merlo, S.; Wang, X.; Heinz, B. A.; Nisenbaum, E. S.; Britton, T. C.; Drago, F.; Sortino, M. A.; Copani, A.; Nicoletti, F. Targeting Group II Metabotropic Glutamate (mGlu) Receptors for the Treatment of Psychosis Associated with Alzheimer's Disease: Selective Activation of mGlu2 Receptors Amplifies B-Amyloid Toxicity in Cultured Neurons, Whereas Dual Activation of mGlu2 and M. *Mol. Pharmacol.* **2011**, *79*, 618–626.
- (128) Durand, D.; Carniglia, L.; Beauquis, J.; Caruso, C.; Saravia, F.; Lasaga, M. Astroglial mGlu3 Receptors Promote Alpha-Secretase-Mediated Amyloid Precursor Protein Cleavage. *Neuropharmacology* **2014**, *79*, 180–189.
- (129) Sun, W.; McConnell, E.; Pare, J.-F.; Xu, Q.; Chen, M.; Peng, W.; Lovatt, D.; Han, X.; Smith, Y.; Nedergaard, M. Glutamate-Dependent Neuroglial Calcium Signaling Differs between Young and Adult Brain. *Science (80-.)*. **2013**, *339*, 197–200.
- (130) DiRaddo, J. O.; Miller, E. J.; Hathaway, H. A.; Grajkowska, E.; Wroblewska, B.; Wolfe, B. B.; Liotta, D. C.; Wroblewski, J. T. A Real-Time Method for Measuring cAMP Production Modulated by G α i/o-Coupled Metabotropic Glutamate Receptors. *J. Pharmacol. Exp. Ther.* **2014**, *349*, 373–382.
- (131) Schweitzer, C.; Kratzeisen, C.; Adam, G.; Lundstrom, K.; Malherbe, P.; Ohresser, S.; Stadler, H.; Wichmann, J.; Woltering, T.; Mutel, V. Characterization of [3 H]-LY354740 Binding to Rat mGlu2 and mGlu3 Receptors Expressed in CHO Cells Using Semliki Forest Virus Vectors. *Neuropharmacology* **2000**, *39*, 1700–1706.
- (132) Monn, J. A.; Valli, M. J.; Massey, S. M.; Hao, J.; Reinhard, M. R.; Bures, M. G.; Heinz, B. A.; Wang, X.; Carter, J. H.; Getman, B. G.; Stephenson, G. A.; Herin, M.; Catlow, J. T.; Swanson, S.; Johnson, B. G.; Mckinzie, D. L.; Henry, S. S. Synthesis and Pharmacological Characterization of 4-Substituted-2-aminobicyclo[3.1.0]hexane-2,6-Dicarboxylates: Identification of New Potent and Selective Metabotropic Glutamate 2/3 Receptor Agonists. *J. Med. Chem.* **2013**, *56*, 4442–4455.
- (133) Monn, J. A.; Valli, M. J.; Massey, S. M.; Hansen, M. M.; Kress, T. J.; Wepsiec, J. P.; Harkness, A. R.; Grutsch, J. L.; Wright, R. A.; Johnson, B. G.; Andis, S. L.; Kingston, A.; Tomlinson, R.; Lewis, R.; Griffey, K. R.; Tizzano, J. P.; Schoepp, D. D. Synthesis, Pharmacological Characterization, and Molecular Modeling of Heterobicyclic Amino Acids Related to (+)-2-Aminobicyclo[3.1.0]hexane-2,6-Dicarboxylic Acid (LY354740): Identification of Two New Potent, Selective, and Systemically Active Agonists. *J. Med. Chem.* **1999**, *42*, 1027–1040.
- (134) Tanabe, Y.; Nomura, A.; Masu, M.; Shigemoto, R.; Mizuno, N.; Nakanishi, S. Signal Transduction, Pharmacological Properties, and Expression Patterns of Two Rat Metabotropic Glutamate Receptors, mGluR3 and mGluR4. *J. Neurosci.* **1993**, *13*, 1372–1378.
- (135) Flor, P. J.; Lindauer, K.; Püttner, I.; Rüegg, D.; Lukic, S.; Knöpfel, T.; Kuhn, R. Molecular Cloning, Functional Expression and Pharmacological Characterization of the Human Metabotropic Glutamate Receptor Type 2. *Eur. J. Neurosci.* **1995**, *7*, 622–629.

- (136) Wroblewska, B.; Wroblewski, J. T.; Pshenichkin, S.; Surin, A.; Sullivan, S. E.; Neale, J. H. N-Acetylaspartylglutamate Selectively Activates mGluR3 Receptors in Transfected Cells. *J. Neurochem.* **1997**, *69*, 174–181.
- (137) Neale, J. H.; Bzdega, T.; Wroblewska, B. N-Acetylaspartylglutamate: The Most Abundant Peptide Neurotransmitter in the Mammalian Central Nervous System. *J. Neurochem.* **2000**, *75*, 443–452.
- (138) Thomas, A. G.; Liu, W.; Olkowski, J. L.; Tang, Z.; Lin, Q.; Lu, X.-C. M.; Slusher, B. S. Neuroprotection Mediated by Glutamate Carboxypeptidase II (NAALADase) Inhibition Requires TGF- β . *Eur. J. Pharmacol.* **2001**, *430*, 33–40.
- (139) Slusher, B. S.; Vornov, J. J.; Thomas, A. G.; Hurn, P. D.; Harukuni, I.; Bhardwaj, A.; Traystman, R. J.; Robinson, M. B.; Britton, P.; Lu, X.-C. M.; Tortella, F. C.; Wozniak, K. M.; Yudkoff, M.; Potter, B. M.; Jackson, P. F. Selective Inhibition of NAALADase, Which Converts NAAG to Glutamate, Reduces Ischemic Brain Injury. *Nat. Med.* **1999**, *5*, 1396–1402.
- (140) Neale, J. H.; Olszewski, R. T.; Zuo, D.; Janczura, K. J.; Profaci, C. P.; Lavin, K. M.; Madore, J. C.; Bzdega, T. Advances in Understanding the Peptide Neurotransmitter NAAG and Appearance of a New Member of the NAAG Neuropeptide Family. *J. Neurochem.* **2011**, *118*, 490–498.
- (141) Koller, K. J.; Coyle, J. T. Characterization of the Interactions of N-Acetyl-L-Aspartyl-Glutamate with [3 H]L-Glutamate Receptors. *Eur. J. Pharmacol.* **1984**, *98*, 193–199.
- (142) Wroblewska, B.; Wroblewski, J. T.; Saab, O. H.; Neale, J. H. N-Acetylaspartylglutamate Inhibits Forskolin-Stimulated Cyclic AMP Levels via a Metabotropic Glutamate Receptor in Cultured Cerebellar Granule Cells. *J. Neurochem.* **1993**, *61*, 943–948.
- (143) Wroblewska, B.; Santi, M. R.; Neale, J. H. N-Acetylaspartylglutamate Activates Cyclic AMP-Coupled Metabotropic Glutamate Receptors in Cerebellar Astrocytes. *Glia* **1998**, *24*, 172–179.
- (144) Berent-Spillson, A.; Robinson, A. M.; Golovoy, D.; Slusher, B.; Rojas, C.; Russell, J. W. Protection Against Glucose-Induced Neuronal Death by NAAG and GCP II Inhibition Is Regulated by mGluR3. *J. Neurochem.* **2004**, *89*, 90–99.
- (145) Thomas, A. G.; Olkowski, J. L.; Slusher, B. S. Neuroprotection Afforded by NAAG and NAALADase Inhibition Requires Glial Cells and Metabotropic Glutamate Receptor Activation. *Eur. J. Pharmacol.* **2001**, *426*, 35–38.
- (146) Fricker, A. C.; Mok, M. H. S.; de la Flor, R.; Shah, A. J.; Woolley, M.; Dawson, L. A.; Kew, J. N. C. Effects of N-Acetylaspartylglutamate (NAAG) at Group II mGluRs and NMDAR. *Neuropharmacology* **2009**, *56*, 1060–1067.
- (147) Chopra, M.; Yao, Y.; Blake, T. J.; Hampson, D. R.; Johnson, E. C. The Neuroactive Peptide N-Acetylaspartylglutamate Is Not an Agonist at the Metabotropic Glutamate Receptor Subtype 3 of Metabotropic Glutamate Receptor. *J. Pharmacol. Exp. Ther.* **2009**, *330*, 212–219.
- (148) Granier, S.; Kobilka, B. A New Era of GPCR Structural and Chemical Biology. *Nat. Chem. Biol.* **2012**, *8*, 670–673.

- (149) Neale, J. H. N-Acetylaspartylglutamate Is an Agonist at mGluR3 in Vivo and in Vitro. *J. Neurochem.* **2011**, *119*, 891–895.
- (150) Thomas, A. G.; Vornov, J. J.; Olkowski, J. L.; Merion, A. T.; Slusher, B. S. N-Acetylated A-Linked Acidic Dipeptidase Converts N-Acetylaspartylglutamate from a Neuroprotectant to a Neurotoxin. *J. Pharmacol. Exp. Ther.* **2000**, *295*, 16–22.
- (151) Yao, Y.; Pattabiraman, N.; Michne, W. F.; Huang, X.-P.; Hampson, D. R. Molecular Modeling and Mutagenesis of the Ligand-Binding Pocket of the mGlu3 Subtype of Metabotropic Glutamate Receptor. *J. Neurochem.* **2003**, *86*, 947–957.
- (152) Glide, Version 6.7, Schrödinger, LLC, New York, NY, 2015.
- (153) Protein Preparation Wizard, Epik Version 2.2, Impact Version 5.7, Prime Version 3.0, Schrödinger, LLC., New York, NY, 2011.
- (154) Bitta, J.; Kubik, S. Cyclic Hexapeptides with Free Carboxylate Groups as New Receptors for Monosaccharides. *Org. Lett.* **2001**, *3*, 2637–2640.
- (155) Hartwig, S.; Nguyen, M. M.; Hecht, S. Exponential Growth of Functional Poly(Glutamic Acid) Dendrimers with Variable Stereochemistry. *Polym. Chem.* **2010**, *1*, 69–71.
- (156) More, S. S.; Vince, R. Inhibition of Glyoxalase I: The First Low-Nanomolar Tight-Binding Inhibitors. *J. Med. Chem.* **2009**, *52*, 4650–4656.
- (157) Koseki, Y.; Yamada, H.; Usuki, T. Efficient Synthesis of Benzyl 2-(S)-[(tert-Butoxycarbonyl)amino- Ω -Iodoalkanoates. *Tetrahedron: Asymmetry* **2011**, *22*, 580–586.
- (158) Brimble, M. A.; Trotter, N. S.; Harris, P. W. R.; Sieg, F. Synthesis and Pharmacological Evaluation of Side Chain Modified Glutamic Acid Analogues of the Neuroprotective Agent Glycyl-L-Prolyl-L-Glutamic Acid (GPE). *Bioorg. Med. Chem.* **2005**, *13*, 519–532.
- (159) Sachs, H.; Brand, E. Benzyl Esters of Glutamic Acid. *J. Am. Chem. Soc.* **1953**, *75*, 4610–4611.
- (160) Couturier, C.; Schlama, T.; Zhu, J. Synthetic Studies Towards (-)-Lemonomycin, Synthesis of Fused Tetracycles. *Synlett* **2006**, *11*, 1691–1694.
- (161) Reddy, A. V.; Ravindranath, B. Synthesis of A-, B-, and Cyclic Spaglumic Acids. *Int. J. Pept. Protein Res.* **1992**, *40*, 472–476.
- (162) Binkowski, B. F.; Fan, F.; Wood, K. V. Luminescent Biosensors for Real-Time Monitoring of Intracellular cAMP. In *Signal Transduction Protocols, Methods in Molecular Biology*; 2011; Vol. 756, pp. 263–271.
- (163) Seamon, K. B.; Padgett, W.; Daly, J. W. Forskolin: Unique Diterpene Activator of Adenylate Cyclase in Membranes and in Intact Cells. *Proc. Natl. Acad. Sci. U. S. A.* **1981**, *78*, 3363–3367.
- (164) Kubo, Y.; Miyashita, T.; Murata, Y. Structural Basis for a Ca²⁺-Sensing Function of the Metabotropic Glutamate Receptors. *Science (80-)*. **1998**, *279*, 1722–1725.
- (165) Kuang, D.; Hampson, D. R. Ion Dependence of Ligand Binding to Metabotropic Glutamate Receptors. *Biochem. Biophys. Res. Commun.* **2006**, *345*, 1–6.
- (166) Johnson, B. G.; Wright, R. A.; Arnold, B.; Wheeler, W. J.; Ornstein, P. L.; Schoepp, D. D. [3H]-LY341495 as a Novel Antagonist Radioligand for Group II Metabotropic Glutamate

- (mGlu) Receptors: Characterization of Binding to Membranes of mGlu Receptor Subtype Expressing Cells. *Neuropharmacology* **1999**, *38*, 1519–1529.
- (167) Johnson, E. C. N-Acetylaspartylglutamate Is Not Demonstrated To Be a Selective mGlu3 Receptor Agonist. *J. Neurochem.* **2011**, *119*, 896–898.
- (168) Baslow, M. H. The Astrocyte Surface NAAG Receptor and NAAG Peptidase Signaling Complex as a Therapeutic Target. *Drug News Perspect.* **2008**, *21*, 251–257.
- (169) Baslow, M. H. A Novel Key-Lock Mechanism for Inactivating Amino Acid Neurotransmitters during Transit Across Extracellular Space. *Amino Acids* **2010**, *38*, 51–55.
- (170) Diraddo, J. O.; Miller, E. J.; Bowman-Dalley, C.; Wroblewska, B.; Javidnia, M.; Grajkowska, E.; Wolfe, B. B.; Liotta, D. C.; Wroblewski, J. T. Chloride Is an Agonist of Group II and III Metabotropic Glutamate Receptors. *Mol. Pharmacol.* **2015**, *88*, 450–459.
- (171) Acher, F. C.; Selvam, C.; Pin, J.-P.; Goudet, C.; Bertrand, H.-O. A Critical Pocket Close to the Glutamate Binding Site of mGlu Receptors Opens New Possibilities for Agonist Design. *Neuropharmacology* **2011**, *60*, 102–107.
- (172) Ogawa, H.; Qiu, Y.; Philo, J. S.; Arakawa, T.; Ogata, C. M.; Misono, K. S. Reversibly Bound Chloride in the Atrial Natriuretic Peptide Receptor Hormone-Binding Domain: Possible Allosteric Regulation and a Conserved Structural Motif for the Chloride-Binding Site. *Protein Sci.* **2010**, *19*, 544–557.
- (173) Prime, Version 3.0, Schrödinger, LLC., New York, NY, 2011.
- (174) Ma, D.; Tian, H.; Sun, H.; Kozikowski, A. P.; Pshenichkin, S.; Wroblewski, J. T. Synthesis and Biological Activity of Cyclic Analogues of MPPG and MCPG as Metabotropic Glutamate Receptor Antagonists. *Bioorganic Med. Chem. Lett.* **1997**, *7*, 1195–1198.
- (175) Suzuki, G.; Tsukamoto, N.; Fushiki, H.; Kawagishi, A.; Nakamura, M.; Kurihara, H.; Mitsuya, M.; Ohkubo, M.; Ohta, H. In Vitro Pharmacological Characterization of Novel Isoxazopyridone Derivatives as Allosteric Metabotropic Glutamate Receptor 7 Antagonists. *J. Pharmacol. Exp. Ther.* **2007**, *323*, 147–156.
- (176) Mena, E. E.; Fagg, G. E.; Cotman, C. W. Chloride Ions Enhance L-Glutamate Binding to Rat Brain Synaptic Membranes. *Brain Res.* **1982**, *243*, 378–381.
- (177) Bridges, R. J.; Kesslak, J. P.; Nieto-Sampedro, M.; Broderick, J. T.; Yu, J.; Cotman, C. W. A L-[³H]Glutamate Binding Site on Glia: An Autoradiographic Study on Implanted Astrocytes. *Brain Res.* **1987**, *415*, 163–168.
- (178) Misono, K. S.; Philo, J. S.; Arakawa, T.; Ogata, C. M.; Qiu, Y.; Ogawa, H.; Young, H. S. Structure, Signaling Mechanism and Regulation of the Natriuretic Peptide Receptor Guanylate Cyclase. *FEBS J.* **2011**, *278*, 1818–1829.
- (179) Lundström, L.; Kuhn, B.; Beck, J.; Borroni, E.; Wettstein, J. G.; Woltering, T. J.; Gatti, S. Mutagenesis and Molecular Modeling of the Orthosteric Binding Site of the mGlu2 Receptor Determining Interactions of the Group II Receptor Antagonist 3H-HYDIA. *ChemMedChem* **2009**, *4*, 1086–1094.
- (180) Malherbe, P.; Knoflach, F.; Broger, C.; Ohresser, S.; Kratzeisen, C.; Adam, G.; Stadler, H.; Kemp, J. A.; Mutel, V. Identification of Essential Residues Involved in the Glutamate

- Binding Pocket of the Group II Metabotropic Glutamate Receptor. *Mol. Pharmacol.* **2001**, *60*, 944–954.
- (181) Fell, M. J.; Svensson, K. A.; Johnson, B. G.; Schoepp, D. D. Evidence for the Role of Metabotropic Glutamate (mGlu)₂ Not mGlu₃ Receptors in the Preclinical Antipsychotic Pharmacology of the mGlu_{2/3} Receptor Agonist (-)-(1R,4S,5S,6S)-4-Amino-2-sulfonylbicyclo[3.1.0]hexane-4,6-Dicarboxylic Acid (LY404039). *J. Pharmacol. Exp. Ther.* **2008**, *326*, 209–217.
- (182) Goudet, C.; Vilar, B.; Courtiol, T.; Deltheil, T.; Bessiron, T.; Brabet, I.; Oueslati, N.; Rigault, D.; Bertrand, H.-O.; McLean, H.; Daniel, H.; Amalric, M.; Acher, F.; Pin, J.-P. A Novel Selective Metabotropic Glutamate Receptor 4 Agonist Reveals New Possibilities for Developing Subtype Selective Ligands with Therapeutic Potential. *FASEB J.* **2012**, *26*, 1682–1693.
- (183) Christopoulos, A.; Changeux, J.-P.; Catterall, W. A.; Fabbro, D.; Burris, T. P.; Cidlowski, J. A.; Olsen, R. W.; Peters, J. A.; Neubig, R. R.; Pin, J.-P.; Sexton, P. M.; Kenakin, T. P.; Ehlert, F. J.; Spedding, M.; Langmead, C. J. International Union of Basic and Clinical Pharmacology. XC. Multisite Pharmacology: Recommendations for the Nomenclature of Receptor Allosterism and Allosteric Ligands. *Pharmacol. Rev.* **2014**, *66*, 918–947.
- (184) Laskowski, R. A.; MacArthur, M. W.; Moss, D. S.; Thornton, J. M. PROCHECK: A Program to Check the Stereochemical Quality of Protein Structures. *J. Appl. Crystallogr.* **1993**, *26*, 283–291.
- (185) Jafurulla, M.; Chattopadhyay, A. Sphingolipids in the Function of G Protein-Coupled Receptors. *Eur. J. Pharmacol.* **2015**, *In Press*.
- (186) Sjögren, B.; Svenningsson, P. Depletion of the Lipid Raft Constituents, Sphingomyelin and Ganglioside, Decreases Serotonin Binding at Human 5-HT_{7a} Receptors in HeLa Cells. *Acta Physiol.* **2007**, *190*, 47–53.
- (187) Singh, P.; Paila, Y. D.; Chattopadhyay, A. Role of Glycosphingolipids in the Function of Human Serotonin_{1A} Receptors. *J. Neurochem.* **2012**, *123*, 716–724.
- (188) Agnati, L. F.; Benfenati, F.; Battistini, N.; Cavicchioli, L.; Fuxe, K.; Toffano, G. Selective Modulation of 3H-Spiperone Labeled 5-HT Receptors by Subchronic Treatment with the Ganglioside GM1 in the Rat. *Acta Physiol. Scand.* **1983**, *117*, 311–314.
- (189) Björkholm, P.; Ernst, A. M.; Hacke, M.; Wieland, F.; Brügger, B.; Heijne, G. von. Identification of Novel Sphingolipid-Binding Motifs in Mammalian Membrane Proteins. *Biochim. Biophys. Acta* **2014**, *1838*, 2066–2070.
- (190) Wu, G.; Lu, Z.-H.; Wei, T. J.; Howells, R. D.; Christoffers, K.; Ledeen, R. W. The Role of GM1 Ganglioside in Regulating Excitatory Opioid Effects. *Ann. N. Y. Acad. Sci.* **1998**, *845*, 126–138.
- (191) Kishi, T.; Mukai, T.; Matsuda, Y.; Iwata, N. Selective Serotonin 3 Receptor Antagonist Treatment for Schizophrenia: Meta-Analysis and Systematic Review. *Neuromolecular Med.* **2014**, *16*, 61–69.
- (192) Meltzer, H. Y.; Massey, B. W. The Role of Serotonin Receptors in the Action of Atypical Antipsychotic Drugs. *Curr. Opin. Pharmacol.* **2011**, *11*, 59–67.

- (193) Fyrst, H.; Saba, J. D. An Update on Sphingosine-1-Phosphate and Other Sphingolipid Mediators. *Nat. Chem. Biol.* **2010**, *6*, 489–497.